

Μοριακή Προσομοίωση Υαλωδών Υλικών

Νικόλαος Ι. Λεμπέσης

Σεπτέμβριος 2013



Ευρωπαϊκή Ένωση
Ευρωπαϊκό Κοινωνικό Ταμείο



ΕΠΙΧΕΙΡΗΣΙΑΚΟ ΠΡΟΓΡΑΜΜΑ
ΕΚΠΑΙΔΕΥΣΗ ΚΑΙ ΔΙΑ ΒΙΟΥ ΜΑΘΗΣΗ
επένδυση στην κοινωνία της γνώσης

ΥΠΟΥΡΓΕΙΟ ΠΑΙΔΕΙΑΣ ΚΑΙ ΘΡΗΣΚΕΥΜΑΤΩΝ
ΕΙΔΙΚΗ ΥΠΗΡΕΣΙΑ ΔΙΑΧΕΙΡΙΣΗΣ

Με τη συγχρηματοδότηση της Ελλάδας και της Ευρωπαϊκής Ένωσης



ΕΥΡΩΠΑΪΚΟ ΚΟΙΝΩΝΙΚΟ ΤΑΜΕΙΟ

Η παρούσα έρευνα έχει συγχρηματοδοτηθεί από την Ευρωπαϊκή Ένωση (Ευρωπαϊκό Κοινωνικό Ταμείο - ΕΚΤ) και από εθνικούς πόρους μέσω του Επιχειρησιακού Προγράμματος «Εκπαίδευση και Δια Βίου Μάθηση» του Εθνικού Στρατηγικού Πλαισίου Αναφοράς (ΕΣΠΑ) – Ερευνητικό Χρηματοδοτούμενο Έργο: Ηράκλειτος ΙΙ. Επένδυση στην κοινωνία της γνώσης μέσω του Ευρωπαϊκού Κοινωνικού Ταμείου.

«Η έγκριση της Διδακτορικής Διατριβής από την Ανώτατη Σχολή Χημικών Μηχανικών του Εθνικού Μετσόβιου Πολυτεχνείου δεν υποδηλώνει αποδοχή των γνώμων του συγγραφέα. (Ν. 5343/1932, Άρθρο 202)»

Στον Θε(ί)ο μου

Ευχαριστίες

Η παρούσα εργασία εκπονήθηκε στο εργαστήριο Υπολογιστικής Επιστήμης και Μηχανικής των Υλικών του τομέα ΙΙΙ της σχολής Χημικών Μηχανικών του Εθνικού Μετσόβιου Πολυτεχνείου υπό την επίβλεψη του Καθηγητή κ. Θεόδωρου Ν. Θεοδώρου.

Λίγες σειρές στο εισαγωγικό σημείωμα μιας εργασίας δεν είναι επ' ουδενί αρκετές για να περικλείσουν τον απέραντο θαυμασμό και την αμέριστη εκτίμηση που νιώθω για το πρόσωπο ενός εξαιρετικού επιστήμονα και ενός ακόμη πιο σπάνιου και ευγενούς ανθρώπου, του επιβλέποντα Καθηγητή μου κ. Θεοδώρου. Είχα την τύχη και την τιμή να συνεργαστώ μαζί του στα πλαίσια της διπλωματικής μου εργασίας και μετέπειτα, κατά την εκπόνηση της διδακτορικής μου διατριβής. Όλον αυτόν τον καιρό δεν έπαυε ποτέ να αποτελεί για εμένα πρότυπο επιστήμονα, επαγγελματία, αλλά πολύ περισσότερο ευγενούς ανθρώπου. Τον ευχαριστώ για όλα.

Χρωστώ πάρα πολλά στη συνεργασία μου με επιφανείς επιστήμονες, αξιόλογους συνεργάτες, καλούς φίλους και προσωπικούς μέντορες, οι οποίοι κατά την διάρκεια των νηπιακών μου βημάτων στον χώρο της προσομοίωσης με μύησαν με αυταπάρνηση, δίχως το παραμικρό ίχνος έπαρσης, σε έναν επιστημονικό κόσμο εντελώς καινούριο για εμένα. Ανάμεσά τους, σε εξέχουσα θέση, οι Δρ. Γεώργιος Μπουλουγούρης, Δρ. Λουκάς Περιστεράς και ο Δρ. Δημήτριος Τσαλίκης. Θα τους είμαι για πάντα ευγνώμων.

Δεν θα μπορούσα να παραβλέψω να ευχαριστήσω όλα τα μέλη της ομάδας Υπολογιστικής Επιστήμης και Μηχανικής των Υλικών για την άψογη συνεργασία και στήριξη. Ιδιαίτερα ευχαριστώ τους συναδέλφους, συνοδοιπόρους και φίλους κ. Γεώργιο Βογιατζή και κ. Ιωάννη Μαθιουδάκη με τους οποίους περάσαμε αμέτρητες

ώρες εργαζόμενοι και συνεργαζόμενοι δίπλα δίπλα. Τους ευχαριστώ και τους εύχομαι από καρδιάς τα καλύτερα.

Περνώντας τώρα στους εκτός ακαδημαϊκού χώρου, θεωρώ πως ό,τι λόγια και να χρησιμοποιήσω δεν θα είναι αρκετά για να μπορέσω να περικλείσω την ευγνωμοσύνη μου προς τα μέλη της οικογένειάς μου, που ενώ τους παίδεψα αρκετά, δεν έπαψαν στιγμή να με στηρίζουν και να πιστεύουν σε εμένα.

Έχει ειπωθεί, κατά καιρούς, από πολλούς λόγιους και με αρκετούς διαφορετικούς τρόπους: Η περιουσία του ανθρώπου είναι οι φίλοι του. Μιχάλη, Θανάση, Χάρη, Δημήτρη, Γιάννη, Γιώργο και Χρήστο είμαι ο πλουσιότερος άνθρωπος του κόσμου. Σας ευχαριστώ!

Τη μεγαλύτερη ευγνωμοσύνη τη χρωστώ στον Θεό που ήταν οδηγός, καταφυγή και στήριγμά μου σε όλα τα βήματα της μέχρι τώρα ζωής μου.

Έρρωσθε

Εκτεταμένη περίληψη

Η παρούσα εργασία αποσκοπεί στην μελέτη των σχέσεων δομής-ιδιοτήτων που διέπουν την ύλη. Συγκεκριμένα, άμεσος στόχος αποτελεί η διερεύνηση μιας ιδιαίτερης κατηγορίας υλικών, αυτής των αμόρφων στερεών. Η κύρια ιδιαιτερότητα των αμόρφων υλικών έγκειται στο γεγονός πως μπορούν και εμφανίζουν χαρακτηρισικά τόσο της στερεάς, όσο και της υγρής φάσης. Συγκεκριμένα, στα άμορφα στερεά μπορεί να παρατηρηθεί έλλειψη τάξεως μακράς εμβέλειας στη δομή τους ενώ εμφανίζουν χρονικά εξαρτώμενη παραμόρφωση ως απόκριση σε μεγάλη εξωτερικά επιβαλλόμενη τάση (συμπεριφορά, ανάλογη με αυτή των υγρών). Από την άλλη μεριά, μπορούν να διατηρούν την γεωμετρία τους, να υποστηρίξουν την επιβολή διατμητικής τάσης, και να επιστρέψουν στο αρχικό τους σχήμα κατόπιν κατάργησης μικρής εξωτερικά επιβαλλόμενης τάσης (συμπεριφορά, ανάλογη με αυτή των στερεών). Υπό αυτή την έννοια, τα άμορφα υλικά εμφανίζουν χαρακτηρισικά τόσο στερεάς, όσο και υγρής φάσης.

Χαρακτηριστικοί αντιπρόσωποι των αμόρφων υλικών είναι οι ύαλοι ή υαλώδη υλικά. Τα υαλώδη υλικά θεωρούνται άμορφα στερεά. Παρά το γεγονός ότι θεωρούνται στερεά, εμφανίζουν διαταραγμένη και ακανόνιστη δομή, όπως τα υγρά, ενώ από την άλλη, η μοριακή κίνηση σε αυτά απαρτίζεται κυρίως από δονήσεις γύρω από καταστάσεις ισορροπίας και η διάχυση εντός τους είναι εξαιρετικά αργή, όπως ακριβώς στα στερεά.

Είναι εμφανές πως η μελέτη των υαλωδών υλικών είναι μεγάλου επιστημονικού ενδιαφέροντος, καθώς μπορεί να αποκαλύψει μέχρι τώρα άγνωστους μηχανισμούς – είτε σε ατομικό, μοριακό, είτε σε περισσότερο αδροποιημένο επίπεδο – οι οποίοι δεν είναι παρόντες σε καμία άλλη περίπτωση υλικών. Επιπρόσθετα, οι περιορισμοί και οι

προϋποθέσεις κάτω από του οποίους οι εν λόγω φυσικοί μηχανισμοί δρουν εμφανίζουν ιδιαίτερο ενδιαφέρον. Είναι γνωστό πως οι ιδιότητες των υαλωδών υλικών εξαρτώνται έντονα αφενός από την διαδικασία σχηματισμού τους, και αφετέρου από τις συνθήκες στις οποίες βρίσκονται. Ένα επιπρόσθετο γνώρισμα των υλικών αυτού του τύπου είναι πως οι ιδιότητές τους παρουσιάζουν χρονική εξάρτηση. Αυτή είναι μία ισχυρή ένδειξη πως αυτά τα υλικά βρίσκονται εκτός θερμοδυναμικής ισορροπίας, ενώ χαρακτηρίζονται από μία διαρκή προσπάθεια προσέγγισής της. Αυτό είναι και το κύριο χαρακτηριστικό γνώρισμα των υαλωδών υλικών, ένα φαινόμενο που είναι ευρύτερα γνωστό ως φυσική γήρανση.

Η κατανόηση των υαλωδών υλικών και κατ' επέκταση η ικανότητα ελέγχου των ιδιοτήτων τους εμφανίζει εξίσου μεγάλο τεχνολογικό ενδιαφέρον. Τα άμορφα στερεά είναι παρόντα σε κάθε πτυχή της σημερινής ζωής και ο ρόλος τους είναι κατά πολύ πιο σημαντικός απ' ότι κάποιος διαισθητικά θα νόμιζε. Αυτό κυρίως οφείλεται στο γεγονός πως η χρήση τους δεν περιορίζεται στα παραδοσιακά ανόργανα γυαλιά, όπως αυτά των μπουκαλιών και των τζαμιών, αλλά εκτείνεται και συμπεριλαμβάνει την πολύ σημαντική κατηγορία των οργανικών (κυρίως πολυμερικών) γυαλιών. Σήμερα είναι γνωστό πως αρκετά πολυμερικά γυαλιά εμφανίζουν υαλώδη μετάπτωση σε θερμοκρασίες πολύ κοντά ή και πάνω από τη θερμοκρασία δωματίου. Υλικά σαν κι αυτά [π.χ. πολυστυρένιο (PS), πολυαιθυλενοτερεφθαλικός εστέρας (PET), πολυμεθακρυλικός μεθυλεστέρας (PMMA), πολυ(ανθρακικός εστέρας της διφαινόλης-A) (PC), πολυιμίδια] βρίσκουν αναρίθμητες εφαρμογές ως δομικά υλικά, υλικά μονώσεως, υλικά συσκευασίας με ελεγχόμενες ιδιότητες φραγής, μεμβράνες με διαπερατότητα και εκλεκτικότητα κατάλληλες για διαχωρισμούς αερίων, υλικά κατασκευής CDs, διηλεκτρικά στη μικροηλεκτρονική, επιφανειακά επιστρώματα κ.ά. Αξίζει να αναφερθεί πως ο πολύ πρόσφατα εφευρεθείς Ουψαλίτης (Upsalite), ονομασθέντας από το πανεπιστήμιο της Ουψάλα, όπου συντέθηκε για πρώτη φορά, αποτελεί ένα ανόργανο άμορφο στερεό (ανθρακικό Μαγνήσιο) με τη μεγαλύτερη ειδική επιφάνεια ($\sim 800 \text{ m}^2/\text{g}$) και εξαιρετικές προσροφητικές ικανότητες.

Οι μηχανικές ιδιότητες των υαλωδών υλικών εμφανίζουν μία μοναδική εξάρτηση από τη χημική σύσταση και την θερμική ιστορία σχηματισμού. Συγκεκριμένα, το σημείο διαρροής μερικών υαλωδών πολυμερών έχει παρατηρηθεί να αυξάνεται κατά την διαδικασία της φυσικής γήρανσης και αντίστροφα. Η τελευταία παρατήρηση βρίσκει θεαματική εφαρμογή στην «μηχανική ανανεοποίηση» (mechanical rejuvenation)

των γυαλιών, όπου κανονικώς ψαθυρά υαλώδη υλικά (π.χ. PS) γίνονται όλκιμα κατόπιν έντονης μηχανικής παραμόρφωσης (πέραςμα από έναν κυλινδρόμυλο). Η όλκιμη συμπεριφορά διαρκεί μερικές ώρες, μέχρις ότου υπερκερασθεί από τη φυσική γήρανση του υλικού.

Οι μοριακές προσομοιώσεις αποτελούν ένα βασικό και αποτελεσματικό εργαλείο για την μελέτη της συμπεριφοράς των υλικών, καθώς είναι σε θέση να εκτιμήσουν με μεγάλη ακρίβεια θερμοδυναμικές, δυναμικές και, αν συνδυαστούν κατάλληλα με άλλες τεχνικές, μηχανικές και ροϊκές ιδιότητες. Επιπρόσθετα, οι μοριακές προσομοιώσεις με την βοήθεια της στατιστικής μηχανικής μπορεί να αποτελέσουν τον συνδετικό κρίκο μεταξύ του μικροσκοπικού και του μακροσκοπικού κόσμου, παρέχοντας τη σύνδεση, με λήψη κατάλληλων στατιστικών μέσων πάνω στις διάφορες μικροκαταστάσεις, μεταξύ μικρόκοσμου και μακροσκοπικά παρατηρούμενων ιδιοτήτων. Σε αυτή την εργασία χρησιμοποιούμε διαφορετικές τεχνικές μοριακών προσομοιώσεων, εκμεταλλευόμενοι τη σχετικά ευρεία ποικιλία σχημάτων για την εφαρμογή αυτών των τεχνικών, με απώτερο σκοπό να προσομοιώσουμε δύο φαινόμενα: α) το φαινόμενο της φυσικής γήρανσης στα υαλώδη υλικά και β) την απόκριση αυτών των υλικών σε μηχανική παραμόρφωση.

Ύψιστος σκοπός αυτής της εργασίας είναι να συνδιαστούν κατάλληλα τα δύο προαναφερθέντα φαινόμενα και να μελετηθούν ως ένα. Αυτό μπορεί να επιτευχθεί μέσω ελέγχου του φαινομένου της φυσικής γήρανσης για την χρονική εξέλιξη του συστήματος, στο οποίο σε τακτά χρονικά διαστήματα επιβάλλεται μία διαρκώς αυξανόμενη εξωτερική παραμόρφωση ώστε προοδευτικά να φτάσουμε σε παραμορφώσεις εντός της πλαστικής περιοχής. Ένα από τα βασικότερα εμπόδια στην προσπάθεια αυτή αποτελεί η επιθυμία μας να προσομοιωθεί η διαδικασία αυτή με επιβαλλόμενους ρυθμούς παραμόρφωσης όσο το δυνατόν πιο κοντά στους πειραματικά χρησιμοποιούμενους, ώστε να είναι εφικτή και η σύγκριση με αντίστοιχες πειραματικά μετρούμενες τιμές ιδιοτήτων.

Κατά την προσπάθειά μας να σχεδιαστεί ένας αυτοσυνεπής, αποτελεσματικός αλγόριθμος ικανός να προσομοιώσει επιτυχώς το παραπάνω πείραμα, αντιμετώπιστηκαν αποτελεσματικά ένα μεγάλο σύνολο από επιμέρους μικρότερα προβλήματα. Συγκεκριμένα, προκειμένου να μελετηθεί η χρονική εξέλιξη του μελετούμενου συστήματος στο χρόνο χρησιμοποιήσαμε την μεθοδολογία των εγγενών

δομών. Σύμφωνα με την μεθοδολογία αυτή, η χρονική εξέλιξη του υαλώδους συστήματος μπορεί να θεωρηθεί ότι συμβαίνει μέσω στοιχειωδών μεταβάσεων μεταξύ λεκανών δυναμικής ενέργειας (basins). Με την εισαγωγή της έννοιας των στοιχειωδών μεταβάσεων μεταξύ λεκανών στην υπερεπιφάνεια ενέργειας και τον υπολογισμό των σταθερών ρυθμού $k_{i \rightarrow j}$ γι' αυτές τις μεταβάσεις, υποθέτοντας ότι το σύστημα παραμένει επί αρκετό χρόνο μέσα σε κάθε λεκάνη μεταξύ διαδοχικών μεταβάσεων, έτσι ώστε να κατανεμηθεί στο εσωτερικό της σύμφωνα με τις απαιτήσεις μιας περιορισμένης (εντός λεκάνης) θερμοδυναμικής ισορροπίας και να «ξεχάσει» πώς ακριβώς εισήλθε στη λεκάνη, η δυναμική του συστήματος αδροποιείται σε μια στοχαστική ανέλιξη Poisson πάνω σε ένα πλέγμα λεκανών (ή «καταστάσεων») συνδεδεμένων μεταξύ τους μέσω των στοιχειωδών μεταβάσεων. Στα πλαίσια αυτής της εργασίας έγινε χρήση μίας νέας μεθοδολογίας, βασισμένη στις ιδιότητες των στοχαστικών ανελιξεων Poisson και τη θεωρία χρόνου πρώτης προσπέλασης (first passage time analysis) για τη χαρτογράφηση αυτού του δικτύου και την παρακολούθηση της κατανομής του συστήματος ανάμεσα στις καταστάσεις συναρτήσει του χρόνου.

Το δίκτυο των λεκανών που προσδιορίζεται κάνοντας χρήση του παραπάνω αλγορίθμου μπορεί να γίνει εξαιρετικά μεγάλο, δυσχεραίνοντας την ταχύτητα των υπολογισμών πάνω σε αυτό. Αυτό αποτελεί ένα επιπρόσθετο πρόβλημα που έπρεπε να υπερκεράσουμε στην προσπάθεια μελέτης της δυναμικής συμπεριφοράς του συστήματος σε μεγάλης κλίμακας χρόνους. Η λύση του προβλήματος αυτού επιτεύχθηκε μέσω της σχεδίασης ενός κατάλληλου αλγορίθμου για την αδροποίηση του αρχικού, μεγάλης διαστατικότητας, συστήματος. Η μεθοδολογία αυτή μειώνει επιλεκτικά την διαστατικότητα ενός οσοδήποτε μεγάλου αρχικού συστήματος. Το προκύπτον ισοδύναμο σύστημα καταστάσεων μειωμένης διάστασης είναι σε θέση να περιγράψει την δυναμική του αρχικού συστήματος καταστάσεων σε μεγάλους χρόνους, δίχως σημαντική απώλεια σε πληροφοριακό πλούτο αναφορικά με αυτήν.

Το δίκτυο λεκανών, όπως προσδιορίζεται από τη μέθοδο DIMW, αποτελεί μια αδροποιημένη, διακριτοποιημένη αναπαράσταση του χώρου απεικονίσεων. Υιοθετώντας την εικόνα μιας στοχαστικής ανελιξης Poisson για τη χρονική εξέλιξη της κατανομής του συστήματος σ' αυτό το δίκτυο, μπορεί κανείς να επιλύσει αναλυτικά το σύστημα διαφορικών εξισώσεων που διέπει την ανέλιξη (master

equation) υπό συγκεκριμένες αρχικές συνθήκες. Η πιθανότητα κατάληψης κάθε λεκάνης προκύπτει ως άθροισμα φθινουσών εκθετικών συναρτήσεων του χρόνου, όπου οι χαρακτηριστικοί χρόνοι των «τρόπων χαλάρωσης» (relaxation modes) που εμφανίζονται στα εκθετικά σχετίζονται άμεσα με τις ιδιοτιμές του πίνακα σταθερών ρυθμού των μεταβάσεων στην εξίσωση master. Με βάση αυτήν την αναλυτική λύση, αναπτύξαμε μια μεθοδολογία στα πλαίσια της παρούσας εργασίας για την γραφική απεικόνιση του συστήματος των καταστάσεων και της χρονικής εξέλιξης αυτού.

Η μεθοδολογία αυτή μπορεί α) να βοηθήσει τον προαναφερθέν αλγόριθμο αδροποίησης να συγκλίνει γρηγορότερα και β) παρέχει μία εναλλακτική γραφική απεικόνιση της υπερεπιφάνειας δυναμικής ενέργειας και της εξέλιξης του συστήματος πάνω σε αυτή. Τα πλεονεκτήματα της εν λόγω μεθόδου έναντι εναλλακτικών μεθόδων απεικόνισης είναι δύο. Αρχικά, η προτεινόμενη μέθοδος, την οποία αποκαλούμε διάγραμμα χρονικής αποσυσχέτισης (temporal disconnectivity graph), εμπεριέχει την έννοια του χρόνου και δίνει την πληροφορία της χρονικής εξέλιξης του συστήματος πάνω στην υπερεπιφάνεια δυναμικής ενέργειας, ενώ άλλες μέθοδοι απεικόνισης παρέχουν στιγμιότυπα (snapshots) της υπερεπιφάνειας του συστήματος. Επίσης, η γραφική αυτή μέθοδος προσφέρει την παρακολούθηση κάθε μιας κατάστασης ξεχωριστά. Με τον τρόπο αυτό προσφέρεται η πληροφορία της ταυτότητας της κάθε κατάστασης και πολύ σημαντικότερα του πότε θα αποκατασταθεί μία περιορισμένη (στα πλαίσια μίας λεκάνης) ισορροπία μεταξύ διαφόρων καταστάσεων. Ως συνέπεια, μπορεί να παρακολουθηθεί η συνδετικότητα μεταξύ καταστάσεων ως συνάρτηση του χρόνου και να αποκαλυφθούν μηχανισμοί διάχυσης μεταξύ των πληθυσμών επικοινωνούντων καταστάσεων.

Η μηχανική παραμόρφωση υαλωδών υλικών αποτελεί το δεύτερο σκέλος του γενικού προβλήματος προσομοίωσης. Το φαινόμενο αυτό προσεγγίζεται με τη βοήθεια κατάλληλα σχεδιασμένου αλγορίθμου, ο οποίος παραμορφώνει το υπό μελέτη σύστημα βηματικά. Και σε αυτήν την περίπτωση, το κύριο πρόβλημα διαχωρίζεται σε περισσότερα του ενός επιμέρους υπο-προβλήματα. Ένα μεγάλο μέρος του αλγορίθμου αφιερώνεται στην διαδικασία παραμόρφωσης των ελαχίστων ενέργειας Gibbs και των παρεμβαλλόμενων σαγματικών σημείων, μέσω των οποίων διέρχεται το σύστημα κατά τις στοιχειώδεις μεταβάσεις μεταξύ ελαχίστων ενέργειας Gibbs. Επιπρόσθετα, η συνδετικότητα μεταξύ των ελαχίστων θα πρέπει να επανεκτιμηθεί κατόπιν παραμορφώσεως. Στη συνέχεια, το αποτέλεσμα αυτής της διαδικασίας θα πρέπει να

συζευκτεί με τον αλγόριθμο χρονικής εξέλιξης του συστήματος (DIMW) ώστε να εξισορροπήσει το σύστημα την επιφερόμενη μεταβολή λόγω παραμορφώσεως. Η παραπάνω διαδικασία επαναλαμβάνεται όσπου να περάσουμε το σημείο διαρροής και να εισέλθουμε στην περιοχή πλαστικής παραμόρφωσης. Όλες οι μέθοδοι που αναπτύχθηκαν στα πλαίσια αυτής της εργασίας έχουν ως άμεση προτεραιότητα να συνεισφέρουν στον απώτερο σκοπό της προσομοίωσης πειραμάτων παραμόρφωσης υαλώδων υλικών υπό ρεαλιστικούς ρυθμούς παραμόρφωσης.

Στην εργασία αυτή εκτιμήθηκαν οι ελαστικές σταθερές (μέτρο Young και λόγος Poisson) του υαλώδους ατακτικού πολυστυρενίου μέσω υπολογιστικών πειραμάτων επιβαλλόμενης μοναξονικής (εφελκυστικής και θλιπτικής) τάσης στην ελαστική περιοχή κάνοντας χρήση της οιονεί αρμονικής προσέγγισης (quasi harmonic approximation) για την εκτίμηση της θερμικής συνεισφοράς του συστήματος στην συνολική ενέργεια. Οι εκτιμηθείσες τιμές βρέθηκαν πολύ κοντά σε πειραματικά μετρούμενες τιμές. Επιπλέον, η θερμοκρασιακή εξάρτηση των εκτιμώμενων ελαστικών σταθερών βρέθηκε να έχει την θεωρητικά αναμενόμενη μορφή και είναι σε πλήρη συμφωνία με την πειραματικά παρατηρούμενη.

Η ογκομετρική συμπεριφορά του υαλώδους ατακτικού πολυστυρενίου προσομοιώθηκε α) με χρήση της οιονεί αρμονικής προσέγγισης και β) μέσω προσομοιώσεων μοριακής δυναμικής και τα αποτελέσματα βρέθηκαν σε παρα πολύ καλή συμφωνία μεταξύ τους, αλλά και με αντίστοιχες πειραματικές μετρήσεις από πειράματα απότομης ψύξης τήγματος ατακτικού πολυστυρενίου. Ακόμα, η θερμοδυναμική συνέπεια της οιονεί αρμονικής προσέγγισης ελέγχθηκε και πιστοποιήθηκε η ορθότητά της. Μέσω της καμπυλότητας των καμπυλών της ελάχιστης ενέργειας Gibbs με την παραμόρφωση υπολογίστηκε το μέτρο Young και βρέθηκε να είναι σε πολύ καλή συμφωνία με τις προκύπτουσες τιμές από την κλίση των καμπυλών τάσης-παραμόρφωσης για την ελαστική περιοχή. Τα αποτελέσματα αυτής της εργασίας δείχνουν πως ο συνδυασμός της χρήσης ελαχίστων στην υπερέπιφάνεια δυναμικής ενέργειας, μαζί με την οιονεί αρμονική προσέγγιση, παρέχει ακριβείς εκτιμήσεις της ογκομετρικής συμπεριφοράς και της μηχανικής απόκρισης του συστήματος σε μικρές παραμορφώσεις στην ελαστική περιοχή για το υαλώδες ατακτικό πολυστυρένιο. Τέλος, παρατηρήθηκε πως η απόκριση του πεδίου ενέργειας σε επιβαλλόμενη μηχανική καταπόνηση μπορεί να οδηγήσει στον σχηματισμό νέων ελαχίστων ενέργειας ή στην καταστροφή

προϋπάρχοντων. Η παρατήρηση αυτή μας οδηγεί στο συμπέρασμα πως η υπερεπιφάνεια ενέργειας αλλάζει το σχήμα της με την επιβολή τάσης παραμόρφωσης.

Τέλος, σημαντικές προσπάθειες καταβλήθηκαν στα πλαίσια της παρούσας εργασίας για την βελτίωση της απόδοσης του αλγορίθμου για την προρομοίωση της φυσικής γήρανσης και της μηχανικής παραμόρφωσης. Στα πλαίσια αυτής της προσπάθειας, ύπο-διεργασίες αυτού του μεγάλου αλγορίθμου τροποποιήθηκαν κατάλληλα ώστε να επιτευχθεί η παραλληλοποίησή τους. Αυτή η τροποποίηση μπορεί να οδηγήσει σε σημαντική μείωση του αναγκαίου υπολογιστικού χρόνου. Απαιτητικές διεργασίες σε υπολογιστικό χρόνο όπως ο υπολογισμός και η ελαχιστοποίηση της ενέργειας, ο υπολογισμός δυνάμεων ως παράγωγοι της δυναμικής ενέργειας ως προς όλες τις καρτεσιανές συντεταγμένες, ο υπολογισμός της εσσιανής μήτρας και η διαγωνοποίησή της τροποποιήθηκαν κατάλληλα ώστε να είναι εφικτός ο παράλληλος υπολογισμός τους. Το επόμενο βήμα στην προσπάθεια παραλληλοποίησης θα είναι η ανάθεση ενός επεξεργαστή σε κάθε μία από τις συνολικά $3N$ διαστάσεις του χώρου των απεικονίσεων, όπου N ο αριθμός των συμμετέχοντων ατόμων.

Summary

This work is dedicated to the study of the structure-property-function relationships of glassy materials by utilizing computational experiments conducted with molecular simulation techniques that translate to the cutting edge of materials research. Glassy materials constitute one basic representative of the category of amorphous materials. Amorphous materials are materials whose properties are a hybrid of solid and liquid properties. In particular, materials belonging to this category can show lack of long-range order in their structure and time-dependent deformation in response to the imposition of large external stresses (as liquids generally do), whereas at the same time they can retain their geometry, support shear stresses and return to their initial shape upon removal of small external stresses (as solids generally do). In that sense, glassy materials have both solid and liquid characteristics. In particular, glasses are considered to be amorphous solids. On the one hand, they exhibit a disordered structure, as liquids do, whereas, on the other hand, molecular motion in them consists mainly of vibrations around equilibrium positions, as in solids, and translational diffusion is very slow.

Clearly, the study of these amorphous materials is of great scientific importance, as it can reveal unknown mechanisms – whether at an atomic, molecular, or more coarse-grained level – which are not applicable to any of the three known states of matter. Moreover, the constraints under which these physical mechanisms act are also of great importance, as it is known that the properties of amorphous materials depend strongly not only on their formation process, but also on the conditions under which they find themselves. Another unique characteristic of this type of materials is that their properties change with time. This is a strong indication that these materials are out of thermodynamic equilibrium and constantly striving to approach it.

Understanding glasses, and therefore being able to control their properties, is of great technological significance as well. Amorphous materials are present in every aspect of our everyday life and their role is far more important and essential than one would intuitively expect. This happens because their use is not limited to the traditional inorganic glasses, such as wine bottles and window panes, but includes also the technologically most important category of organic (usually polymer) glasses. Today, polymer glasses exhibiting glass transition at temperatures above room temperature [e.g. polystyrene (PS), polyethylene terephthalate (PET), poly(methyl methacrylate) (PMMA), polycarbonates (PC) and polyimides] find countless applications as construction and insulation materials, membranes with specific permeability and selectivity etc. It's worth mentioning that recently developed Upsalite, named after the University of Uppsala where it has been synthesized for the first time, is an inorganic amorphous solid (magnesium carbonate) with world record breaking surface area ($\sim 800 \text{ m}^2/\text{g}$) and water adsorption abilities.

The mechanical properties of glassy materials show a unique dependence on their chemical constitution and their thermal-mechanical history of formation. In particular, the yield point of some glassy polymers has been seen to increase over natural ageing and reversely, to decrease when the glassy specimen is subjected to large plastic deformation. The later observation finds tremendous usage in mechanical rejuvenation of glasses, where initially brittle glassy materials (e.g. PS) become ductile upon imposition of plastic deformation. All the above observations make obvious the necessity for additional research of this type of materials.

Molecular simulations constitute one basic and efficient tool for materials research, as they can in many cases accurately estimate thermodynamic, dynamic and, if appropriately coupled to other techniques, mechanical and flow properties. In addition, molecular simulations with the help of statistical mechanics are able to provide the missing link between the microscopic world and macroscopically observed properties, providing insight into mechanisms of phenomena taking place at the microscopic level whose effect is observed as a change in one or more macroscopic properties of the system, e.g., increase of the modulus of elasticity. In this work, we make use of different molecular simulation techniques and we exploit the relatively large variety of schemes which can be applied to each one of them in order to simulate two phenomena

observed in glassy materials: a) the physical ageing of glasses and b) their response to mechanical deformation.

The ultimate objective of this work is to couple the two above mentioned phenomena and study them as one through monitoring the physical ageing of a glassy material which is being deformed by gradually increasing deformations that reach deep into the plastic regime. One of the basic obstacles in realizing this objective is that the rate of the deformation experiments should be as close as possible to experimentally applied rates. In order to succeed in providing a self-consistent algorithm able to successfully simulate the above experiment, several other difficulties encountered during this effort have to be overcome. According to our approach, initially designed by former members of our research group, the evolution in time is viewed as a succession of infrequent events. It proceeds via accessing new states, or basins of the energy in configuration space, which are connected via transition paths to an already existing network of states. When new connections between states are explored and the rate of transitions for those connections is calculated, the system can be allowed to evolve in time.

Another basic obstacle we have to overcome is that a way has to be found to efficiently reduce the number of states that have to be considered as the system evolves in time and therefore the network of accessed states expands. This is accomplished through a specially designed lumping algorithm which selectively reduces the size of the original network of states. The resulting lumped system is in a position to fully describe the long-time dynamics of the original system without severe loss of information. Moreover, a technique has been developed for visualizing the network, which can (a) help the lumping algorithm converge to a solution faster and (b) provide an alternative representation of the time evolution of the system instead of the typical snapshot-representation. This graphical representation, which we call temporal disconnectivity graph, reveals new information that is not available through currently available representation schemes. In particular, each single state can be separately monitored over time, as its identity is known and can be tracked at different times to see how this state changes with time. As a consequence, connectivity between given states can also be monitored over time, revealing diffusion mechanisms between the populations of communicating states.

The mechanical deformation of glassy materials, constituting the second part of the general simulation problem, is treated through specially designed algorithms which deform the studied system stepwise. Again this particular problem is broken down into several sub-problems. A large part of the designed algorithm is dedicated to the deformation of the potential energy minima and the first order saddle points traversed through transition paths between the minima. In addition, the connectivity between the distorted minima has to be re-evaluated through a re-scaling methodology applicable to the already existing connectivity prior to deformation. Then, the result of this process has to be successfully coupled to the time-evolution mechanism described above in order to relax the system and let it evolve in time through exploration of new states. This process repeats itself until the yield point is surpassed and the plastic regime is reached. All methods developed in the context of this work contribute to the purpose of simulating glass deformation at realistic strain rates by solving several problems arising on the way.

In addition, significant efforts in this thesis have been devoted to increasing the computational efficiency of the algorithm developed for tracking physical ageing and deformation. To this end, sub-processes of this major-algorithm which cost both in computation time and in memory space have been appropriately modified in order to run in parallel. This modification can lead to very significant reduction of computational time. Computational expensive processes such as potential energy calculation and minimization, force calculation, Hessian-matrix calculation and diagonalization have been appropriately designed to run in parallel. The next step of parallelization would be to dedicate each involved processor in exploring one certain direction of the $3N$ -dimensional configuration space, N being the number of participating atoms.

Contents

1. Introduction	1
1.1 Amorphous solids	1
1.2 Motivation and scope of this work	8
2. Glassy materials	11
2.1 Crystal, supercooled liquid, and glassy state	11
2.2 General aspects of the glassy state	20
2.3 Theories describing the glass transition	25
2.3.1 Free volume theory	26
2.3.2 Configurational entropy theory	30
2.3.3 Mode coupling theory	34
2.3.4 Other theories	37
2.4 Molecular simulation techniques for glassy materials	40
2.4.1 Force field and initial configuration generation	42
2.4.2 Molecular mechanics	50
2.4.3 Molecular dynamics	52
2.4.4 Monte Carlo simulation techniques	60

3. Structural rearrangement in transitions between basins and metabasins	66
3.1 Introduction	68
3.2 Rare event theory	72
3.2.1 Poisson process	75
3.2.2 Monomolecular reaction system	76
3.3 Topological structure of the potential energy hypersurface: Basins and metabasins	78
3.4 Results and discussion	82
4. Structural and temporal coarse-graining with respect to long-time dynamics: Lumping analysis	88
4.1 Introduction	89
4.2 The lumping algorithm	93
4.2.1 The transformation matrix \mathbf{M}	93
4.2.2 Monte Carlo moves on the transformation matrix	95
4.2.3 The lumping criteria	98
4.3 Structure of simulations	105
4.4 Implementation of the lumping algorithm	114
4.4.1 Time evolution of the system	116
4.4.2 Lumping	118
4.5 Conclusions	126
5. Temporal evolution on the potential energy landscape	129
5.1 Introduction	130

5.2 A new graphical representation of the potential energy landscape: the temporal disconnectivity graph	134
5.3 Methodological and computational details	142
5.4 Results and discussion	143
5.5 Conclusions	154
6. Mechanical deformation computational experiments on glassy atactic polystyrene	156
6.1 Introduction	157
6.2 Model system and methods	159
6.2.1 Generation of glassy configurations	161
6.2.2 Quasiharmonic approximation	161
6.3 Computational deformation experiments	167
6.4 Results and discussion	171
6.5 Conclusions	186
7. Main conclusions and innovations	188
8. Research outlook	191
9. List of typical symbols	194
10. References	201

Appendix A: Force field description and contributions to the total potential energy function for the united atom model of atactic polystyrene **212**

Appendix B: Assessment of the efficiency of the Wang-Landau Algorithm in sampling the configuration space of the lumping problem **221**

Curriculum Vitae **227**

Chapter 1

Introduction

This work is focused on the molecular simulation of the response of glass forming materials to the imposition of different external stimuli and time. Glasses are characteristic representatives of a more general category of materials; the amorphous solids. Due to their great technological and fundamental significance, amorphous solids will constitute the main point of interest of this chapter. In the following sections, amorphous solids will be sufficiently described and analyzed and it will be shown that their complexity and unique properties motivated the current work.

1.1 Amorphous solids

Traditionally, when one speaks of solid state it is in most cases understood that the discussion is about crystalline solids. Solidity and crystallinity are two terms that are often used interchangeably as being synonymous. Yet, one of the most active fields of solid-state research in recent years has been the study of solids that are not crystalline. These are solids in which the arrangement of atoms lacks one fundamental characteristic of crystalline solids, the long-range order. In other words, the periodicity that characterizes crystal lattices and allows the formation of the entire crystal from the equilibrium positions of a small number of atoms constituting the unit cell is absent in amorphous solids. In particular, the fundamental difference between crystalline and amorphous solids lies in the basic nature of their microscopic

structure. In crystals, the equilibrium positions of atoms or ions exhibit long-range order, whereas in amorphous solids, long-range order is absent; the set of equilibrium atomic positions is strongly disordered.

Figure 1.1 schematically represents the most notable characteristics of the atomic arrangements in amorphous solids as opposed to crystalline solids. Additionally, a drawing of the atomic arrangements in a gas is also included as a point of comparison. For the sake of simplicity all three parts of Figure 1.1 are drawn in two dimensions, but the essential points carry over to their actual, three-dimensional counterparts. For the two sketches representing the ideal crystal (a) and amorphous solid (b), the solid dots denote the equilibrium positions about which the atoms are expected to oscillate. For the gas (c), the dots correspond to a snapshot of one atomic configuration – out of infinite possible ones – of instantaneous atomic positions.

By observing Figure 1.1 it is obvious that for the amorphous solid, the essential aspect in which its structure differs from that of a crystalline solid is the absence of long-range order. There is no translational periodicity. On the other hand, the atomic positions in the amorphous solid are not completely randomly distributed in space. This is more or less the case with the third part of Figure 1.1, describing the gas, where atoms are expected to move in a completely uncorrelated and random fashion, at least in the low-density limit in which the atoms of the gas may be viewed as point particles.

Direct comparison of Figures 1.1(b) and 1.1(c) makes evident at a glance that in the case of the amorphous solid there is a high degree of local correlation. Each atom has a given number of first-neighbors (in the example used here these are three but this can vary depending on the case) located at nearly the same distance from its center. Nearest-neighbor atoms are connected through lines in the figure and the “bond angles” formed where these lines meet at an atomic center are also nearly equal. In the crystalline case of Figure 1.1, both the number of nearest-neighbor atoms to a given atom and the nearest-neighbor bond angles are exactly the same, as these are dictated by the equilibrium positions of the crystal lattice. It is thus obvious that amorphous solids are characterized by a high degree of short-range order, which is a consequence of the chemical bonding or physical interactions responsible for holding the solid together. Hence, while a lack of long-range order in amorphous solids implies

randomness at large distances, the atomic-scale structure of such a material is highly nonrandom at a length scale of a few interatomic distances about any given atom. This restricted symmetry characterizing amorphous materials is responsible for the fact that one cannot fully reproduce their structure when only a certain subset of atomic positions is known.

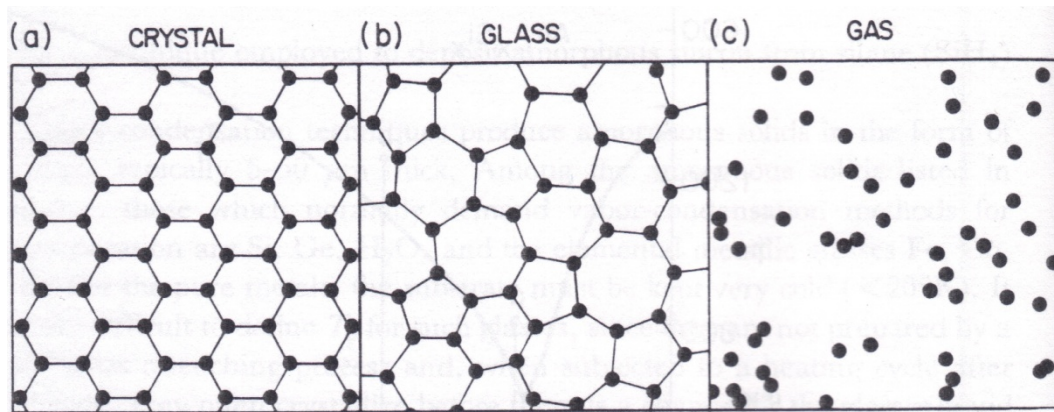


Figure 1.1: Schematic representation of the atomic arrangements in (a) a crystalline solid, (b) an amorphous solid, and (c) a gas. ¹

Many scientists from all over the world characterize the amorphous state as a kinetically trapped state, meaning that there is some kind of motional entrapment responsible for the distorted structure of the material compared to the completely ordered structure of the ideal crystal. This kinetic interpretation of the structure and geometry of amorphous solids is strengthened by the fact that their properties actually change with time, a phenomenon widely known as physical ageing. From a thermodynamic point of view, amorphous materials can be considered as being kinetically trapped in a metastable condition, meaning that they are not in the thermodynamically favored state. According to thermodynamics, for the given set of temperature and pressure, a simple glass-forming material should be in the energetically more stable crystal state, as the chemical potential of the crystalline state μ_c is smaller than the corresponding chemical potential of the liquid state μ_l , $\mu_c < \mu_l$. There are, however, cases of materials, such as atactic polymers, where a fully ordered crystalline state in which the molecules can pack may not exist. In any case, the crystalline state is thermodynamically preferable in comparison to the liquid state. This means that the equilibrium material should be a crystal, when available. For reasons that will be clarified as we proceed in this chapter this is not the case, and

amorphous materials combine – as mentioned above – characteristic properties from both liquids and solids.

One explanation of this behavior is based on the time needed for the amorphous material to make the transition from the adopted metastable state to the thermodynamically stable crystalline state. This time – also known as relaxation time – is a measure of how fast or slow these materials respond to a certain applied change – such as rapid cooling – and move towards the new thermodynamical equilibrium. Hence, for kinetic reasons – originating in the complex structure of the potential energy landscape of these materials, as we will see in Chapter 3.3 – the transition towards thermodynamic equilibrium is being hindered and takes place extremely slowly. That said, amorphous materials are considered to be away from thermodynamic equilibrium, undergoing a prolonged dynamical transition towards the equilibrium state (physical ageing). The basic reason why these materials become kinetically trapped originates largely in the way they are formed.

At this point, a note of terminology is in order. The term amorphous solid is the general one, applicable to any kind of solid showing a non-periodic atomic lattice as outlined above. The term glass (a notion that will be further investigated in Chapter 2.1) is sometimes being used to refer to amorphous solids created based on the most common way of producing amorphous solids, i.e., quenching of a melt. Since there are other ways of producing amorphous solids than melt-quenching, the term glass is the more restrictive one, but often used interchangeably to describe the most general term of amorphous solid. In this work, this ambiguity will not be adhered to and both terms will be used synonymously. Hence, we have the term “glass” to set in opposition to “crystal”, or equivalently the term “amorphous solid” versus “crystalline solid”.

As mentioned above, amorphous solids can be created through a large variety of techniques. Given the fact that the properties of the formed amorphous material depend strongly on time, it can be concluded that the production method plays a significant role for the final properties of the amorphous material, since it undeniably affects and defines the formation “history” of the material. The dependence of glass properties on the formation history is so strong that, even when using one and the same method to create an amorphous solid with only some initial specification details

changed between two different experiments, the two experiments will lead to a completely different kind of amorphous material with totally different properties characterizing it. Nowadays many methods have been developed to create amorphous solids. These methods can initially be classified under three different categories based on which is the starting phase: the liquid, the gas or the crystalline phase. In the first category the amorphous solid is being created by preserving the relative disorder of the liquid phase, whereas in the second category a gas solidifies directly to an amorphous material. Finally, in the third category the long-range order characterizing crystalline solids is being distorted. More specifically, the basic methods to produce amorphous solids are the following:

1. **Abrupt cooling of a liquid-melt (Quenching):** This is the oldest and still the most common method for amorphous solids production. Earlier it was believed that only a certain group of materials can form amorphous solids through quenching from the melt. This viewpoint has been abandoned and now it is believed that nearly all materials can be prepared as amorphous solids, if cooled fast and far enough (“Fast” and “far” will be further explained and analyzed in Chapter 2.1). A prominent example supporting this belief is the formation of metallic glasses, when the melt is quenched with extremely high cooling rates $\dot{T} \sim 10^6 \text{ K/s}$, experimentally achieved with the technique presented in Figure 1.2:

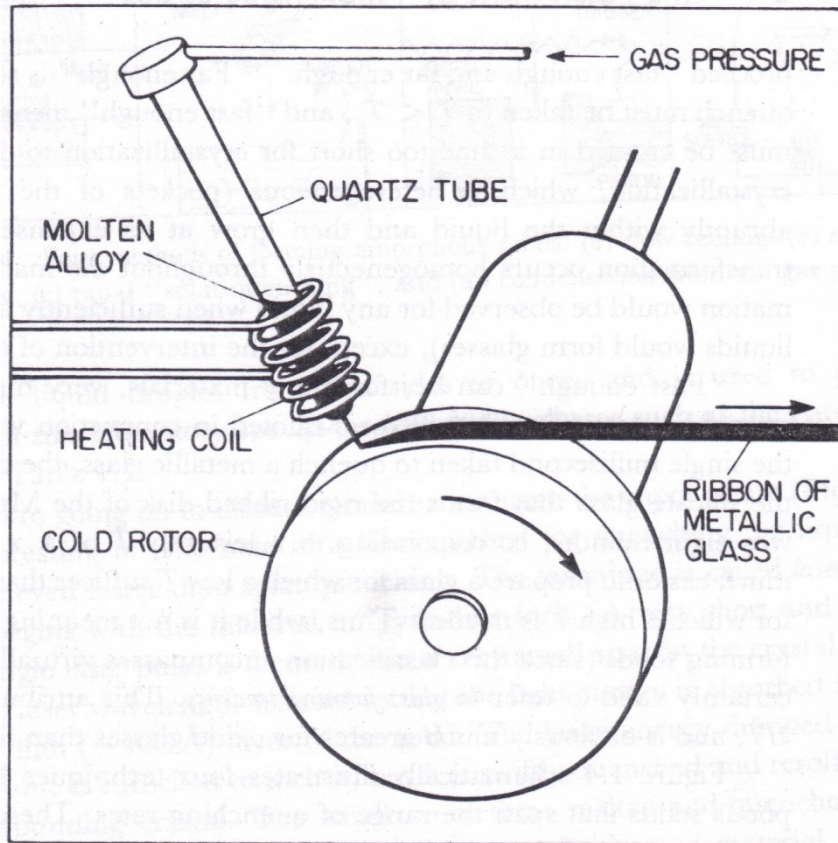


Figure 1.2: Experimental device for the production of metallic amorphous solid.¹

The technique shown in Figure 1.2, known as melt-spinning, is used for achieving very high cooling rates to form amorphous solids. A jet of hot molten metal is ejected against the metallic surface of a rapidly rotating cylinder, which is used as a heat sink. Since metals have high thermal conductivity, the liquid cools and solidifies extremely fast. This technique can be implemented for quenching many materials other than metallic melts. The characteristic difference is the adopted cooling rate, which may vary depending on the ease with which the material can be trapped in the amorphous state. This “ease” is a measure of how high or low the applied cooling rate should be. Metallic materials, because of their intrinsic tendency to crystallize, are considered to be one of the most difficult classes of materials to form an amorphous solid structure. In this case, the “ease” to crystallize is low and the cooling rate to be applied should be high. In other words, the tendency of a given material to form an amorphous solid is related inversely with the applied

cooling rate. The bigger the cooling rate (as in metallic melts), the more difficult it is for this material to solidify in an amorphous manner.

2. **Thermal evaporation:** According to this method, the amorphous material is produced directly from the gas phase. The principle on which this method is based is quite simple: The material to be solidified is being evaporated and its molecules go into the gas phase. These molecules are then brought in contact with an appropriate substrate of low temperature and solidify on it. The low temperature of the deposition surface reduces the diffusive motion of the gas molecules, causing the molecules to preserve their random positions obtained during their evaporation. The heat necessary for the evaporation is being delivered either by applying electric voltage (applicable for materials of low melting point), or by bombarding the material with pulses or beams of high-energy electrons (used for materials of higher melting point). The described method has been recently used by Mark Ediger and coworkers for the preparation of ultra-stable polymeric glasses ². In addition to that, this process has been simulated by Juan de Pablo and coworkers ³ using a simple Lennard-Jones mixture model.
3. **Sputtering:** This method is more complex, but also more adjustable than thermal evaporation. It is based on the bombardment of a target-material via ions of low pressure plasma, resulting in the ejection of atoms from this target-material. The removed atoms are then being deposited on a suitable substrate. The atom deposition upon the cool surface leads to the formation of an amorphous solid for the same reasons described in the previous method.
4. **Chemical vapor deposition (CVD):** This method is based on the chemical decomposition of gas molecules of the desired material to be solidified via chemical reaction triggered by appropriate reactants leading to the creation of amorphous films on the surface of the substrate via deposition.
5. **Irradiation:** Under given conditions the interaction between ionized high-energy particles and atoms of a crystal lattice can lead to the destruction of the crystalline state and its transformation to an amorphous state. The produced amorphous material exhibits completely different properties from the original crystalline solid, to which it can return via an annealing process. The

reversibility of this technique is found to be extremely useful in the semiconductor industry.

6. **Pressure-induced amorphization:** The application of high pressure to a crystalline solid can, under certain conditions, lead to its transformation to an amorphous solid via externally imposed distortion of the equilibrium lattice positions. It is also believed that some local meltdown due to high pressure and re-solidification takes place in the inner of the crystal lattice leading to the amorphous solid.

It should be clear at this point that amorphous materials are of high scientific and industrial interest. For their creation many techniques have been developed and applied, depending on the use and properties of the desired amorphous material.

1.2 Motivation and scope of this work

The biggest difference between amorphous solids and other, conventional solids originates from the fact that they are continuously evolving and change with time, as they are materials out of thermodynamic equilibrium. While thermodynamics clearly demonstrates that these materials should be in the crystal state (when available), for kinetic reasons this never happens, at least over the time scales of observing these materials. This means that there are certain kinetic drawbacks preventing the material from going towards its thermodynamically stable condition. This kinetic prevention doesn't mean restriction. The metastable material actually evolves towards the thermodynamically stable state, but it does so at an extremely slow pace. The time needed for the material to reach the thermodynamic more stable structural states characterizing equilibrium is known as relaxation time and a "relaxed" material is considered to be in equilibrium. Sometimes, the material exhibits so long relaxation times on its way to a stable thermodynamic state that hardly anything changes over the time window of observation. Under such conditions it may be useful to consider it as being in local equilibrium within a confined region of its configuration space, although it still evolves towards thermodynamic equilibrium. The process of

constantly evolving towards thermodynamic equilibrium is a phenomenon known as physical ageing.

Physical ageing constitutes a phenomenon of great technological significance, as it describes the behavior of amorphous solids. Amorphous solids are being formed by a wide range of different materials of varying chemical constitution and properties and are present in many applications of our everyday life. Their role in our everyday life is far more important and essential than one would intuitively expect. This is because their use is not limited to the traditional inorganic glasses, such as wine bottles and window panes, but includes also the technologically most important category of organic (usually polymer) glasses. Today, amorphous polymers with glass-transition temperature T_g (we will explain this notion in detail in Chapter 2.1) far above room temperature [e.g. polystyrene (PS), polyethylene terephthalate (PET), poly(methyl methacrylate) (PMMA), polycarbonates (PC) and polyimides] find countless applications as construction materials, thermal, sound or light insulation materials, packaging materials with controlled permeability properties, membranes with selectivity and permeability designed for gas separation techniques, CDs etc.

It is, hence, clear that amorphous materials have both fundamental scientific interest, as they are materials out of thermodynamic equilibrium, and technological importance, as they find use in many applications of our everyday life due to their unique properties. Much of the intellectual fascination about the amorphous solid state arises from the fact that scientific insight must be achieved without the help of the mathematical amenities which accompany periodicity, symmetry and long-range order of the crystalline solid state. The atomic-scale structure of an amorphous solid still constitutes one of its great mysteries and in most the cases structural information is won with great effort. On the other hand, the technological significance of these materials stimulates the scientific community to further analyze and model their structural behavior in an as general a manner as possible. The basic motivation and scope of the current work is to shed some light and gain physical insight into the mechanisms that govern structural evolution of amorphous glassy materials and through this knowledge to develop, test and apply rigorous simulation methods for estimating their thermodynamic, mechanical and structural properties.

In the following chapter glassy materials will be introduced and their method of preparation by cooling from the melt will be thoroughly described, with emphasis on the thermodynamics of the glass transition. Several theories describing the glassy state will be briefly discussed and the basic tools used in this work to model and simulate the behavior of these materials will be presented. In Chapter 3, some basic notions of rare event theory will be elaborated and their connection to the model of a Poisson process will be shown. The notion of basins and metabasins of the potential energy landscape will be defined and the adopted theoretical kinetic model for transitions between these regions of configuration space will be developed. Finally, in the last part of Chapter 3 some simulation results will be shown verifying “cage-breaking” events in an atomic level for intra-metabasin and inter-metabasin transitions. In Chapter 4, the lumping algorithm will be presented for reducing the number of states used in describing the temporal evolution of a glassy system without suffering any significant loss concerning the long-time dynamics. In Chapter 5, we present an alternative, temporal representation of the potential energy landscape and show how this can provide a good first estimate for the lumping algorithm. In Chapter 6, we present some mechanical properties for our model glass calculated via simulations of mechanical deformation experiments, whereas in Chapter 7 we summarize all main conclusions and innovations of this work. Finally, in the last chapter an outlook is presented for future work concerning time dependent mechanical properties of our model glass.

Chapter 2

Glassy materials

As already mentioned in the previous chapter, the term “glass” is often used in the literature to describe amorphous solids in general. This happens mainly because glassy materials are actually the most prominent representatives of this category of materials, as evidenced by their countless technological applications in many aspects of today’s life. Glassy materials are commonly being produced through abrupt cooling of their melts, a process better known as quenching. The systems investigated in the context of this work are computer models for amorphous materials that have been vitrified through quenching from the melt. Since quenching constitutes the basic method of producing glassy materials in this work, the following section of this chapter is dedicated to a detailed description of this process, while at the same time making the competition between crystallization and vitrification mechanisms clearer.

2.1 Crystal, supercooled liquid, and glassy state

It is common practice in most textbooks in the literature dealing with glassy materials to go through a detailed description of the quenching procedure via a cooling experiment depicted with the help of a certain graph. We adopt this practice here. The procedure of quenching a melt can be described with the help of Figure 2.1. In this figure, the volume of the material is being plotted against temperature $V = V(T)$ under constant pressure. Alternatively, in the place of the system’s volume one could depict another thermodynamic property such as the entropy of the system S , the

enthalpy H , or even the internal energy U . Figure 2.1 should be read from right to left, since time runs in that direction during the course of the cooling experiment.

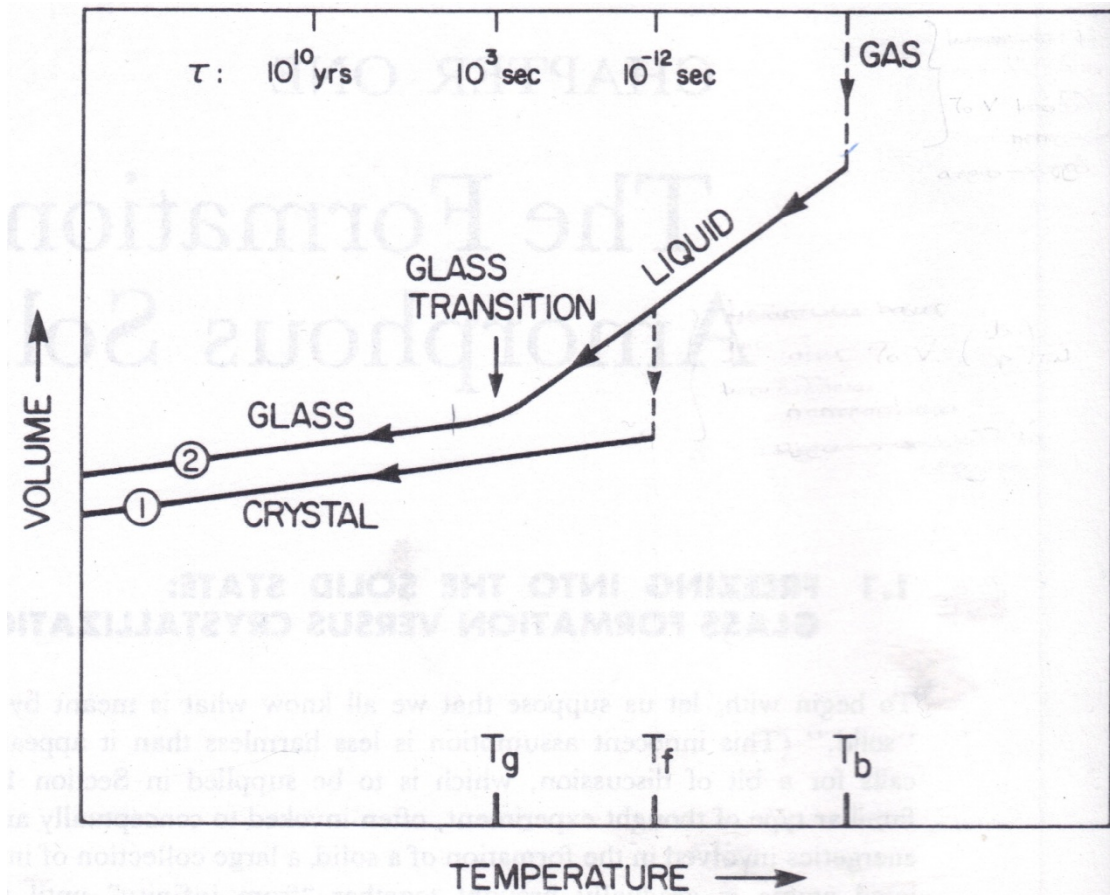


Figure 2.1: Representation of a glass forming system's volume as a function of temperature during an isobaric quenching procedure. The two general, competitive cooling paths that characterize passing from the liquid to the solid state are shown. Route 1 represents the crystallization path, whereas route 2 describes the vitrification path due to extremely rapid cooling (high cooling rates).¹

Assuming that the gas of the substance to be cooled down is in thermodynamic equilibrium at a temperature higher than its boiling temperature T_b , we begin to lower the temperature at a constant cooling rate \dot{T}_1 observing at the same time the value of the volume. A sharp break in $V(T)$ indicates a change of phase or a first order phase transition in the Ehrenfest classification⁴, involving discontinuities in the first partial

derivatives of the Gibbs energy G with respect to its natural variables temperature and pressure, i.e. in the entropy $S = -\left(\frac{\partial G}{\partial T}\right)_{p,n}$ and volume $V = \left(\frac{\partial G}{\partial p}\right)_{T,n}$ when plotted versus temperature T . As a consequence, at a first-order phase transition the second derivatives of G with respect to T and p diverge. More specifically, infinite changes are observed in the thermal expansion coefficient:

$$\alpha_p = \frac{1}{V} \left(\frac{\partial V}{\partial T} \right)_p \quad (2.1)$$

in the isothermal compressibility:

$$\kappa_T = -\frac{1}{V} \left(\frac{\partial V}{\partial p} \right)_T \quad (2.2)$$

and in the heat capacity under constant pressure:

$$C_p = \left(\frac{\partial H}{\partial T} \right)_p = T \left(\frac{\partial S}{\partial T} \right)_p \quad (2.3)$$

when plotted versus temperature T . Condensation from the gas phase shown at the extreme right of Figure 2.1, exhibits these characteristics. The phase change *gas* \rightarrow *liquid* occurs when with decreasing temperature the gas condenses to the liquid phase at the boiling temperature T_b and is a first-order thermodynamic phase transition. Continued cooling below T_b now decreases the liquid volume in a continuous fashion, where the slope of the smooth $V(T)$ curve defines the liquid's thermal expansion coefficient $\alpha_p = \frac{1}{V} \left(\frac{\partial V}{\partial T} \right)_p$. Eventually, when the temperature is brought to a low enough value, a *liquid* \rightarrow *solid* transition takes place. The transition mentioned before can be meant in two different ways, depending on the applied cooling rate during the cooling experiment:

1. Discontinuous solidification of the liquid to a crystalline solid at the freezing temperature T_f , in the vicinity of the equilibrium melting temperature, or
2. Continuous solidification of the liquid to an amorphous solid (glass) at temperature T_g .

These two quite different solidification scenarios are labeled, correspondingly, as routes 1 and 2 in Figure 2.1 and lead to quite different solids. Route 1 occurs theoretically (we'll explain shortly what actually happens) at the equilibrium melting point. Depending on the applied cooling rate, the system will follow either route 1, or route 2. In particular, when the cooling rate is sufficiently low, route 1 is followed and the crystalline solid is formed. The higher the cooling rate, the greater the possibility of suppressing crystallization (i.e. route 1) and favor vitrification (route 2).

In many cases crystallization does not start exactly at the equilibrium melting point T_m . The system then enters a metastable condition which is more widely known as supercooled or undercooled liquid. The supercooled liquid is still undoubtedly liquid and must not be confused with the glass. The supercooled liquid has temporarily equilibrated at a metastable state, although it should according to thermodynamics go over to the solid phase which is more stable (of lower Gibbs energy). As the temperature is lowered, the strength of this fragile equilibration decays as the dominance of the thermodynamically stable phase (solid) becomes more pronounced. Finally, the expected transition occurs and the system goes over to the solid state. The width of the temperature interval $T_m - T_f$ (undercooling) between the equilibrium melting point T_m and the freezing point T_f , at which the crystallization transition actually occurs, depends mainly on the material. In Figure 2.1, for the sake of simplicity, no distinction is made between T_m and T_f and the initialization of the crystallization procedure (route 1) has been drawn as occurring at strictly constant temperature T_f . Crystallization is a first order thermodynamic transition, as is evidenced by the change in volume that accompanies it.

On the contrary, the competitive vitrification process (route 2) starts at a lower temperature, until which the system exists as a metastable supercooled liquid. The temperature at which the vitrification begins is called the glass transition temperature T_g . From Figure 2.1 it is obvious that: $T_g < T_f < T_b$.

During the glass transition there is no volume discontinuity; instead, $V(T)$ bends over to acquire the small slope (similar to that of the crystal) characteristic of the low thermal expansivity of a solid. Both crystals and glasses are considered to be solids and share the essential attributes of the solid state. Their fundamental difference lies

in the nature of their microscopic, atomic-scale structure. As mentioned in Chapter 1, in crystals the equilibrium positions of the atoms form a periodic lattice and long-range order is present. In amorphous materials (glasses in particular), long-range order is absent. The key element in the preparation of an amorphous solid is speed. It is generally known that crystallization takes time, as small crystalline centers (embryos) must initially be formed (through a process called nucleation) and then grow by outward propagation of the crystal/liquid interfaces. As described by classical nucleation theory, the formation of an embryo entails a free energy cost, due to the new interface formed. Only embryos larger than a critical size are able to grow, and the formation of such embryos is an activated process. Small embryos form and dissolve all the time until an embryo manages to surpass the critical size.

As soon as the temperature of the quenched melt becomes lower than the equilibrium melting temperature T_m and the crystalline phase becomes the thermodynamically more stable phase, two simultaneous processes appear: One is crystallization through the nucleation process outlined above; the other is relaxation of the existing liquid to a metastable equilibrium at lower and lower temperatures upon imposition of the temperature change. The characteristic relaxation time of the liquid increases very strongly as temperature decreases. If the cooling rate imposed is very high, there comes a point at which the metastable liquid cannot keep up with the rate of change in temperature, and the liquid falls out of equilibrium, its configuration being trapped into that of an amorphous solid. This is glass formation. Thus, there are two competing mechanisms for formation of a solid upon cooling a liquid: crystallization and glass formation. Which one of the two competitive mechanisms will finally prevail is a question of how high or low the imposed cooling rate is, i.e., how abrupt or mild the imposed change is.

When the imposed cooling rate $\dot{T} = \frac{\Delta T}{\Delta t}$ is high, one or more of the following three

possible scenarios are true:

1. Either the temperature change ΔT (decrease, as we speak of cooling) is big, or
2. the time interval Δt given to the system to adjust to a fixed temperature change ΔT , is extremely small, or

3. Both the imposed temperature change ΔT is relative large, and the given time for adjustment Δt is small.

The relationship between those two quantities, namely ΔT and Δt (i.e., the cooling rate), is what defines which one out of the two competitive mechanisms (crystallization or vitrification) will prevail. If the imposed temperature change is large and the time given to the system to adjust (i.e. equilibrate) to this imposed change is small (time window of observation) in comparison to the time actually needed to equilibrate (relaxation time), then the system due to kinetic reasons resides in the metastable liquid state. If we continue the cooling experiment by further decreasing the temperature, then the supercooled liquid will continue adjusting to the new “cooler” state with increasing difficulty, as the relaxation times needed for equilibration are becoming increasingly higher. These times will never be reached as the imposed cooling rate grants the system only a small time window Δt , much smaller than the relaxation times actually needed to equilibrate. The increase of relaxation times with decreasing temperature proceeds faster than what an Arrhenius temperature dependence would imply. At a certain temperature, the relaxation time becomes so large that the system is no longer in position to relax and “absorb” the imposed temperature change. This incapability reflects itself by a bend in the smooth $V(T)$ curve, signifying the onset of the glass transition.

In the case where the cooling rate \dot{T} is relative small (i.e., small imposed ΔT , or large observation time window Δt , or both) then the more time-demanding crystallization process will overrule glass formation. At which temperature and density the system will glassify depends on the cooling rate. This means that the imposed cooling rate during quenching actually defines the properties of the final material, i.e., the produced glass depends on its formation history. Figure 2.2 shows how different cooling rates can lead to different glassy materials. As shown in Figure 2.2, the glass transition temperature T_g depends on the cooling rate, as it is a property of the formed glass and hence depends on its formation history, i.e., the process used to create it. The smaller the cooling rate (smoother change), the lower the glass transition temperature, as the time provided to the system through the cooling rate to adjust is now larger, allowing it to equilibrate more deeply in the supercooled liquid regime. The higher the cooling rate (more abrupt change), the higher the glass

transition temperature, as the time given to the system through the imposed cooling rate is now small and the system immediately goes over to the glassy state.

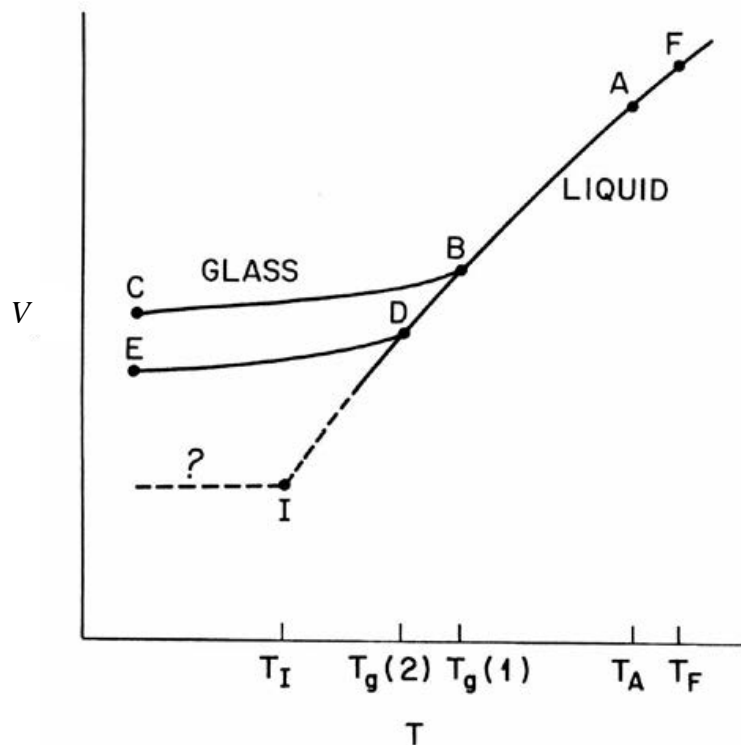


Figure 2.2: Volume versus temperature curve for quenching experiments conducted under varying cooling ratio. Graphical representation of the glass transition temperature dependence on the cooling rate used.⁵

In Figure 2.2 the volume is plotted against the temperature. Figure 2.2 is intimately related to Figure 2.1, since any thermodynamical property can be plotted as ordinate, the most interesting ones being V , S , H . Both in Figure 2.1 and in Figure 2.2 the selected property is the volume V . The results exported from both diagrams are completely analogous. According to Figure 2.2, when performing the quenching of the melt under the cooling rate \dot{T}_1 the system follows the route $FABC$ of Figure 2.2 resulting in a glass (C) with given properties and glass transition temperature $T_g(1)$. Point F in Figure 2.1 represents the freezing point and point A represents an arbitrary point in the supercooled liquid regime. When the same experiment is repeated, using this time a smaller cooling rate $\dot{T}_2 < \dot{T}_1$ (yet, \dot{T}_2 should be sufficiently large to bypass

crystallization), then the followed course is FADE in Figure 2.2 and the resulting glass (E) has different properties than the previous one (C), obtained using the initial cooling rate. Since the formation history of glass (E) is different, its properties will also be different. Hence, the glass transition temperature will be in this case lower $T_g(2) < T_g(1)$ due to the reasons mentioned above. Finally, point I in Figure 2.2 represents a glassy material that will be obtained under an even lower cooling rate $\dot{T}_3 < \dot{T}_2 < \dot{T}_1$, exhibiting an even lower glass transition temperature $T_I < T_g(2) < T_g(1)$.

Defining the formation history of a glass-forming material has been proven to be subtle and not an easy thing to do. Recent studies ⁶ have shown that in the vicinity of the glass temperature, the history of the glass-forming material cannot be uniquely defined by the cooling rate. In other words, the observation times dictated by the imposed cooling rate are not sufficient to fully determine the formation history, and hence the properties, of the formed glass. It has been shown ⁶ that the length of time spent at each temperature level during a simulated cooling procedure over a range of temperatures, where the simulation time is smaller or comparable to the equilibration (relaxation) time, is significant and plays a key role in defining the quality, and hence the properties, of the glass to be formed. In other words, ΔT and Δt play a role, and not only their ratio \dot{T} , when Δt is comparable to or shorter than the relaxation time of the glass forming material. All this becomes evident with the help of Figure 2.3, in which the instantaneous values of potential energy minima visited by a glass-forming binary Lennard-Jones system under constant pressure are shown, for three temperatures, in five computational cooling experiments of duration 14.5 ns at each temperature level, conducted with exactly the same cooling rate 2×10^9 K/s. Whereas in the liquid region the reduced trajectories for the five experiments are statistically indistinguishable, they differentiate themselves after vitrification.

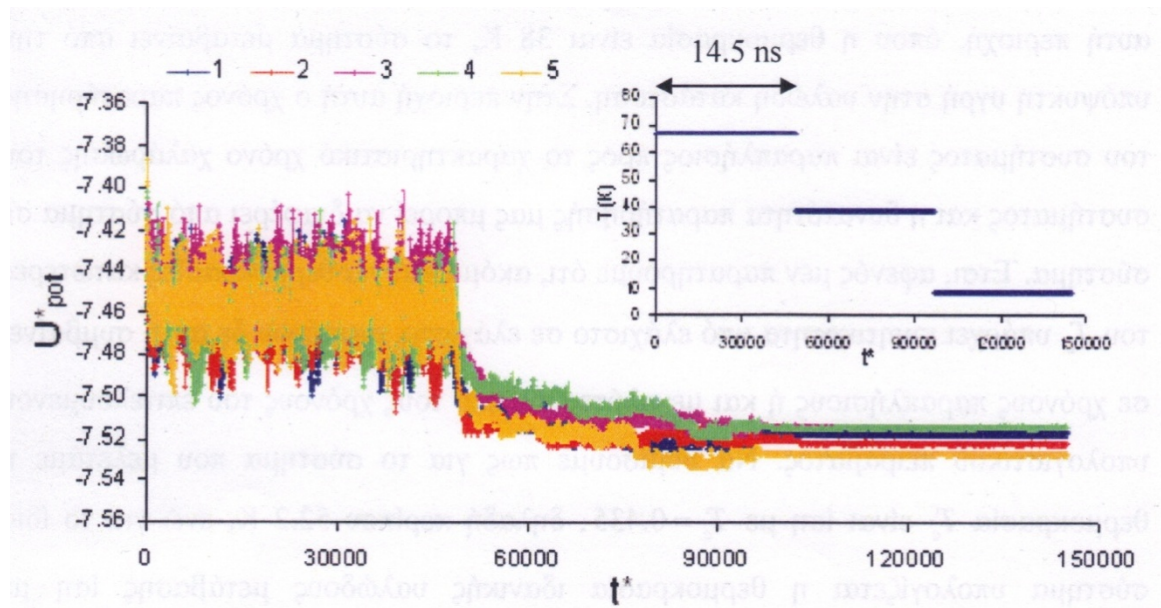


Figure 2.3: Representation of the potential energy per atom at the minimum during the cooling process of a binary Lennard-Jones system – initially proposed by Kob et al. ⁷ – of totally 641 united atoms. The potential energy per atom and time are both given in reduced units ⁶⁻⁷. In the inset diagram, the evolutionary course of stepwise cooling, involving the three studied temperature levels, is presented. ⁶

Despite the same cooling rate, it is clear that at the lowest temperature ($T = 9 \text{ K}$) the five glasses retrieved are different and depend strongly on the time interval spent at the intermediate, transition temperature of $T = 38 \text{ K}$. The intermediate temperature of $T = 38 \text{ K}$ is very close to the estimated glass transition temperature $T_g = 38.4 \text{ K}$ ⁸ and signifies the transition between the supercooled liquid (described in Figure 2.3 by the highest temperature of $T = 67 \text{ K}$) and the glass. By observing Figure 2.3, it is evident that the time spent in the second temperature region, i.e., observation time during simulation, actually determines the properties of the glass, as the five resulting glasses diversify from one another exactly at this temperature region.

In the next section of this chapter, the basic theories concerning glass transition will be introduced and briefly analyzed.

2.2 General aspects of the glassy state

In the past years there has been a lot of debate whether the glass transition constitutes a phase transition, and if so, what is the order of this phase transition according to the Ehrenfest classification (As seen from Figure 2.1, the break in the slope of V and S resembles what would be expected of a second-order phase transition according to Ehrenfest). Is the glass transition a bona fide thermodynamic transition? Is there an underlying thermodynamic transition that is disguised by kinetic effects? Or is glass formation a purely kinetic phenomenon? Many theories (which will be outlined further in this section) have been developed during the past years based on the assumption that the glass transition is a thermodynamic transition. All these theories, although well defined, suffer from a certain disadvantage: Until today, no order parameter or characteristic length has been found to appropriately describe (by becoming infinite at a non-zero temperature) the alleged phase transition. An additional difficulty in supporting the theories for the existence of a thermodynamic phase transition has to do with the conditions that have to be fulfilled, as discussed below.

If we accept that the glass transition actually constitutes a phase transition, then according to the Ehrenfest classification this phase transition should have a certain order. If the order of this transition is one (as in the case of the majority of the common phase changes, e.g. evaporation, condensation, solidification, melting, sublimation etc) then the first order derivatives of the Gibbs energy G with respect to temperature and pressure (characteristic variables of G) should change discontinuously at the transition temperature:

$$\left(\frac{\partial G}{\partial T}\right)_p = -S \quad (2.4)$$

and

$$\left(\frac{\partial G}{\partial p}\right)_T = V \quad (2.5)$$

According to this scheme, the entropy and the volume of the system should change discontinuously at the transition temperature T_g . As we have seen from Figures 2.1

and 2.2, described in the previous section, the volume of the system at the glass transition temperature changes continuously, exhibiting no discontinuity (as in crystallization), but only a small change in slope. Thus, the vitrification process is not a first order phase transition.

If we further examine the behavior of the second partial derivatives of the Gibbs energy G with respect to temperature and pressure, in order to determine whether the glass transition is a second order phase transition, we obtain expressions that include the heat capacity under constant pressure C_p , the isothermal compressibility κ_T and the thermal expansion α_p , as defined in equations (2.3) to (2.1) respectively:

$$\left(\frac{\partial^2 G}{\partial T^2}\right)_p = \frac{\partial}{\partial T} \left(\frac{\partial G}{\partial T}\right)_p \stackrel{\text{Eq. 2.4}}{=} -\left(\frac{\partial S}{\partial T}\right)_p \stackrel{\text{Eq. 2.3}}{=} -\frac{C_p}{T} \quad (2.6)$$

$$\left(\frac{\partial^2 G}{\partial p^2}\right)_T = \frac{\partial}{\partial p} \left(\frac{\partial G}{\partial p}\right)_T \stackrel{\text{Eq. 2.5}}{=} \left(\frac{\partial V}{\partial p}\right)_T \stackrel{\text{Eq. 2.2}}{=} -\kappa_T \cdot V \quad (2.7)$$

$$\left(\frac{\partial^2 G}{\partial T \partial p}\right) = \frac{\partial}{\partial T} \left(\frac{\partial G}{\partial p}\right)_T \stackrel{\text{Eq. 2.5}}{=} \left(\frac{\partial V}{\partial T}\right)_p \stackrel{\text{Eq. 2.1}}{=} \alpha_p \cdot V \quad (2.8)$$

Thus, in the light of equations (2.6) and (2.7), one has to examine how the compressibility, the heat capacity under constant pressure and the volumetric thermal expansion coefficient change during the glass transition. If that change is discontinuous, then the glass transition can be characterized as a second order phase transition. Furthermore, it can be shown that, for a true second order thermodynamic transition, the following relation between the discontinuities in second derivative properties should hold:

$$\frac{dT_g}{dp} = \frac{T \cdot V \cdot (\alpha_p^{(g)} - \alpha_p^{(l)})}{C_p^{(g)} - C_p^{(l)}} = \frac{T \cdot V \cdot \Delta \alpha_p}{\Delta C_p} \quad (2.9)$$

where the index (g) corresponds to the value of the relevant property in the glassy state, and similarly the index (l) describes the value of the considered property in the liquid phase. In an analogous way followed to extract equation (2.9), the following equation can be obtained:

$$\frac{dT_g}{dp} = \frac{\Delta\kappa_T}{\Delta\alpha_p} \quad (2.10)$$

The properties C_p , α_p and κ_T do change discontinuously across the glass transition (see Figure 2.1 for α_p). Through experimental measurements of the values of the quantities ΔC_p , $\Delta\alpha_p$ and $\Delta\kappa_T$ during the vitrification of several materials, it has been observed that equation (2.9) holds in almost every case. This is, however, not the case for equation (2.10). In particular, the right-hand side of equation (2.10) is found to be significantly larger than the left-hand side of the same equation. This is a strong indication that glass transition is not a simple, common second order phase transition. Moreover, Prigogine and Defay⁹ have shown, without making any assumption concerning second order phase transition, that the ratio:

$$R \equiv \left(\frac{\text{Eq. 2.10}}{\text{Eq. 2.9}} \right) = \frac{\Delta\kappa_T \cdot \Delta C_p}{T \cdot V \cdot (\Delta\alpha_p)^2} \quad (2.11)$$

is equal to one, when only one order parameter sufficiently describes in full the equilibrium state of a system relaxing towards it. On the contrary, when more than one order parameters are required for the same purpose, ratio R becomes larger than one. The later observation seems to be the case for the vitrification process. This conclusion undeniably strengthens the argument that glass transition is a more complex phenomenon than an ordinary second order phase transition.

Many properties of glassy materials depend strongly on their formation history. One characteristic example is the glass transition temperature, which, as we have seen above, depends on the applied cooling rate during quenching. In addition to that, the exact specification of the glass transition temperature is purely a matter of convention. In particular, many scientists adopt the following criterion: the glass transition temperature of a given material is the temperature at which the longest relaxation time in this material becomes of the order of 10^3 s. According to another convention, the glass transition temperature is considered to be the temperature at which the viscosity of the material equals 10^{13} P (poise). Regardless of the fact that many properties of the glassy material depend strongly on its formation history and on the nature of the

material itself, there are certain properties and characteristics of glassy materials that exhibit similar behavior across wide categories of glass-forming materials.

One example of such universal behavior is the dependence of the relaxation times τ on temperature. It is generally accepted, that relaxation times increase dramatically with decreasing temperature in glassy materials. In addition, the way relaxation times increase with decreasing temperature is faster than an Arrhenius dependence ($\tau(T) \propto \exp(A/T)$) would imply. The later assertion becomes clearer with the help of Figure 2.4. Figure 2.4 is usually called “Angell-diagram” or “Angell plot”, named after C. Austen Angell, who introduced such a diagram for the first time¹⁰. This plot shows how the decimal logarithm of viscosity (which can be considered as proportional to the relaxation time τ) changes with the reduced inverse temperature T_g/T in the range of temperatures $T > T_g$. For the creation of this diagram Angell used the second of the two above mentioned definitions of the glass transition temperature, i.e., the temperature at which the viscosity of the system becomes 10^{13} P.

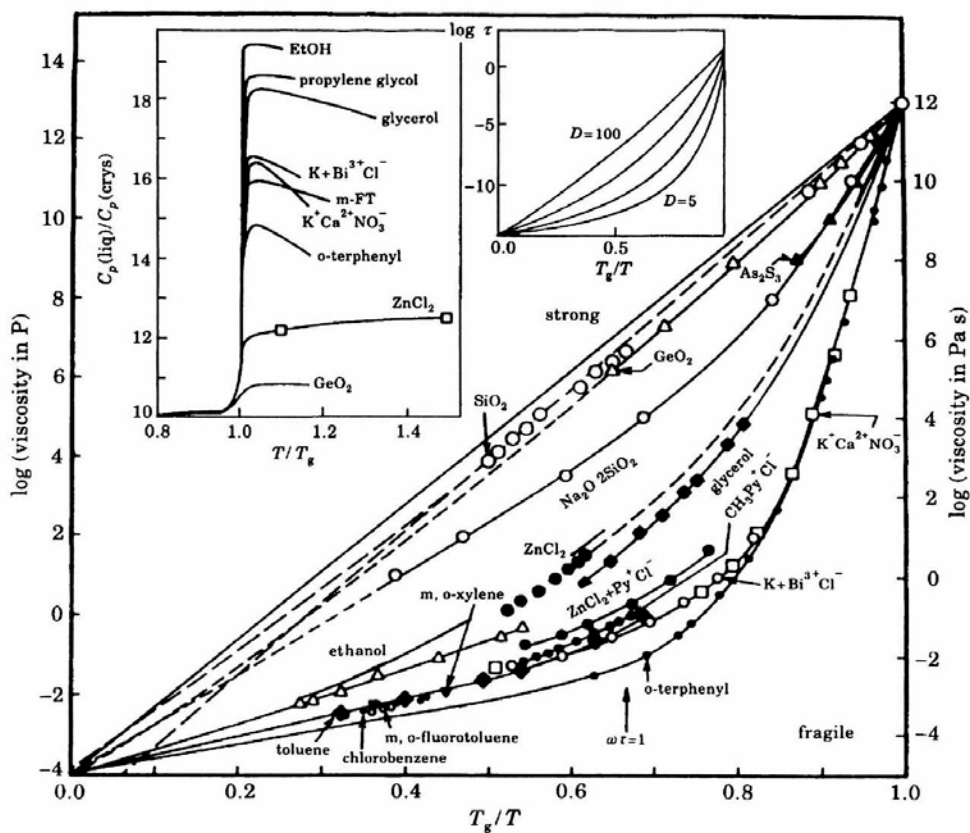


Figure 2.4: Temperature dependence of the dynamic viscosity (proportional to relaxation time) for a series of glass-forming materials as a function of the reduced inverse temperature T_g/T .¹⁰

In this diagram, a linear dependence would correspond to an Arrhenius-type behavior. As can be seen from the main diagram of Figure 2.4, the change of relaxation time τ (i.e. logarithm of viscosity) with temperature is of Arrhenius type only for a small number of materials, while the large majority of glass-forming materials deviate from this linear behavior. A classification of glassy materials proceeds with the help of the Angell-diagram. Glass-forming materials showing slight deviations from an Arrhenius behavior are named “strong” glass formers, whereas materials exhibiting large deviations from an Arrhenius dependence are named “fragile” glass formers. For the latter category of materials, the Vogel-Fulcher-Tammann relation is being used to better describe the temperature dependence of the relaxation time τ :

$$\tau(T) \propto \exp\left(\frac{B}{T - T_0}\right) \quad (2.12)$$

According to equation (2.12), the relaxation time becomes infinite at a non-zero temperature T_0 . This has been interpreted as an indication that at this finite temperature an actual phase transition may exist. Moreover, the temperature T_0 seems to be identical to the so-called Kauzmann temperature T_K , at which the entropy of the supercooled liquid equals the entropy of the crystalline phase.¹¹

As can be seen from the left inset to the diagram of Figure 2.4, “fragile” glass formers usually exhibit a large change in their heat capacity under constant pressure C_p at the glass transition temperature. In the second inset plot are shown the occurring curves after usage of the Vogel-Fulcher-Tammann relation (Eq. (2.12)) for several values of the dimensionless “activation energy” $D \equiv B/T_0$. As becomes obvious, the temperature dependence of “strong” glass-formers corresponds to large values of energy barriers D , whereas for “fragile” glass-formers to low energy barriers D .

Apart from the distinction of glass-formers into “strong” and “fragile”, another distinction proposed by Sciortino¹² distinguishes glasses into attractive and repulsive. The molecular origin of attractive glasses lies in the existence of strong (in relation to temperature) attractive forces. In cases where the range of attractive forces is much shorter than the particle size, the glassy state can be found at very low densities¹³. On the other hand, repulsive glasses result from of hard-core interatomic interactions due to the short-range repulsion of the electron clouds and are usually observed at high densities, where repulsive interactions become dominant. At this point it should be mentioned that, beyond the Vogel-Fulcher-Tammann equation (Eq. (2.12)), other empirical or semi-empirical relations have been proposed to quantitatively describe the temperature dependence of the relaxation time τ . One such example is the following relation⁵:

$$\tau(T) \propto \exp\left(\frac{B}{T^2}\right) \quad (2.13)$$

which also provides satisfactory fitting to experimental measurements.

2.3 Theories describing the glass transition

During the past years the complex – and still incompletely understood – phenomenon of the glass transition has attracted the interest of many scientists. In an effort to address all questions raised about this phenomenon, various theories have been proposed. The complexity of the glass transition problem is underlined by the fact that a large number of disparate theoretical proposals have been suggested over the years to explain it. In this section of Chapter 2, the basic theories for the interpretation of the glass transition are being presented and briefly analyzed. Each theory has its advantages and covers well some issues concerning the studied phenomenon, while none of the theories can describe the glass transition completely and without constraints. Nevertheless, given the high complexity of this phenomenon, every one of the theories mentioned below explains relatively well different aspects of the glass transition.

2.3.1 Free volume theory

One of the most famous and well established theories for the interpretation of glass formation is free volume theory. It was initially proposed by Fox and Flory¹⁴ in the early 1950's and is thus considered to be one of the initial complete theories dealing with the phenomenon of glass formation. It is based on the correlation between the ability of atoms to diffuse and the space (or free volume) that is actually available for this diffusive motion. According to this theory, the relative reduction in the ability of atoms to freely diffuse, which is observed in the vicinity of the glass transition temperature, is directly correlated to the reduction of the available free volume for the diffusion of atoms. For the definition of the notion of "free volume" one simple model system is used; the model system of hard spheres. According to this model, the atoms are represented by ideally spherical hard particles of given diameter σ . Attractive interactions are completely absent in this model, whereas infinite repulsion is present in the case of particles overlapping. In other words, the force field characterizing non-bonded (a notion to be further analyzed in Chapter 2.4) interactions in this model has the following functional form:

$$V_{\text{NB}}^{\text{HS}}(r_{ij}) = \begin{cases} +\infty, & r_{ij} < \sigma \\ 0, & r_{ij} \geq \sigma \end{cases} \quad (2.14)$$

The graphical representation of the potential energy as a function of the center to center distance of two atoms i, j , $r_{ij} = |\mathbf{r}_i - \mathbf{r}_j|$, is shown in Figure 2.5:

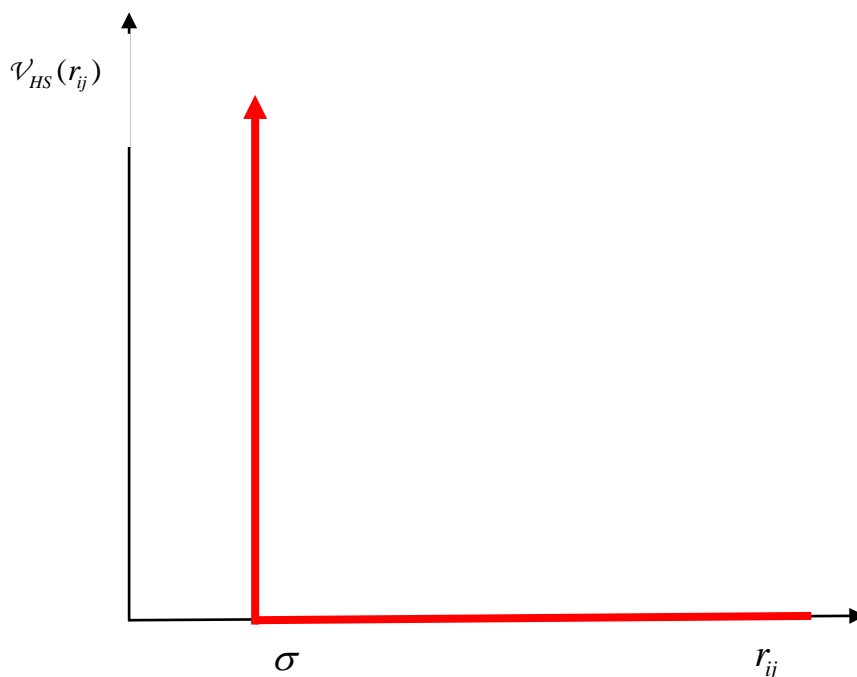


Figure 2.5: Typical graphical representation of a hard sphere potential as a function of the interatomic distance r_{ij} of two given atoms i, j

Figure 2.6 depicts the two-dimensional floor plan of a hard sphere system (actually Figure 2.6 shows a system of hard discs), where the shaded areas represent the free volume (free surfaces in 2D) available for diffusion for three different atoms: A, B and C. Particularly, the free volume of every atom is defined as the locus (set) of points which are allowed to be visited by the center of this atom without this causing any overlapping effects with neighboring atoms, given that all neighboring atoms do not move. The free volume constitutes in other words a measure of atomic motion ability within a “frozen” environment. At this point a clarification is in order. The free volume should in no case be confused with the vacant (or void) volume, i.e. the volume of the system which is not filled with atoms. The vacant volume results directly from subtraction of the net volume of the atoms from the total volume of the system.

In general, one can define the accessible volume to a spherical probe of given radius as the locus of points where the center of the probe can be placed such that it does not overlap with any of the atoms in the system¹⁵. The vacant volume is the accessible

volume to a probe of zero radius. The free volume of an atom is the cluster of accessible volume ¹⁵ to a probe of radius equal to that of the atom in the configuration obtained by removing the atom in question from the system; by definition, this cluster contains the original position of the atom. The accessible volume is, in general, smaller than the vacant volume and its physical meaning is directly connected to the fraction of vacant volume accessible to atoms during their diffusive motion without causing any overlapping effects.

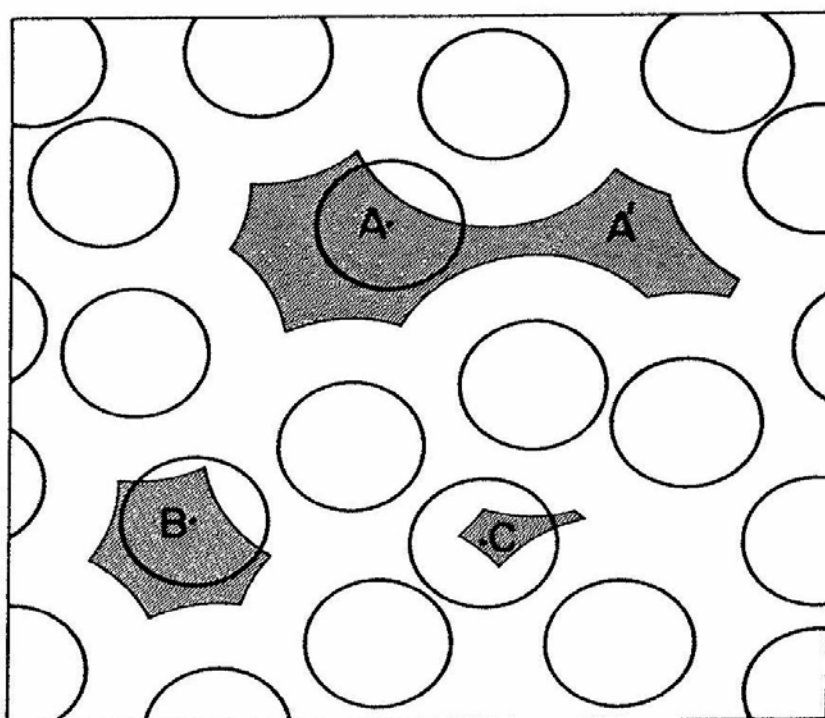


Figure 2.6: Graphical representation of the free volume for a 2D system of hard discs. The shaded areas correspond to the free volume for atoms A, B and C, provided that all neighboring atoms remain still. ¹

As can be seen in Figure 2.6, the free volume of atom A is larger than those of atoms B and C. Thus, molecular mobility – connected with and analogous to the free volume – is expected to be larger for atom A than for atoms B and C, which are more confined by their first neighbors. But this is not the only difference between atom A and atoms B and C. A closer look at Figure 2.6 leads to the conclusion that the first neighbors of atom A are more distant in comparison to the first neighbor-cell of atoms

B and C. This property allows, as already mentioned, atom A to move more freely. It could thus diffuse through a free volume bottleneck towards position A' . At this position, four out of the six initial first neighbors (before the diffusive jump) of atom A have been changed. An analogous diffusive jump for atoms B and C is impossible, unless their neighbors move. In other words, the amount of free volume accessible to an atom is directly connected to its ability of performing diffusive jumps and cage-breaking events (a notion which will be thoroughly investigated in Chapter 3). Moreover, the diffusive behavior of atom A in this example points to the general diffusive behavior in a liquid, where the atomic mobility is relatively higher than the mobility in a solid and diffusive jumps happen often. On the contrary, the diffusive behavior of atoms B and C reminds one how atoms move in a solid, i.e. atoms vibrate around their equilibrium positions. Because glassy materials combine properties of both liquid and solid (as amorphous materials in general do), the cage-jumping behavior presented in Figure 2.6 is expected to be although present, not dominant in such materials.

The above described connection between the microscopic diffusivity of a particle and the amount of free volume surrounding it led to the development of the free volume theory. According to this theory, the glass transition phenomenon correlates with the changes in the free volume distribution of particles. Initially, for as long as the system is in the liquid (or supercooled liquid) state the particle free volume is large and the diffusive jumps make the system relax easily in response to the imposed temperature drop. As temperature decreases, the available free volume decreases as well and diffusive jumps become sparser. Once the glass transition temperature T_g is reached, the free volume becomes minimal and the fluid becomes kinetically arrested leading to the known behavior of glassy materials under their glass transition temperature. The development of free volume theory, initially by Cohen and Turnbull¹⁶ followed by Cohen and Grest¹⁷, is built upon four different assumptions:

1. To each particle a local volume v of molecular size is assigned.
2. Once the local molecular volume v exceeds a critical value v_c , the volume excess can be viewed as free volume.
3. Molecular movement happens only when, due to free volume redistribution, larger gaps are being formed than a critical volume value v^* .

4. No free energy is needed for the redistribution of the free volume.

This theory distinguishes between two types of atomic cells around any given atom: “liquid” cells and “solid” cells. The criterion for this distinction is the value of the free volume in comparison to the critical volume value v_c . In particular, “liquid” cells are being formed when the accessible volume around them becomes larger than the critical value $v > v_c$, whereas “solid” atomic cells are present when $v < v_c$. According to the second assumption of this theory, free volume is built once the critical value v_c is surpassed. Hence, only particles belonging to “liquid” cells have free volume. It is therefore of great importance to quantify the volume distribution of the different types of cells being built around any individual particle. This volume distribution plays a dominant role in the context of this theory, as it defines how free volume changes. It is to expect that this distribution is temperature dependent. Once the volume distribution function $P(v_f)$ is determined, several properties of the material can be derived. One example is the Doolittle relation ¹⁸ (named after A. K. Doolittle, who initially developed it based on the behavior of the liquid phase of many simple hydrocarbons) to evaluate the fluidity (inverse viscosity):

$$n^{-1} = n_0^{-1} \cdot \int_{v_f^*}^{\infty} P(v_f) dv_f \quad (2.15)$$

2.3.2 Configurational entropy theory

An alternative approach for describing the glass transition phenomenon constitutes the configurational entropy theory or cooperative relaxation theory. It was initially proposed by Gibbs and DiMarzio ¹⁹ and further developed by Gibbs and Adam ²⁰ and examines the dynamical relaxation of supercooled liquids and glassy materials from a statistical-mechanical point of view. The initial approach of Gibbs and DiMarzio is based on the assumption that the glass transition at T_g is connected to a thermodynamic transition at a lower temperature $T_2 < T_g$. The abrupt increase of relaxation times observed as T_g is approached from higher temperatures is attributed

to a significant reduction of the available microstates of the system, a measure of which is the system's "configurational entropy". The higher the number of available microstates is, the higher the configurational entropy of the systems and vice versa. In the context of this theory, T_2 is the "ideal" temperature at which the configurational entropy of the system becomes equal to zero and consequently the glass transition is viewed as a second order phase transition. Under T_2 the configurational entropy of the system remains zero, instead of taking negative values, which lack of course any physical meaning. In the context of this theory, temperature T_2 is identified to be identical to the Kauzmann temperature T_K (mentioned in Chapter 2.2)

The continuation of this theory, introduced by Gibbs and Adam, is based on the idea that relaxation of the macroscopic system occurs due to cooperative rearrangement of molecular clusters. It is obvious that the higher the number of cooperatively rearranging clusters is, the easier the relaxation (equilibration) of the system will occur and vice versa. These groups of molecules define the cooperatively rearranging regions as independent sub-systems of the macroscopic system. In these cooperatively rearranging regions, it is possible, due to variations of the energy, to observe local structural rearrangements which, however, leave the surrounding atoms intact. The rearranging regions are supposed to co-exist within the macroscopic system under mechanical and thermal equilibrium. Thus, the most appropriate statistical ensemble for their description is the isothermal-isobaric ensemble (n, p, T) . The corresponding partition function for this ensemble is given by Eq. (2.16):

$$Q(z, p, T) = \sum_{E, V} w(z, E, V) \cdot \exp\left(-\frac{E}{k_B T}\right) \cdot \exp\left(-\frac{P \cdot V}{k_B T}\right) \quad (2.16)$$

where z is the number of atoms in a cooperatively rearranging sub-system and $w(z, E, V)$ is the multiplicity of every microstate of energy E and volume V . One can directly calculate the Gibbs energy G with the help of Eq. 2.16:

$$G(z, p, T) = z \cdot \mu(p, T) = -k_B T \cdot \ln Q(z, p, T) \quad (2.17)$$

During the derivation of Eqs. (2.16) and (2.17) it becomes obvious that every microstate has been considered, regardless of their ability or not to show rearrangement. If we repeat the above procedure, limiting the calculations to the

microstates that actually show structural rearrangements, then only a fraction of sub-systems can show structural rearrangements:

$$p = \frac{Q'}{Q} = \exp\left(-\frac{G' - G}{k_B T}\right) \quad (2.18)$$

where Q' is the partition function occurring if the sum of Eq. (2.16) is restricted only to those values of E and V that allow structural rearrangements of the z participating atoms. G' symbolizes the corresponding value of the Gibbs energy. The possibility of actually observing a structural rearrangement event of z atoms W_z is directly proportional to p , as Eq. (2.19) reveals:

$$W_z(T) = A \exp\left(-\frac{z \cdot \Delta\mu}{k_B T}\right) \quad (2.19)$$

where $z \cdot \Delta\mu \equiv z(\mu' - \mu) = G' - G$ and the pre-exponential factor A is a constant considered to be independent of temperature and z .

In order to calculate the total probability of structural rearrangement $W(T)$, the individual probabilities of rearranging sub-groups consisting of z atoms should be accumulated. The lower limit of the summation cannot be zero. There should be a limiting value of the number of atoms constituting each sub-system z^* , below which the rearrangement in at least two stable structures is impossible. Hence, the lower limit of the summation should be equal to the total number of particles z minus the minimum requirement on atoms for stable structural rearrangements z^* :

$$\begin{aligned} W(T) &= \sum_{z=z^*}^{\infty} A \cdot \left[\exp\left(-\frac{\Delta\mu}{k_B T}\right) \right]^z \\ &= \frac{A}{1 - \exp(-\Delta\mu/k_B T)} \cdot \exp\left(-\frac{z^* \cdot \Delta\mu}{k_B T}\right) \end{aligned} \quad (2.20)$$

The denominator $[1 - \exp(-\Delta\mu/k_B T)]$ of Eq. (2.20) is normally very close to unity, hence, it can be considered as temperature independent. Therefore, we can safely conclude that for every temperature the largest probability of appearance of

cooperatively structural rearrangements can be observed for clusters of atom-number very close to the minimal allowed value z^* , as Eq. (2.21) shows:

$$W(T) \approx A \cdot \exp\left(-\frac{z^* \cdot \Delta\mu}{k_B T}\right) \quad (2.21)$$

With the help of Eqs. (2.16) and (2.17) the configurational entropy may be defined by differentiating of the Gibbs energy with respect to temperature:

$$s_c = -\left(\frac{\partial G}{\partial T}\right)_p \quad (2.22)$$

The configurational entropy of the entire system can be defined with the help of Eq. (2.22) under the assumption of equivalence and independence between the individual n microscopic sub-systems comprising the macroscopic system:

$$S_c = n \cdot s_c \quad (2.23)$$

The main output of the configurational entropy theory is Eq. (2.24) which expresses the probability of structural rearrangement $W(T)$. This quantity is reversely proportional to the system's relaxation time τ .

$$W(T) = A \cdot \exp\left(-\frac{\Delta\mu \cdot s_c}{T \cdot S_c}\right) = A \cdot \exp\left(-\frac{C}{T \cdot S_c}\right) \quad (2.24)$$

This theory predicts the glass transition temperature slightly higher than the corresponding experimental value. If T_2 is the temperature at which the configurational entropy becomes zero $S_c(T_2) = 0$, then $T_g > T_2$ and therefore every glassy system has a residual of configurational entropy. This residual can be calculated with thermodynamic measurements close to absolute zero temperature. At this temperature vibrational contributions influencing the conducted measurements are absent and hence the observed entropy difference between the glassy system and the crystalline phase can be entirely attributed to the residual configurational entropy of the glassy system during the quenching of the melt.

$$\Delta S = (S_{glass} - S_{crystal})_{T=0} = S_c \quad (2.25)$$

Moreover, if ΔC_p is the difference of C_p between the glass and the liquid, then the configurational entropy can be expressed as:

$$S_c = \int_{T_2}^{T_g} \frac{\Delta C_p}{T} dT \quad (2.26)$$

By assuming that ΔC_p is constant in the temperature interval $[T_2, T_g]$, Bestul and Chang²¹ estimated $S_c \approx \Delta C_p \cdot \ln\left(\frac{T_g}{T_2}\right)$ and by replacing the experimentally measured values of S_c and ΔC_p the ratio T_g/T_2 has been calculated for a series of glassy systems $T_g/T_2 = 1.29 \pm 10.9\%$

If for the temperature dependence of the C_p , the expression $\Delta C_p(T) = D/T$ is adopted²², then Eq. (2.24) takes the form:

$$W(T) = A \cdot \exp\left(-\frac{B}{T - T_2}\right) \quad (2.27)$$

Equation (2.27) corresponds to the known Vogel-Fulcher-Tammann-equation [cf. Eq. (2.12)].

2.3.3 Mode coupling theory

Over the last years the phenomenon of glass transition has been approached from a different point of view. In Particular, many hydrodynamic and kinetic models have been developed and proposed for describing the dynamical behavior of the supercooled liquid. According to the philosophy of those theories, glass transition does not constitute a thermodynamical phase transition, but merely a phenomenon leading to loss of system's ergodicity. The independent seminal work of many researchers, such as Leutheusser²³, Bengtzelius, Götze and Sjölander²⁴ and others²⁵, has led to a concrete mathematical formalism describing this aspect. In the course of these efforts, it has been observed that a special case of the mode coupling theory

(MCT) of liquids can lead to a dynamical abnormality showing characteristics similar to those of glass transition.

As mentioned above, MCT attempts to describe the dynamic behavior of strongly supercooled liquids at temperatures above the glass transition temperature T_g . More precisely, during the glass transition phenomenon the behavior of the density is of great interest. In particular, the entrapment of the system during glass transition leads to a certain loss of its diffusive capability, resulting in a long-term stabilization of the density fluctuations. An effective way to monitor these density fluctuations is through the intermediate scattering function, which is given by Eq. (2.28) in a normalized form:

$$\Phi_q(t) = \langle \rho^*(\mathbf{q}, t) \rho(\mathbf{q}, 0) \rangle / \langle |\rho(\mathbf{q}, 0)|^2 \rangle \quad (2.28)$$

Eq. (2.22) is the autocorrelation function of the spatial Fourier transformation of the density function and can be directly measured through scattering experiments. $\rho(\mathbf{q}, t)$ is the spatial Fourier transform of the density function $\rho(\mathbf{r}, t)$. MCT makes use of the general equation for relaxing materials that function $\Phi_q(t)$ – as defined in Eq. (2.28) – should fulfill according to the classical hydrodynamic theory:

$$\ddot{\Phi}_q(t) + \gamma_q \dot{\Phi}_q(t) + \Omega_q^2 \Phi_q(t) + \Omega_q^2 \int_0^t m_q(t-t') \dot{\Phi}_q(t') dt' = 0 \quad (2.29)$$

satisfying the following initial conditions $\Phi_q(0) = 1$, $\dot{\Phi}_q(0) = 0$. In relation (2.29), the parameter Ω_q corresponds to a microscopic frequency, whereas the function $m_q(t)$ represents a “memory” function depending on the “velocities” $\dot{\Phi}_q$ for every time t' smaller than time t . For a more thorough description of the derivation of Eq. (2.29) the reader is referred to reference ²⁶. It is not within the goals of this work to go more deeply in detail concerning this matter.

MCT is based on the general relationship shown in Eq. (2.29). In its simplest version, the so-called ideal MCT, the model predicts the existence of a temperature T_c at which the system goes from ergodic to nonergodic behavior. In particular, in the ideal

MCT the self-consistent assumption is made, that the “memory”-function $m_q(t)$ depends parabolically on the autocorrelation function Φ_q :

$$m_q(t) \propto 4 \cdot \lambda \cdot \Phi_q^2(t) \quad (2.30)$$

where λ represents a coupling parameter. With the help of this model (ideal MCT) many interesting results are obtained. First of all, the prediction for the relaxation of the function $\Phi_q(t)$ changes from simple exponential (for small values of λ) to stretched exponential, as the coupling parameter λ increases and approaches the critical value of $\lambda_c = 1$. As the coupling parameter λ increases and approaches the value of 1, the temperature decreases approaching the critical value T_c . At T_c (i.e. $\lambda_c = 1$) the autocorrelation function ceases to relax within a finite time interval of observation and remains “frozen” at a non-zero value exhibiting a plateau as shown in Figure 2.7:

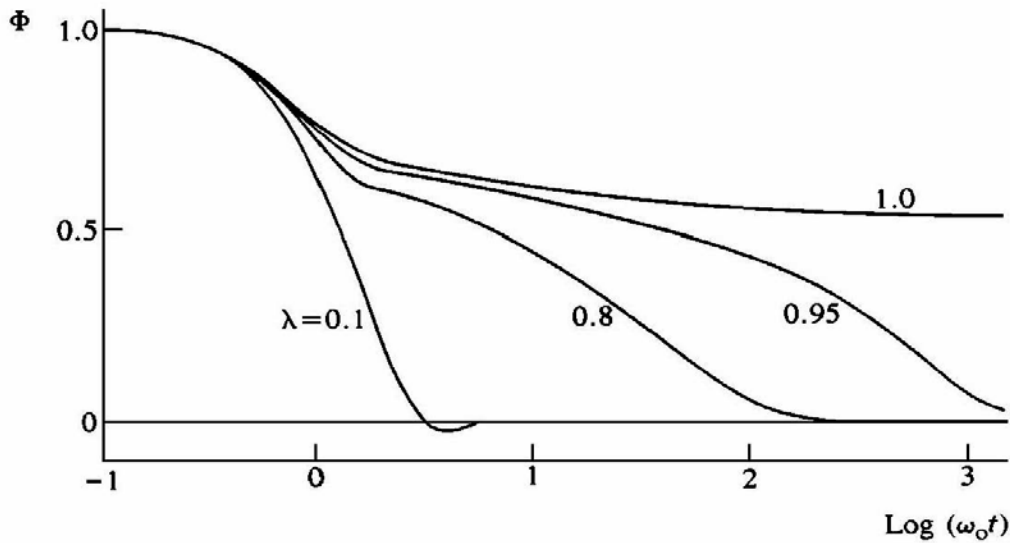


Figure 2.7: Typical representation of a dynamical slowdown of the relaxation process of the autocorrelation function $\Phi_q(t)$, as the coupling parameter λ increases approaching the critical value of $\lambda_c = 1$.²⁷

In other words, MCT constitutes a relatively simple model that predicts from a purely hydrodynamic point of view the existence of a dynamical glass transition which reflects the incapability of the system to relax within a finite time interval. It is generally accepted that the mode coupling theory provides results in good agreement with experimental measurements for temperatures above the glass transition temperature, whereas as the glass transition temperature is being approached results tend to deviate from experimental findings.

2.3.4 Other theories

Up to this point it should be clear that all mentioned theories converge to the fundamental conclusion that structure determines dynamics: e.g. liquids are disordered and thus flow and relax (in the sense that there is a certain decorrelation from their initial condition), while crystals are ordered and do not. More precisely, sudden changes in dynamical behavior follow from similar sudden changes in structure. A characteristic example of this is the common first order phase transition from liquid to crystal. The glass transition, however, does not fit within this paradigm in an obvious way. A supercooled liquid slows down, to the point of complete arrest, while at the same time maintaining its liquid structure. This leads to what is probably the fundamental question in the field ²⁸: Is the glass transition, as observed experimentally, purely a dynamical phenomenon, where the fluid becomes kinetically arrested, or is the observed dynamics the consequence of an underlying phase transition from the fluid to the glassy state?

In this section of Chapter 2 two relatively new theories are being introduced and briefly described while trying to examine glass transition from both a purely thermodynamic perspective, and a fundamentally kinetic one. Starting from the kinetic perspective, it has been found ²⁹ that there is an undeniable connection between the glass transition (even before that, during the supercooled liquid state as described below) and the dynamical heterogeneity of the system ³⁰. This phenomenon is prevalent even before the glass transition temperature and signifies one salient difference – besides the exceedingly slow dynamics – between a high-temperature liquid and a supercooled liquid. More precisely, high-temperature liquids are

homogenous both in space and time: there is no significant difference in the way particles move in different regions of the liquids, nor is there a difference in the way a given particle moves now and, say, a fraction of a relaxation time later. Supercooled liquids (and hence glassy materials) are not like that. They are characterized by spatial clusters of fast- and slowly-moving particles. Moreover, a given particle can remain slow for a certain amount of time and then become fast later. This phenomenon, initially observed in supercooled liquids, was later shown to be also present and characterize many glass forming materials ³¹.

In order for the notion of dynamic heterogeneity to become clearer, Figure 2.8 can be of use. In this figure a projection in space of an equilibrium trajectory (a notion which will be described in the following section of this chapter) of a two-dimensional supercooled liquid is shown, from reference ³²; particles colored according to overlap with initial positions (displacement by a particle diameter or more is dark red, and no displacement is dark blue). According to this figure, spatial segregation of dynamics is evident. By carefully looking at Figure 2.8, another facet of dynamical heterogeneity can be observed: dynamic facilitation (DF), which is actually the name of the kinetic-based theory trying to explain the glass transition phenomenon.

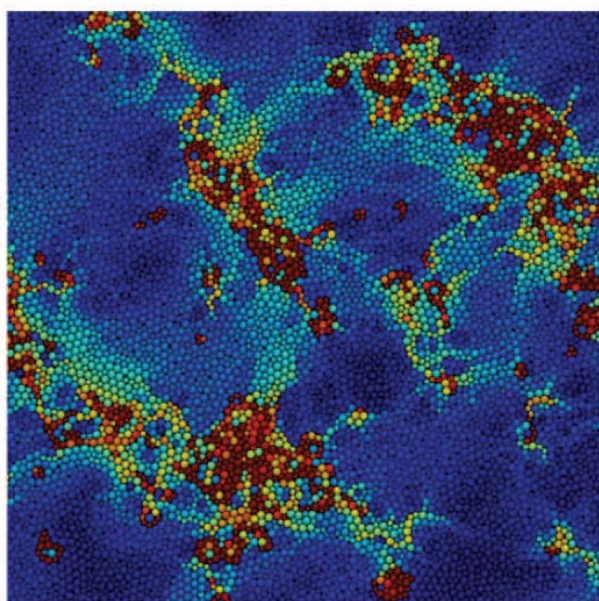


Figure 2.8: Graphical two-dimensional projection of an equilibrium trajectory of a supercooled liquid. Particles colored according to their relative mobility: dark red corresponds to higher mobility, whereas dark blue to no displacement at all. ³²

Dynamic facilitation is the property by which a local region which undergoes relaxational motion gives rise to – or facilitates – a neighboring local region to subsequently move and relax. Dynamical facilitation is the key property of kinetically constrained models of glasses. In other words, a local relaxation has a very high probability of happening nearby another local relaxation. The basic difficulty within the context of this theory is that one has to disentangle motion which does not lead to relaxation (e.g. rattling and local vibrations) from the one that effectively does so. By applying this discrimination on a large variety of supercooled liquids undergoing glass transition, it has been shown³²⁻³³ that facilitation indeed takes place and accounts for a substantial part of the global relaxation. Hence, DF has shown that facilitated relaxation is present and becomes increasingly the dominant mechanism for global relaxation when lowering the temperature and approaching the glass transition. In that sense, other means of motion, i.e. local relaxations not induced by facilitation, although present do not play a substantial role in this regime.

On the other hand, there is the so-called random first-order transition theory (RFOT)³⁴ which combines many aspects of the previously mentioned configurational entropy theory and the mode coupling theory (MCT). In particular, the RFOT theory predicts a finite temperature T_k , at which a thermodynamic transition takes place. During this transition long-range order sets in, whereas time and length-scales diverge following an activated dynamic scaling. The typical length-scale diverges as a power law³⁵:

$$\xi \propto (T - T_k)^{-1/(d-8)} \quad (2.31)$$

and the time-scale in an exponential way³⁵:

$$\tau(T) \propto \exp[(T - T_k)^{-\psi/(d-8)}] \quad (2.32)$$

One first difficulty that arises within the context of this theory is that the time-scale increases so dramatically fast that before approaching temperature T_k the system falls out of equilibrium. Thus, this effect makes more difficult the attempt of showing that there is a phase transition. A possible way to short-circuit this difficulty was proposed recently³⁶ and can be considered a counterpart of the procedure outlined for the DF

theory. As a matter of fact, there is an increasing tendency of combining the two previously mentioned theories to extract results and bypass certain difficulties. Recently ³⁷, the DF theory has been taken into account within the RFOT theory, remaining, however, a by-product and not the key ingredient in this context.

The RFOT theory is based on the assumption that there are exponentially many amorphous glass phases in which a supercooled liquid can freeze. The supercooled liquid exists and does not freeze precisely because it has too many choices for doing so. The tendency to lower the free energy by ordering in a given amorphous phase is compensated by the gain in energy obtained by disrupting the long-range order and sampling all the possible different phases. By approaching T_k , the configurational entropy decreases, i.e., the number of available glass phases diminishes, and the system eventually orders at $T = T_k$. The main idea is that by pinning a fraction c of particles randomly chosen from an equilibrium configuration at temperature T , one biases the configurations sampled by the system and decreases the number of available glass phases: only the ones compatible with the positions of the unpinned particles survive. In this way, the degrees of freedom of the system are being reduced.

Thus, the configurational entropy decreases when increasing c . It is expected that, within the RFOT theory, the configurational entropy of the system will eventually vanish at a certain $c_K(T)$, hence inducing a glass transition.

2.4 Molecular simulation techniques for glassy materials

Molecular simulation encompasses all theoretical methods and computational techniques used to model or mimic the behavior of molecules. Molecular simulation techniques are evidently very useful, as they can be used to simulate the behavior of a large variety of materials. One reason why molecular simulation techniques have been developed is to provide means of predicting macroscopic material properties from microscopic information (i.e., inter- and intra-molecular interactions, atomic coordinates and velocities, etc), bridging, in this way, the gap between macroscopic observations and microscopic phenomena. Beyond that, the role of molecular simulations is dual and can be depicted with the help of Figure 2.9:

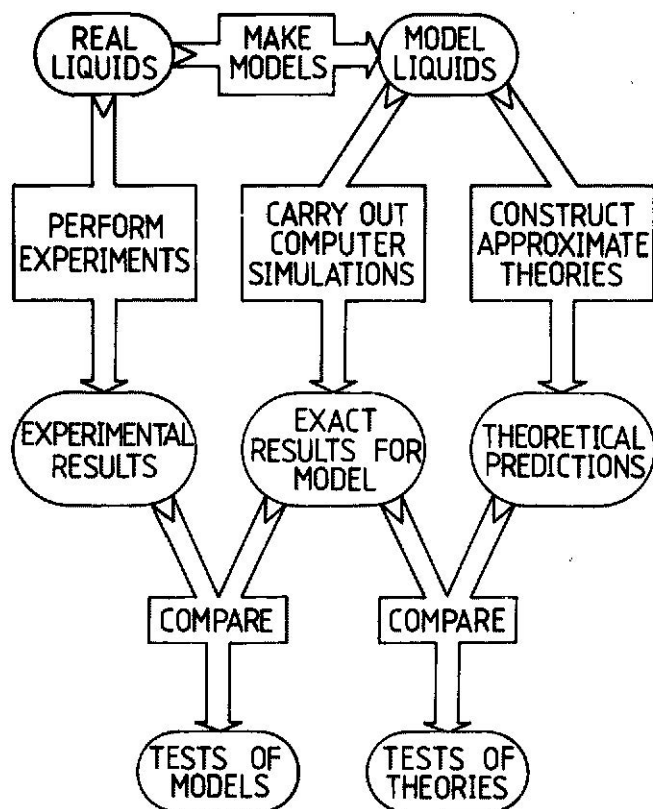


Figure 2.9: Schematic elucidation of the dual role of computer aided molecular simulations, conducted – in this example – for liquid materials. Molecular simulation techniques serve as a bridge between experimental findings and theoretical predictions.³⁸

Figure 2.9 should be read from left to right, starting by performing experiments on real materials. One main role of molecular simulation becomes clear by comparing the outer left and middle branches of the flowchart of Figure 2.9. Once a model to describe the studied material has been built, its accuracy can be tested by comparing the results of molecular simulations conducted using the model against corresponding experimental results from the real material. In this way, the correctness of the constructed model can be checked. Moreover, once a model appears to be correct by providing some initial encouraging results, its portability to other materials comes into question. Furthermore, the model's effectiveness can be also improved by making it faster or by reducing the computational power and/or memory requirements needed. Therefore, there are many levels of improvement of a certain model.

It is obvious that once a reliable, generally accepted model has been built to simulate materials, the actual experiment can be completely omitted. Even in cases where actual experimentation is out of the question, e.g. measuring the temperature of the surface of the sun, simulations based on concrete and verified models can give an answer. On the other hand, once a correct, self-consistent model is available, its simulation results can be compared to corresponding results coming from a theory under construction. In this way, the investigated theory can be tested for its correctness and be further improved. This is the second role of molecular simulation techniques, which is depicted by the middle and the outer right branch of Figure 2.9. Hence, it should now be clear that molecular simulation techniques aim in reducing the gap between experimentation and theory.

Three different kinds of molecular simulation techniques were used within the context of this work: molecular mechanics, molecular dynamics, and Monte Carlo. In the following paragraphs of this section the three above mentioned kinds of molecular simulation techniques will be presented.

2.4.1 Force field and initial configuration generation

Molecular mechanics constitutes one aspect of molecular simulations. It refers to the use of classical/Newtonian mechanics to describe the physical basis behind models of molecular systems. It makes use of the interactions between atoms to simulate or mimic the physical behavior of the modeled system under various conditions. Several models have been designed over the past years and they all aim in finding the appropriate functional form of the potential energy function \mathcal{V} that depicts, as accurately as possible, the above mentioned interactions between atoms (or structural units in general). Based on these interactions, the potential energy function of the system \mathcal{V} can be obtained, and therefore, the response of the system to every change related to the independent variables of the potential energy function \mathcal{V} , can be predicted. In particular, we assume that the independent variables of the potential energy function \mathcal{V} are the Cartesian coordinates of every atom of the investigated system. Thus, for a system consisting of n structural units (atoms, particles etc) the

potential energy function depends only on the n position vectors \mathbf{r} defining the corresponding Cartesian coordinates of the system's n structural units:

$$\mathcal{V} = \mathcal{V}(\mathbf{r}_1, \mathbf{r}_2, \mathbf{r}_3, \dots, \mathbf{r}_n) \quad (2.33)$$

Due to the key role of the potential energy function for a comprehensive understanding of this work, a special section of this paragraph will be dedicated to analyzing its basic characteristics. For the calculation of the potential energy function, it is in many cases convenient to divide the total potential energy function \mathcal{V} into two main summands: the part of the potential energy due to bonded interactions and the part of the total potential energy due to non-bonded interactions:

$$\mathcal{V} = \mathcal{V}_B + \mathcal{V}_{NB} \quad (2.34)$$

Both summands on the right-hand side of Eq. (2.34) are considered to depend only on the position vectors of the participating structural units. There is a huge variety of functional forms available in the relevant literature for both bonded and non-bonded interactions, depending on the investigated system. Nevertheless, considering the non-bonded interaction term an assumption is invoked in almost all cases, although sometimes it is tacit. More precisely, the part of the potential energy due to non-bonded interactions may be further divided into terms depending on the coordinates of individual atoms, pairs of atoms, triplets of atoms etc.:

$$\mathcal{V}_{NB} = \sum_i \mathcal{V}_1(\mathbf{r}_i) + \sum_i \sum_{j>i} \mathcal{V}_2(\mathbf{r}_i, \mathbf{r}_j) + \sum_i \sum_{j>i} \sum_{k>j>i} \mathcal{V}_3(\mathbf{r}_i, \mathbf{r}_j, \mathbf{r}_k) + \dots \quad (2.35)$$

The $\sum_i \sum_{j>i}$ notation indicates a summation over all distinct pairs i and j without counting any pair twice (i.e. as ij and ji). The same care must be taken for triplets etc. The first term of Eq. (2.35) represents the effect of an external field on the system. The remaining terms represent non-bonded particle interactions. In particular, the second term \mathcal{V}_2 , is considered to be the most important. The pair potential depends only on the pair separation distance $r_{ij} = |\mathbf{r}_i - \mathbf{r}_j|$ between the interacting atoms i and j and may be written as $\mathcal{V}_2(r_{ij})$. The third term in Eq. (2.35), involving triplets of structural units, is undoubtedly significant at liquid densities. Despite that,

these terms are only rarely included in the force field functional form, due to the tremendous increase on computational requirements that these terms bring about. The pairwise approximation gives a remarkably good description of liquid properties because the average three-body effects can be partially included by defining an “effective” pair potential. In our study, the non-bonded part of the potential energy is completely based on pair interactions:

$$\mathcal{V}'_{\text{NB}} \approx \sum_i \sum_{j>i} \mathcal{V}_2^{\text{eff}}(\mathbf{r}_i, \mathbf{r}_j) \quad (2.36)$$

The aforementioned pair interactions are considered between minimum image pairs. Minimum image pairs are being formed by using periodic boundary conditions for our simulation box. Periodic boundary conditions is a widely used technique in computer simulations used to simulate large systems by modeling a small representative part of the system’s bulk; the unit cell. According to this technique, a relatively small unit cell with given spatial extend is considered. In this way, the entire system is tiled with adjacent unit cells of the same geometry. Then, we turn our attention to one unit cell. All pair interactions are summed between atoms which reside in the the same unit cell. If a part of a molecular chain exits the unit cell, then its exact image enters the unit cell from the opposite face. One basic advantage of the implementation of periodic boundary conditions is that bulk properties are being simulated by examing only a small part of the system, which, however, contains all pairwise interactions through the use of images.

There are many famous pair potentials commonly used in computer simulations. Maybe the most common one is the so-called Lennard-Jones potential or 12-6 potential first proposed in 1924 by John Lennard-Jones³⁹:

$$\mathcal{V}'_{\text{NB}}{}^{\text{LJ}}(r) = 4\varepsilon \left(\left(\frac{\sigma}{r} \right)^{12} - \left(\frac{\sigma}{r} \right)^6 \right) \quad (2.37)$$

where the parameters ε and σ are characteristic constants of the studied material. The first one (called epsilon) depicts the depth of the potential energy well, as shown in Figure 2.10, whereas the second one (called sigma) represents the separation distance between atoms i and j forming the pair ij , at which the potential energy changes sign.

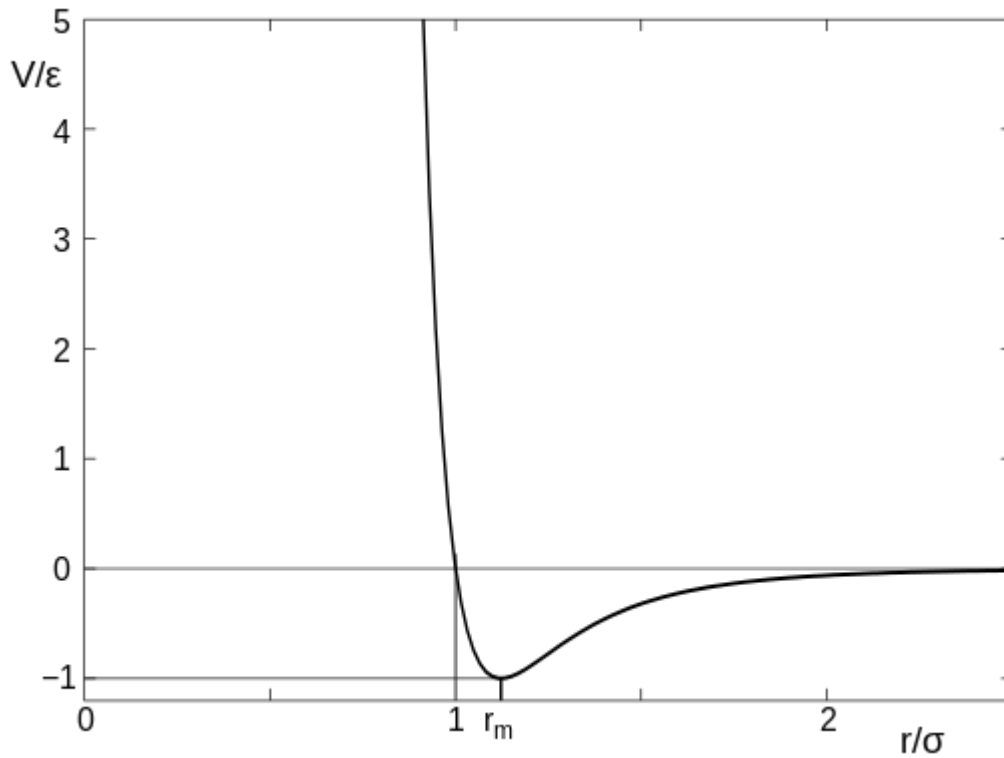


Figure 2.10: Graphical representation of a typical Lennard-Jones potential. With r_m is depicted the distance between the atoms i and j , at which the potential energy exhibits a minimum, whose energy value is $-\varepsilon$.

The Lennard-Jones potential consists of two different terms, one repulsive and one attractive. The first one, $\left(\frac{\sigma}{r}\right)^{12}$, is dominant at small interatomic distances, where repulsive forces are prevalent. The second term, $\left(\frac{\sigma}{r}\right)^6$, prevails over the previous term at large distances, where attractive forces are dominant. Beyond the Lennard-Jones non-bonded potential, other famous potential energy functions have appeared over the past years. One example of these is the so-called Buckingham pair-potential⁴⁰, in which an exponential term is used to describe the existing repulsive interactions:

$$V_{\text{NB}}^{\text{Buck}}(r) = A \exp(-Br) - \frac{C}{r^6} \quad (2.38)$$

According to this approach, the repulsion is due to the interpenetration of the closed electron shells. For the purpose of investigating general properties of liquids, and for

comparison with theory, highly idealized pair potentials may be of value. These are relatively simple and, although unrealistic, are extremely convenient and simple to use. The most important pair potentials in this category are: the hard-sphere potential, as defined in Eq. (2.14) and represented in Figure 2.5, the square-well potential:

$$\mathcal{V}_{\text{NB}}^{\text{SW}}(r) = \begin{cases} \infty, & r < \sigma_1 \\ -\varepsilon, & \sigma_1 \leq r < \sigma_2 \\ 0, & r \geq \sigma_2 \end{cases} \quad (2.39)$$

and the soft-sphere potential:

$$\mathcal{V}_{\text{NB}}^{\text{SS}}(r) = \varepsilon \cdot \left(\frac{\sigma}{r}\right)^{\nu} = \alpha \cdot r^{-\nu} \quad (2.40)$$

where ν is a parameter, often chosen to be an integer. In this work, the Lennard-Jones potential, as depicted in Eq. (2.37), has been exclusively used to describe inter- and intra-molecular non-bonded pair interactions.

Concerning bonded interactions, described by the first summand of Eq. (2.34) \mathcal{V}_{B} , it can be further divided into more terms, each of which accounts for a different kind of bonded intra-molecular interaction.

$$\mathcal{V}_{\text{B}} = \mathcal{V}_{\text{BONDS}} + \mathcal{V}_{\text{ANGLES}} + \mathcal{V}_{\text{TORSION}} + \mathcal{V}_{\text{IMPROPER}} + \mathcal{V}_{\text{ELECTRO}} \quad (2.41)$$

At this point it should be mentioned that bonded interactions are only present within one and the same molecule. There are no bonded interactions between different parts of different polymer chains existing in a melt. Thus, bonded interactions are only located between atoms (or structural units) of one and the same molecule (e.g. polymer chain). In Eq. (2.41), a possible combination of different kinds of bonded interactions is presented. This is by no means unique. It rather adjusts to the needs of the system investigated each time. For example, the interaction potential used in all implemented simulations in this work concerning the united-atom model for atactic polystyrene is the one proposed by Lyulin et. al.⁴¹:

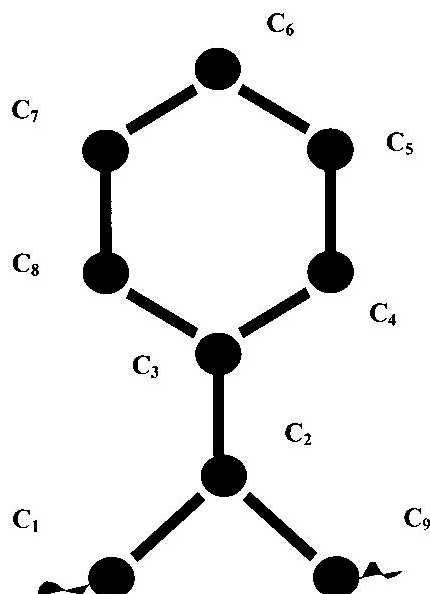


Figure 2.11: The monomer unit with numbered atoms of the united-atom model for simulating atactic polystyrene. ⁴¹

According to the adopted united-atom model, all the hydrogens are being absorbed into the carbon atoms with which they are connected. In this way, “united-atoms” are formed (represented in Figure 2.11 as spherical atoms) in place of simple carbon-hydrogen (CH) groups, methylene groups $-(CH_2)-$, or methyl groups $-CH_3$.

The adopted interaction potential for atactic polystyrene takes into account the following contributions to the system total potential energy: (i) Lennard-Jones non-bonded interaction potential between all united atoms that are three or more bonds apart or belong to different images of the parent chain [Eq. (2.31)], whereas no tail corrections are used; (ii) harmonic bond stretching potential for every covalent bond, with l symbolizing the bond length :

$$\mathcal{V}_{\text{BOND LENGTH}}^{\text{BOND}} = \sum_{\text{all bonds } i} \frac{1}{2} k_{\text{bond}} (l_i - l_{i,0})^2 \quad (2.42)$$

(iii) bending potential for all bond angles, including those in the phenyl rings:

$$\mathcal{V}_{\text{ANGLE}}^{\text{BOND}} = \sum_{\text{all bond angles } i} k_{\theta} (\theta_i - \theta_{i,0})^2 \quad (2.43)$$

$$\mathcal{V}_{\text{BOND ANGLE}}^{\text{PHENYL}} = \sum_{\text{all aromatic bond angles } i} \hat{k}_{\theta} (\hat{\theta}_i - \hat{\theta}_0)^2 \quad (2.44)$$

(iv) torsional potential for all rotatable backbone bonds:

$$\mathcal{V}_{\text{BACKBONE}}^{\text{TORSIONAL}} = \sum_{\text{all torsion angles } i} k_{\phi} (1 - \cos 3\phi_i) \quad (2.45)$$

(v) torsional potential for the torsions of phenyl rings around their stems:

$$\mathcal{V}_{\text{PHENYL}}^{\text{TORSIONAL}} = \sum_{\text{all phenyl torsion angles } i} k_{\chi} \cos^2(\chi_i - \chi_0) \quad (2.46)$$

(vi) out-of-plane bending potential to preserve the coplanarity of the phenyl and the phenyl stem:

$$\mathcal{V}_{\text{COPLANARITY}}^{\text{PHENYL}} = \sum_{\text{all phenyls } i} k_{\psi} (\psi_i - \psi_0)^2 \quad (2.47)$$

(vii) torsional potential about all bonds connecting aromatic carbons in the phenyl ring, to preserve the planarity of the ring:

$$\mathcal{V}_{\text{PLANARITY}}^{\text{TORSIONAL RING}} = \sum_{\text{all phenyl torsion angles } i} \hat{k}_{\phi} (1 + \cos 2\hat{\phi}_i) \quad (2.48)$$

(viii) improper torsional potential to preserve the chirality of all carbons bearing a phenyl substituent:

$$\mathcal{V}_{\text{IMPROPER}} = \sum_{\text{all chiral carbons } m} \frac{1}{6k'} (\Delta_{129,m} + \Delta_{123,m} + \Delta_{329,m})^6 \quad (2.49)$$

where $\Delta_{ijk} = \cos \theta_{ijk} - \cos \theta_0$ and $\theta_0 = 109.5^\circ$ and θ_{ijk} is the bending angle formed by the C_i, C_j and C_k united atoms according to the numbering of Figure 2.11. Hence, the potential energy functional form for the atactic polystyrene system has the following form:

$$\begin{aligned}
 \mathcal{V} &= \mathcal{V}'_{\text{NB}} + \mathcal{V}'_{\text{B}} = \\
 &= \sum_{\text{all nonbonded pairs of atoms } ij \text{ within } r_c} 4\epsilon_{ij} \left(\left(\frac{\sigma_{ij}}{r_{ij}} \right)^{12} - \left(\frac{\sigma_{ij}}{r_{ij}} \right)^6 \right) + \sum_{\text{all bonds } i} \frac{1}{2} k_{\text{bond}} (l_i - l_{i,0})^2 + \sum_{\text{all bond angles } i} k_{\theta} (\theta_i - \theta_{i,0})^2 + \\
 &+ \sum_{\text{all aromatic bond angles } i} \hat{k}_{\theta} (\hat{\theta}_i - \hat{\theta}_0)^2 + \sum_{\text{all torsion angles } i} k_{\phi} (1 - \cos 3\phi_i) + \sum_{\text{all phenyl torsion angles } i} k_{\chi} \cos^2(\chi_i - \chi_0) + \\
 &+ \sum_{\text{all phenyls } i} k_{\psi} (\psi_i - \psi_0)^2 + \sum_{\text{all phenyl torsion angles } i} \hat{k}_{\phi} (1 + \cos 2\hat{\phi}_i) + \sum_{\text{all chiral carbons } m} \frac{1}{6k'} (\Delta_{129,m} + \Delta_{123,m} + \Delta_{329,m})^6
 \end{aligned} \tag{2.50}$$

A detailed description of every energy term contributing to the total potential energy is shown in Appendix A along with a table (Table A.1) containing the arithmetic values of all involved parameters. Returning to molecular mechanics techniques, two different techniques belonging in this category were widely used in the context of this work. The first method is the polymer builder and it has been used to build a polymer chain out of its structural units. The polymer chain has a given stereochemical structure, tacticity, and molecular weight. Also, the condensed phase of chains being simulated has a specified temperature and density. Through the help of a polymer builder software called MAPS⁴² (Materials Processes and Simulations simulation platform), developed by Scienomics SARL, one or more parent polymer chains, with specific desired characteristics, can be built. The polymer chain is being built after choosing the structural units (or monomer units) from which it will be constructed and the potential energy force field that defines the interactions between the structural units of the molecule. By doing so, one is certain that in the constructed molecule there is no overlap between parts of the polymer chain and their periodic images (a correctly chosen force field should prevent such phenomena) and the geometry of the constructed molecule is as expected (e.g. the phenyl-group has the expected hexagonal planar ring shape).

Once the desired initial configuration has been constructed using an appropriately chosen force field, its total potential energy is calculated by summing all the energy contributions presented in Eqs. (2.34), (2.36) and (2.41). For the system of atactic polystyrene, the individual contributions to the total potential energy are given by Eq. (2.50). It is obvious that, depending on the studied system, some of the above mentioned summands of the total potential energy may vanish and additional ones

(e.g. Coulombic interactions between partial charges on the atoms) may arise, depending on the force field. The calculated total potential energy of the initial configuration is expected to be high, because repulsive “excluded volume” interactions have been taken into account only coarsely during the process of Monte Carl growth of the chains. To achieve more realistic energies, the potential energy must be minimized with respect to all microscopic degrees of freedom. This takes place to the molecular mechanics technique used in this work.

2.4.2 Molecular mechanics

The problem of finding the minimum potential energy and corresponding configuration of a given molecular system is not new. According to mathematical terminology, this problem belongs to the general category of optimization problems. An optimization problem translates in finding the appropriate values for the independent variables x_1, x_2, \dots, x_n of the function $f(x_1, x_2, \dots, x_n)$ to be optimized. In our case, the function to be optimized is the total potential energy function $\mathcal{V} = \mathcal{V}(\mathbf{r}_1, \mathbf{r}_2, \dots, \mathbf{r}_n)$ and the optimization problem translates into an energy minimization problem. We aim, therefore, at finding the appropriate values of the independent variables of \mathcal{V} that lead to a local minimum value of the total potential energy. To this end, a system of non-linear equations has to be solved. In general, the solution to the above problem may proceed either analytically or arithmetically. In many cases, though, the arithmetic approach appears to be the only feasible choice. In molecular systems the number of the independent variables is typically extremely high and the dependence of the objective function on the variables is very complex, making an analytical solution of the above system of non-linear equations very difficult, or impossible. In these cases, the arithmetic approach for optimizing – in our case, minimizing– an objective function is the only solution ⁴³.

There is a large variety of iterative optimization algorithms, all of which have two common characteristics: a) the direction of the optimization $\mathbf{h}(\mathbf{x}_i)$, towards which the independent variables will be changed to achieve a new value of the objective function $f(\mathbf{x})$ that is lower than the previous one $f(\mathbf{x}_{i+1}) < f(\mathbf{x}_i)$ and b) the step

length α_i of the attempted step in the chosen direction $\mathbf{h}(\mathbf{x}_i)$. In this way, the new value of variable \mathbf{x} is defined through the following equation:

$$\mathbf{x}_{i+1} = \mathbf{x}_i + \alpha_i \cdot \mathbf{h}(\mathbf{x}_i) \quad (2.51)$$

In Eq. (2.51), $\mathbf{h}(\mathbf{x}_i)$ is a n -tuple vector and α_i is a real scalar number. In each iteration \mathbf{x}_i and $\mathbf{h}(\mathbf{x}_i)$ are known and \mathbf{x}_{i+1} is determined through unidimensional minimization of the objective function f with respect to the scalar parameter α_i . The main difference between all the available optimization algorithms lies basically in the definition of the optimization direction $\mathbf{h}(\mathbf{x}_i)$.

Some simple optimization algorithms demand as input only an initial value for the variable \mathbf{x} . Also, a subroutine must be provided that uses \mathbf{x} as input and returns as output the value of $f(\mathbf{x})$, where f is the objective function to be optimized (in our case, the total potential energy function \mathcal{V}). The algorithms that require only the above input are called direct search methods. There are, however, many algorithms that go beyond the above second requirement. An important category of algorithms require that the user provide subroutines that compute the gradient of the objective function, $\nabla f(\mathbf{x})$, in addition to f itself, given point \mathbf{x} . These algorithms are called 1st order algorithms and converge generally faster than the direct search methods. Thus, whenever the gradient calculation can proceed without any trouble, 1st order algorithms are being preferred. The famous Newton optimization algorithm requires the calculation of the matrix of second order derivatives $\frac{\partial^2 f(\mathbf{x})}{\partial \mathbf{x} \partial \mathbf{x}^T}$ and does not belong to the 1st order algorithms. The second order derivatives calculation is in many cases extremely time consuming, if not impossible, hence the Newton-method is often not preferred. Algorithms which approximate the Hessian matrix $\frac{\partial^2 f(\mathbf{x})}{\partial \mathbf{x} \partial \mathbf{x}^T}$ with suitable expressions based on first-derivative information constitute the quasi-Newton category, which is invoked quite often. They have higher memory requirements (to store the estimate of the Hessian) and higher demands in central processing unit (CPU) time per iteration, but may require less iterations than conventional 1st order algorithms.

Among the most important 1st order algorithms for optimization problems are the steepest descent and the conjugate gradients methods, both of which were widely used to minimize objective functions defined throughout this work. In general, the conjugate gradients method is faster than the steepest descent method. Its basic disadvantage is related to the calculation of the step length α_i . If the accuracy for this calculation is high enough, then not only is the fast convergence of the method is lost, but also it is not certain any more that the method will converge at all ⁴³. Both the steepest descent and the conjugate gradients methods applied for the minimization problem of the total potential energy \mathcal{V} constitute prominent examples of molecular mechanics simulations.

2.4.3 Molecular dynamics

Computer aided molecular simulations generate information at the microscopic level (atomic and molecular positions, velocities etc.). Converting this very detailed information into common macroscopic properties (pressure, internal energy, enthalpy etc.) is the realm of statistical mechanics. Statistical mechanics constitutes, therefore, a powerful mathematical tool that becomes very handy in molecular simulations. The microscopic state of a given system may be specified in terms of the positions and momenta of all particles constituting the system. In classical mechanics the state of a system of n particles can be fully described through a set of generalized coordinates:

$$\mathbf{q} \equiv (\mathbf{q}_1, \mathbf{q}_2, \dots, \mathbf{q}_n) = (q_{11}, q_{12}, q_{13}, q_{21}, q_{22}, q_{23}, \dots, q_{n1}, q_{n2}, q_{n3}) \quad (2.52)$$

and a set of generalized momenta:

$$\mathbf{p} \equiv (\mathbf{p}_1, \mathbf{p}_2, \dots, \mathbf{p}_n) = (p_{11}, p_{12}, p_{13}, p_{21}, p_{22}, p_{23}, \dots, p_{n1}, p_{n2}, p_{n3}) \quad (2.53)$$

From Eq. (2.52) it is evident that, for a system of n particles, the dimensionality of the domain, from which the generalized coordinates take their values is $3n$. This domain (or set of permissible points) is called the configuration space. In an analogous way, Eq. (2.47) shows that the domain from which the generalized momenta take their values is also of dimensionality $3n$, called the momentum space. The superposition of the two above vector spaces defines the so-called phase space Γ

, whose dimensionality is $6n$. In classical mechanics, any vector defined within the phase space $\mathbf{X} \equiv (\mathbf{q}, \mathbf{p}) = (\mathbf{q}_1, \mathbf{q}_2, \dots, \mathbf{q}_n; \mathbf{p}_1, \mathbf{p}_2, \dots, \mathbf{p}_n)$ is depicted by a single point within the phase space and corresponds to a certain microstate. As the system evolves in time, driven by the potential developed due to the inter- and intra-molecular interactions, the above mentioned point in phase space moves accordingly, tracing a trajectory $\mathbf{X}(t)$. This trajectory is a line, each point of which fully describes the system at a certain time t .

This is exactly what the knowledge of the system's Hamiltonian \mathcal{H} can provide. According to quantum mechanics, the Hamiltonian \mathcal{H} is an operator, the exact knowledge of which can fully describe a system. In classical mechanics, the Hamiltonian \mathcal{H} is the total energy of a system, which can be expressed as a function of the particle positions and velocities $\mathcal{H} = \mathcal{H}(\mathbf{X}) = \mathcal{H}(\mathbf{p}, \mathbf{q})$. If the Hamiltonian does not depend directly on time $\mathcal{H} \neq \mathcal{H}(\mathbf{p}, \mathbf{q}, t)$ – but its time-dependence originates only from the time-dependence of \mathbf{p} and \mathbf{q} which change with time along a trajectory –, then the Hamiltonian constitutes a constant of motion. Moreover, if we assume that the potential energy of the system \mathcal{V} depends only on the generalized coordinates \mathbf{p} , and the kinetic energy of the system \mathcal{K} depends only on the generalized momenta \mathbf{q} , then the Hamiltonian can be written as:

$$\mathcal{H}(\mathbf{p}, \mathbf{q}) = \mathcal{V}(\mathbf{p}) + \mathcal{K}(\mathbf{q}) \quad (2.54)$$

It has been shown⁴⁴, that some problems in statistical mechanics are exactly soluble. By this, we mean that a complete specification of the microscopic properties of a system leads directly to a set of interesting results for macroscopic properties. To this end, two steps are necessary. First the Hamiltonian of the studied system has to be constructed and then, provided that knowledge of the system's Hamiltonian is available, the statistical mechanical problem has to be solved. The biggest challenge of the two is the second one. There are only a handful of non-trivial, exactly soluble problems in statistical mechanics; the two-dimensional Ising model is a famous example. This fact constitutes the main difficulty and weakness of statistical mechanics, i.e., although there is a strict formalism^{38, 45} available for the prediction of macroscopic properties through the use of a calculated Hamiltonian, most problems

are not exactly soluble. While not exactly soluble, they still succumb to analysis based on a straightforward approximation scheme. Many analytical theories (e.g. integral equations and operator theories, perturbation theories, Bragg-Williams approximation for a lattice model etc.) have been developed over the past years in order to produce solution to this statistical mechanical problem. All those theories are, nevertheless, bound to constraints and approximations. An alternative strategy to this end is based on numerical solution of the above statistical mechanical problem.

Molecular dynamics (MD) constitutes a simulation technique for tracking the temporal evolution of a system. This method is based on numerical solution – i.e., integration – of the differential equations of motion, which describe the evolution of the system's trajectory over time. The equations of motion describing the temporal evolution of the system along a trajectory spanned in phase space can be written in three different ways. According to Newton's expression for the equation of motion, they have the following form:

$$m \cdot \ddot{\mathbf{r}}_i = \mathbf{F}_i \quad (2.55)$$

where $\mathbf{F}_i = -\nabla_{\mathbf{r}_i} \mathcal{V}$. Eq. (2.55) describes a system of second order differential equations, the number of which – for a system consisting of n atoms – is equal to $3n$. Alternatively, if the Hamilton approach is adopted, then the equations of motion have the following form:

$$\begin{aligned} \dot{\mathbf{p}}_i &\equiv \frac{\partial \mathbf{p}_i}{\partial t} = -\nabla_{\mathbf{r}_i} \mathcal{H}(\mathbf{p}, \mathbf{q}) \\ \dot{\mathbf{r}}_i &\equiv \frac{\partial \mathbf{r}_i}{\partial t} = \nabla_{\mathbf{p}_i} \mathcal{H}(\mathbf{p}, \mathbf{q}) \end{aligned} \quad (2.56)$$

The alternative representation of the equations of motion offered by Eq. (2.56) is completely equivalent to the one shown in Eq. (2.55). In Eq. (2.55) the Cartesian coordinates \mathbf{r}_i have been used to describe the system, whereas in Eq. (2.56) the set of generalized coordinates \mathbf{p}_i and momenta \mathbf{q}_i have been used for the same purpose. In addition, Eqs. (2.56) constitute a system of first order differential equations, the number of which is – for a system consisting of n atoms – equal to $3n + 3n = 6n$. Hence, if the Newton description is chosen, the motion of the system in time is described by a system of $3n$ second order differential equations for a system

consisting of n atoms, whereas if the Hamilton description is chosen the time evolution of the system is described through a system of $6n$ first order differential equations. Finally, the Lagrange description of the motion of the system in phase space leads to a similar formalism to Newton's approach.

Regardless of the description (they are all equivalent) chosen for tracking the temporal evolution of the system, the system of equations to be solved should fulfill two conditions. First, the total energy of the system should be preserved and secondly, time-reversibility of the obtained trajectory must be ensured. In particular, regarding the first requirement, the Hamiltonian of the system should be a constant of motion,

i.e. it should not depend on time $\dot{\mathcal{H}} \equiv \frac{d\mathcal{H}}{dt} = 0$. This statement is fulfilled if the forces acting upon every atom of the system are a function only of the coordinates, but not of the velocities and/or time. The second requirement related to time reversibility can be checked very easily. If the signs of all atomic velocities are reversed at time $t + \delta t$, then the atoms should acquire the exact same positions that they had during the previous time t by following the exact reverse trajectory.

The primary target of an MD algorithm is, as mentioned above, the numerical solution of the equations of motion describing the temporal and spatial evolution of a studied system in phase space. To this end, several algorithms have been proposed for the numerical integration of the differential equations describing the motion. In general, these methodologies can be divided in two major categories: a) high order integration methods (or predictor-corrector algorithms)⁴⁶ and b) the Verlet methods^{46b, 47}. Methods belonging to the first category proceed in a very simple way. The basic idea is as follows. Given the molecular positions, velocities, and other dynamic information (such as the potential energy function) at time t , we attempt to obtain the positions and velocities at a later time $t + \delta t$, to a sufficient degree of accuracy. Given the fact that the classical trajectory is continuous, an estimate of the positions, velocities, etc. at time $t + \delta t$ may be obtained by Taylor expansion about time t :

$$\begin{aligned}
\mathbf{r}^p(t + \delta t) &= \mathbf{r}(t) + \mathbf{v}(t) \cdot \delta t + \frac{1}{2} \ddot{\mathbf{r}}(t) \cdot \delta t^2 + \frac{1}{6} \dddot{\mathbf{r}}(t) \cdot \delta t^3 + \frac{1}{24} \mathbf{r}^{(4)}(t) \cdot \delta t^4 \dots \\
\mathbf{v}^p(t + \delta t) &= \mathbf{v}(t) + \dot{\mathbf{r}}(t) \cdot \delta t + \frac{1}{2} \ddot{\mathbf{r}}(t) \cdot \delta t^2 + \frac{1}{6} \dddot{\mathbf{r}}(t) \cdot \delta t^3 + \dots \\
\ddot{\mathbf{r}}^p(t + \delta t) &= \ddot{\mathbf{r}}(t) + \dddot{\mathbf{r}}(t) \cdot \delta t + \frac{1}{2} \mathbf{r}^{(4)}(t) \cdot \delta t^2 + \dots \\
\ddot{\mathbf{r}}^p(t + \delta t) &= \ddot{\mathbf{r}}(t) + \dddot{\mathbf{r}}(t) \cdot \delta t + \dots
\end{aligned} \tag{2.57}$$

The superscript “p” on the left hand side of Eqs. (2.57) indicates that these are “predicted” values. Equations like Eqs. (2.57) cannot generate correct trajectories as time advances, because they do not make use of the equations of motion. These enter through the correction step. According to this step, we may calculate from the new positions $\mathbf{r}^p(t + \delta t)$ at time $t + \delta t$, the forces at time $t + \delta t$ by using the equations of motion and hence the correct accelerations $\ddot{\mathbf{r}}^c(t + \delta t)$, indicated by the superscript “c”. These can be compared with the predicted accelerations from Eqs. (2.57) to estimate the size of the error in the prediction step during the calculation of the accelerations:

$$\Delta \ddot{\mathbf{r}}(t + \delta t) = \ddot{\mathbf{r}}^c(t + \delta t) - \ddot{\mathbf{r}}^p(t + \delta t) \tag{2.58}$$

The calculated error and the results of the predictor step, are then fed into the corrector step:

$$\begin{aligned}
\mathbf{r}^c(t + \delta t) &= \mathbf{r}^p(t + \delta t) + c_0 \cdot \Delta \ddot{\mathbf{r}}(t + \delta t) \\
\mathbf{v}^c(t + \delta t) &= \mathbf{v}^p(t + \delta t) + c_1 \cdot \Delta \ddot{\mathbf{r}}(t + \delta t) \\
\ddot{\mathbf{r}}^c(t + \delta t) &= \ddot{\mathbf{r}}^p(t + \delta t) + c_2 \cdot \Delta \ddot{\mathbf{r}}(t + \delta t) \\
\ddot{\mathbf{r}}^c(t + \delta t) &= \ddot{\mathbf{r}}^p(t + \delta t) + c_3 \cdot \Delta \ddot{\mathbf{r}}(t + \delta t)
\end{aligned} \tag{2.59}$$

The idea is that $\mathbf{r}^c(t + \delta t)$ and the other terms on the left side of Eqs. (2.59) are now better approximations to the true positions, velocities etc. There are certain proposed ways to define the coefficients c_0, c_1, c_2, c_4 in order to allow a faster convergence to the “true” values^{46a, 46b}. In this way, through this iterative predictor-corrector process, MD trajectories can be obtained.

The second category of proposed methodologies for the numerical integration of the equations of motion includes various expressions of the so-called Verlet algorithm^{46b},

⁴⁷. Among all possible expressions of this algorithm (Verlet's original method, leap-frog alternative and velocity-Verlet form), we will briefly describe here the velocity-Verlet algorithm which is the most efficient of all Verlet-based algorithms and constitutes the numerical method used in the MD computational experiments conducted in this work. This algorithm constitutes a direct solution of the second-order differential equation Eq. (2.55) (Newton's formulation). The basic advantage of this version of the Verlet algorithm is that this formulation handles the calculation of the velocities in a very efficient way, whereas previous versions calculate the velocities at a different time than the one for positions and accelerations. The velocity-Verlet formulation stores positions, velocities and accelerations all at the same time t ⁴⁸. A schematic representation of the way the velocity-Verlet algorithm proceeds is shown in Figure 2.12. From the same figure, the superiority of this formulation (velocity-Verlet, part (c) of Figure 2.12) becomes obvious in relation to the velocity problem mentioned above over the other two formulations of the general Verlet algorithm (original algorithm and leap-frog version shown as parts (a) and (b) of Figure 2.12 respectively):

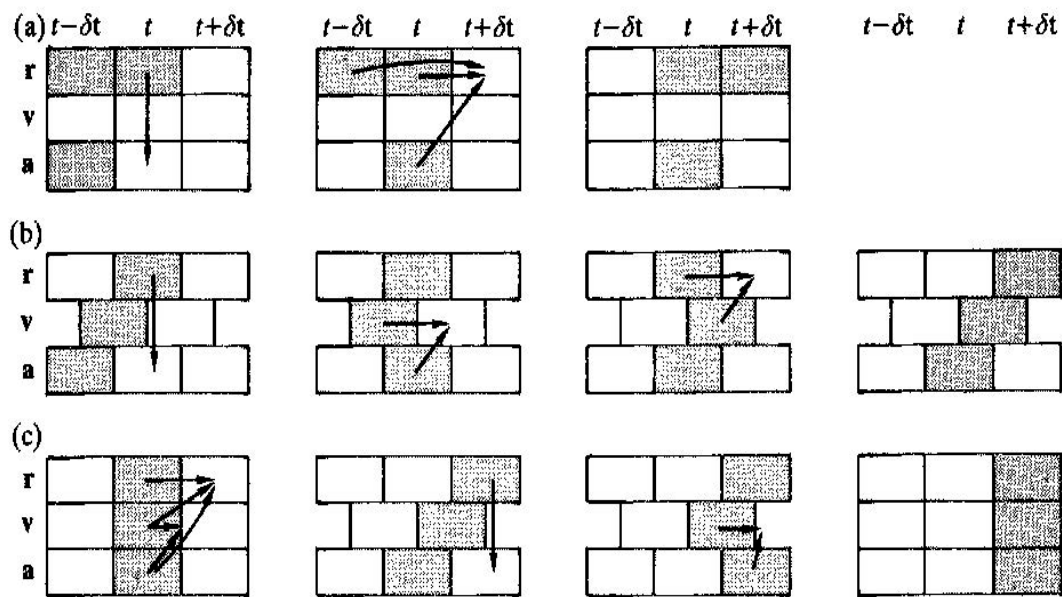


Figure 2.12: Schematic representation of the sequence of calculations for the three different versions of the Verlet algorithm for numerical integration of the equations of motion. Part (a) shows Verlet's original method, part (b) represents the leap-frog form and part (c) shows the velocity-Verlet formulation.

By observing and comparing the rightmost element for each one of the three parts of Figure 2.12, we conclude that the velocity-Verlet formulation (part c) calculates positions, velocities and accelerations all at the same time $t + \delta t$, whereas the other two versions do not. The mathematical formalism with the help of which the velocity-Verlet algorithm calculates MD trajectories in phase space is the following ³⁸:

$$\begin{aligned} \mathbf{r}(t + \delta t) &= \mathbf{r}(t) + \mathbf{v}(t) \cdot \delta t + \frac{1}{2} \mathbf{a}(t) \cdot \delta t^2 \\ \mathbf{v}(t + \delta t) &= \mathbf{v}(t) + \frac{1}{2} [\mathbf{a}(t) + \mathbf{a}(t + \delta t)] \cdot \delta t \end{aligned} \quad (2.60)$$

Regardless of the method followed for integrating the equations of motion, two types of input should be available for the initialization of the algorithm. All particle coordinates and corresponding velocities should be known at a certain time t (which for simplicity reasons we define as $t = 0$), hence: $\mathbf{r}_i(t = 0)$ and $\dot{\mathbf{r}}_i(t = 0)$ should be available for every particle i . The basic scheme according to which a typical MD-simulation proceeds is shown in Figure 2.13:

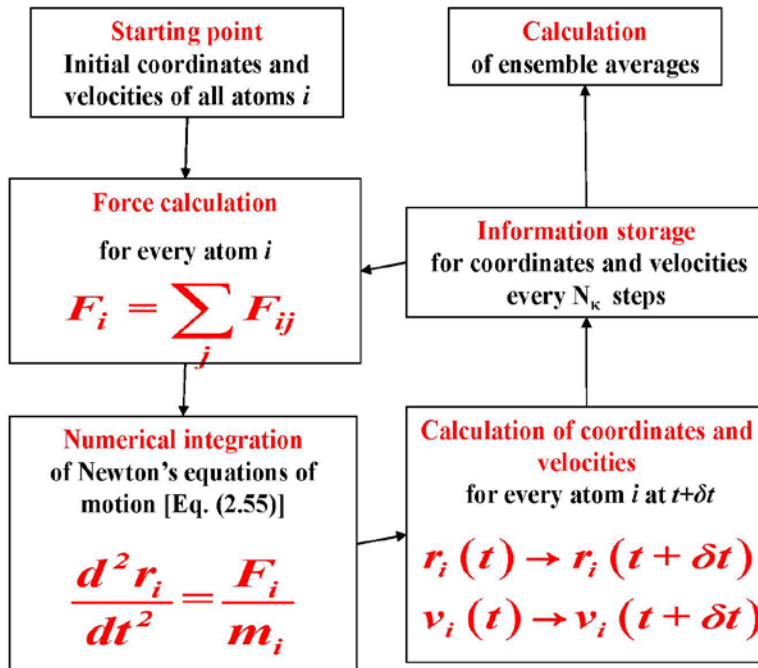


Figure 2.13: Schematic flow chart of a typical molecular dynamics simulation.

In the recursive procedure described in Figure 2.13, the equations of motion are being integrated for a small time interval δt , between t and $t + \delta t$. The time step δt , over which the integration ensues, is a user defined quantity. In general, the smaller the time step is, the bigger the accuracy of the algorithm. This result would probably lead us to the conclusion that δt should be made as small as possible, so that property fluctuations may be minimal. The reason for not doing so is because δt also determines how far in time we evolve at every integration step, depicted as a closed loop in Fig. 2.13, by solving the equations of motion. If the chosen value for δt is extremely small, in order to minimize losses, then the algorithm will evolve in time extremely slowly and it will take a tremendously large number of steps to cover a certain time interval between t_1 and t_2 . Thus, the choice of the integration time step δt should be made cautiously and should express a good compromise between accuracy in calculations and evolution speed. Clever and extremely useful multiple-time step modifications have been developed over the past years⁴⁹ discriminating between fast and slow processes, i.e., processes that contribute to the total potential energy and change rapid or slowly with time, and applying to each one of them a different time step, allowing in this way the integration of the equations of motion to proceed faster.

MD-simulations are characterized as a deterministic way for exploring the behavior of a system and calculating macroscopic properties as ensemble averages of microstates. In particular, molecular dynamics techniques are based on the numerical solution of a concrete set of equations, i.e, the equations of motion and thus, MD simulation techniques are characterized as a deterministic approach for tracking the temporal evolution of a system evolving through a certain trajectory in phase space. MD simulation methods are, therefore, appropriate for estimating structural and dynamical properties by recursively solving the equations of motion. Within this approach, time has a physical meaning and several properties are calculated as a function of time t . Besides, it should not be forgotten that the numerical integration of the equations of motion taking place in the context of an MD simulation, is ultimately an integration over time t . In the next section of this chapter an alternative approach for calculating macroscopic properties will be presented.

2.4.4 Monte Carlo simulation techniques

It has been found during the solution of several statistical problems⁵⁰ that deterministic mathematical problems can be alternatively treated by finding a probabilistic analogue which is then solved based on a stochastic sampling experiment. These sampling computational experiments involve the generation of random numbers and the execution of a certain experiment a large number of times. The Monte Carlo (MC) method takes advantage of the above finding. Its conclusion and finds use in the calculation of thermodynamic averages through a stochastic sampling procedure. The name “Monte Carlo”, alluding to casinos and games of chance, was chosen by the developers of the algorithm Neumann, Ulam and Metropolis⁵¹ because of the extensive use of random numbers.

The way MC algorithms proceed in the calculation of a certain property can be initially approached by the following example. Let’s suppose that the following definite integral needs to be calculated:

$$I = \int_a^b f(x) \cdot dx \quad (2.61)$$

According to the first mean value theorem for integrals, it can be proven that the right part of Eq. (2.61) is equal to:

$$\int_a^b f(x) \cdot dx = (b - a) \cdot f(c) \quad (2.62)$$

where $f(c)$ denotes the unweighted average of $f(x)$ on $[a, b]$. In other words, $f(c)$ is a mean value of $f(x)$ over the interval $[a, b]$ and therefore it can be symbolized as $\langle f(x) \rangle$ and the integral I of Eq. (2.61) becomes then equal to:

$$I = (b - a) \cdot \langle f(x) \rangle \quad (2.63)$$

If a MC algorithm is designed appropriately and applied to evaluate $f(x)$ for a large amount of randomly distributed x values over the interval $[a, b]$, then the average

value $\langle f(x) \rangle$ can be easily calculated and hence the integral value I over $[a, b]$. It is clear that, as the number of sampled values of x approaches infinity, this procedure should yield the “correct” value for I . The above example constitutes a simple representation of the usage of a stochastic algorithm. Such an algorithm is confronted with many kinds of difficulties. One basic difficulty concerns the execution time of a certain calculation. In particular, assume that in the above example not all points in the interval $[a, b]$ have the same importance in the calculation of the mean value $\langle f(x) \rangle$, i.e. the distribution of x in $[a, b]$ is not uniform.

Assume that the continuous random variable x is distributed according to the probability density function $\rho(x)$ in the interval $[a, b]$. In general, $\rho(x)$ is a non-negative function satisfying the normalization condition $\int_a^b \rho(x) dx = 1$. It is highest in the most probable (or “important”) regions and lowest in the least probable (or “non-important”) regions of x -space. If one discretizes the space from which the random variable x takes values into intervals of length dx , then $N(x) = \rho(x) dx$ is the probability of finding the random variable within an interval of length dx around the point x . We will use the term “microstate x ” to denote such an interval. These considerations can be readily generalized to the case where x takes values from a multidimensional configuration space; in the latter case it is a vectorial quantity, usually denoted as \mathbf{x} . How can a way be found to sample as much as possible the important points and neglect the non-important points for the given calculation? In other words, how should we distribute our sampling through the interval $[a, b]$, so that points are chosen according to the probability distribution defined by $\rho(x)$?

In statistical mechanics, the probability density $\rho(x)$ is usually proportional to the factor $\exp(-\beta U)$, where U , a function of x , is an algebraic quantity and generally represents the property that defines a point as “important” or “non-important” for a given calculation, while β is a positive constant. The factor $\exp(-\beta U)$ is called Boltzmann factor or Boltzmann weight. We define as “important” those points to be sampled, whose value of U is low, and “non-important” those points, for which the value of property U is high. So, “important” points have a large Boltzmann factor

and “non-important” points have a small Boltzmann factor. In the canonical ensemble, specifying the probability density in configuration space of a system under the macroscopic constraints of constant number of molecules N , volume V , and temperature T , U is the potential energy \mathcal{V} and $\beta=1/(k_B T)$ with k_B being Boltzmann’s constant. A tremendous amount of computational time can be saved if – somehow – we could limit our sampling only to the “important” points of our sampling space. This is accomplished by the Metropolis scheme of a Monte Carlo stochastic algorithm, which makes use of the Boltzmann factor for the calculation of macroscopic properties as average values over many microstates sampled from the configuration space.

The general scheme according to which every Monte Carlo algorithm proceeds is the following. At first, an initial state is being defined and denoted with the letter “ o ” for “old.” Subsequently, a new trial configuration – denoted by letter “ n ” for “new” – is generated by adding a small random displacement to the old configuration “ o ”. Now, we must decide whether the new trial configuration will be accepted or rejected according to an acceptance criterion. The way the acceptance criterion is formed is the following. We start off from the detailed balance condition (or microscopic reversibility condition) depicted in equation (2.64):

$$N(o) \cdot \pi(o \rightarrow n) = N(n) \cdot \pi(n \rightarrow o) \quad (2.64)$$

The above equation reads as follows: The probability of being in the old configuration $N(o)$ times the transition probability for going from the old configuration to the new one $\pi(o \rightarrow n)$ should be equal to the product of the probability of being in the new configuration $N(n)$ times the transition probability of the reverse move, i.e. going from the new configuration to the old one $\pi(n \rightarrow o)$. Many possible forms of the transition probability $\pi(o \rightarrow n)$ satisfy equation (2.64). Let us look how $\pi(o \rightarrow n)$ is constructed in practice. A Monte Carlo move consists of two stages. First, we perform a trial move from state o to state n . Let $\alpha(o \rightarrow n)$ be the probability of attempting this transition. The next stage is the decision to either accept or reject the attempted trial move. The probability of accepting the trial move from o to n is

denoted as $acc(o \rightarrow n)$. Hence, the total probability of the attempted move $\pi(o \rightarrow n)$ can be expressed as:

$$\pi(o \rightarrow n) = \alpha(o \rightarrow n) \cdot acc(o \rightarrow n) \quad (2.65)$$

In an analogous way, the total probability $\pi(n \rightarrow o)$ for the reverse move is:

$$\pi(n \rightarrow o) = \alpha(n \rightarrow o) \cdot acc(n \rightarrow o) \quad (2.66)$$

Therefore, Eq. (2.64) can be rewritten with the help of Eqs. (2.65-2.66) in the following form:

$$N(o) \cdot \alpha(o \rightarrow n) \cdot acc(o \rightarrow n) = N(n) \cdot \alpha(n \rightarrow o) \cdot acc(n \rightarrow o) \quad (2.67)$$

Many choices for $acc(o \rightarrow n)$ satisfy the condition depicted in Eq. (2.67) (and also the obvious condition that the probability $acc(o \rightarrow n)$ cannot exceed 1). The final acceptance criterion whether the attempted trial move ($o \rightarrow n$) will be accepted or not is formed depending on the MC scheme to be followed. In the conventional Metropolis scheme of a MC algorithm, the acceptance criterion is as follows:

$$acc(o \rightarrow n) = \begin{cases} \frac{N(n)}{N(o)} \cdot \frac{\alpha(n \rightarrow o)}{\alpha(o \rightarrow n)} & \text{if } \frac{N(n)}{N(o)} \frac{\alpha(n \rightarrow o)}{\alpha(o \rightarrow n)} < 1 \\ 1 & \text{if } \frac{N(n)}{N(o)} \frac{\alpha(n \rightarrow o)}{\alpha(o \rightarrow n)} \geq 1 \end{cases} \quad (2.68)$$

Equation (2.68) describes the acceptance criterion for a slight variation of the conventional Metropolis scheme, called the smart Monte Carlo algorithm. In conventional Metropolis Monte Carlo the two α 's are equal. The acceptance criterion of the smart MC scheme shown in Eq. (2.68) is in some textbooks stated as follows:

$$acc(o \rightarrow n) = \min \left[1, \frac{N(n)}{N(o)} \cdot \frac{\alpha(n \rightarrow o)}{\alpha(o \rightarrow n)} \right] \quad (2.69)$$

Eq. (2.69) can be further simplified using Boltzmann factors. In the canonical ensemble, the probability of being at a state o , $N(o)$ is equal to the probability density at o times an elementary volume in configuration space:

$$N(o) = \frac{\exp[-\beta \cdot \mathcal{V}(o)]}{Z} d^f r^{(o)} \quad (2.70)$$

with f (usually equal to 3 times the number of atoms) symbolizing the number of configurational degrees of freedom and Z being the configurational integral, which ensures that the probability density in configuration space is normalized:

$$Z \equiv \int \exp[-\beta \cdot \mathcal{V}(\mathbf{r})] \cdot d^f r \quad (2.71)$$

By observing the Boltzmann factor used in Eq. (2.70) and by comparing it with the general definition provided above, some basic conclusions can be drawn. At first, the property which defines a state as “important” or “non-important” in the context of the Metropolis scheme is the potential energy \mathcal{V} of the system. The physical meaning of Eq. (2.70) is the following. The numerator (Boltzmann factor) expresses the number of microstates with configuration between $\mathbf{r}^{(o)}$ and $\mathbf{r}^{(o)} + d\mathbf{r}^{(o)}$, whereas the denominator [Eq. (2.71)] represents the total number of microstates of the system. By applying Eq. (2.70) to the general form of the acceptance criterion of Eq. (2.69), the smart MC acceptance criterion for the trial move $o \rightarrow n$ can be extracted:

$$acc(o \rightarrow n) = \min \left[1, \exp \left\{ -\beta [\mathcal{V}(n) - \mathcal{V}(o)] \right\} \cdot \frac{\alpha(n \rightarrow o) d^f r^{(n)}}{\alpha(o \rightarrow n) d^f r^{(o)}} \right] \quad (2.72)$$

The ratio of volumes $d^f r^{(n)} / d^f r^{(o)}$ amounts to a Jacobian of the transformation of coordinates involved in going from the old to the new configuration in attempting a move. It equals 1 in most useful MC schemes. The way to proceed for implementing Eq. (2.72) is the following. The change in potential energy $\mathcal{V}(n) - \mathcal{V}(o)$ in going from the initial “ o ” to the new “ n ” state is calculated. The Boltzmann factor of this change in energy is evaluated, the attempt probabilities for the forward $\alpha(o \rightarrow n)$ and reverse move $\alpha(n \rightarrow o)$ are assessed, and the Jacobian $d^f r^{(n)} / d^f r^{(o)}$ is computed, if different from unity. Thus, the acceptance value $acc(o \rightarrow n)$ is evaluated according to

Eq. (2.72). In order to decide whether to accept or reject the trial move, a random real number is generated in the interval $[0,1]$ from a uniform distribution where all numbers are equally probable. If the generated number is smaller than the calculated value of $acc(o \rightarrow n)$ the attempted move is accepted, otherwise it is rejected.

During process described above, a very important assumption is tacitly made, namely that every point in the configuration space to be sampled can be reached from any other point in a finite number of Monte Carlo trial steps. This implies that the algorithm is ergodic. This is not always the case for arbitrary MC schemes and extra caution should be taken in this direction⁴⁵. One basic difference between MD and MC simulations (besides the conceptual difference that the first are deterministic and the second ones are stochastic) is that time is not involved in MC runs. More precisely, there is no trajectory in the context of an MC run, i.e. there is no sequence of points, each of which represents a different time t . On the contrary, in MC simulations one finds stochastically dispersed points in configuration space resembling shots from a shot gun.

In this thesis, three basic Monte Carlo schemes are used. The first one is the smart MC scheme described above. The second one is the *Wang-Landau* scheme, which will be thoroughly analyzed in Chapter 4. In addition to that, an elaborate algorithm, part of which involves a *kinetic Monte Carlo* scheme is used to track the temporal evolution of a system by simultaneously generating a large number of stochastic trajectories towards many directions of the configurational space⁵². In contrast to Monte Carlo sampling, kinetic Monte Carlo does admit a straightforward dynamic interpretation. Due to the great importance of this algorithm, a special section in Chapter 6 is dedicated to describing it in detail.

Chapter 3

Structural rearrangement in transitions between basins and metabasins

The molecular simulation techniques described in the last section of the previous chapter, although conceptually correct, suffer from serious drawbacks. In particular, MD techniques are intrinsically constrained to simulating systems up to relatively short timescales in comparison to the corresponding relaxation times needed to achieve equilibration. Especially, when materials with large heterogeneity in relaxation times (such as glassy systems) are examined, the spectrum of characteristic times for molecular motion may cover more than 20 orders of magnitude. The breadth of timescales observed in polymeric materials can become clearer with the help of Figure 3.1:

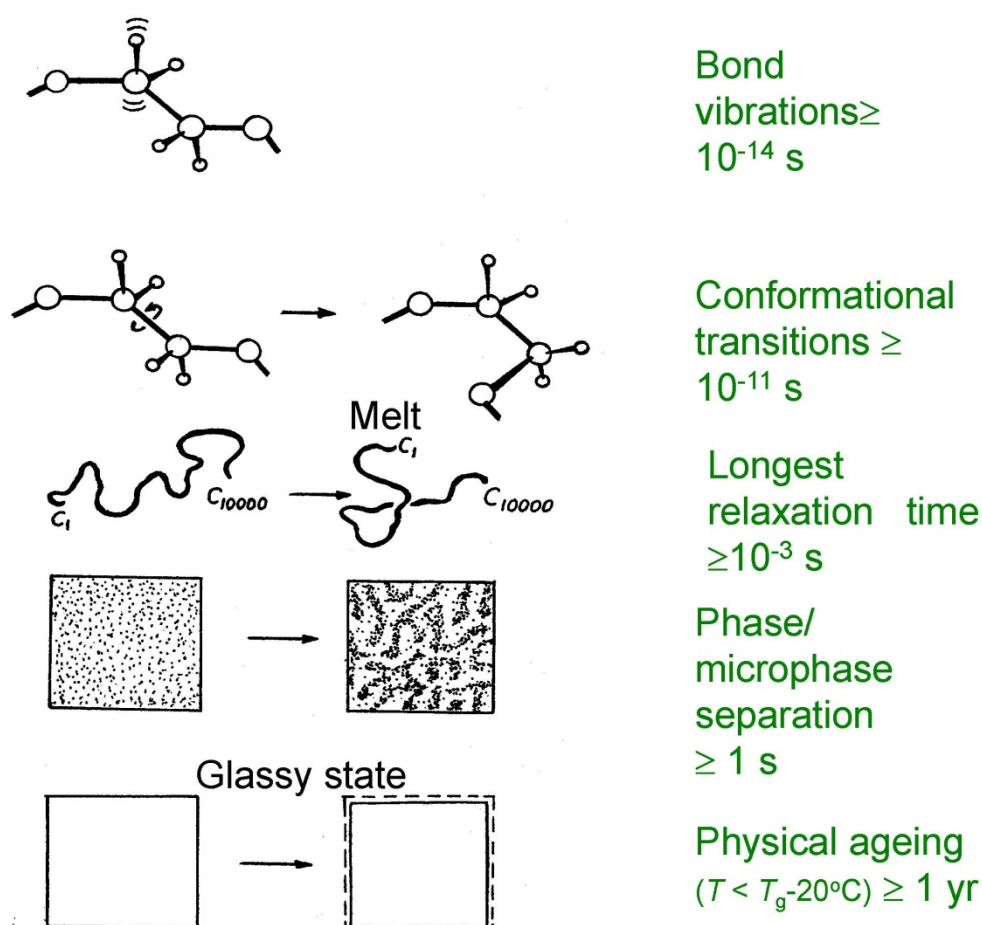


Figure 3.1: Schematic representation of the large width of relaxation times observed in a typical glass forming material⁵³.

Molecular mechanisms related to physical ageing have been widely studied over the past years through the use of several relaxation measurements (structural, volumetric, enthalpy, mechanical and dielectric⁵⁴) which have provided results concerning the α -relaxation of glasses. It has been found that the relaxation times for an α -relaxation process is of the order of ~ 100 s in the vicinity of T_g , whereas only 20° C below T_g this characteristic time becomes of the order of years ($\sim 10^7$ s). It is, therefore, evident that it is extremely difficult to run a single MD simulation and cover the entire spectrum of relaxation times, when state of the art MD-methods conducted in high performance computing centers have barely reached relaxation times up to several

microseconds ($\sim 10^{-6}$ s). It should be noted, however, that millisecond-long MD simulations on specialized hardware have been reported recently ⁵⁵. This is, nevertheless, still too short by many orders of magnitude in comparison to the experimental time scales of most relaxation phenomena of interest.

Beyond the multiple time step MD strategy previously described, another helpful approach to get around this problem is the design of highly parallelized MD algorithms ⁵⁶ or even the use of temperature-accelerated dynamics simulations, as originally proposed by Voter and collaborators ⁵⁷. Even in these cases, however, the desired long-time relaxation processes are still unreachable in the context of simulation experiments. In the following section an additional, commonly used, alternative approach to deal with this kind of problems is being described.

3.1 Introduction

In order to overcome or to moderate the problem of long times outlined above, an alternative simulation approach is followed. This approach is based on coarse-graining of the (multidimensional) configuration space. More precisely, according to this approach a simple MD-trajectory evolving in configuration space can be relatively easily mapped onto a sequence of local minima of the potential energy landscape (PEL). This mapping proceeds through potential energy minimizations starting from each configuration-space point visited by the trajectory. The potential energy of the system at any point of configuration space is calculated via Eq. (2.34) or Eq. (2.50) and subsequently subjected to minimization with the help of one of the techniques described in Section 2.4.1. This minimization process will lead – up to a certain accuracy – to a point of configuration space that constitutes a local minimum of the potential energy.

Stillinger and Weber ⁵⁸ named the local minima sampled with the above mentioned procedure inherent structures (ISs); these are stable stationary points of the potential energy with respect to all degrees of freedom, around which the system is expected to spend most of its time trapped, at least at low temperatures in the vicinity of and below the glass transition temperature T_g . A potential energy minimum or IS constitutes the lowest lying point of a potential energy basin on the PEL.

A basin, which we shall also call “state”, constitutes a region of the configuration space that contains a single local minimum of the potential energy with respect to the system’s generalized coordinates. The term “basin” will be used throughout this work to denote the set of configuration space points from which a steepest descent construction in the potential energy leads to a given local minimum. A clarification is in order at this point. A basin contains a single local energy minimum, but is not an energy minimum itself. It includes a set of configurations, all of which lead to the same local minimum (IS) upon steepest descent minimization of the energy. For a system with two configurational degrees of freedom, the energy as a function of configuration space within a basin, when plotted in 3D, resembles a funnel, the bottom of which is located at the inherent structure. Adjacent basins are separated from one another by dividing multi-dimensional surfaces, i.e., hypersurfaces of dimensionality by one less than that of the configuration space, which pass through first-order saddle points and are everywhere tangent to the gradient vector of the potential energy. In this way, the entire configuration space can be tessellated into basins as shown in Figure 3.2.

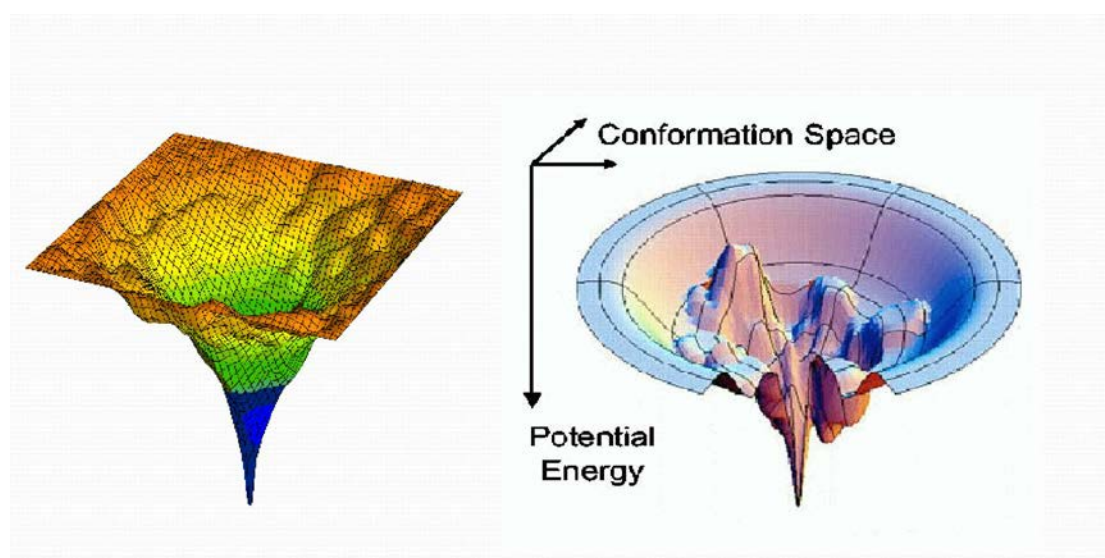


Figure 3.2: Left: 3D representation of a single basin of the potential energy. The inherent structure, depicted with blue color, is the configuration corresponding to the bottom of the funnel-shaped basin. Right: A series of neighboring potential energy basins separated by dividing lines going through first-order saddle points, providing a coarse-grained representation of the configuration space.

In the left-hand side plot of Figure 3.2 the PEL of a single basin is plotted for a system with two configurational degrees of freedom. As we can see, depending on the level of accuracy, other smaller basins can be detected on the surface of the major basin. The resulting coarse-graining of the configuration space can be better understood with the help of Figure 3.3:

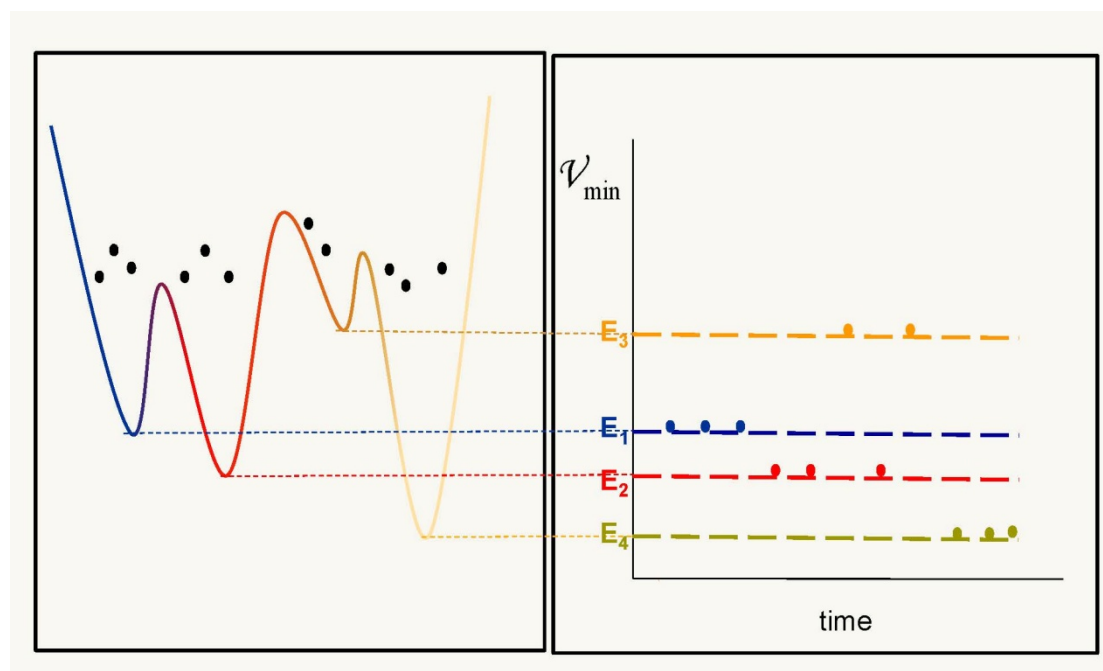


Figure 3.3: Schematic representation of the coarse-graining procedure of a single MD-trajectory evolving in configuration space to potential energy space. For simplicity, a system with one degree of freedom is considered. Left hand side figure: The trajectory, shown as a succession of points, evolving in time generally (but not strictly) from left to right. The curve is the PEL, parts corresponding to different basins being shown in different colors. Simplified 2D mapping of a MD-trajectory evolving through time to the PEL. Right hand side figure: Depiction of the energy levels for every one of the four inherent structures of the PEL on the left. Each point of the trajectory on the left is mapped onto an IS through potential energy minimization. This leads to a reduced trajectory, consisting of the sequence of ISs (and corresponding basins) visited by the trajectory as a function of time.

In the example described in the left drawing of Figure 3.3, eleven points of a MD-trajectory evolving in configuration space are shown. Minimization of the potential

energy \mathcal{V} starting from each one of these points leads to a certain inherent structure in the PEL. Four inherent structures are shown in Figure 3.3. In this way, the eleven points of the initial MD-trajectory are being projected to four energy classes represented by the four inherent structures obtained after minimization of the system's potential energy. As can be seen from Figure 3.3, more than one trajectory points may lead to the same inherent structure. These points are expected to belong to the same basin of the PEL which is characterized by a certain inherent structure. In the simplified 2D representation of Figure 3.3, the inherent structures are separated from one another not by first-order saddle points but by maxima of the potential energy function.

The dynamics of many physical, chemical, materials and biological systems is slow because it proceeds as a succession of infrequent transitions between basins (or states). Representing each state in a coarse-grained sense by a point in configuration space and connecting all pairs of states between which a transition is possible, one obtains a graph, or network of connected states. Many phenomena related to dynamics can be modeled as occurring through a succession of transitions in a network of states⁵⁹. A more efficient strategy than “brute-force” MD is to construct a network of communicating states i and compute the rate constants $k_{i \rightarrow j}$ between them from atomic-level information. Throughout this work the symbol $k_{i \rightarrow j}$ represents the rate constant for the transition between states i and j , starting from state i and ending up in state j . By definition, the rate constant $k_{i \rightarrow j}$ is a conditional probability per unit time that a transition to state j will occur, provided the system is initially in state i . Once states and interstate rate constants are known, the system evolution at the state level can be tracked by solving the so-called master equation:

$$\frac{\partial P_i(t)}{\partial t} = \sum_{j \neq i} P_j(t) \cdot k_{j \rightarrow i} - P_i(t) \cdot \sum_{j \neq i} k_{i \rightarrow j} \quad (3.1)$$

or equivalently written in vector form:

$$\frac{\partial \mathbf{P}(t)}{\partial t} = \mathbf{K} \cdot \mathbf{P}(t) \quad (3.2)$$

Equation (3.2) indicates that the probability of being in state i at time t , $P_i(t)$, is only an element of the probability column vector $\mathbf{P}(t)$ at time t . Analogously, the rate constant $k_{i \rightarrow j}$ is related to an element of the rate constant matrix \mathbf{K} . In particular, in this work the matrix element k_{ij} is the element located in the i th-row and the j th-column of the rate constant matrix \mathbf{K} . By comparing Eqs. (3.1) and (3.2), one readily obtains $k_{ij} = k_{j \rightarrow i}$ for $j \neq i$, $k_{ii} = -\sum_{j \neq i} k_{i \rightarrow j}$

3.2 Rare event theory

The transition rate constants k_{ij} included as elements in the transition rate matrix \mathbf{K} are independent of time, thanks to the time scale separation which makes the transition an infrequent event⁶⁰. Especially when the temperature is low and the energy barriers between two adjacent basins become high we consider that the system spends a sufficient amount of time sampling configurations within one and the same basin before escaping from it through a transitions to a neighboring basin. In that sense, we assume that a kind of restricted local equilibration has been established among configurations of one basin. These configurations communicate with one another via relatively fast transitions compared to the time needed to escape from the basin to an adjacent one.

Once this restricted equilibrium has been set, it is expected that the basin has been thoroughly explored and every configuration belonging to it has been sampled. When sufficient time has elapsed, so that local equilibration within a given basin is established, i.e., an exhaustive sampling of configurations in the basin has occurred, a transition to a neighboring basin may occur. In this sense, transitions between basins are considered to be infrequent – or rare – events. In other words, it is expected that in glassy systems at temperatures in the vicinity of or below T_g the time needed for fully exploring a basin – with the help of fast intra-basin motions – is short in relation to the time needed for escaping from this given basin, making this escape transition to a neighboring basin a rare event.

Once states have been defined, the transition rate constants $k_{i \rightarrow j}$ can be computed by a variety of methods. Infrequent event analyses based on dynamically corrected transition-state theory have found widespread use in the computation of rate constants from simulations. These analyses are based on the theory of Bennett⁶¹ and Chandler⁶⁰, which was extended to multistate systems by Voter and Doll^{59e}. As discussed by Chandler and Voter and Doll, thanks to the time scale separation making exit from state i an infrequent event, $k_{i \rightarrow j}$ will practically reach a time-independent plateau value at times sufficiently longer than the time required for internal equilibration within state i .

Rate constants for transitions between states have been calculated within this work with the help of transition state theory (TST). Transition state theory rests on an approximation: It assumes that, whenever the system finds itself on the boundary surface of state i with momentum directed towards the outside of state i , then a successful transition out of state i will occur. In reality, this is not necessarily the case because of fast recrossings events of the boundary surface at short times. Mathematically, $k_{i \rightarrow j}^{\text{TST}}$ can be calculated with the help of the partition function Q_i of the system confined in the origin state i and the partition function Q_{ij}^\ddagger of the system confined in the boundary surface of i that is common with the boundary surface of a neighboring state j :

$$k_{i \rightarrow j}^{\text{TST}} = \frac{k_{\text{B}}T}{h} \cdot \frac{Q_{ij}^\ddagger}{Q_i} \quad (3.3)$$

where the factor $k_{\text{B}}T/h$, with h being Planck's constant, takes care of the different dimensionalities of the phase spaces to which the two partition functions refer. Eq. (3.3) is applicable beyond the classical analysis adopted here, in systems where quantum mechanical effects are important. For a system under constant pressure, where volume fluctuations are important in effecting transitions out of state i , Q_i and Q_{ij}^\ddagger can be interpreted as isothermal-isobaric partition functions. Recalling the connection between Gibbs energy and isothermal-isobaric partition function, Eq. (3.3) can be recast in the form:

$$k_{i \rightarrow j}^{TST} = \frac{k_B T}{h} \cdot \exp \left[- \left(\frac{G_{ij}^\ddagger - G_i}{k_B T} \right) \right] \quad (3.4)$$

where G_i symbolizes the Gibbs energy at the origin basin i and G_{ij}^\ddagger represents the Gibbs energy of the system confined to the separating surface between communicating basins i and j . Eq. (3.4) will be extensively used in this work to calculate rate constants for transitions between communicating basins. As we will see in Chapter 7, depending on the studied phenomenon, Eq. (3.4) can be further simplified after substituting the Gibbs energy of the system with an appropriate mathematical expression characterizing the studied phenomenon. The TST approximation is more appropriate in the case of low temperatures, where the energy barriers between states are high in relation to $k_B T$ and rate constants are correspondingly low.

The transitions between states cannot be sampled adequately by straightforward MD, as these are infrequent events. One way to get around this problem is to resort to temperature-accelerated dynamics simulations, as originally proposed by Voter and collaborators⁵⁷ and effectively combine them with conventional “brute-force” MD simulations⁶² to obtain rate constants for transitions in the course of structural relaxation of a glassy material.

If transitions between basins are, nevertheless, subject to relatively low energy barriers (say, up to $7 k_B T$), such that rate constants $k_{i \rightarrow j}$ are relatively high (say, up to ns^{-1}), then rate constants can be estimated by MD simulation. All one needs is a technique to map every configuration recorded in the course of a MD trajectory onto a state. Very often, when states are defined as regions around local minima in configuration space, this mapping is accomplished by direct energy minimization leading eventually to the closest energy minimum or “inherent structure”. A reduced trajectory of states visited is thus accumulated in parallel with the MD trajectory. Rate constants can be computed by statistical analysis of the reduced trajectory. A simple and efficient method that can be used for this cause is “hazard plot analysis”⁶³. Both of the above mentioned methods for rate constant calculation rely on the validity of the assumption that the infrequent event transitions between states constitute a Poisson process⁶⁴.

3.2.1 Poisson process

As mentioned before, the transition rate constants k_{ij} appearing in the transition rate matrix \mathbf{K} are independent of time, thanks to the time scale separation. This is because, once the system enters state i which is in a region surrounded by high energy barriers, it will quickly thermalize, i.e., distribute itself according to the requirements of a restricted equilibrium within state i and “forget” how it came there in the first place. One of the main characteristics of a Poisson process, named after the French mathematician Siméon-Denis Poisson, is that such a process has no memory. In other words, the fact that there is an occurrence at a particular time says nothing about the probability of an occurrence at, or around, a later or earlier time. Equivalently, there seems to be some kind of independence with respect to various occurrences. In that sense, the next occurrence of a stochastic process cannot be predicted from current and past information. The fact that something happened in the past has no effect on the probabilities for future occurrences. The justification of this assumption in the description of transitions between basins comes from the fact that the time spent within a given basin suffices for establishing restricted local equilibration (exhaustive sampling of the basin) and, due to this sufficiently long residence time, the system “forgets” its past.

The above statement imparts a Markovian character to the process of infrequent transitions between basins. In particular, in probability theory and statistics a Markov process, named after the Russian mathematician Andrey Markov, is a stochastic process satisfying a certain property, called the Markov property. According to this property, a stochastic system that undergoes transitions from one state to another, between a finite or countable number of possible states, is characterized as memoryless, if the next state depends only on the current state and not on the sequence of events that preceded it. This specific kind of “memorylessness” is called the Markov property. In this way, the succession of Markovian transitions forms a sequence of independent states which is called a Markov chain. Markov chains can be of different order. A Markov chain of order m is a discrete-time chain of states in which each state depends on the past m states. Therefore, the Poisson process is the continuous-time counterpart of a Markov chain of first order, in which the choice of

the following state depends only on the current state at which the system currently resides.

By virtue of the Poisson process nature of interbasin jumps, hazard plot analysis can be used to calculate transition rates between slowly communicating basins. For a more thorough description of ways to calculate rate constants the reader is referred to reference ⁶⁵.

3.2.2 Monomolecular reaction system

We will now diverge somewhat to examine a simple model for a network of chemical reactions, a problem extensively analyzed by chemical engineers because of its industrial importance ⁶⁶. We will show that this problem bears a striking similarity to the temporal evolution of glassy system on its energy landscape, discussed above, enabling us to capitalize on methodologies developed for chemical reactions to address the structural relaxation of glasses.

Among all the conceivable chemical reaction systems, we particularly consider the monomolecular reaction system. The monomolecular reaction system constitutes a complex first-order kinetic system such as the one presented in Equation (3.5) for a system consisting of n states:

$$\frac{\partial \mathbf{A}(t)}{\partial t} = \mathbf{K} \cdot \mathbf{A}(t) \quad (3.5)$$

The rationale behind Equation (3.5) is that the temporal dependence of composition vector \mathbf{A} is being modeled through a first order differential equation, which determines the influx and efflux of property \mathbf{A} to a certain state i over time. In other words, Eq. (3.5) constitutes a balance equation of property \mathbf{A} for every one of the n states of the system. Through transitions from one state to another, defined by the rate constant matrix \mathbf{K} , the concentration of a chemical species i changes with time, $A_i(t)$. Within the monomolecular reaction assumption adopted here, we assume that the kinetics of all time-dependent properties of the system can be well reproduced by an equation such as the one shown in Eq. (3.5).

Our choice to use a relatively simple equation, such as Eq. (3.5), to monitor how properties change over time because of transitions from one state to another is by all means rational. All one has to do in order to justify this choice is to compare Eq. (3.5) with Eq. (3.2). We remind that Eq. (3.2) is the master equation describing how the distribution of occupancy probabilities changes over time for every state of the system. The resemblance between Eq. (3.2) and the monomolecular reaction balance equation (Eq. (3.5)) is obvious. Hence, we choose to investigate monomolecular reaction systems because by definition their kinetics can be well modeled through a relative simple equation showing great resemblance to the master equation.

By virtue of Eq. (3.5), the rate constant matrix \mathbf{K} has the following characteristics ^{66b}:

1. Nonnegative rate constants as elements:

$$k_{ij} \geq 0, \quad i \neq j \quad (3.6)$$

2. Diagonal elements should complete the balance:

$$k_{ii} = -\sum_{j \neq i} k_{i \rightarrow j} = -\sum_{j \neq i} k_{ji} \quad (3.7)$$

and

3. there exists an equilibrium composition vector \mathbf{A}^{eq} , such that:

$$\mathbf{K} \cdot \mathbf{A}^{\text{eq}} = 0 \quad (3.8)$$

where the elements of the equilibrium column vector \mathbf{A}^{eq} are positive $A_i^{\text{eq}} > 0$ for $i = 1, 2, \dots, n$.

The third condition states that, by virtue of Eq. (3.5), there comes a time when property \mathbf{A} has reached a steady state value, after which it doesn't change over time any more. For times larger than this, property \mathbf{A} preserves its equilibrium value \mathbf{A}^{eq} for as long as the system remains unperturbed. For a more thorough description of the monomolecular reaction systems and their significance the reader is referred to references ^{66b, 67}.

3.3 Topological structure of the potential energy hypersurface: Basins and metabasins

As described in paragraph 3.1, the idea of projecting configuration space onto a set of basins by use of the potential energy landscape, and consequently reducing MD-trajectories evolving in that space into sequences of visited basins, switches between basins occurring as infrequent transitions, has proven to be an extremely useful tool in tracking the dynamics of glasses^{6, 68}. Both the problem of the time scale separation characterizing transition rates between neighboring basins of the PEL of glassy materials below T_g , and the related broad spectrum of relaxation times have been addressed in the previous sections of this work. In particular, the broad distribution of characteristic times is intimately related to the broad distribution of barrier heights seen in the earliest analyses of potential energy landscapes for glassy systems⁶⁹.

The idea of mapping the PEL to a set of basins has been applied in the past to a large variety of systems including water^{58b}, gas clusters⁷⁰, proteins⁷¹ and glass forming materials^{6, 68}. All the above applications constitute clear evidence that a better understanding of the PEL's structure can lead to useful physical conclusions, providing insight into complex mechanisms. The depth, number and overall geometry of the basins surrounding the potential energy minima play a dominant role when attempting to describe a PEL in detail⁷². Following the pioneering work of Heuer⁷³, Bouchaud⁷⁴ and Kob⁷⁵, we will refer to a collection of relatively fast communicating basins as a "metabasin" (MB). In the literature, several definitions have been proposed for the identification of a MB. Heuer⁷⁶ proposed an algorithm based on the IS trajectory, which can be summarized in the following two steps: a) determine the time regions between the first and the last occurrence for each IS; and b) group into a MB all basins for which there is an overlap in the corresponding time regions beyond a predefined time scale set to discard recrossings phenomena. Within this approach, the whole trajectory can be regarded, a posteriori, as a succession of different MBs.

An alternative definition, independent from a specific trajectory, has been proposed by Mauro and Loucks⁷⁷. Starting from rates between inherent structures, subsets are identified based on whether equilibration can be achieved within a prefixed time. As compared to the previous definitions, this allows one in some limit to perform a

partitioning of the configuration space into MBs, where the relaxation times within a MB are short compared to that of an observation (simulation) time scale. However, in practice, many details of the potential energy landscape have to be discarded in order to apply this approach.

An efficient way to identify metabasins is based on an “on the fly” method in the course of a MD simulation, as described in the work of Tsalikis et al.⁵⁶. In that work, based on the rate of identifying new, not already visited, basins, MBs are defined in the course of a canonical MD run. By definition, a set of basins constitutes a metabasin if the time required for the system to escape from this particular set of basins is significantly longer than the time needed for the system to establish a restricted equilibrium among the basins in the set. In a plot of the number of distinct basins visited versus time in the course of a MD simulation, this reflects itself as a plateau, as shown in Figure 3.4:

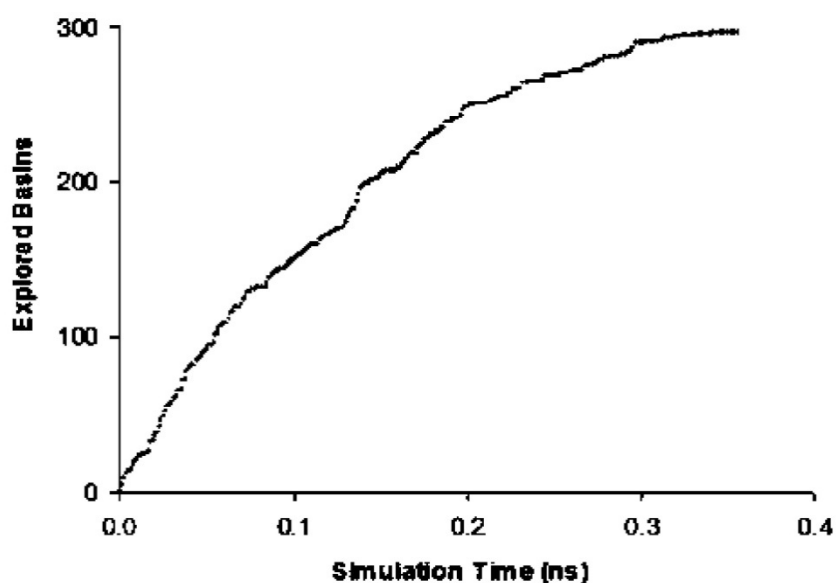


Figure 3.4: Number of explored minima as a function of simulation time for a binary Lennard-Jones glass⁷. When a plateau is observed for a prefixed time interval, the system configuration circulates within a confined collection of basins which are considered to belong to the same MB.⁵⁶

In this way, we accomplish to group into a MB all the minima that are accessible from a starting minimum for a specific time window and to discriminate them from all

other minima, for which sufficient sampling will require more computational effort. By construction, transitions from one MB toward its neighboring MBs will occur over a significantly longer time compared to the inner basin-to-basin transitions and to the simulation time used to define the MB. Therefore, the efficient sampling of transitions between MBs is at least an order of magnitude more demanding than sampling the inner MB. This conclusion makes inter-MB transitions infrequent events, imparting to these processes a Poisson character. More details regarding MBs in glass-forming systems can be found in the review article of Heuer⁷⁸.

Through a methodology⁶² specially designed for improving dynamical sampling of atomistic simulations of glassy materials in the vicinity of T_g , the idea of projecting configuration space onto an equivalent space of MBs can be used to fully reproduce the dynamical behavior of the system, even at temperatures far below T_g ^{6, 68}. In order for this to happen, one assumes that the overall dynamics of the system can be decomposed into slow and fast processes, with the slow processes comprising a Poisson process. This assumption is by no means strange and difficult to be fulfilled, since by definition MBs are constructed based on infrequent transitions between sets of basins of the PEL, which in turn are characterized by Poisson statistics. In particular, approaching T_g from below, the number of “relevant” minima and saddle points increases dramatically. As a consequence, the computational cost for saddle-point calculations becomes prohibitively high. In order to overcome this obstacle, we have investigated the role of ISs in the vitrification process of glass-forming materials using a simple methodology, which is based on a combination of MD and potential energy minimization and on an extension of hazard plot analysis. This approach⁶ showed that the dynamical transitions between basins can be described by a first-order kinetic scheme (monomolecular reaction system). More precisely, it was shown⁶⁸ that it is possible to reconstruct completely the dynamics of the atomistic system at a finite temperature, below T_g , based on the first-order kinetic network of inter-basin transitions. This reconstruction corresponds to a “lifting”⁷⁹ of the coarse-grained Poisson process model of a succession of inter-basin transitions to the detailed atomistic level.

A necessary step for coarse graining the dynamics into the IS picture is the evaluation of rate constants for basin-to-basin transitions. This can be done with a variety of methods^{59e, 80}. In the past we have extensively used two distinct approaches for the rate calculations: (a) a saddle-point search in combination with Fukui's intrinsic reaction coordinate (IRC) construction⁸¹ and a harmonic approximation⁵², and, (b) MD simulations^{6, 68} in combination with hazard plot analysis^{63, 82}. The applicability of each approach depends on its computational demands. For temperatures far below T_g , an approach based on MD would suffer, since the system remains trapped in the vicinity of a handful of basins and does not escape even for times so long as to be inaccessible by classical MD, while a saddle-point search/IRC will show a much weaker dependence on barrier height and, therefore, will be preferable. On the other hand, for temperatures above T_g saddle-point search suffers from the tremendous multitude of basins (several thousands in the course of nanoseconds for the model system sizes considered here) that need to be sampled, while brute force MD is expected to perform more efficiently. For the temperature range that is of primary interest in this chapter, in the vicinity of T_g , both methods suffer. The large number of visited basins makes the saddle-point search method computationally unaffordable, while classical MD must be pushed to its limits.

Within the context of this work an efficient sampling method for this temperature range is developed by achieving maximum parallelization⁵⁶. With the help of this self-consistent methodology (results of which will be demonstrated in Section 3.4) optimal use of MD over a wide range of temperatures is achieved. Here, by the term "optimal use", we refer to the ability of the method to automatically tune the length of MD trajectories used in order to sample inter- and intra-metabasin transitions in an uncoupled fashion. For short times and low temperatures, the transitions between individual basins are rare events, while at higher temperatures, close to T_g , traditional MD can sample several basin-to-basin transitions, but the rare event is now the transition between collections of basins. Results obtained via this methodology will be presented and thoroughly interpreted in the following section of this chapter.

3.4 Results and discussion

All the above indicate that the usage of MBs in tracking the dynamical evolution of a system through transitions is of great importance and has proven to be a very useful tool. Beyond the utility of the notion of MBs in tracking the temporal evolution of a system with the help of transitions, structural rearrangement mechanisms related with inter- and intra-metabasin transitions have been revealed and explained. Recently ⁸³, the existence of MBs has been correlated with specific changes in the configuration space governed by the potential energy landscape of atomic glass-forming systems, more precisely with the extent of cage-breaking (i.e., the molecular mechanism where the first neighbors of individual atoms are changing).

All the results presented in this section concern a two-component Lennard-Jones (LJ) mixture, whose total number of atoms is 641. The selection of the specific system is based on the existence of extensive prior research results on it. One of its main advantages is the suppression of the tendency for crystallization present in pure LJ systems. The binary system, initially proposed by Kob et al. ⁷, consists of two different types of atoms, A and B. The mixture has a concentration of 80% in A atoms and 20% in B atoms, that is 513 A's and 128 B's. The parameters of the model have been selected ⁷ in such a way that, although the two species have different sizes and interaction strengths, demixing is suppressed in order to suppress nucleation. Although A atoms are larger than B atoms, they are assumed to be of equal mass $m_A = m_B = 6.634 \times 10^{-26}$ kg. The LJ interaction parameters for this system are $\epsilon_{AA} = 1.65678 \times 10^{-21}$ J, $\sigma_{AA} = 3.4 \times 10^{-10}$ m, $\epsilon_{BB} = 0.82839 \times 10^{-21}$ J, $\sigma_{BB} = 2.992 \times 10^{-10}$ m, $\epsilon_{AB} = 2.48517 \times 10^{-21}$ J and $\sigma_{AB} = 2.72 \times 10^{-10}$ m. The unit for reducing time is selected ⁷ as $\left[m_A \sigma_{AA}^2 / (48 \epsilon_{AA}) \right]^{1/2} = 3.10 \times 10^{-13}$ s, and the unit for temperature is $\epsilon_{AA} / k_B = 120$ K. If the above LJ interaction parameters are reduced ³⁸ by the values of the A – A interaction parameters, they read $\epsilon_{AA} = 1.0$, $\sigma_{AA} = 1.0$, $\epsilon_{BB} = 0.5$, $\sigma_{BB} = 0.88$, $\epsilon_{AB} = 1.5$ and $\sigma_{AB} = 0.8$.

For this system in the supercooled state, Kob ⁸⁴ and Shell et al. ⁸ have performed extensive studies, on the basis of which the mode-coupling critical temperature T_c is reported as 0.435 in reduced units (~ 52.2 K) ⁸⁴. For the same system, the glass

transition temperature has been predicted ⁸ to be $T_g = 0.32$, that is ~ 38.4 K. In all calculations reported here, the molecular density of the system is $1.1908 \cdot \sigma_{AA}^{-3}$.

Through the development and application of an automated self-consistent method which can operate on the fly within a molecular dynamics simulation ⁵⁶, the identification of collections of basins and their characterization as metabasins is achieved. With the help of this methodology vigorous sampling is accomplished by distributing the computational cost within the parallel procedure, that demands the same computational cost as a conventional MD-run, but the results are obtained on a real-time scale more than two orders of magnitude faster. The proposed approach gives the ability to calculate the presence of a MB on the fly, the “minute” the system is trapped in a part of its configuration space. The identification of a MB is followed by a calculation of the individual rate constants governing transitions between the basins constituting the MB (intra-metabasin transitions) and transitions toward basins that do not belong to the current MB (inter-metabasin transitions).

Using the proposed methodology ⁵⁶, we have gained very useful insights into the molecular motion relevant to relaxation in the vicinity of the glass transition, namely the “cage-breaking” process. More precisely, the change in the number and identity of first neighbors accompanying a transition (whether intra- or inter-metabasin) in the potential energy landscape has been thoroughly examined in the work of Souza and Wales ⁸⁵. In our work, we also see cage-breaking events, as depicted in Figure 3.5, where a “central” atom jumps to a new cage after a single relative fast intra-metabasin transition.

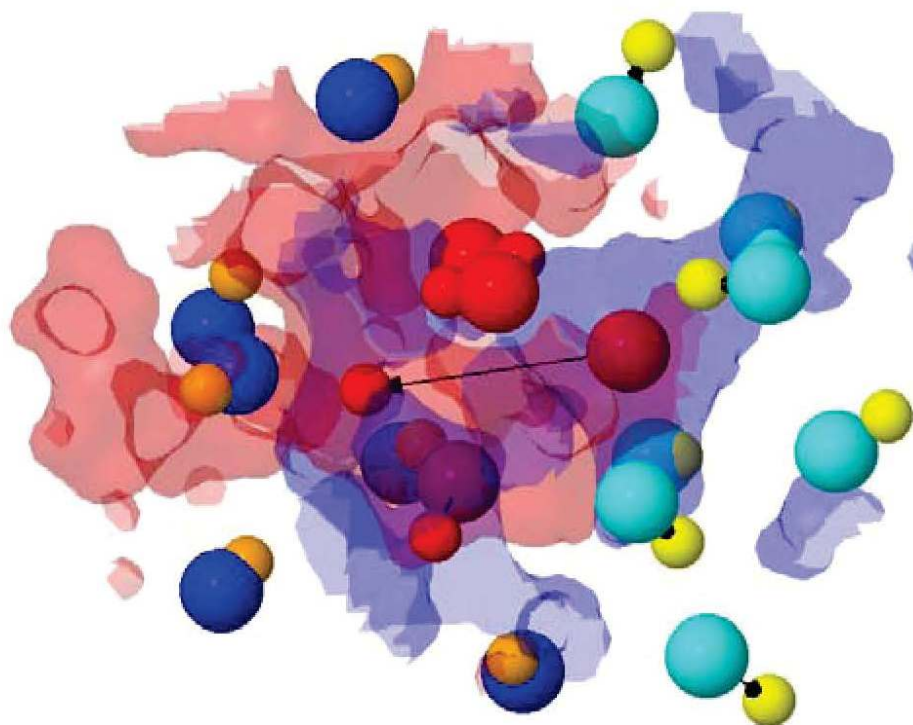


Figure 3.5: Schematic representation of a cage-breaking event in a single elementary jump from one potential energy minimum to a neighboring one belonging to the same MB. The positions of the atoms that participate in the transition are plotted with different sizes (initial: big spheres; final: small spheres), and vectors are drawn to indicate their displacements accompanying the transition. With red color we represent the atoms that remain first neighbors to the central atom experiencing the cage-breaking event, which is also shown in red. Cyan represents atoms that used to be first neighbors of the central atom but cease being so after the transition; their new positions are shown in yellow. Dark blue represents atoms which were not first neighbors of the central atom but come into its first coordination shell after the transition; their new positions are shown in orange. The blue surface depicts the volume accessible to the central molecule initially and the red finally, illustrating the cage change accompanying the transition.

The observation of cage-effects in glassy materials in the vicinity of their glass transition verifies the connection between structural rearrangements, such as structural entrapment, and dynamical relaxation phenomena, such as the time scale separation. In

particular, the separation of time scales characterizing relaxation mechanisms for temperatures below T_g seems to have a rational explanation connected with structural rearrangement due to cage effects, such as the one shown in Figure 3.5. More precisely, it can be concluded that cage effects describe the underlying mechanism responsible for the dynamical entrapment of glassy materials. Every particle is trapped in the cage formed by the neighboring particles that surround it, and a long (relaxation) time is needed for the particle to escape from its cage and relax through diffusive motion. Note that the particles forming the cage are, as expected, trapped themselves in cages as well, and thus, the motion of all particles is slowed down, a phenomenon which is observed by the time scale separation of relaxation times. With decreasing temperature, cage effects become more pronounced, and thus, the motion of all particles is even less, a fact which leads to an increase of the time needed for breaking these cages.

On the other hand, when we investigate MB-to-MB transitions, we do not only see an enhancement of the cage effect, but also observe more complex relaxation mechanisms as shown in Figure 3.6:

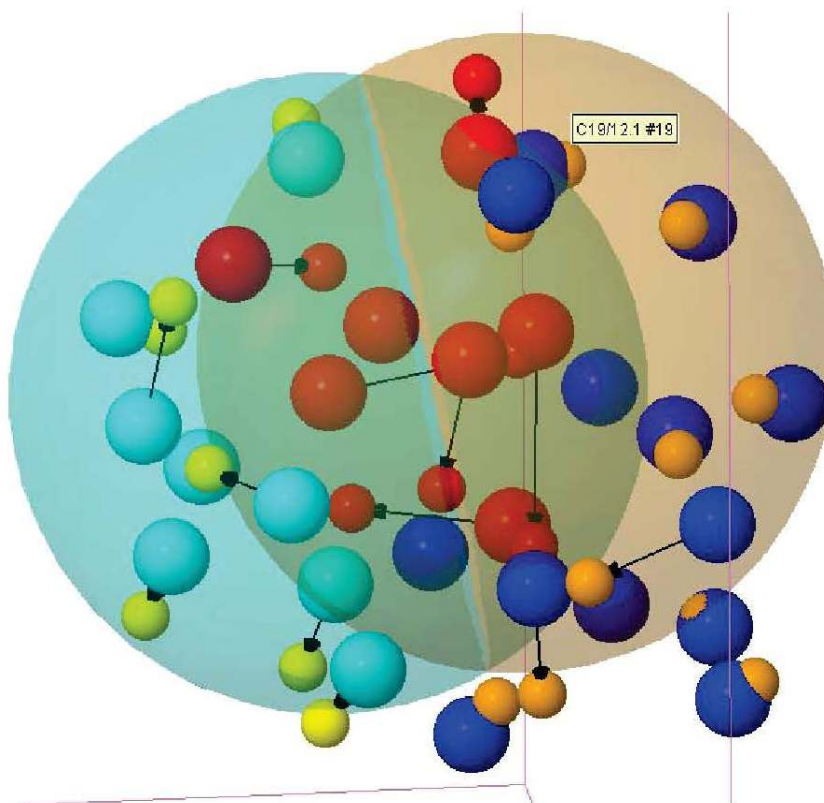


Figure 3.6: Schematic representation of a more complex relaxation event that takes place in a single jump from one potential energy minimum to a neighboring one, belonging to a different MB. Coloring is as Figure 3.5. We have additionally drawn cyan and light-brown spheres representing the first coordination shell, centered at the initial and final positions of the atom with the largest displacement. In this complex elementary move, atoms look like they are moving in a concerted way, exchanging their positions in a dance-like fashion.

According to Figure 3.6, a series of atoms including the “protagonist” of the first coordination shell shown, take part in a more complex structural rearrangement. More precisely, a collection of atoms seem to take each other’s positions moving in a, more or less, stringlike fashion, as if they were “dancing” in accordance with the “stringlike cooperative motion” demonstrated in the work of Donati et al.⁸⁶. According to their work, by analyzing the van Hove correlation function produced via MD simulation for the same model system, Donati et al. showed that there is a fraction of mobile particles that at a characteristic time replace each other, executing a stringlike cooperative motion, very similar to the one represented in Figure 3.6. Our result suggests that such a motion can be actually seen as a transition between structures of the PEL intimately related with the MB-to-MB transitions.

By comparing Figure 3.5 and Figure 3.6 to each other we notice that two different kinds of atom movements are observed. In one hand (Figure 3.5) a simpler move is being noticed, wherein a simple atom “escapes” from a cage, within which it was trapped, formed by its first neighbors. Due to the reduced atomic mobility caused by the low temperature level (far below or in the vicinity of T_g), this motion demands the contemporaneous motion of first neighbors so that a certain cavity of free volume is created letting each central atom eventually escape from an initial cage and consequently be trapped in a new one. Energetically speaking, this kind of motion is related, due to its relative simplicity, to overcoming low energy barriers between neighboring basins. On the contrary, the atomic motion described in Figure 3.6 demands a more cooperative motion. The energetic cost the system has to pay in order for the atoms to acquire the right positions for such a motion, is higher since more atoms are now involved and it is expected to be “energetically” (but also

“entropically”) more difficult for this arrangement to occur. Therefore, this kind of motions are more rare than the cage-break motions, a fact that is related with the infrequency of MB-to-MB transitions in comparison to the more frequent and faster intra-metabasin transitions. As a consequence of that, cooperative motions such as the one described in Figure 3.6 are expected to be related with overcoming relatively higher energy barriers of the PEL.

The notion of basins and metabasins as structural characteristics of the PEL, as well as transitions between those structures will be further used in the context of this work to explain and approach several other mechanisms existing in glassy materials. In the following chapter, a specially designed methodology is presented which on its basis can potentially deal with enormous numbers of basins or states by lumping them in such a way, so that short-time phenomena, accessible through many simulation techniques, are given small attention and long-time relaxation processes, inaccessible for almost all simulation techniques, are being favored. The idea of basins and MBs will be further used in Chapter 5, where an alternative graphical representation of the PEL will be presented.

Chapter 4

Structural and temporal coarse-graining with respect to long-time dynamics: Lumping analysis

In this chapter we present, test and implement a methodology that is able to perform, in an automated manner, “lumping” of a high-dimensional, discrete dynamical system onto a lower-dimensional space. Our aim is to develop an algorithm which, without any assumption about the nature of the system’s slow dynamics, is able to accurately reproduce the long-time dynamics with minimal loss of information. Both the original and the lumped systems conform to master equations [Eqs. (3.1-3.2)], related via the “lumping” analysis introduced by Wei ^{66b}, and have the same limiting equilibrium probability distribution. The proposed method can be used in a variety of processes that can be modeled via a first order kinetic reaction scheme (monomolecular reaction systems). Lumping affords great savings in the computational cost and reveals the characteristic times governing the slow dynamics of the system.

Our goal is to approach the best lumping scheme with respect to three criteria, in order for the lumped system to be able to fully describe the long-time dynamics of the original system. The criteria used are: (a) the lumping error arising from the reduction process; (b) a measure of the magnitude of singular values associated with long-time evolution of the lumped system; and (c) the size of the lumped system. The search for the optimum lumping proceeds via Monte Carlo simulation based on the Wang-Landau scheme ⁸⁷, which enables us to overcome entrapment in local minima in the above criteria and therefore increases the probability of encountering the global optimum. The developed algorithm is implemented to reproduce the long-time dynamics of a

glassy binary Lennard-Jones mixture described in paragraph 3.4 of this work, based on the idea of “inherent structures”, where the rate constants for transitions between inherent structures have been evaluated via hazard plot analysis of a properly designed ensemble of molecular dynamics trajectories.

4.1 Introduction

In this paragraph we propose a lumping strategy designed for the investigation of the dynamic behavior of systems evolving via rare event transitions between discrete states. Examples are chemically reacting systems whose composition evolves according to a reaction network obeying first order kinetics^{66, 88}, or glassy materials, where physical ageing can be described in terms of transitions between basins on their potential energy hypersurface^{6, 68}. Unfortunately, in most applications, problems arise in simulating the long-time dynamics of such systems due to the extremely large number of transitions between states that need to be tracked. This often prohibits the extraction of meaningful conclusions concerning the dynamical behavior of these systems. Likewise, the considered transitions are not of equal importance for dynamical evolution over long time scales, which are usually of most interest. The time scale of observation determines which transitions are the most important ones. In practice, for example, elementary transitions governing the volumetric, mechanical and thermal properties of a glassy material cover a range of rates, spreading over 10 to 20 orders of magnitude on the time scale. Eventually, this results in a full dynamical simulation being practically impossible. To alleviate this problem, one needs to “coarse-grain” the network of transitions by “eliminating” or replacing transitions that do not affect the system dynamics at long times.

The approach presented in this chapter is designed to systematically reduce the dimensionality of model discrete stochastic systems whose evolution is governed by a first order master equation. It can also be applied to continuous systems, once they have been mapped to a discrete network of states. How this mapping can be performed has been shown for atomistic models of glass formers^{62, 89}. The idea behind the mapping is to tessellate the continuous configuration space into discrete states, transitions between the states being rare events. States in glassy systems can be defined

as “basins” in configuration space surrounding “inherent structures”, i.e., local minima of the potential energy with respect to all microscopic degrees of freedom. The system evolves in time via a succession of transitions between basins. Each basin contains one local minimum of the potential energy. The term “metabasin” describes a cluster of connected basins. Every single basin included in a specific metabasin communicates with its surrounding neighboring basins through fast transitions. By definition, the time needed for the system in order to explore basins belonging to the same metabasin is significantly shorter in comparison to the time needed for the system to escape from the considered metabasin. In essence, a set of basins communicating through fast transitions, relative to the residence time in the set, are grouped into the same metabasin.

Finding a mathematical transformation capable of simplifying the computational estimation of the dynamical behavior of systems which evolve in time through a succession of transitions between states obeying a first order kinetic model, into a network of fewer discrete states, without loss of important information, is one of the main accomplishments described in this chapter. The strategy is based on the idea of coarse-graining the original network of states via a grouping, or “lumping” procedure^{66b, 66c}. Two or more original states are lumped together beyond a specific time after which internal equilibration between the states lumped is expected to be established.

According to Wei and Kuo^{66b}, lumping of a dynamical system can be divided into two categories: exact lumping and approximate lumping. The first category fulfils the necessary and sufficient conditions under which the kinetics of the lumped states can be exactly described by a complex first-order reaction scheme, i.e., the lumped system is assumed to constitute a monomolecular reaction system. In approximate lumping the kinetics of the lumped system cannot be exactly described by a first-order reaction scheme; hence, one needs to establish the magnitude of the errors that accompany lumping. Lumping, whether exact or approximate, can be further distinguished into three subclasses: proper, semi-proper, and improper lumping. In proper lumping each original state (chemical species) is by definition assigned to only one lumped state (cluster). In semi-proper and improper lumping, each chemical species is not necessarily assigned to a unique cluster. The difference between semi-proper and improper lumping is that the lumped system resulting from semi-proper lumping follows a monomolecular reaction scheme, whereas that resulting from improper

lumping does not. Further to the work of Wei and Kuo, a general analysis of exact and approximate lumping in chemical kinetics has been presented by Li and Rabitz⁹⁰.

Lumping is a widely used technique in many fields. Characteristic applications may be found, for example, in the oil catalytic cracking industry⁹¹. Lumping can also be implemented to describe reaction networks which obey nonlinear kinetics⁹². For such systems one speaks of constrained and unconstrained lumping⁹³. In constrained lumping some variables of the system are left unlumped, whereas unconstrained, nonlinear lumping gives a reduced system of differential equations cast in terms of new variables, which are nonlinear functions of the original ones. In addition to that, different lumping schemes have been proposed in the past based upon both potential energy and free energy landscape data in order to extract or validate information about the system's structural topology, connectivity and equilibration times⁹⁴. Moreover, coarse-graining of minima has been implemented by using an empirically chosen threshold rate constant to determine how the minima group together both for model polyanilines⁹⁵ and for glassy binary Lennard-Jones systems⁹⁶. Moreover, a different approach to lumping, cast in terms of the invariant response principle, has been proposed by Coxson and Bischoff⁹⁷.

In the context of this work we investigate both exactly and approximately, properly lumpable, systems whose dynamics can be fully described via first-order differential equations. More precisely, part of this work is dedicated to calculating the quality of lumping, in the sense of how close to exact lumpability the implemented lumping is.

The mathematical formalism employed in our work incorporates in essence a transformation from an initial n -tuple space (n describes the number of initial states) to another space of lumped states, or meta-states, of smaller dimensionality $\hat{n} < n$. Besides the introduction of such a mathematical transformation, it is also essential to control the amount of information loss by tracking the system's dynamical behavior, which results from application of this methodology. The proposed methodology can be easily linked to common spectral clustering methods used for dimensionality reduction and depiction of complex, high dimensional landscapes. These methods constitute a class of techniques, which rely on the eigenstructure of a similarity matrix to partition points into clusters. In particular, spectral clustering goes back to Donath and Hoffman⁹⁸, who first suggested to construct graph partitions based on eigenvectors of the

adjacency matrix. Since then, spectral clustering has been widely used and extended⁹⁹. Unlike spectral clustering methods, the proposed algorithm enables lumping of datasets, and therefore the study of long-time dynamics without postulating the diagonalization of the studied system. This fact becomes of greater importance as the system size grows.

All simulations and corresponding calculations concerning glass relaxation were carried out on the two-component Lennard-Jones system described in Section 3.4. In Tsalikis et al.⁵⁶ four different neighboring metabasins have been explored with the help of an automated self-consistent method operating on-the-fly. The applied method offers the ability to calculate the presence of a metabasin as soon as the system is temporarily trapped in a region of its configuration space. The designation of those four metabasins proceeds using as a criterion the rate of exploration of new local minima of the potential energy landscape during the progression of a molecular dynamics (MD) simulation in the canonical (NVT) ensemble. Every one of the metabasins contains a certain number of neighboring basins, which – by definition – communicate with each other via fast transitions in comparison to the time needed to escape from the metabasin to another neighboring metabasin. The identification of the four metabasins was followed by a calculation of the individual rate constants governing transitions between the basins constituting the metabasin and transitions towards basins that are parts of other metabasins, different from the current one.

For further analysis we consider our LJ system – having the aforementioned characteristics - encompassing n explored discrete states. We assume that the dynamical behavior of the system is described through transitions which obey a first order kinetic model described in Eqs. (3.1-3.2) and thus the system is considered as a monomolecular reaction system. With $P_i(t)$ we denote the probability of finding the system in state i with ($1 \leq i \leq n$). Collecting all state probabilities, we form an n -dimensional vector $\mathbf{P}(t)$. Equations (3.1-3.2) are equivalent and are better known as the master equation, since they describe the evolution of the system with given initial distribution among states $\mathbf{P}(0)$. With \mathbf{K} we denote the $n \times n$ rate constant matrix of the full system. This is the matrix which contains as elements the rate constants for every transition that takes place in the initial system^{60, 100}. The specific characteristics of this matrix have been thoroughly elucidated in paragraph 3.2.2 of this

thesis, as well as in the seminal work of Wei and Kuo^{66b, 66c}. Provided that the rate constant matrix \mathbf{K} for the system is known, the developed lumping methodology can be applied straightforwardly.

4.2 The lumping algorithm

The developed algorithm is based on the Monte Carlo stochastic sampling method, i.e. a stochastic simulation is implemented over all possible lumping combinations. The acceptance, or rejection, of every lumping combination is weighted according to our three lumping criteria (which will be thoroughly analyzed in Section 4.2.3). Microscopic reversibility is fulfilled and taken into consideration in the developed algorithm. The different lumping combinations are being implemented by the transformation matrix \mathbf{M} , which is actually the quantity that characterizes the outcome of lumping. At every trial MC-step a small change in the matrix \mathbf{M} is being realized.

4.2.1 The transformation matrix \mathbf{M}

The transformation matrix \mathbf{M} is the most important quantity of the lumping methodology. It reflects the essence of lumping, since it is the transformation matrix that operates on the original system and induces lumping. Thus, lumping is nothing else but a linear transformation of a n -tuple probability (or composition) vector, $\mathbf{P}(t)$, into a \hat{n} -tuple vector, $\hat{\mathbf{P}}(t)$, of smaller dimension ($\hat{n} < n$) by means of the $\hat{n} \times n$ transformation matrix \mathbf{M} , as illustrated in Figure 4.1:

$$\hat{\mathbf{P}} = \mathbf{M} \mathbf{P}$$

Figure 4.1: Schematic representation of lumping under application of the transformation matrix \mathbf{M} on the *a priori* probability vector \mathbf{P} ^{66b}.

A detailed description of the basic characteristics of the structure of the transformation matrix \mathbf{M} , as well as the way this matrix acts upon any initial, non-lumped matrix of dimensionality $n \times \hat{n}$, where integer $\hat{n} \in [1, n)$ can be found in the seminal work of Wei and Kuo ^{66b, 66c}. In particular, here we emphasize those properties of matrix \mathbf{M} which play an important role in better understanding the proposed methodology. In order to avoid confusion, the states of the system occurring after lumping will be called clusters. The most important characteristics of matrix \mathbf{M} are:

1. The elements of the \mathbf{M} matrix are either “0” or “1”.
2. Every column of the \mathbf{M} matrix contains exactly one “1”. The physical meaning behind this constraint is that every state of the initial system (i.e., every column of \mathbf{M}) belongs to one cluster only (i.e. to exactly one row of \mathbf{M}).
3. The position of “1” in every column of \mathbf{M} describes to which lumped state (row of \mathbf{M}) the state of the initial system it is being lumped.

In order to further clarify the characteristics of the transformation matrix, a simple example of a small 3×5 \mathbf{M} matrix is illustrated in Figure. 4.2:

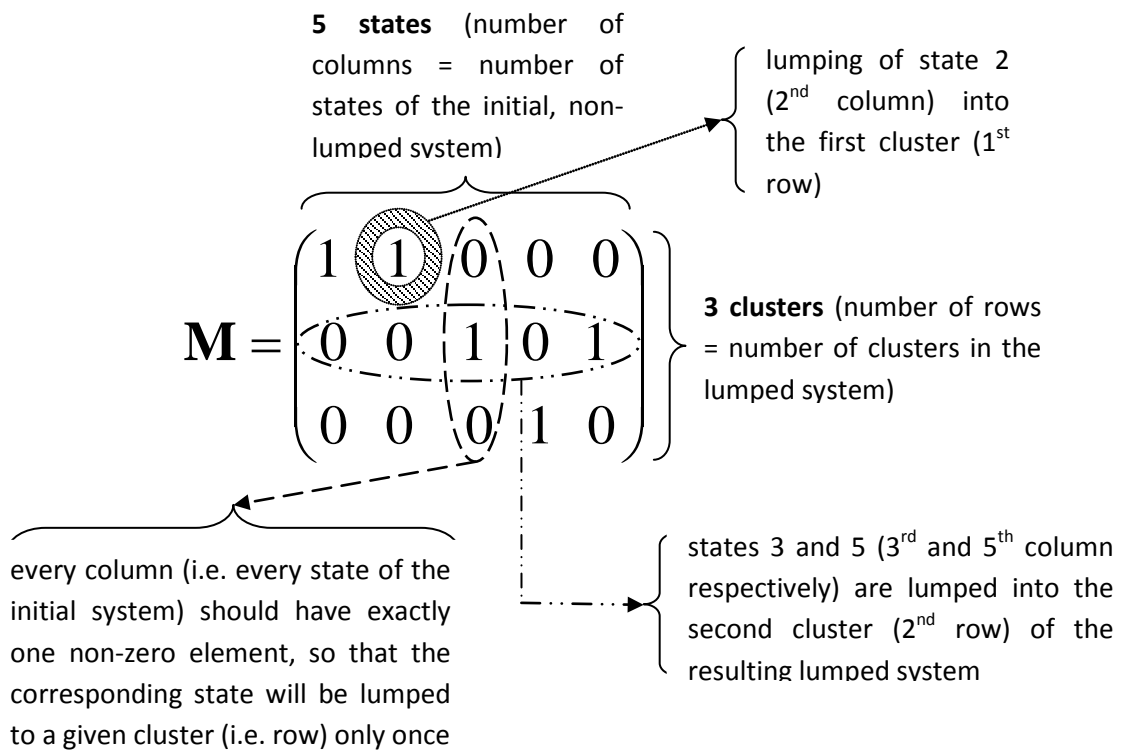


Figure 4.2: Characteristic example of an arbitrary 3×5 transformation matrix \mathbf{M} for the interpretation of its structure. According to the above matrix, three clusters are being formed after lumping. The first cluster (first row) consists of states 1 and 2 (columns 1 and 2 respectively) of the initial system, the second cluster (2nd row) emerges after lumping states 3 and 5 (3rd and 5th columns, respectively) of the initial system and finally the third cluster (3rd row) consists of only one state, namely state 4 of the initial system (4th column).

4.2.2 Monte Carlo moves on the transformation matrix

In the Monte Carlo algorithm we have designed for sampling different lumping schemes (see below), three different kinds of changes (trial moves) in matrix \mathbf{M} are considered to be possible. In order to ensure microscopic reversibility, the forward and back transition probabilities are calculated for every kind of trial move.

In the first type of move (“shift” move), matrix \mathbf{M} preserves its dimensionality, i.e., its number of rows, meaning that the number of clusters generated via lumping is held

constant. The only change that is being implemented is the shifting of a “1” from an arbitrarily chosen row to a different row of matrix \mathbf{M} . The moved “1” remains in the same column, as it corresponds to a certain state, which, as a result of the considered change, is being lumped to a different cluster. In order to move a “1”, a row has to be selected out of a total of \hat{n} rows. Every row of matrix \mathbf{M} is assigned the same probability, so the probability to choose a specific row is equal to $P_1^{\text{att}} = 1/\hat{n}$. In a similar way, the probability to choose a second row from the remaining rows is $P_2^{\text{att}} = 1/(\hat{n}-1)$. The probability for attempting a specific shift of a “1” is thus

$$\alpha_{\text{forw}} = P_1^{\text{att}} P_2^{\text{att}} = \frac{1}{\hat{n}(\hat{n}-1)} \quad (4.1)$$

Similarly, the probability for attempting the reverse move is

$$\alpha_{\text{back}} = P_1^{\text{att}} P_2^{\text{att}} = \frac{1}{\hat{n}(\hat{n}-1)} \quad (4.2)$$

In the second type of trial move (“merger” move), the number of rows of matrix \mathbf{M} is being reduced by one. This change refers to the number of clusters produced after lumping. The number of columns of matrix \mathbf{M} is fixed and remains constant, as it equals the number of states in the original system. The reduction in number of rows that is being realized here takes place by merging two different rows. Thus, after a MC-move of this type, the dimensionality of matrix \mathbf{M} is reduced by one. The first row to be merged is chosen from a uniform discrete distribution with probability $P_1^{\text{att}} = 1/\hat{n}$ and the second is chosen randomly from the remaining rows, with probability $P_2^{\text{att}} = 1/(\hat{n}-1)$. The second row is added into the first row, i.e. the position of the merged row is the same as that of the first row chosen to be merged. The forward move for merging of two rows is attempted according to the following probability

$$\alpha_{\text{forw}} = P_1^{\text{att}} P_2^{\text{att}} = \frac{1}{\hat{n}(\hat{n}-1)}. \quad (4.3)$$

In the inverse of the merger move (“split” move), a certain row of matrix \mathbf{M} , initially containing $(\hat{n}-1)$ rows, is split into two different rows. Note that the row of \mathbf{M} to be

split in two should be chosen with caution. A basic prerequisite for a row to be split is that the row contain more than one “1”, so that each of the two emerging rows includes at least one “1”. The choice of the row to be split is made with probability $P_1^{\text{att}} = 1/\hat{n}_s$, where $\hat{n}_s \leq \hat{n} - 1$ is the number of splittable rows (rows containing two or more “1” elements each) fulfilling the above prerequisite. If $\hat{n}_s = 0$, the split move and its inverse merger move are impossible. Following the choice of the row to be split, we consider the possible populations (numbers of “1” elements) of the two rows resulting from the split of the chosen row. In general, if the chosen row contains nun elements equal to “1”, then it can be split in $(nun - 1)$ different ways into two rows containing $nun1$ and $nun2$ elements equal to “1”, with $nun = nun1 + nun2$. For example, if the chosen row has $nun = 5$ elements equal to “1”, then the possible combinations of populations of the two rows obtained by splitting this row are $(nun - 1) = (5 - 1) = 4$: 1+4, 2+3, 3+2, 4+1. Each of these combinations of populations is attempted with equal probability during the split. The probability to choose the specific populations that characterized the two rows of matrix \mathbf{M} that were merged in the merger move which constitutes the reverse of the considered split move is thus $P_2^{\text{att}} = 1/(nun - 1)$. The number of ways in which $nun1$ elements equal to “1”, out of a total of nun , will be retained in the first of the two rows resulting from the split is $\binom{nun}{nun1}$. The probability of generating, through the chosen split, the specific configuration that the two rows had before the merger that constitutes the inverse move of the split is thus

$$P_3^{\text{att}} = \frac{1}{\binom{nun}{nun1}} = \frac{nun1!(nun - nun1)!}{nun!} = \frac{nun1!nun2!}{nun!} \quad (4.4)$$

The first row resulting from the split replaces the parent row that was split in matrix \mathbf{M} . The second row resulting from the split is inserted with equal probability before, in-between, or after the pre-existing rows of \mathbf{M} . The probability that the second row is assigned the index that it had before the merger move which constitutes the inverse of the considered split move is thus $P_4^{\text{att}} = 1/\hat{n}$. The attempt probability for the split move to lead to the specific form that \mathbf{M} had before the inverse merger move is thus equal to

$$\alpha_{\text{back}} = P_1^{\text{att}} P_2^{\text{att}} P_3^{\text{att}} P_4^{\text{att}} = \frac{nun1!nun2!}{\hat{n}_s (nun-1) nun! \hat{n}} \quad (4.5)$$

The third possible trial move employed in our MC algorithm is a “split” move, in which the dimensionality of matrix \mathbf{M} increases by one. This move has already been described above as the reverse of the merger move. According to the arguments presented in the previous paragraphs, the attempt probability for a split move to occur in a specific way is equal to

$$\alpha_{\text{forw}} = \frac{nun1!nun2!}{\hat{n}_s (nun-1) nun! (\hat{n}+1)} \quad (4.6)$$

where \hat{n} and \hat{n}_s , respectively, are the total number of rows and the number of splittable rows of \mathbf{M} before the move, nun is the number of “1” elements in the row chosen for splitting and $nun1$, $nun2$ are the numbers of “1” elements in the rows resulting from the split. On the other hand, the attempt probability for the inverse merger move is

$$\alpha_{\text{back}} = \frac{1}{(\hat{n}+1)\hat{n}} \quad (4.7)$$

The change in dimensionality of matrix \mathbf{M} will have a significant effect on the other two lumping criteria, the lumping error E and the long-time dynamics parameter W , discussed extensively in the following section.

4.2.3 The lumping criteria

In every trial step of the developed lumping algorithm, three different quantities need to be calculated. These are the three different lumping criteria, which determine whether each stochastic trial move will be rejected or accepted. In other words, the lumping criteria are required to follow a prescribed probability distribution. The calculation of two out of the three lumping criteria is based on the Frobenius norm. The Frobenius norm is calculated for an arbitrary non-square $m \times n$ matrix \mathbf{B} , through the following equations:

$$\|\mathbf{B}\|_F = \sqrt{\sum_{i=1}^m \sum_{j=1}^n |b_{ij}|^2} = \sqrt{\text{trace}(\mathbf{B}^* \cdot \mathbf{B})} = \sqrt{\sum_{i=1}^{\min\{m,n\}} \sigma_i^2} \quad (4.8)$$

where \mathbf{B}^* denotes the conjugate transpose of matrix \mathbf{B} , and σ_i are the singular values of matrix \mathbf{B} . The Frobenius norm, among other matrix norms (e.g., the maximum absolute value of the elements of matrix \mathbf{B}), is better, because it takes into account not only one element, but the entire matrix \mathbf{B} and thus constitutes a more characteristic measure for the quality of lumping. A detailed description of the significance of the three implemented lumping criteria, and all necessary information for the calculation of the parameters by which they are expressed, is provided in the following paragraphs.

1. The first and most important lumping criterion, the lumping error, describes the quality of lumping – with respect to the original system kinetics. The calculation of this quantity is based on the work of Kuo and Wei^{66b, 66c}. The lumping error is calculated with the help of an error matrix \mathbf{E} , according to:

$$\mathbf{E} \equiv \mathbf{M} \cdot \mathbf{K} - \hat{\mathbf{K}} \cdot \mathbf{M} \quad (4.9)$$

$\hat{\mathbf{K}}$ stands for the $\hat{n} \times \hat{n}$ rate constant matrix of the lumped system. Calculation of this matrix proceeds in a straightforward manner, see Eqs. (4.10-4.12), having as a minimum requirement the knowledge of the transformation matrix \mathbf{M} , the rate constant matrix \mathbf{K} and the $n \times n$ concentration matrix \mathbf{A} :

$$\hat{\mathbf{K}} = \mathbf{M} \cdot \mathbf{K} \cdot \mathbf{A} \cdot \mathbf{M}^T \cdot \hat{\mathbf{A}}^{-1} \quad (4.10)$$

where

$$\hat{\mathbf{A}} = \mathbf{M} \cdot \mathbf{A} \cdot \mathbf{M}^T \quad (4.11)$$

and hence

$$\hat{\mathbf{A}}^{-1} = (\mathbf{M} \cdot \mathbf{A} \cdot \mathbf{M}^T)^{-1} \quad (4.12)$$

For a given transformation matrix \mathbf{M} , matrix \mathbf{E} shows how close to perfect lumping the realized lumping is. For a system that is exactly lumpable by matrix \mathbf{M} , matrix \mathbf{E} is unique and is a null matrix. For a system approximately lumpable by matrix \mathbf{M} , matrix \mathbf{E} is neither a null matrix, nor unique. This is

because matrix \mathbf{E} depends on the choice of matrix \mathbf{M} . Matrix \mathbf{E} does not depend on time. It is a measure of how close to exact lumpability the imposed lumping is. If a relevant time-dependent measure is needed, the eigenvalues and eigenvectors of the initial system need to be known, which is exactly what the lumping methodology aims to avoid.

The concentration matrix \mathbf{A} is, by definition, a diagonal matrix, whose diagonal elements equal the elements of the equilibrium probability vector $\mathbf{P}(\infty)$. The equilibrium probability vector $\mathbf{P}(\infty)$ is an n -long column vector, which is equal to the real part of the right eigenvector corresponding to the zero eigenvalue of the rate constant matrix \mathbf{K} . $\mathbf{P}(\infty)$ can be calculated via one of the two options described below. Specifically, upon diagonalization of a square, real, stochastic matrix that is similar to a symmetric matrix (see below), the resulting eigenvalues should be real, of similar (in the case of \mathbf{K} , negative) sign and one of them should be equal to zero¹⁰¹. The eigenvector corresponding to the zero eigenvalue of \mathbf{K} is the equilibrium vector $\mathbf{P}(\infty)$. Of course, this method requires the diagonalization of matrix \mathbf{K} , which can be laborious and of questionable accuracy for big systems. Another possibility for calculating the equilibrium vector without diagonalizing matrix \mathbf{K} is to adopt an iterative process, i.e., apply an iterative scheme to solve the master equation at equilibrium [Eq. (3.1)]:

$$P_i(t) \cdot \sum_{j \neq i} k_{i \rightarrow j} = \sum_{j \neq i} P_j(t) \cdot k_{j \rightarrow i} \Rightarrow P_i^{(m+1)}(t) = \frac{\sum_{j \neq i} P_j^{(m)}(t) \cdot k_{j \rightarrow i}}{\sum_{j \neq i} k_{i \rightarrow j}} \quad (4.13)$$

For a given system, under the assumption that its rate constant matrix is known, every single transformation matrix \mathbf{M} leads to a certain lumping scheme. In the present work, the lumping error, emerging from the implementation of a specific matrix \mathbf{M} , is taken as the Frobenius norm of the resulting non-symmetric $n \times \hat{n}$ error matrix \mathbf{E} :

$$E = \|\mathbf{E}\|_F = \sqrt{\sum_{i=1}^n \sum_{j=1}^{\hat{n}} |E_{ij}|^2} \quad (4.14)$$

Obviously, successful lumping is described by a small lumping error E . Small E means that there is only small difference between the corresponding eigenvalues of the original and the lumped system. Of course, the lumped system has only a fraction of the eigenvalues of the initial system, but E makes sure that the small system has, although less, similar eigenvalues to the ones of the initial system.

2. The second lumping criterion used is a measure of the efficiency of the applied lumping in describing accurately the dynamics of the system at long times. A quantity which captures this ability well is the sum of the squares of the absolute values of the real parts of all eigenvalues of the rate matrix $\hat{\mathbf{K}}$ of the lumped system:

$$Q = \left(\sum_{i=1}^{\hat{n}} |\operatorname{Re}(\sigma_i)|^2 \right)^{1/2} \quad (4.15)$$

where σ_i are the singular values of matrix $\hat{\mathbf{K}}$. Realization of such a calculation requires the investigated rate constant matrix $\hat{\mathbf{K}}$ to be diagonalized, so that its singular values are obtained. Therefore all eigenvalues and the corresponding (right) eigenvectors need to be calculated. This calculation is in most cases – especially for matrices of large dimensionality – costly, in terms of both time and computational power. Therefore, an alternative route has to be found, without reducing the accuracy of the calculation. In order to overcome this obstacle, we again use the Frobenius norm. By application of Eq. (4.8) for the rate constant matrix $\hat{\mathbf{K}}$, which is a square $\hat{n} \times \hat{n}$ stochastic matrix that is similar to a symmetric matrix¹⁰² and therefore has real eigenvalues, the following relationship is obtained:

$$W = \|\hat{\mathbf{K}}\|_F = \sqrt{\sum_{i=1}^{\hat{n}} \sum_{j=1}^{\hat{n}} |\hat{k}_{ij}|^2} = \sqrt{\operatorname{trace}(\hat{\mathbf{K}}^* \cdot \hat{\mathbf{K}})} = \sqrt{\sum_{i=1}^{\hat{n}} \sigma_i^2} \quad (4.16)$$

Direct comparison between the quantities defined in Eqs. (4.15) and (4.16), informs us that the quantity Q we wish to calculate is exactly the same as W given by Eq. (4.16). In order to describe more accurately the slow processes of the original system by the kinetics of the lumped system, the value of the

Frobenius norm should be as small as possible. Although the lumping error E is the criterion ensuring that the difference in eigenvalues between initial and lumped system is minimal, there is no guarantee that the surviving eigenvalues will be in a position to describe long characteristic times. Associated with long time dynamics are the eigenvalues with small absolute value. The second lumping criterion forces $\hat{\mathbf{K}}$ to include those eigenvalues of small absolute values and hence the lumped system to adhere to the long-time dynamics of the original system. The simultaneous minimization of the two mentioned lumping criteria offers a good lumping, since E makes sure that the difference in eigenvalues between the two systems is as small as possible, while W ensures that, among the eigenvalues of the lumped system, are maintained the small eigenvalues of the original system, being able to describe long-time dynamics. By minimizing W , *while at the same time minimizing E* , we force the lumping to focus on reproducing the long time behavior of the original system. By requiring both E and W to be small, we are telling $\hat{\mathbf{K}}$ to sacrifice short time (fast process) information in trying to match \mathbf{K} , and rather focus on long-time information. Moreover, despite the fact that the value of W can be dominated by the largest eigenvalues of $\hat{\mathbf{K}}$ (the fastest processes described by $\hat{\mathbf{K}}$), the applied algorithm for finding the optimal transformation matrix is extremely sensitive in tracking even the slightest changes in the objective function to be minimized (see Eq. (4.25) below), caused by differences in E and W . Hence, even a minor change in W favors a matrix \mathbf{M} which corresponds to a smaller value of the objective function, provided that the remaining two parameters E and \hat{n} are identical.

3. The third lumping criterion describes the size of the system that results after lumping. To be precise, this quantity defines the number of the lumped species (clusters of states) \hat{n} . Once the number of the lumped species is defined, the dimensionality of the transformation matrix \mathbf{M} is also defined. It is obvious that the higher the number of the lumped species \hat{n} , the more difficult all calculations will be at the lumped level. The dimensionality of the lumped system should be small for lumping to be characterized as “successful”.

The ideal lumping procedure depends a lot on the problem investigated. In our case, ideal lumping demands that each one of the above three quantities become as small as possible. Minimizing the three mentioned lumping criteria is not equally important for every occasion. Most important of all is to minimize the emerging lumping error E . Next in significance is the minimization of the second lumping criterion, i.e. the square root of the sum of squares of the singular values of the lumped system's rate matrix. This requirement will ensure that the lumped system is in a position to describe the slow processes of the original system sufficiently accurately, mostly because these processes define to a large degree the system's long time dynamics. We wish to reproduce the full dynamics of the original system for long times. Finally, the demand for an as small as possible system dimensionality, which corresponds to the third of our lumping criteria \hat{n} , is important for cutting computational cost in calculations conducted at the lumped level, once lumping has been accomplished. Of course it is *a priori* expected that, the smaller the lumped system, the greater the lumping error, since more original states are lumped into new states (clusters), and this contributes to information loss with respect to the original system dynamics. Fig. 4.3 shows a typical interdependence among the three lumping criteria.

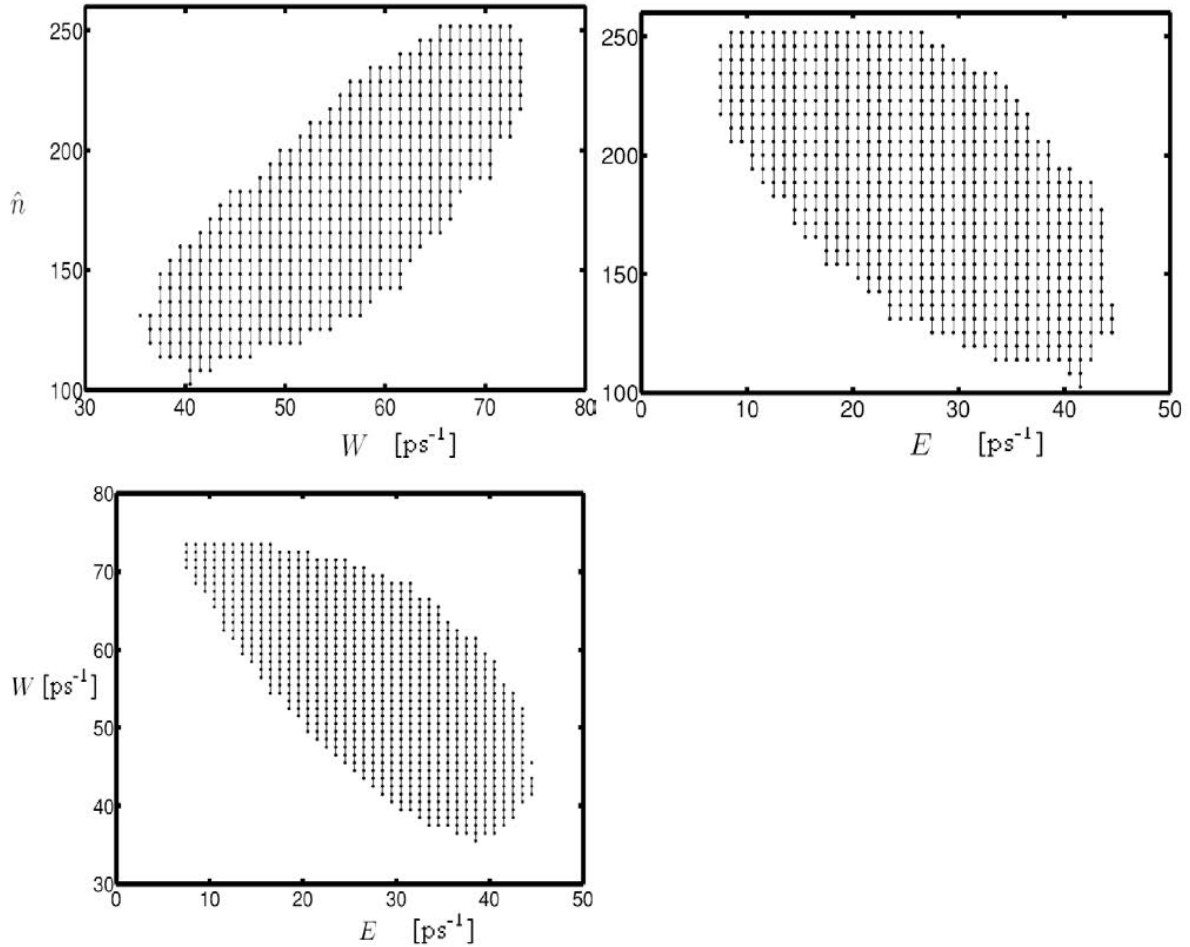


Figure 4.3: Characteristic examples of the behavior of the lumping criteria when plotted against each other. The displayed results are obtained after a Wang-Landau MC-simulation run (see Section 4.3) of 2×10^7 steps for an initial system of 290 states. (a) Relation between the size of the lumped system \hat{n} and the measure of the ability of the lumped system to describe long-time dynamics, W . (b) Relation between the lumping error E and the dimension \hat{n} of the lumped system. (c) Relation between the lumping error and the long-time dynamics parameter W . Parts (a) and (b) have the same vertical axis, the title of which is omitted in part (b). Each point corresponds to a state encountered in Wang-Landau sampling with probability higher than 1×10^{-7} .

Figure 4.3(a) shows that the long-time dynamics parameter W grows as the lumped system becomes larger. This is expected, because, by increasing the lumped system size, the number of singular values of the lumped rate matrix $\hat{\mathbf{K}}$, Eq. (4.16), also

increases. There are more summations to be accumulated on the right-hand side of Eq. (4.16), leading to a larger value of W . Note that the order of magnitude of W is determined by the elements of the rate constant matrix $\hat{\mathbf{K}}$. An increase in the lumped system size leads to a decrease of the lumping error (Fig. 4.3(b)). This is because, as the lumped system approaches the size of the original system, the loss of information due to lumping is reduced, leading to a decrease in the corresponding lumping error. By comparing Figs. 4.3(a) and 4.3(b), one notices that the lumping error E changes inversely with the parameter W (Fig. 3(c)). From Figure 4.3 we conclude that the minimization of all three lumping criteria is not straightforward, as two of them vary inversely with the third. This means that perfect lumping is defined as the best compromise of those criteria with respect to a certain level of accuracy. In our work we consider the lumping error E to be the most important of all three.

4.3 Structure of simulations

The procedure for finding the best lumping scheme with respect to the three adopted lumping criteria includes two sets of MC simulation runs. Before going into details of the two different sets of simulations, a clarification is essential. In the context of our optimization work, we consider a three-dimensional space spanned by the three coordinates E, W, \hat{n} . Any lumping scheme (choice of lumped system size \hat{n} and lumping matrix \mathbf{M}) is mapped onto a point \mathbf{X} in this three-dimensional space. A given value of \hat{n} and transformation matrix \mathbf{M} defines a “microstate” in the space of all possible lumpings. Each microstate is characterized by three “energy functions”, namely the three parameters or lumping criteria we wish to minimize. We denote these three functions collectively by \mathbf{X} :

$$\mathbf{X} = \mathbf{X}(\hat{n}, \mathbf{M}) = (E(\hat{n}, \mathbf{M}), W(\hat{n}, \mathbf{M}), \hat{n}) \quad (4.17)$$

Any simple change in the lumped system size \hat{n} and/or in matrix \mathbf{M} yields a different microstate, generally characterized by different values of \mathbf{X} , i.e., of the parameters E, W, \hat{n} . The number of microstates $g(\mathbf{X})=g(E, W, \hat{n})$ with error between E and $E+dE$, long-time dynamics parameter between W and $W+dW$, and lumped system size \hat{n} , per unit volume $dE dW$, defines a density of states in the three-dimensional space (E, W, \hat{n}) .

The first set of simulations involves MC runs based on the Wang-Landau density of states method⁸⁷. A set of eight consecutive Wang-Landau MC runs is undertaken to estimate the density of states $g(\mathbf{X})$. Microstates are sampled with a probability density inversely proportional to the current estimate of $g(\mathbf{X})$ which is continuously updated, until convergence to a flat histogram in (E, W, \hat{n}) space is obtained. The maximum values of E , W , \hat{n} are calculated with the help of an initial, large MC run, which simulates an exhaustive random walk over possible microstates. The minimum values of all three parameters E , W , \hat{n} are set to zero, since all three parameters are positive, real numbers.

The second set of simulations consists of a single MC-run. It capitalizes on the knowledge of the density of states gained through the first set, in order to access preferentially microstates characterized by small values of lumping error E , long-time dynamics parameter W , and lumped system dimensionality \hat{n} . The flat histogram in (E, W, \hat{n}) space obtained from the previous set is now tilted through appropriate design of the MC selection criterion, causing the MC run to preferentially access microstates near the origin. During this second set of MC simulation, microstates which are characterized by small values for all three lumping criteria are sampled preferentially.

During the first set of MC simulations we aim to obtain an, as much as possible, flat histogram in (E, W, \hat{n}) space. The Wang-Landau algorithm used here estimates the density of states $g(\mathbf{X})$ by carrying out a random walk in the space spanned by all microstates (all lumped system sizes \hat{n} and transformation matrices \mathbf{M}) with probability density proportional to $1/g(\mathbf{X})$ instead of the usual Boltzmann weight used in conventional Metropolis MC simulation¹⁰³. As a consequence, the frequency of visiting each point \mathbf{X} in (E, W, \hat{n}) space converges to an almost constant value. The basic reason for using the Wang-Landau scheme instead of the conventional Metropolis scheme based, e.g., on a probability density proportional to $e^{-\beta E}$, $\beta > 0$, is that we wish to sample the space of microstates as boldly as possible and avoid being trapped in local minima of \mathbf{X} . With a probability density decaying exponentially with E, W, \hat{n} there may only be a minute probability of visiting high \mathbf{X} microstates and thereby escaping from local minima of \mathbf{X} . The Wang-Landau scheme is more appropriate for exploring a wide variety of microstates evenly¹⁰⁴. This is shown

characteristically in Figures B.1-B.5 of Appendix B, in which the performance of the Wang-Landau scheme is quantitatively compared to that of a conventional Metropolis Monte Carlo algorithm for sampling the configuration space of the lumping problem.

The simulations of the first set are performed such that, if $g(\mathbf{X}_1) = g(\mathbf{X}(\hat{n}_1, \mathbf{M}_1))$ is the density of states of the current microstate and $g(\mathbf{X}_2) = g(\mathbf{X}(\hat{n}_2, \mathbf{M}_2))$ is the density of states of a possible trial microstate, the acceptance probability of the move is given by:

$$P_{\text{acc}}(\mathbf{M}_1 \rightarrow \mathbf{M}_2) = \min \left[\frac{1/g(\mathbf{X}_2) \cdot \alpha_{\text{back}}}{1/g(\mathbf{X}_1) \cdot \alpha_{\text{forw}}}, 1 \right] = \min \left[\frac{g(\mathbf{X}_1) \cdot \alpha_{\text{back}}}{g(\mathbf{X}_2) \cdot \alpha_{\text{forw}}}, 1 \right] \quad (4.18)$$

with α_{forw} and α_{back} being the attempt probabilities for forward and backward shift, merger, and split moves in \mathbf{M} discussed in Section 4.2.2. For each accepted configuration we accumulate an “energy” histogram $H(\mathbf{X})$. Since the density of states is not known *a priori*, Wang and Landau proposed to set initially $g(\mathbf{X})=1$ and $H(\mathbf{X})=0$, for all microstates⁸⁷. In view of Eq. (4.17), Eq.(4.18) can be written more explicitly as:

$$P_{\text{acc}}(\mathbf{M}_1 \rightarrow \mathbf{M}_2) = \min \left[\frac{g(E_1, W_1, \hat{n}_1) \cdot \alpha_{\text{back}}}{g(E_2, W_2, \hat{n}_2) \cdot \alpha_{\text{forw}}}, 1 \right] \quad (4.19)$$

\mathbf{X} -space is divided into three-dimensional bins and the random walk in \mathbf{M} is classified in these bins, as it evolves during the MC simulation. As the random walk in microstate space is performed, whenever a move to a trial microstate with parameters \mathbf{X}_2 is accepted, the density of states $g(\mathbf{X}_2)$ is updated by multiplying it by a “modification factor” $f > 1$ that accelerates the diffusion of the random walk, and a unit is added to the corresponding histogram $H(\mathbf{X}_2)$:

$$g(\mathbf{X}_2) \rightarrow g(\mathbf{X}_2) \cdot f \quad (4.20)$$

and

$$H(\mathbf{X}_2) \rightarrow H(\mathbf{X}_2) + 1 \quad (4.21)$$

An interpretation of the physical meaning of the modification factor f is to consider it as a “punishment” which a certain trial microstate receives if it is accepted. As a result, it becomes more and more difficult for this microstate to be accepted again, and therefore to further increase its frequency of occurrence in the MC sampling. Thus, less favorable microstates, which eventually are being selected, are ultimately visited with equal frequency as those which were more probable at the beginning of the run. The density of states is multiplied by f until the accumulated histogram $H(\mathbf{X})$ becomes as flat as possible within the given number of MC steps. The density of states obtained after completion of each one of the totally eight simulation runs of the first set is set equal to the initial density of states for the next run, which is undertaken with a new, reduced value of f according to the following empirical rule:

$$f_{i+1} = \sqrt{f_i}, \quad i = 1, 2, \dots, 7 \quad (4.22)$$

In the beginning of each run, the histogram $H(\mathbf{X})$ is reset to $H(\mathbf{X}) = 0$ for all \mathbf{X} . In the simulations implemented in this work, in order to obtain a good estimation of the density of states, the initial choice of f was set to $f = 4$. The simulation converges to a good estimate of the true density of states $g(\mathbf{X})$ when f is approximately equal to 1. After a sequence of eight successive simulation runs, the modification factor was reduced to a value of 1.01, which indicates that the outcome of the simulation is practically independent of f [Eq. (4.20)]. At that point, we consider the calculated density of states as a good estimate of the density of states of the system. In Table 4.1 the values of f and the length of each of the eight Wang-Landau MC runs realized in the context of the first set of simulations are listed.

Table 4.1: Information about the length and the modification factor f for each one of the totally eight, successive Wang-Landau MC simulation runs for the achievement of a flat probability distribution of the sampled microstates.

run	1	2	3	4	5	6	7	8
MC steps	2×10^7	2×10^7	2×10^7	2×10^7	2×10^7	2×10^7	2×10^7	2×10^7
f [-]	4	2	1.41	1.19	1.09	1.04	1.02	1.01

In fact, $H(\mathbf{X})$ can never reach perfect flatness, so some criterion must be used. In our simulations the criterion of flatness was taken as each value of the histogram deviating from the mean value by less than 10% of the difference between the maximum and the minimum value of $H(\mathbf{X})$. In Figure 4.4 is shown the behavior of the histogram in \mathbf{X} -space of the sampled microstates after the completion of the first set of simulation runs:

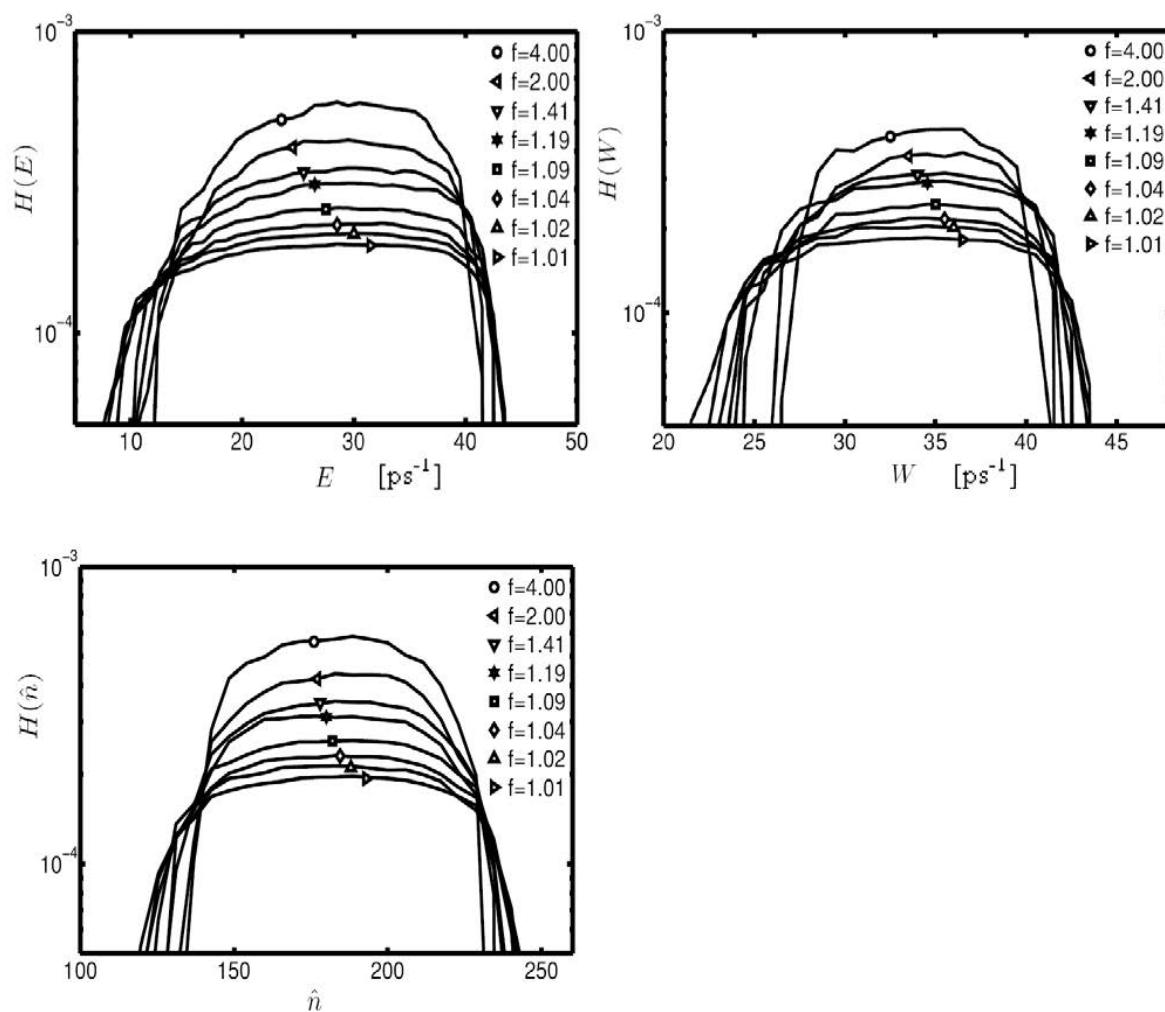


Figure 4.4: Schematic representation of the histogram of sampled states with respect to (a) E , (b) W and (c) \hat{n} for every one of the totally eight Wang-Landau MC runs of the first simulation set.

According to Eq. (4.17), every microstate is characterized by three parameters E , W and \hat{n} . Hence, if one wished to plot the histogram $H(\mathbf{X})$ or $H(E, W, \hat{n})$, a four-dimensional plot would be required. Figure 4.4 shows the projections of the hypersurface $H(E, W, \hat{n})$ (marginal distributions) on each one of the following three planes: $(E, H(E))$, $(W, H(W))$ and $(\hat{n}, H(\hat{n}))$. A clearer and more detailed view of the histogram is given in the three-dimensional plots of Figure 4.5. Each one of these three plots presents a two-dimensional projection of the histogram, each time as a function of two of the three independent variables E, W, \hat{n} :

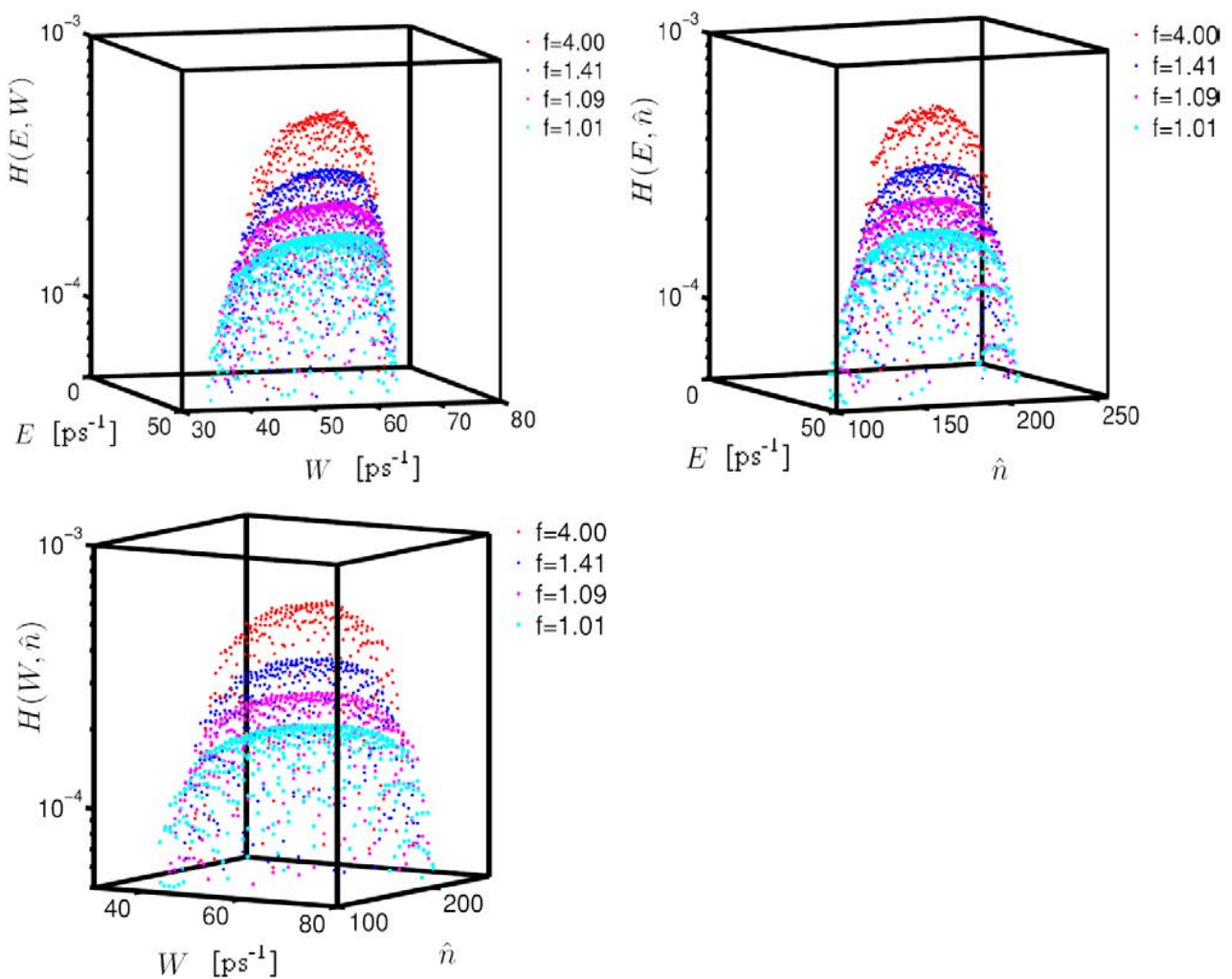


Figure 4.5: Projections of the three-dimensional histogram $H(E, W, \hat{n})$ on the two dimensional spaces spanned by two of the three independent variables E, W, \hat{n} . (a) $H(E, W)$ projection, (b) $H(E, \hat{n})$ projection, (c) $H(W, \hat{n})$ projection.

As soon as the first set of simulation runs is completed, a reasonably flat histogram is obtained. In that histogram, microstates (i.e., transformation matrices \mathbf{M}) are sampled such that the corresponding combinations of E, W, \hat{n} parameters are equally probable. This sampling can easily be manipulated to yield higher probability for certain combinations of E, W, \hat{n} . In other words, one can transform the flat histogram to make certain microstates more probable. The microstates we wish to favor are those which are characterized by small lumping error E , small long-time dynamics parameter W and as small as possible lumped system dimensionality \hat{n} .

To accomplish this, an additional MC run is implemented, using as initial density of states the one obtained from the last Wang-Landau MC run of the previous set of simulations. The acceptance criterion in this run is designed such that microstates with small values of the lumping criteria become more probable. This is realized by inserting an appropriate weighting function $h(\mathbf{X})$ which decays with E, W, \hat{n} and thus tilts the flat histogram of the Wang-Landau method to one in which microstates with small lumping criteria are visited more frequently. The acceptance criterion for this MC run is now the following:

$$P_{\text{acc}}(\mathbf{M}_1 \rightarrow \mathbf{M}_2) = \min \left[\frac{g(\mathbf{X}_1)}{g(\mathbf{X}_2)} \cdot \frac{h(\mathbf{X}_2)}{h(\mathbf{X}_1)} \cdot \frac{\alpha_{\text{back}}}{\alpha_{\text{forw}}}, 1 \right] \quad (4.23)$$

In Eq. (4.23) $g(\mathbf{X})$ is known and equal to the density of states resulting from the first set of simulations. The functional form of $h(\mathbf{X})$ is arbitrarily chosen. The only constraint it should fulfill is that it should tilt the flat probability distribution (Fig. 4.4) such that microstates characterized by small values of lumping criteria become more probable. In our work the adopted functional form of $h(\mathbf{X})$ is the following:

$$h(\mathbf{X}) = h(E, W, \hat{n}) = a \cdot E + b \cdot W + c \cdot \hat{n} + d \quad (4.24)$$

where the parameters a, b, c and d are constants defined before the simulation. Parameters a, b, c should have a negative sign, so that the resulting histogram in E, W, \hat{n} has a negative slope. Parameter d should be positive and sufficiently large to ensure nonnegativity of $h(\mathbf{X})$ over the considered E, W, \hat{n} domain; it corresponds to the intercept of the histogram at the origin of \mathbf{X} -space. Results from this additional MC

simulation run are shown in Figure 4.6. The values of the above parameters used in our simulations are $a = -2 \times 10^{-5}$ ps, $b = -4 \times 10^{-5}$ ps, $c = -7 \times 10^{-6}$ and $d = 10^{-3}$.

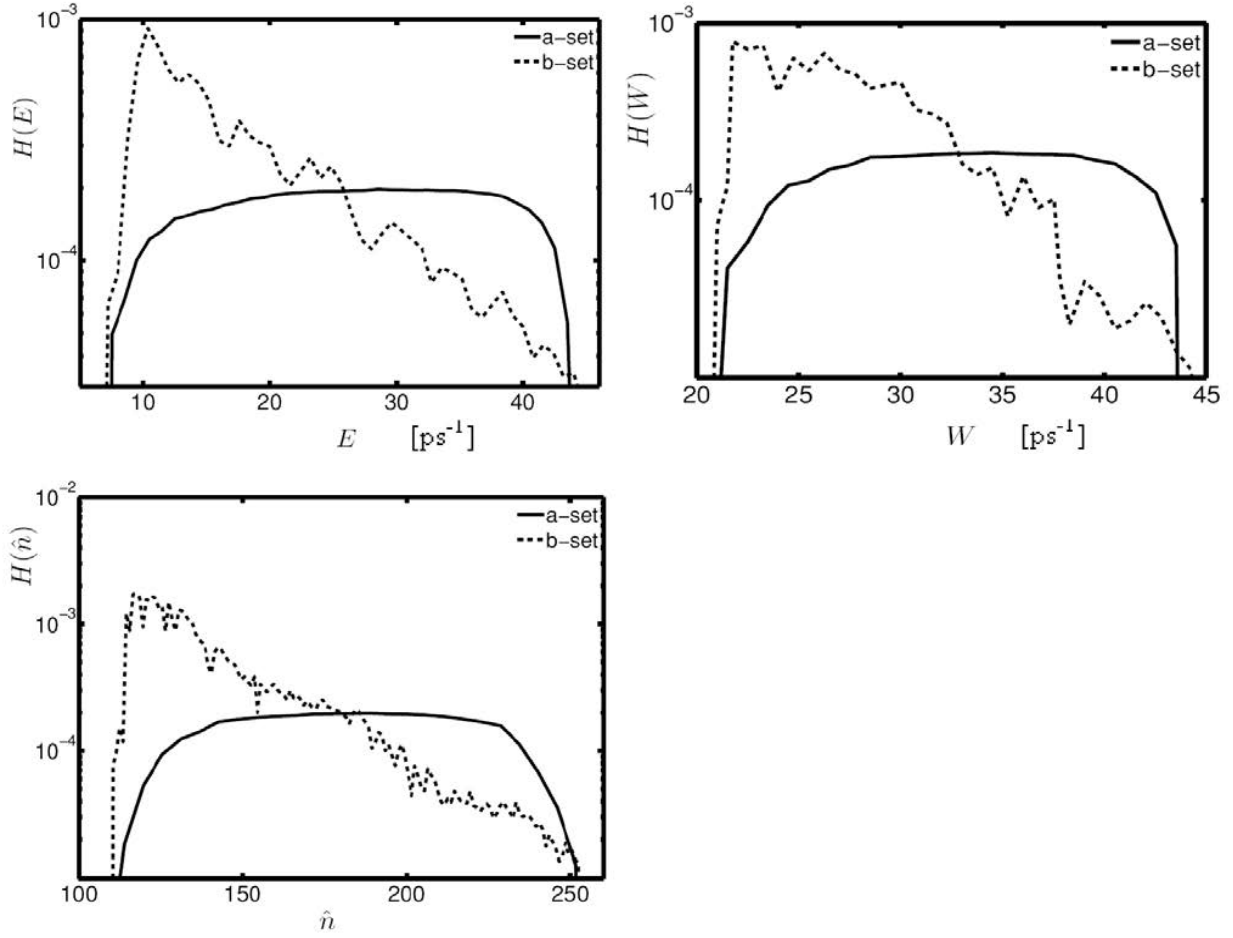


Figure 4.6: Schematic representation of the histogram of sampled \mathbf{M} -microstates in \mathbf{X} -space, projected onto the E (a), W (b), and \hat{n} (c) axes. In this figure is being represented the last run ($f = 1.01$, cf. Fig. 4.4) of the first set (a-set) of Wang-Landau runs, as well as the additional MC run constituting the second set (b-set) of simulation runs of the lumping methodology.

Figure 4.6 shows that, after the additional MC simulation of the b-set of runs, microstates (i.e. \mathbf{M} -matrices) with small values of all three lumping criteria become more probable and thus easier to select via realization of the lumping algorithm. Among all \mathbf{M} matrices sampled by the MC-algorithm one has to be chosen to perform lumping. This matrix corresponds to the one that exhibits the smallest value of a defined objective function $z(\mathbf{X})$. In our work we define this function as follows:

$$z(\hat{n}, \mathbf{M}) = z(E, W, \hat{n}) = z_1 E + z_2 W + z_3 \hat{n} \quad (4.25)$$

The \hat{n} value and \mathbf{M} matrix corresponding to the minimum value of this objective function is the most appropriate to perform lumping. Parameters z_1, z_2, z_3 weight our need to approach exact lumping (minimal lumping error E), to describe long-time dynamics (small W) and to keep the dimensionality of the lumped system as small as possible (\hat{n}). Hence, z_1 should have the biggest influence on the value of the objective function $z(\mathbf{X})$, whereas z_2 should follow, letting z_3 have the smallest influence on $z(\mathbf{X})$. For the needs of our work the parameters z_1, z_2, z_3 have the values listed in Table 4.2:

Table 4.2: Values of the parameters of the objective function $z(\mathbf{X})$ (Eq. (4.27)), specifying the importance of each one of the three lumping criteria for the final result.

z_1 [ps]	z_2 [ps]	z_3 [-]
0.5	0.3	0.2

From the above, one can conclude that the developed algorithm performs a stochastic, discrete optimization in respect to the three lumping criteria E, W and \hat{n} . The “continuum” alternative of this formulation would be $\min_{\hat{n}, \mathbf{M}} (z_1 W + z_2 E + z_3 \hat{n})$, with E given by Eqs. (4.14) and (4.9-4.12), W given by Eqs. (4.16) and (4.10-4.12), and z_1, z_2, z_3 being pre-defined constants. The objective function is minimized with respect to the dimensionality \hat{n} of the lumped system and with respect to the structure of the \mathbf{M} matrix, which can only be defined once \hat{n} has a specific value. Given that \mathbf{K} and, therefore, \mathbf{A} are fixed, the objective function $z_1 W + z_2 E + z_3 \hat{n}$ is indeed a function of \hat{n} and \mathbf{M} . The minimization has to take place subject to the constraints on the structure of \mathbf{M} spelt out in Section 4.2.1. One has to determine an optimal value for the integer \hat{n} and also decide which elements of \mathbf{M} should be ones, subject to the constraints on \mathbf{M} .

4.4 Implementation of the lumping algorithm

The methodology was initially tested on small, predefined networks of chemical reactions^{66b, 66c, 91b}, for which the optimum lumping result, with respect to specific factors, is known. The results obtained from lumping were in full agreement with those reported in the literature. Afterwards, the lumping algorithm was applied to a much bigger network of transitions of the glassy binary Lennard-Jones system described in Section 3.4. The network consists of 1503 states (i.e. basins of the potential energy hypersurface in configuration space, each basin constructed around an individual inherent structure, i.e. local minimum of the potential energy with respect to all configurational degrees of freedom). These states have been found to belong to four different metabasins of the potential energy landscape⁵⁶. The algorithm produced the best, with respect to our specific criteria, lumped system size \hat{n} and transformation matrix \mathbf{M} which lumps the initial system to an equivalent one of lower dimensionality, taking into account the dynamics at long times. The ability of the lumped system to fully describe the dynamical behavior of the initial system at long time scales was confirmed by applying the lumping methodology in two different ways. More specifically, Fig. 4.7 shows the two different routes followed in order to approach the same point which describes the lumped system at time t (point Q):

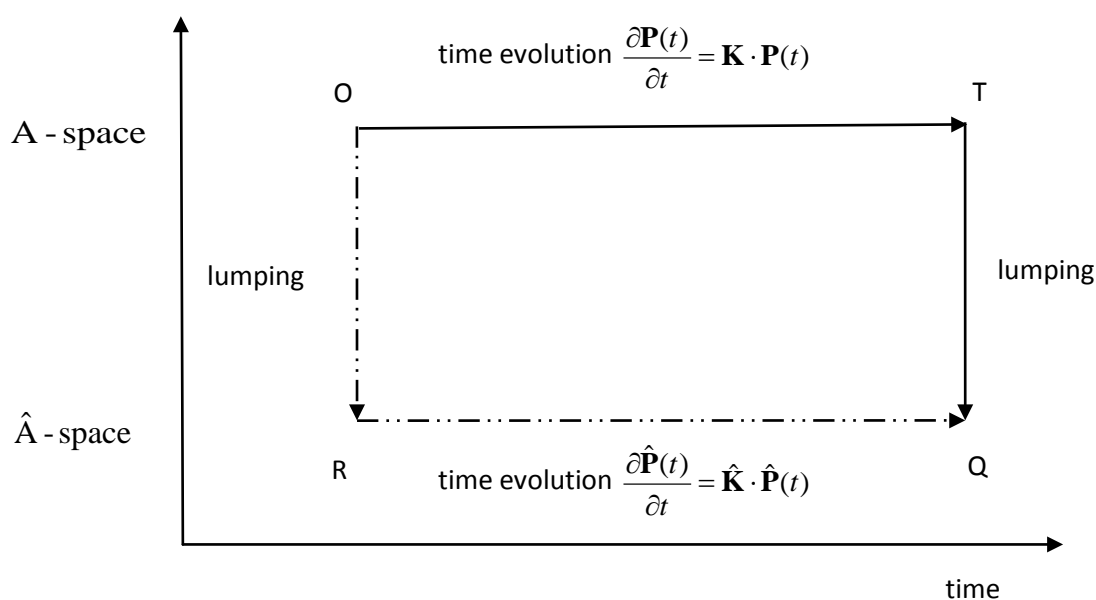


Figure 4.7: Schematic representation of two different routes followed to lump the initial system at time 0 (point O) into a system of smaller dimensionality at time t (point Q)

(point Q). The system of smaller dimensionality should be able to describe the dynamics of the original system at long times. The two displayed routes differ in the order in which time evolution and lumping are realized. In route O-T-Q we first let the system evolve in time (OT) and then we lump (TQ), while in route O-R-Q we first lump and then let the lumped system evolve in time.

In Fig. 4.7 the vertical axis gives a measure of the dimensionality of the system, whereas the horizontal axis represents time evolution, obtained through analytical solution of the master equation, Eq. (3.1).

The state space of the original system is called the A -space and has, for our system, a dimensionality $n = 1503$; the state space after lumping is called \hat{A} -space and has a dimensionality $\hat{n} = 600$. If our methodology is correct, the probability distribution among lumped states at Q obtained via route O-T-Q and via route O-R-Q should be the same.

Instead of comparing the two aforementioned routes, one can alternatively follow two different routes, e.g. routes OT and ORQT. The comparison this time would take place at point T. Along route OT we let the original system evolve in time, whereas along route ORQT the system is lumped, let to evolve in time, and then returned to its original dimensionality. Matrix \mathbf{M} is responsible for lumping (sub-path OR) and maps the A -space into the \hat{A} -space. In order to implement route QT we need to redistribute the occupancy probabilities of lumped states among the original states according to the requirements of local equilibrium within the lumped states. There exists a reverse mapping procedure^{66b} which makes use of matrix $\mathbf{A} \cdot \mathbf{M}^T \cdot \hat{\mathbf{A}}^{-1}$, where, as mentioned in Section 4.2.3, $\mathbf{A} = \text{diag}(P_1(\infty), \dots, P_n(\infty))$ and $\hat{\mathbf{A}} = \mathbf{M} \cdot \mathbf{A} \cdot \mathbf{M}^T$ [Eq. (4.11)]. This matrix will map the \hat{A} -space back into the A -space. The use of both matrices \mathbf{M} and $\mathbf{A} \cdot \mathbf{M}^T \cdot \hat{\mathbf{A}}^{-1}$, i.e. the premultiplication by matrix $\mathbf{A} \cdot \mathbf{M}^T \cdot \hat{\mathbf{A}}^{-1} \cdot \mathbf{M}$, creates an endomorphism^{66b} of the A -space.

4.4.1 Time evolution of the system

Consider a system consisting of n states. For this system the square matrix \mathbf{K} , whose elements are formed from the rate constants for transitions from state to state, is known. It is preferable to work with the symmetric rate constant matrix¹⁰² \mathbf{K}_s . The symmetrization of the rate constant matrix \mathbf{K} is straightforward when the equilibrium vector $\mathbf{P}^{\text{eq}} \equiv \mathbf{P}(\infty)$ for this matrix is known. The equilibrium vector is calculated with help of an iterative process [Eq. (4.13)]. If the equilibrium vector is known, the symmetric matrix \mathbf{K}_s can be calculated as a weighted – by the equilibrium vector – average of the two rate constants for the forward and backward transition:

$$k_{s,ij} = \frac{\left(\frac{P_i^{\text{eq}}}{P_j^{\text{eq}}}\right)^{1/2} k_{i \rightarrow j} + \left(\frac{P_j^{\text{eq}}}{P_i^{\text{eq}}}\right)^{1/2} k_{j \rightarrow i}}{2} \quad (4.26)$$

Note that the two terms being averaged in Eq. (4.26) should be equal, if the condition of microscopic reversibility $k_{ij} \cdot P_i(\infty) = k_{ji} \cdot P_j(\infty)$ is strictly obeyed. With the symmetric rate constant matrix \mathbf{K}_s known, the time evolution of the system is calculated by solving the corresponding master equation (see also Eq. (3.1)):

$$\frac{\partial \tilde{\mathbf{P}}(t)}{\partial t} = \mathbf{K}_s \cdot \tilde{\mathbf{P}}(t) \quad (4.27)$$

with the reduced probabilities being defined as $\tilde{P}_i(t) = P_i(t) / \sqrt{P_i(\infty)}$ (see Ref. 29b). The diagonalization of the symmetric matrix \mathbf{K}_s lets this matrix to be expressed as a product of three different matrices:

$$\mathbf{K}_s = \mathbf{V} \cdot \mathbf{D} \cdot \mathbf{V}^{-1} \quad (4.28)$$

where matrix \mathbf{V} is of dimension $n \times n$ and has as columns the eigenvectors of matrix \mathbf{K}_s , whereas matrix \mathbf{D} is a $n \times n$ diagonal matrix with diagonal elements the (non-positive) eigenvalues of matrix \mathbf{K}_s appearing in the same sequence as the eigenvectors in matrix \mathbf{V} . According to the above, the solution of Eq. (4.27) is written as:

$$\tilde{\mathbf{P}}(t) = \tilde{\mathbf{P}}(0) \cdot \exp(\mathbf{K}_s \cdot t) = \tilde{\mathbf{P}}(0) \cdot \exp[(\mathbf{V} \cdot \mathbf{D} \cdot \mathbf{V}^{-1}) \cdot t] \quad (4.29)$$

The exponential of a matrix can be calculated as follows:

$$\left. \begin{aligned} \exp(\mathbf{K}_s \cdot t) &= \sum_{x=0}^{\infty} \frac{1}{x!} \cdot (\mathbf{K}_s \cdot t)^x \\ \mathbf{K}_s &= \mathbf{V} \cdot \mathbf{D} \cdot \mathbf{V}^{-1} \end{aligned} \right\} \Rightarrow \exp(\mathbf{K}_s \cdot t) = \sum_{x=0}^{\infty} \frac{1}{x!} \cdot (\mathbf{V} \cdot \mathbf{D} \cdot \mathbf{V}^{-1})^x \cdot t^x \quad (4.30)$$

However:

$$(\mathbf{V} \cdot \mathbf{D} \cdot \mathbf{V}^{-1})^x = (\mathbf{V} \cdot \mathbf{D}^x \cdot \mathbf{V}^{-1}) \quad (4.31)$$

and hence Eq. (4.30) gives:

$$\exp(\mathbf{K}_s \cdot t) = \sum_{x=0}^{\infty} \frac{1}{x!} \cdot (\mathbf{V} \cdot \mathbf{D}^x \cdot \mathbf{V}^{-1}) \cdot t^x \quad (4.32)$$

Matrix \mathbf{V} and therefore matrix \mathbf{V}^{-1} do not depend on x . Hence Eq. (4.32) can be written as:

$$\left. \begin{aligned} \exp(\mathbf{K}_s \cdot t) &= \mathbf{V} \cdot \sum_{x=0}^{\infty} \frac{1}{x!} \cdot (\mathbf{D} \cdot t)^x \cdot \mathbf{V}^{-1} \\ \sum_{x=0}^{\infty} \frac{1}{x!} \cdot (\mathbf{D} \cdot t)^x &= \exp(\mathbf{D} \cdot t) \end{aligned} \right\} \Rightarrow \exp(\mathbf{K}_s \cdot t) = \mathbf{V} \cdot \exp(\mathbf{D} \cdot t) \cdot \mathbf{V}^{-1} \quad (4.33)$$

According to Eq. (4.33), Eq. (4.29) gives:

$$\tilde{\mathbf{P}}(t) = \tilde{\mathbf{P}}(0) \cdot \mathbf{V} \cdot \exp(\mathbf{D} \cdot t) \cdot \mathbf{V}^{-1} \quad (4.34)$$

Eq. (4.34) describes the time evolution of the probability of the various states adopted by the system. However, Eq. (4.34) gives rise to a serious computational problem. Specifically, the inverse of the eigenvector matrix \mathbf{V}^{-1} is – for large systems – very difficult to calculate correctly. This justifies our choice to work with the symmetric rate constant matrix \mathbf{K}_s , instead of \mathbf{K} . For a real, symmetric matrix, the matrix of eigenvectors resulting by its diagonalization is orthogonal¹⁰¹. Therefore, matrix \mathbf{V} is orthogonal. An important property is that the inverse of an orthogonal matrix is equal to its transpose, i.e.:

$$\mathbf{V}^{-1} = \mathbf{V}^T \quad (4.35)$$

This makes the calculation of \mathbf{V}^{-1} trivial. Eq. (4.34) takes the final form:

$$\tilde{\mathbf{P}}(t) = \tilde{\mathbf{P}}(0) \cdot \mathbf{V} \cdot \exp(\mathbf{D} \cdot t) \cdot \mathbf{V}^T \quad (4.36)$$

It is worth mentioning that the calculation of the exponential of the matrix of eigenvalues \mathbf{D} is straightforward if the following property, which applies for diagonal matrices, is taken into consideration:

$$\exp(\mathbf{D}t) = \begin{bmatrix} e^{D_{11}t} & 0 & 0 & \dots & 0 \\ 0 & e^{D_{22}t} & 0 & \dots & 0 \\ 0 & 0 & e^{D_{33}t} & \dots & 0 \\ \dots & \dots & \dots & \dots & \dots \\ 0 & 0 & 0 & \dots & e^{D_{nn}t} \end{bmatrix} \quad (4.37)$$

In equation (4.36) all parameters are either known, or directly calculable. With the help of equation (4.37) the reduced probabilities $\tilde{\mathbf{P}}(t)$ are calculated for different, successive times t . With the help of equation $\tilde{P}_i(t) = P_i(t) / \sqrt{P_i(\infty)}$ it is straightforward to calculate the corresponding probability distribution $\mathbf{P}(t)$ among all states for the initial system for different times t . The methodology as described above refers to the initial, non-lumped system and describes the route OT in Fig. 4.7. In a similar way it is applied to the lumped system, a process which corresponds to route RQ in Fig. 4.7. Here the role of \mathbf{K} is played by the rate matrix of the lumped system $\hat{\mathbf{K}}$, which is known. This matrix results from the rate constant matrix of the initial system \mathbf{K} through lumping.

4.4.2 Lumping

Unlike the calculation of the time evolution of the system, for which the structure is similar for both routes of Fig. 4.7 (OT and RQ), the process of lumping is applied differently for each of the two routes of Fig. 4.7 (OR and TQ). Specifically, for the route OTQ of Fig. 4.7, lumping is implemented upon the already calculated probability distribution of the initial system $\mathbf{P}(t)$:

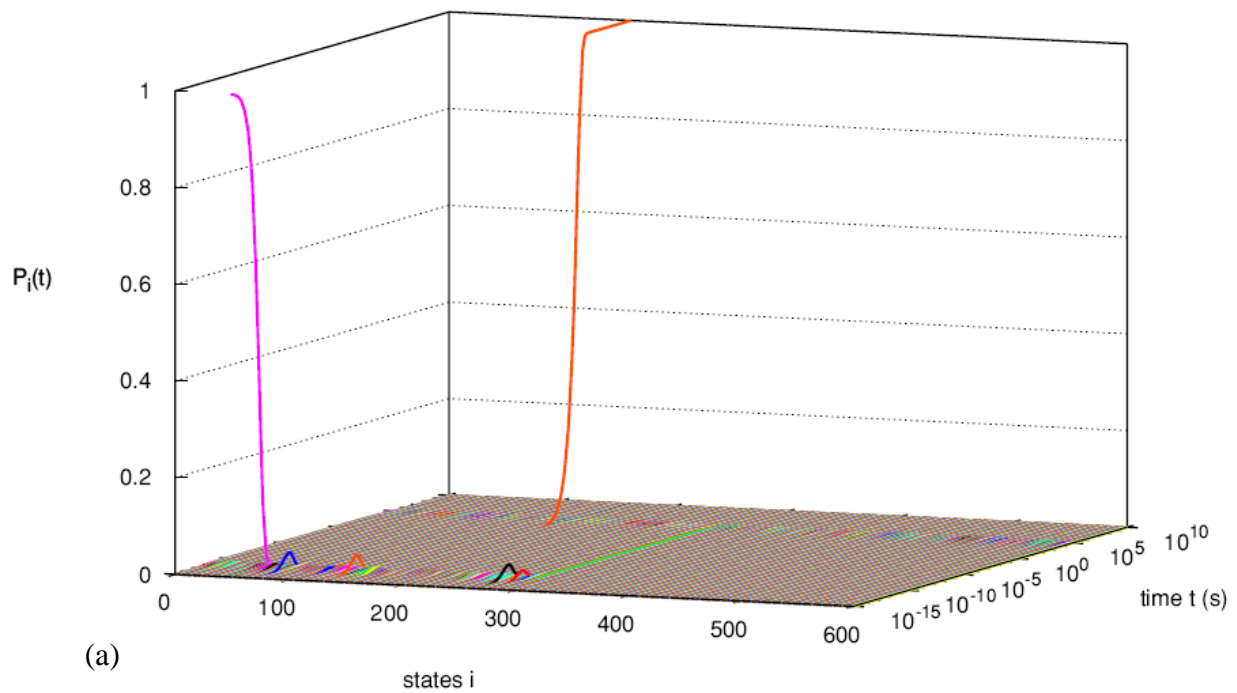
$$\hat{\mathbf{P}}(t) = \mathbf{M} \cdot \mathbf{P}(t) \quad (4.38)$$

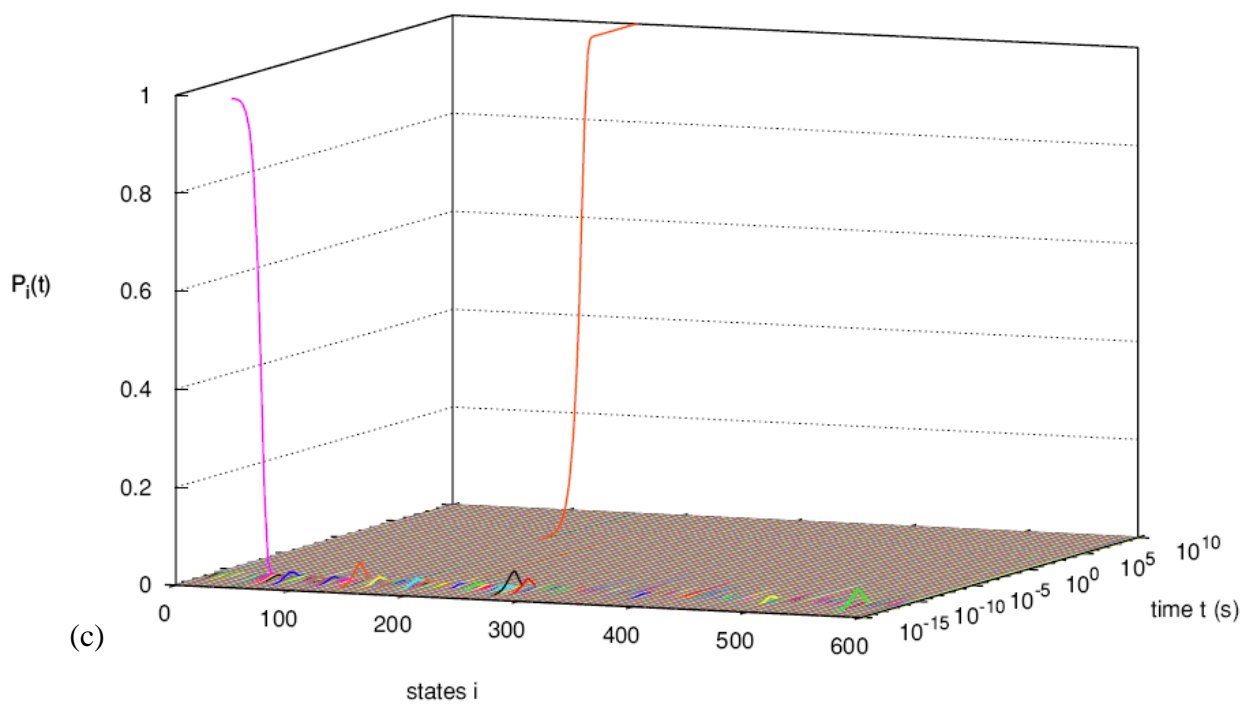
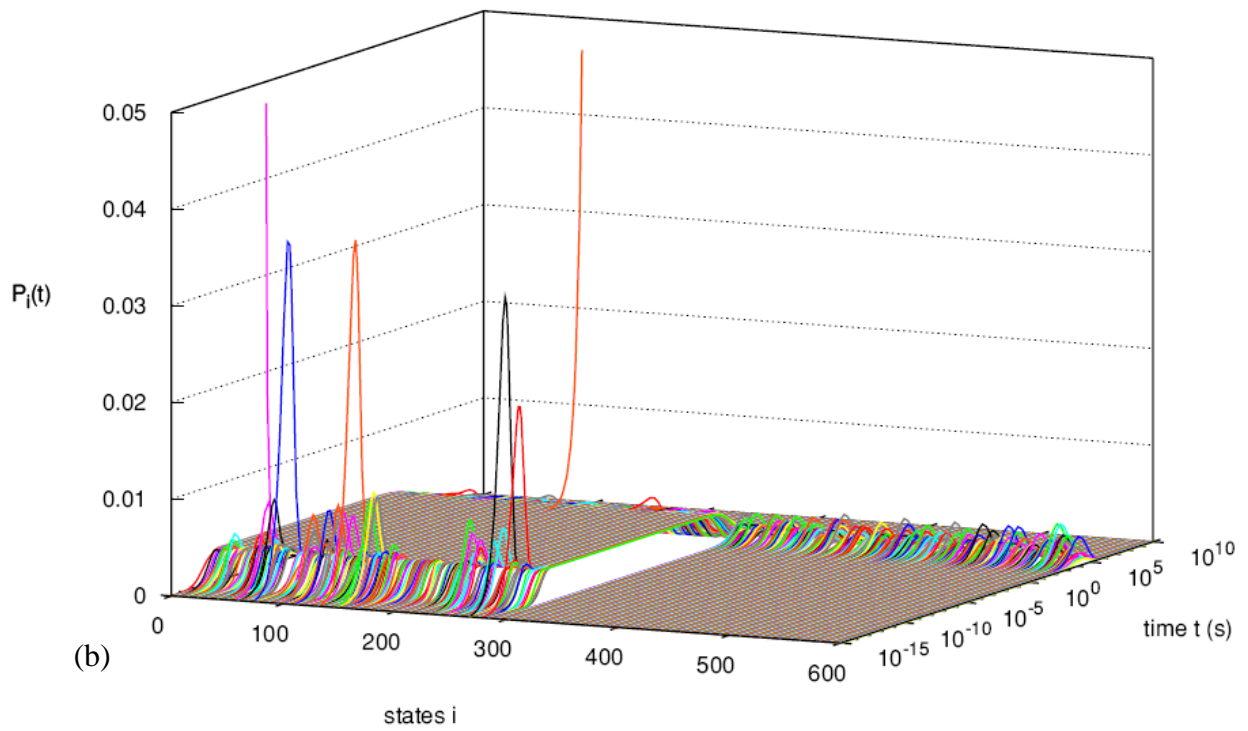
Here the probability density $\mathbf{P}(t)$ is calculated during the previous step of time evolution of the original system (path OT), as described in Section 4.4.1. Matrix \mathbf{M} has to be known for the implementation of lumping, Eq. (4.38). For the route ORQ of Fig. 4.7, lumping takes place first (path OR). The initial rate constant matrix \mathbf{K} is lumped to the corresponding matrix of the lumped system $\hat{\mathbf{K}}$:

$$\left. \begin{aligned} \hat{\mathbf{K}} &= \mathbf{M} \cdot \mathbf{K} \cdot \mathbf{A} \cdot \mathbf{M}^T \cdot \hat{\mathbf{A}}^{-1} \\ \hat{\mathbf{A}} &= \mathbf{M} \cdot \mathbf{A} \cdot \mathbf{M}^T \end{aligned} \right\} \Rightarrow \hat{\mathbf{K}} = \mathbf{M} \cdot \mathbf{K} \cdot \mathbf{A} \cdot \mathbf{M}^T \cdot (\mathbf{M} \cdot \mathbf{A} \cdot \mathbf{M}^T)^{-1} \quad (4.39)$$

With the known matrix \mathbf{M} , the diagonal matrix \mathbf{A} , whose diagonal elements are the elements of the equilibrium vector of matrix \mathbf{K} , is calculated via Eq. (4.13). As soon as matrix $\hat{\mathbf{K}}$ is calculated, the time evolution of the lumped system is followed as described in Section 4.4.1.

After executing all of the above, the time evolution of the probability distribution for every lumped state is obtained for both routes (OT-TQ and OR-RQ in Fig. 4.7). The result of this calculation is shown in Fig. 4.8:





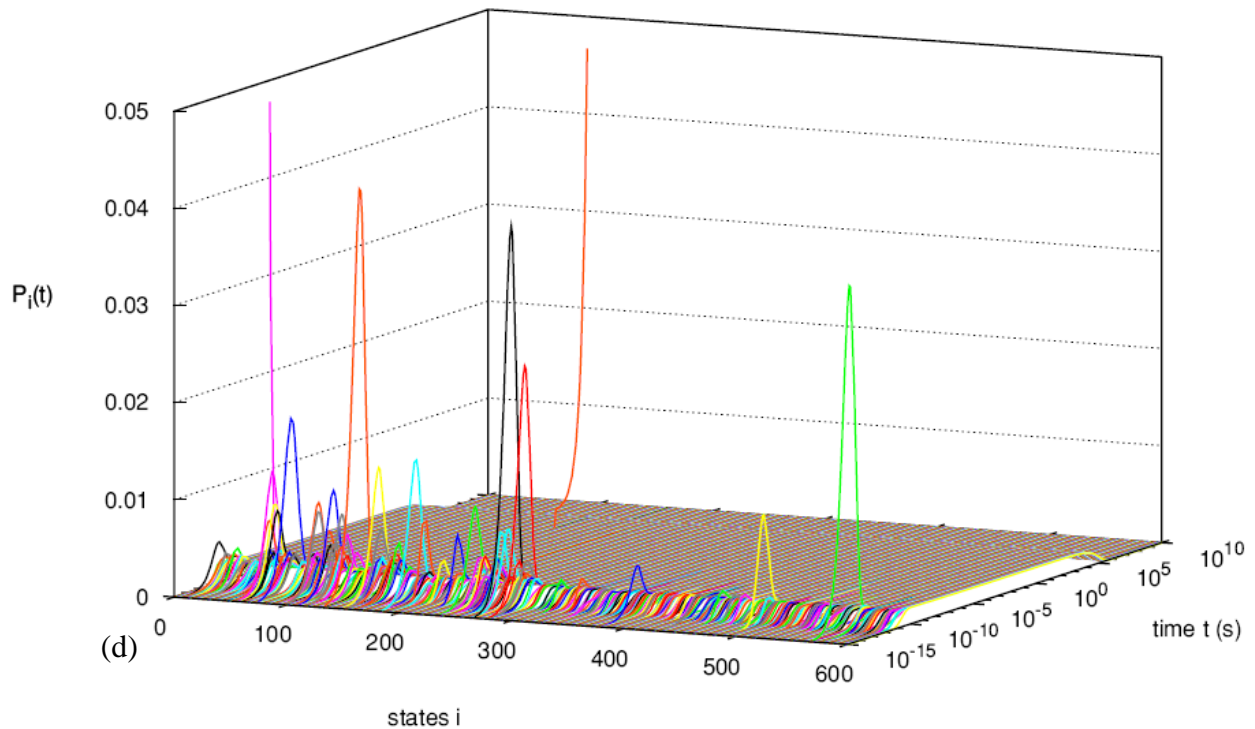
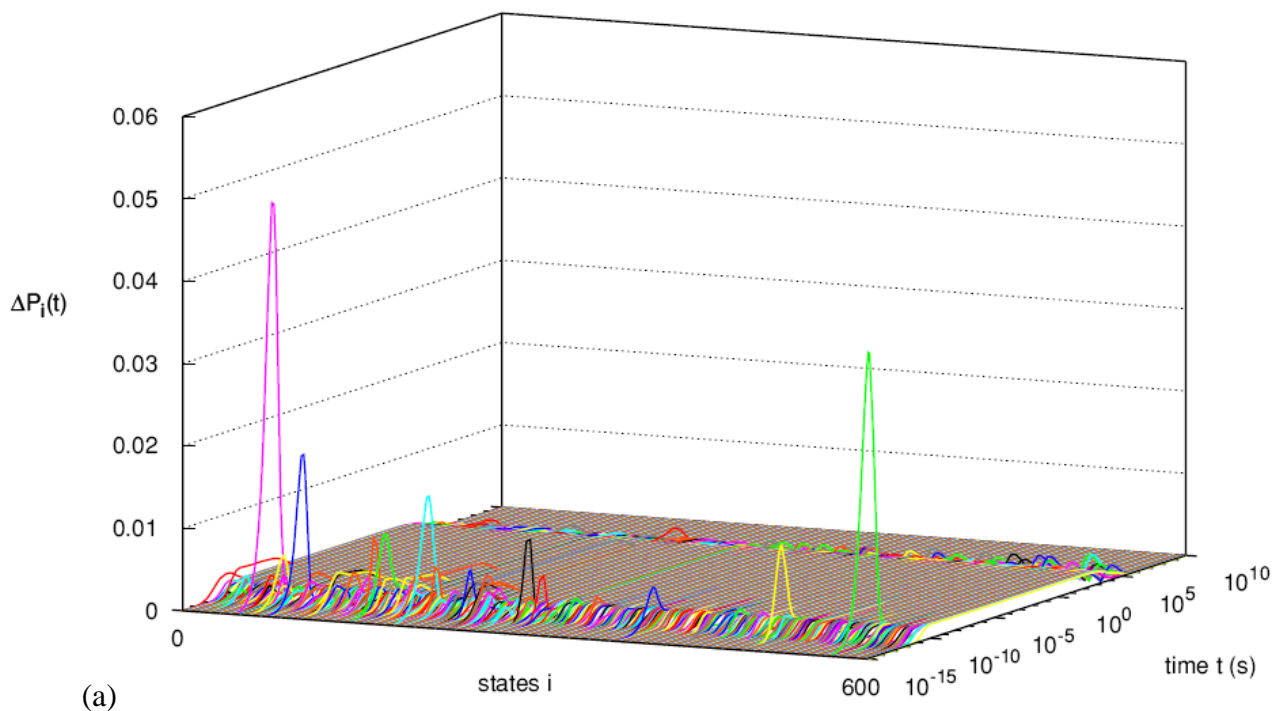


Figure 4.8: Representation of the probability distribution $P_i(t)$ as a function of time t for every cluster i of the lumped system ($i=1, 2, \dots, \hat{n}$ with $\hat{n} = 600$), computed along (a) path OTQ in Fig. 4.7 (evolving and then lumping) and (b) detail of the same path OTQ, focusing on low probability values (c) path ORQ (lumping and then evolving), and (d) detail of the same path ORQ, focusing on low probability values. Each colored line corresponds to a different cluster (lumped state) in all plots.

In the calculation of Fig. 4.8 we give an arbitrarily chosen cluster of states an initial occupancy probability of 1 at $t=0$, while all other clusters are empty (delta function initial condition). Thereafter we let the system evolve in time and monitor the probability distribution among lumped states. A direct comparison between Figs. 4.8(a) and 4.8(c) (or, in more detail, Figs. 4.8(b) and 4.8(d)) shows that the two different routes to calculate the probability distribution (Fig. 4.7) converge to similar results at all time scales. This becomes evident in Fig. 4.9(a), where the absolute difference between Fig. 4.8(a) and 4.8(c) is plotted. Figs. 4.8(a) and 4.8(c) do not make evident the details of the evolution over intermediate times. In fact, one has the impression that, for intermediate times, the probability distribution decays to zero for all clusters.

This, of course, cannot be true, since the probability plotted in Fig. 4.8 is normalized and hence the total probability equals unity at all times. In fact, Figs. 4.8(b) and 4.8(d) show that, at intermediate times, every cluster has a small, non-zero probability. The initial, dominant probability which a cluster had at small times is being distributed via infrequent transitions to every other cluster of the system, and this “diffusive” process remains active over a wide range of time scales. For long times, a dominant cluster (the same one between routes OTQ and ORQ of Fig.4.7) absorbs all the probability, while the occupancy probability of all the other clusters decays to practically zero. Of course, at long times compared to the negative inverse of the largest nonzero eigenvalue of $\hat{\mathbf{K}}$, one expects the probability of every cluster to become constant and equal to the equilibrium probability for the considered set of states.



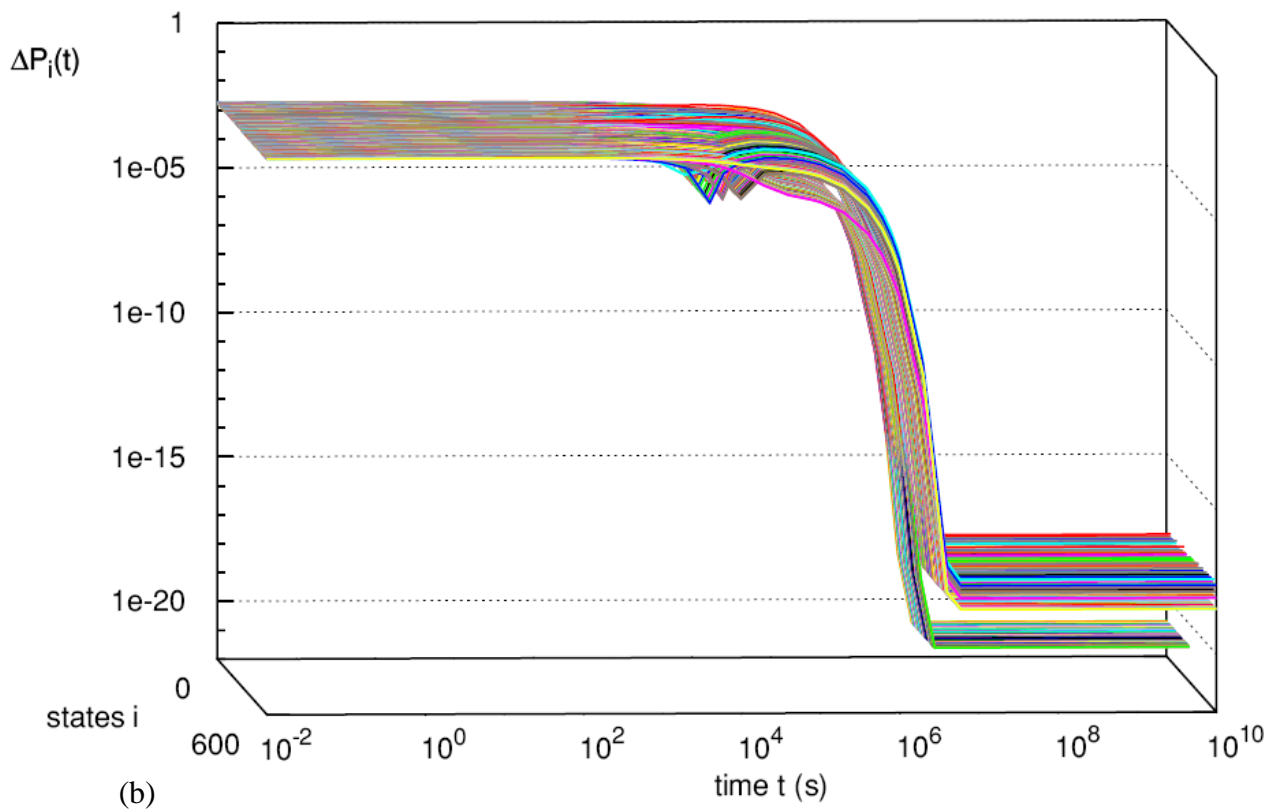


Figure 4.9: Absolute difference of the time-dependent probabilities for every cluster of the lumped system between routes OTQ and ORQ of Fig. 4.7 for (a) all time scales and (b) long time scales. Each colored line corresponds to a different cluster (lumped state) in all plots.

Fig. 4.9(b) shows that there is no important difference introduced by lumping with respect to the system's long-time dynamics. This means that the two routes depicted in Fig. 4.7 converge to the same dynamical result. This provides a strong indication that the lumping algorithm has successfully calculated the appropriate transformation matrix \mathbf{M} to perform lumping. This conclusion is strengthened by the similarity between the histogram of the logarithm of the negative inverse eigenvalues $-\frac{1}{\lambda_i}$ for both the initial (matrix \mathbf{K}) and the lumped (matrix $\hat{\mathbf{K}}$) system (Fig. 4.10). According to Fig. 4.10, the dynamical behavior for both initial and lumped system is similar, since the distributions of the highest nonzero eigenvalues for these two systems are nearly identical. This is clear evidence that the lumped system, although of smaller

dimensionality, is in a position to describe well the long-time dynamics of the original system.

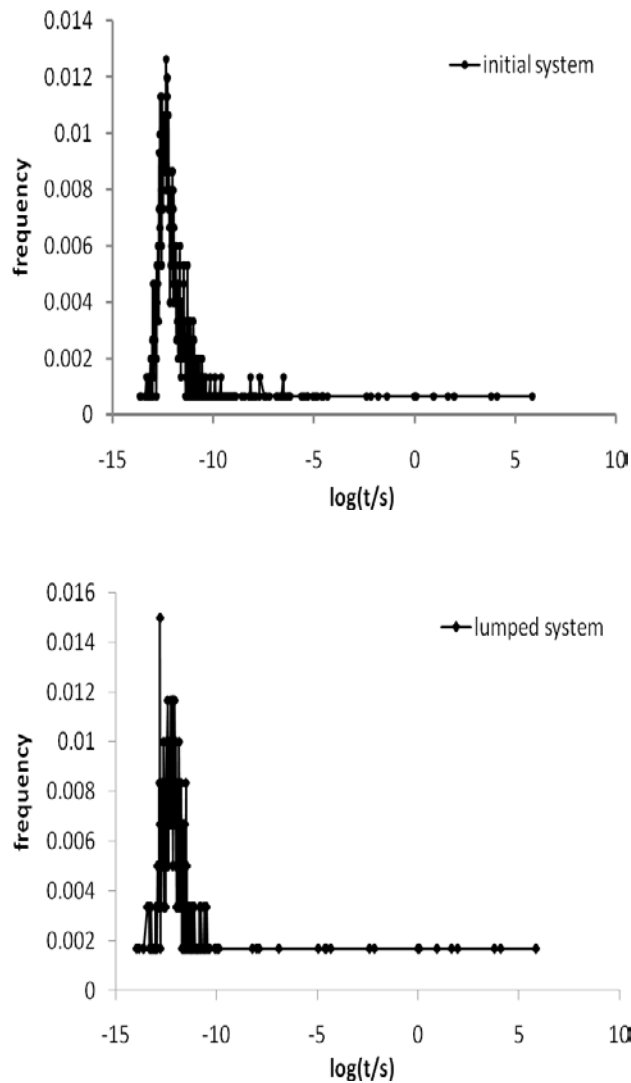


Figure 4.10: Histogram of the negative inverse eigenvalues for (a) the initial system and (b) the lumped system. The abscissa represents the characteristic times, in seconds, calculated by inverting the negative eigenvalues of the two systems. The ordinate describes the probability density of the corresponding eigenvalues. There are $n = 1503$ eigenvalues in (a) and $\hat{n} = 600$ eigenvalues in (b).

Fig. 4.10 clearly shows the wide spectrum of characteristic times which governs dynamics in our model glassy system. There are characteristic times which differ from

each other by more than twenty orders of magnitude. The longest times have been accessed thanks to the specially designed infrequent event techniques described in Ref. ⁵⁶. By comparing Fig. 4.10(a) and (b) we see that the very tails of the two distributions are identical. This can also be seen in Table 4.3, which compares the 10 largest nonzero eigenvalues of the two systems:

Table 4.3: Comparison of the ten largest nonzero eigenvalues between the initial and the lumped system.

Initial system λ_i [s ⁻¹]	Lumped system λ_i [s ⁻¹]
-1.396×10^{-6}	-1.399×10^{-6}
-7.812×10^{-5}	-7.724×10^{-5}
-0.0001597	-0.0001613
-0.01076	-0.01076
-0.02142	-0.02120
-0.1136	-0.1138
-0.8497	-0.8557
-0.9960	-1.004
-65.35	-144.65
-144.6	-252.2

The remaining 590 eigenvalues of $\hat{\mathbf{K}}$ are supposed to mimic what the remaining 1493 eigenvalues of \mathbf{K} do. A quantitative comparison is difficult, but the overall shapes of the distributions of eigenvalues shown in Figure 4.10 compare favorably between original and lumped descriptions. Important differences between the distributions of eigenvalues of Fig. 4.10 arise in the region 10^{-10} to 10^{-2} s. This can also be seen in

Figures 4.8(b) and 4.8(d), and also in Fig. 4.9(a), where the absolute difference between the time evolutions of the original and the lumped systems is plotted. We see that the biggest differences appear in this region of time. This is logical, since lumping always causes a certain information loss. The biggest gain of this methodology is that we manage to constrain this information loss in a time-region which is not important to long-time dynamics. The developed methodology provides a way to accurately reproduce long-time dynamics of the initial system.

4.5 Conclusions

In this Chapter we have described a lumping algorithm for dynamical systems that are capable of adopting discrete states. The evolution of the system is assumed to occur through elementary transitions between the states obeying a first order kinetic scheme, governed by rate constants that are known, e.g., from atomic-level infrequent event analysis. Through lumping, the network of states and the corresponding master equation are mapped onto a network of clusters and a master equation of reduced dimensionality. Each cluster consists of a set of states of the original system among which transitions are relatively facile, such that local equilibration within the cluster is achieved over times short relative to the escape time from the cluster. A basic requirement is that original and lumped systems exhibit similar long-time dynamics.

Our algorithm is fully automated, requiring as sole input the rate constant matrix of the original system. It approximates the best lumping scheme with respect to three different lumping criteria: the lumping error E , which indicates how close to exact lumpability the implemented lumping is; the long-time dynamics parameter W , which places emphasis on the long-time dynamics of the lumped system; and the size (number of clusters) of the lumped system \hat{n} . The dimensionality of the network of lumped states can be *a priori* controlled. Conventional molecular simulation techniques are very limited in their ability to reach realistic experimental time scales and therefore record corresponding structural relaxation phenomena. In contrast to these, the lumping scheme proposed here enables monitoring long-time relaxation phenomena of glassy materials by tracking the dynamical response of a network of substantially smaller dimensionality than the full network of basins. This rigorous

treatment of the lumping problem differentiates our work from previous lumping work on energy landscapes.

The transformation matrix \mathbf{M} implementing the lumping is optimized through a stochastic scheme. This scheme is based on two successive sets of Monte Carlo (MC) simulations inspired by the Wang-Landau density of states algorithm. The first set of MC simulations aims at determining the density of \mathbf{M} -“microstates” in the three-dimensional space spanned by E , W , and \hat{n} . The second set of MC simulations utilizes this density of microstates to induce preferential sampling of \mathbf{M} that yield low values of E , W , and \hat{n} .

After verifying the developed algorithm for a number of chemical reaction networks of small dimensionality found in the literature, for which the \mathbf{M} -matrix for exact lumping is known, we have implemented our lumping methodology to a glassy binary Lennard-Jones system of 641 particles at temperature $T = 0.308\varepsilon_{AA} / k_B = 37\text{K}$ and molecular density $1.1908 \sigma_{AA}^{-3} = 3.03 \times 10^{28} \text{ m}^{-3}$, slightly below its glass temperature $T_g = 38.4 \text{ K}$ and about 15 K below its critical mode-coupling temperature $T_c = 52.2 \text{ K}$. A network of $n = 1503$ states was considered for this system, each state corresponding to a basin surrounding a local minimum of the potential energy (inherent structure) in 1920-dimensional configuration space. The connectivity and rate constants between states in this network have been determined through atomistic infrequent-event analysis, hence the rate constant matrix of the original system is known.

The lumped system obtained through application of our method is of smaller dimensionality, $\hat{n} = 600$, and could be further lumped to an even smaller one by attributing different weights to the three lumping criteria. By monitoring the temporal evolution of the probability of occupancy for all states in the lumped system, we concluded that the calculated transformation matrix \mathbf{M} is in a position to capture the long-time dynamics of the original system very well. Evolving the dynamics of the lumped system yielded a very similar distribution among lumped states as evolving the dynamics of the original system followed by lumping. The importance of the algorithm developed lies in the fact that every network of states, in which evolution is described through a master equation with rate constants conforming to first-order kinetics, as one typically obtains from detailed infrequent event analysis of interstate transitions, can be

reduced to an equivalent network of considerably smaller dimensionality, which is still capable of describing the long-time dynamics of the initial system. Furthermore, as pointed out in Section 4.4, the evolution of the lumped system can be mapped back to the original system description, if desired.

Chapter 5

Temporal evolution on the potential energy landscape

In the previous chapter a self-consistent algorithm has been presented, thoroughly tested and applied for coarse-graining the dynamics of a system evolving in time through a succession of infrequent transitions in configuration space. The system starts off within a confined region of phase space (e.g., a basin of the PEL in which it has been trapped by glass formation). As time elapses, its probability distribution among basins of the PEL expands according to rate constants for interbasin transitions computed from detailed atomistic information. At long times, neighboring basins communicating through relatively fast transitions are lumped into metabasins, allowing a drastic reduction in the number of states that need to be considered. One way to graphically represent the PEL has been introduced in Figure 3.2, but is clearly not applicable for systems whose configuration space has a dimensionality higher than 2.

In this chapter, an alternative graphical representation of the PEL is developed and applied to a binary Lennard-Jones glassy system, providing insight into the unique topology of the system's potential energy hypersurface. With the help of this representation one is able to monitor the different explored basins of the PEL, as well as how – and mainly when – subsets of basins communicate with each other via transitions in such a way that details of the prior temporal history have been erased, i.e., local equilibration between the basins in each subset has been achieved and the hopping process can be safely enough assumed to obey Poisson statistics. In this way, apart from detailed information about the structure of the PEL already provided by conventional PEL representations such as the one shown in Figure 3.2, the system's

temporal evolution on the PEL is described. In order to gather all necessary information about the identities of two or more basins that are connected with each other, we consider two different approaches. The first one is based on consideration of the time needed for two basins to mutually equilibrate their populations according to the transition rate between them, in the absence of any effect induced by the rest of the landscape. The second approach is based on an analytical solution of the master equation (as described through Eqs. (4.27) to (4.37) for the lumped system) that explicitly takes into account the entire explored landscape. We see that both approaches lead to the same result concerning the topology of the PEL and dynamical evolution on it. Following this approach for graphically representing the PEL, a “temporal disconnectivity graph” is introduced to represent a lumped system stemming from the initial one. The lumped system is obtained via the specially designed algorithm described in Chapter 4. The temporal disconnectivity graph provides useful information about both the lumped and the initial systems, including the definition of “metabasins” as collections of basins that communicate with each other via transitions that are fast relative to the observation time. Finally, the two examined approaches are compared to an “on the fly” molecular dynamics-based algorithm for the definition of metabasins on the PEL⁵⁶.

5.1 Introduction

A better understanding of the structural details of the PEL of molecular systems is of great importance, not only because the PEL is undeniably connected to the calculation of both thermodynamic and dynamical behavior¹⁰⁵, but principally because a visual representation of the topology and geometry of the PEL can provide insight into physical phenomena that shape dynamical and equilibrium properties¹⁰⁶. The emergence of seminal ideas¹⁰⁷ concerning the study of the PEL and the possibility of using its characteristics to extract conclusions about physical properties^{59d, 108}, along with the pioneering work of Stillinger and Weber on describing, using molecular dynamics (MD) simulation with the help of a mapping procedure, the multimimum PEL of large systems^{58a}, set the stage for a wide range of applications in a large variety of systems^{59c, 109}.

The PEL is a multi-dimensional surface, on which the dependence of the system's potential energy on the coordinates of the atoms or molecules is depicted^{78, 110}. Because of the complexity of this hypersurface, associated with the large number of degrees of freedom it entails, some basic characteristics are used in order to describe it. The most commonly used notions are basins, potential energy minima, and saddle points, through which minima are connected. These terms will be used throughout this chapter and have the physical meaning given to them in chapter 3

The exploration of an ever expanding network of basins (or inherent structures) communicating via transitions provides a “mapping” of the PEL. For most materials or biomolecular systems, this exploration out to experimentally relevant times is a formidable problem. Tsalikis et al.⁶² have calculated the rate constants of transitions sampled via their temperature accelerated dynamics/histogram reweighting scheme in a Lennard-Jones mixture. They have correlated these rate constants with the distance traversed in configuration space and with the cooperativity of the transitions. Following this methodology, the rate constant matrix for the transitions between the explored ISs can be calculated. The connectivity between explored ISs and the rate constants of transitions between them suffice for a description of the temporal evolution of the system towards equilibrium by use of the master equation approach¹⁰⁰. This description is greatly helped by the fact that infrequent transitions in the network of basins constitute a Poisson process.

Via application of the DIMW methodology (a process which will be thoroughly described in Chapter 6), Boulougouris and Theodorou⁵² used multidimensional transition state theory within the harmonic approximation combined with the dimer saddle-point search method^{80c} in order to evaluate rate constants for transitions out of ISs of a glassy system being explored on the fly. As already mentioned in Section 3.3, the rugged potential energy landscape of glass-forming systems gives rise to a very broad distribution of characteristic times for elementary transitions and a complex connectivity among basins. This broad distribution of characteristic times is intimately related to the broad distribution of barrier heights observed in PELs of glassy materials. This observation makes clear that it is impossible to build a complete map of all basins and transitions between them in the rugged potential energy landscape of a glassy system even of modest size n .

A way out of this difficulty is provided by the fact that, when one studies structural relaxation, one typically starts from an initial distribution among states that is highly localized (e.g. from a single basin in the potential energy landscape, where the system was trapped via the glass formation history that was followed to obtain it). The region of configuration space where the system resides is thus initially very confined, and expands gradually as transitions between basins take place. Despite the facilitation provided by the above methodology, an additional difficulty with PEL-exploring approaches may arise. In particular, the number n of states to be tracked becomes prohibitively large at long times. A way to tackle this problem is to group, or “lump,” states communicating via transitions that are fast in relation to the observation time into single clusters of states. If performed judiciously, this lumping does not result in loss of essential information, as evidently shown in Chapter 4. At long observation times, the system distributes itself among fast-communicating states according to the requirements of a restricted equilibrium, so clusters of such states behave as single “meta-states,” for all practical purposes.

Given the complexity and high dimensionality of the PEL, simplified graphical representations of it have proven to be a constructive tool. A major step in this direction, inspired by graph theory, was undertaken by Becker and Karplus^{105b}, who introduced the disconnectivity graph. This graph has been developed and applied extensively to a wide variety of problems by Wales and collaborators^{59d, 85, 108}. The general shape and form of disconnectivity graphs have been reviewed^{85, 105b, 111}. Nevertheless, it is wise to address here some basic characteristics of this kind of graphs. In Figure 5.1 the basic form of a disconnectivity graph is represented.

The interpretation of a disconnectivity graph is the following: All branches of the “inverted tree” in a disconnectivity graph correspond to kinetic transitions and terminate at local minima of the energy (inherent structure) described in Figure 1 as the lowest lying open symbols (at the level E_1 or T_1). Relative energies (or temperature levels) can be read off on the vertical axis. All the tips of branches above the first level ($E > E_1$ or $T > T_1$) of the “inverted tree” describe sets of basins, grouped with each other based on the relatively fast transitions between them. The energy (or temperature) level shown in the graph, describing the energy level of the entire group

of basins, corresponds to the lowest lying saddle point that must be traversed to establish communication among all basins being grouped.

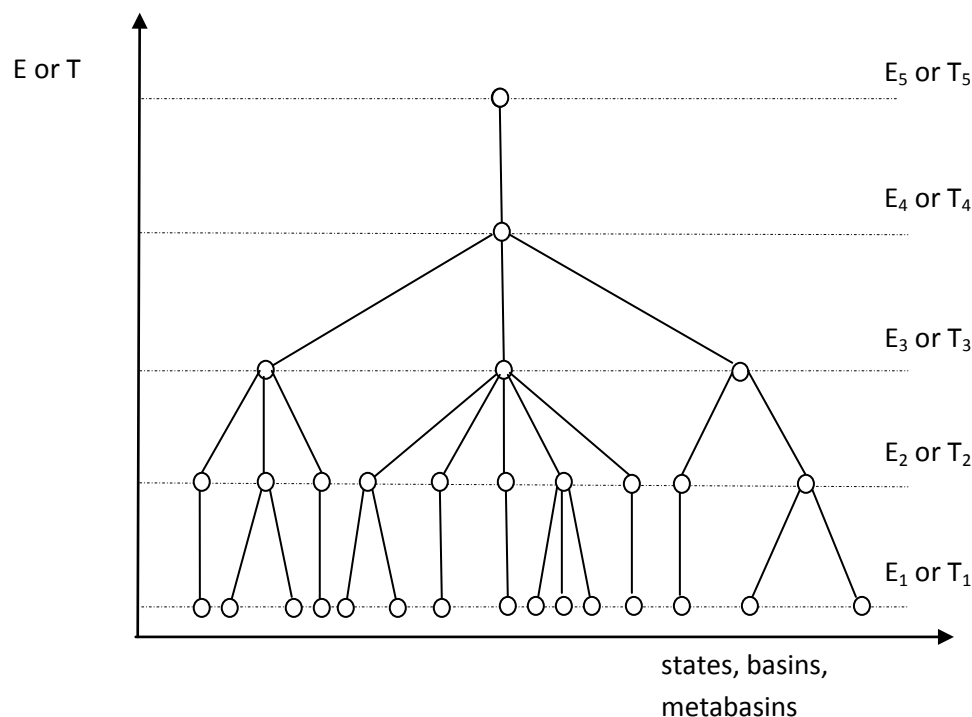


Figure 5.1: Schematic representation of a typical disconnectivity graph. The y-axis can represent either energy or temperature levels. The x-axis describes the several fast communicating basins connected by low barriers grouped into metabasins of a higher energy or temperature level, which in turn merge into meta-metabasins at an even higher energy or temperature level.

In Figure 5.1, for clarity, nodes in each generation are depicted as belonging to the same energy level (nodes lying on the same horizontal line). This is, of course, a simplification, since energy levels of different basins and of the saddle points between them are generally different. In respect to the participating basins (\mathbf{x} -axis), each node depicts a group of relatively fast-communicating basins. In other words, a node (e.g. at energy level E_3) created from two nodes of a lower energy level (e.g. E_2) corresponds to a meta-structure (metabasin) containing all basins of the two united nodes. In this way, at every energy level (except the lowest one) one has “metabasins” consisting of basins. In turn, metabasins are connected to form meta-metabasins and so on. From the “willow tree” appearance^{108a} of the graph it is clear if there are sets of basins (“metabasins”) communicating through relatively fast transitions, sets of metabasins

communicating through slower transitions etc., i.e., the potential energy landscape exhibits a hierarchical structure.

In order to represent a certain PEL, knowledge of a certain network of states (ISs, basins or metabasins) is a prerequisite.

In the present chapter we attempt a synthesis between the master equation solution-based description of the dynamics of systems evolving on rugged potential energy hypersurfaces, lumping, the definition of metabasins, and disconnectivity graphs. We develop and present a “temporal” disconnectivity graph, in which rate constant-based local equilibration times between “states” (basins and metabasins) are used in place of energies. We examine several ways in which these times can be computed, each way entailing a different computational cost, and find internal consistency among them. Furthermore, we will show that the grouping into metabasins achieved by the disconnectivity graph presented here arises naturally from the systematic procedure of lumping mentioned in Chapter 4. The system whose PEL we explore is a binary Lennard-Jones mixture extensively described in Section 3.4 of this work that has constituted the “drosophila” of computational studies of glass-forming systems. All results presented in this chapter have been obtained by post-processing the network of states acquired through temperature accelerated dynamics/histogram reweighting by Tsalikis et al.⁶².

Paragraph 5.2 of this chapter reviews some theoretical concepts associated with the master equation and its solution and explains our computational methodology. Some computational details are elaborated in Section 5.3. Results are presented, validated and discussed in Section 5.4 and conclusions summarized in Section 5.5.

5.2 Graphical representation of the PEL: A new approach

As already mentioned in Section 3.1, the master equation is a system of differential equations describing the temporal evolution of the probabilities of occupying states in a Markovian system. The time-dependent observed value of any property \mathcal{A} that is only a function of the state can be expressed as an ensemble average $\langle \mathcal{A} \rangle$ using the solution of that differential equation under given initial conditions on the state

occupancy probabilities. According to Eqs. (3.1) and (3.2), the master equation can be written in terms of the conditional probabilities $P_{\tau=0,i \rightarrow \tau=t,j}$ for the system to be in a certain state (in our case, basin or metabasin) j at time $\tau=t$, provided it was in a different state i at time $\tau=0$. In terms of these probabilities and the above formalism a more general form of master equation occurs:

$$\frac{\partial P_{\tau=0,i \rightarrow \tau=t,j}}{\partial t} = \sum_{m \neq j} P_{\tau=0,i \rightarrow \tau=t,m} \cdot k_{m \rightarrow j} - P_{\tau=0,i \rightarrow \tau=t,j} \cdot \sum_{m \neq j} k_{j \rightarrow m} \quad (5.1)$$

The rate constant $k_{m \rightarrow j}$ is the probability per unit time that a transition from state m to state j will occur. This is independent of time by virtue of the time scale separation that makes exiting state m an infrequent event and imparts a Markovian character to the process. Summing over i on both sides of Eq. (5.1), one obtains a simpler master equation in terms of the probabilities $P_j(t) = \sum_i P_{\tau=0,i \rightarrow \tau=t,j}$ for the system to be in state j at time τ , regardless of its original state:

$$\frac{\partial P_j}{\partial t} = \sum_{m \neq j} P_m \cdot k_{m \rightarrow j} - P_j \cdot \sum_{m \neq j} k_{j \rightarrow m} \quad (5.2)$$

or, in matrix form,

$$\frac{\partial \mathbf{P}}{\partial t} = \mathbf{K} \cdot \mathbf{P} \quad (5.3)$$

where \mathbf{K} is the rate constant matrix. Eqs. (5.2) and (5.3) are exactly identical to Eqs. (3.1) and (3.2) correspondingly. The above master equation is solved in our approach for a given set of initial conditions for the state occupancy probabilities leading to all results presented in this work.

There are several ways to solve Eq. (5.2) for given initial probability distribution $\mathbf{P}(0)$ provided that a) a network of states (basins or ISs of the PEL) for the given system has been explored, i.e., a network is known, b) all relevant transitions connecting the explored states with each other have been located, that is the connectivity between states has been defined, and c) the rate constant for every transition between connected

states is known. A numerical solution of Eq. (5.2) is possible ⁶, however subject to errors. An analytical solution of the master equation is, on the other hand, also feasible as demonstrated in paragraph 4.4.1 of this work and can lead to accurate results. In order to proceed with the analytical solution of Eq. (5.2), the rate constant matrix \mathbf{K} for all transitions, as well as a given initial probability vector $\mathbf{P}(0)$ should be known. The rate constant matrix \mathbf{K} is created based on the work of Tsalikis et al. ⁶² and the master equation is then solved for a given set of arbitrarily chosen initial conditions $\mathbf{P}(0)$. Because, by construction, our results do not have detailed balance built-in and numerical noise is expected to lead to deviations from it, we have imposed the detailed balance condition in the solution of the master equation.

According to Eq. (4.34), the analytical solution of the master equation provides the probability distribution of all involved states at all times:

$$\tilde{\mathbf{P}}(t) = \tilde{\mathbf{P}}(0) \cdot \mathbf{V} \cdot \exp(\mathbf{D} \cdot t) \cdot \mathbf{V}^{-1} \quad (5.4)$$

where \mathbf{D} is a diagonal matrix having as non-zero elements the eigenvalues of the symmetrized rate constant matrix $\tilde{\mathbf{K}}$ and \mathbf{V} describes the matrix of eigenvectors of $\tilde{\mathbf{K}}$.

As described in paragraph 4.4.1 Eq. (5.4) refers to the symmetrized probability vector $\tilde{\mathbf{P}}(t)$ which can be easily transformed to the conventional probability vector $\mathbf{P}(t)$ described in Eqs. (5.1) to (5.3) according to the linear transformation elaborated by Boulougouris and Theodorou ¹⁰². One reason for preferring to work with the symmetrized probability vector $\tilde{\mathbf{P}}(t)$ instead of the conventional one $\mathbf{P}(t)$ is that the corresponding symmetrized rate constant matrix $\tilde{\mathbf{K}}$ exhibits a better behavior during diagonalization. Secondly and more importantly, is that the Euclidean space spanned by the eigenvectors of the transformed matrix is the same as the one in which the time-dependent ensemble averaged value of any observable \mathcal{A} evolves, as shown by the EROPHILE representation ¹⁰².

One should note that deterministic graph transformation procedures have been developed in the past ^{108c, 112}, which allow large databases to be analyzed without loss of precision. These algorithms could potentially be – depending on the system – significantly faster than direct diagonalization of the rate constant matrix and therefore

overcome problems that may arise in networks of higher dimensionality than the ones studied here. Of course, at long times the system is expected to adopt its equilibrium probability distribution among states, $\mathbf{P}(\infty)$, which is the steady-state solution of the master equation for the considered set of states.

Having calculated, by the analytical solution of the master equation, the probability distribution for every state of the system $P_i(t)$ at all times t , the temporal disconnectivity graph can be created. In particular, if the occupancy probability $P_i(t)$ for every state i is known, then the necessary time for internal equilibration between two given states i and j can be found simply by examining when the following relation holds:

$$\frac{P_i(t)}{P_j(t)} = \frac{P_i(\infty)}{P_j(\infty)} \quad (5.5)$$

Eq. (5.5) ensures that, from a dynamical point of view, states (minima, basins, metabasins) i and j behave in the same manner. By checking the validity of Eq. (5.5) for states i and j one is able to calculate the time which signifies that, from that point on, internal equilibration between these states holds. From that time on these states, being in pairwise equilibrium can be grouped into a cluster of states (“meta-state”). By checking the validity of Eq. (5.5) for every pair of states of the system one is able to calculate how basins merge to metabasins, metabasins to meta-metabasins and so on. This knowledge provides, beyond any doubt, a concrete description of the temporal evolution of connectivity and thermodynamic irreversibility as the system evolves on its PEL, since, once a set of states have reached local equilibration, information on the prior state of the system has been lost and the free energy of the system has been reduced¹⁰².

One practical question is how one decides that Eq. (5.5) is satisfied. Although there are concrete and rigorous criteria that examine the equality of the two parts of Eq. (5.5)^{108b}, in this work we consider the two sides of Eq. (5.5) to be equal when the absolute difference between them becomes smaller than a certain tolerance ε . The adopted tolerance is set to be close to the arithmetic error incurred in calculations with double precision real numbers, i.e., $\varepsilon = 1 \times 10^{-15}$.

The heart of the proposed temporal disconnectivity graph lies in the creation of a graph that analyzes the progress of local equilibration as a function of the observation time, which of course is equivalent to the condition of perfectly lumpable^{66b} transition matrices. In Figure 5.2(a) we summarize all the necessary steps for the extraction of the temporal disconnectivity graph according to the master-equation-based approach.

The calculation of the probability distribution by analytically solving Eq. (5.3) is one way to create the temporal disconnectivity graph. In the context of this work we examine a second, alternative way to obtain such a temporal disconnectivity graph, however this time without having to solve the corresponding master equation. This alternative approach is based on the assumption that, for any pair of connected states, the presence of any transition other than the forward and backward transitions between the two states does not affect their mutual local equilibration. This method again requires as input the three basic parameters describing a system as they have been stated above, that is the network (set of potential energy minima), connectivity (transitions between minima) and rates (the rate constants characterizing the transitions between minima).

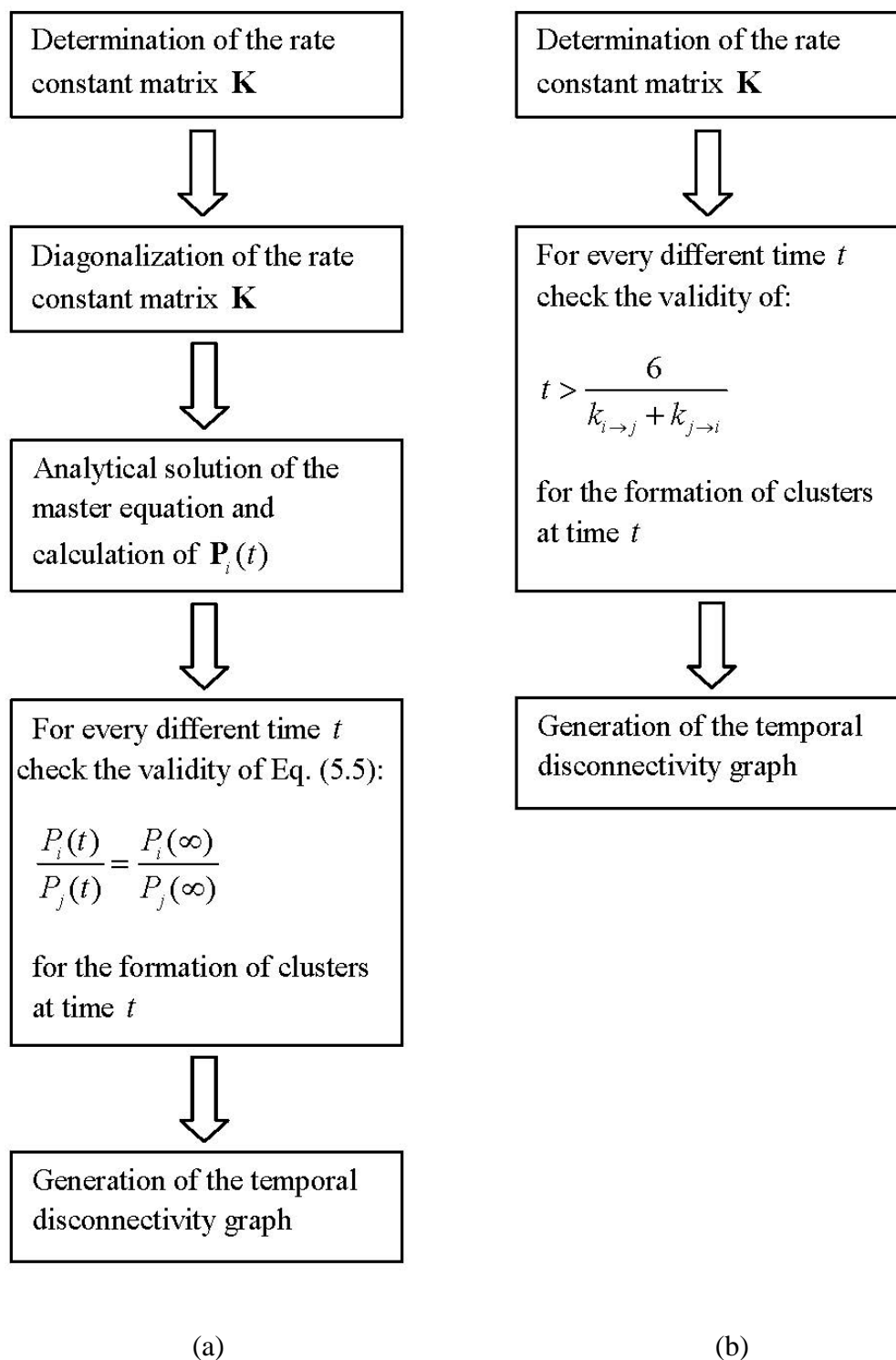


Figure 5.2: Schematic representation of the two implemented approaches for the creation of the temporal disconnectivity graph based on (a) the analytical solution of the master-equation under a given set of initial conditions and (b) the pair-connectivity assumption.

The idea is based on the hypothesis that the time needed for local equilibration between two given states i and j depends only on the two considered states. Thus, according to this approach, pairs of states are formed until every state of the system has been taken into consideration. It is relatively easy to prove that, for a pair of states, the non-zero eigenvalue of the two-state system will be equal to:

$$\lambda_{ij} = k_{i \rightarrow j} + k_{j \rightarrow i} \quad (5.6)$$

The contribution to the state probabilities corresponding to this eigenvalue behaves proportionally to the following quantity:

$$\mathbf{X}_{ij} \propto e^{-\lambda_{ij} t} \quad (5.7)$$

This means that for times roughly $t > \frac{6}{\lambda_{ij}}$ the corresponding contribution to the probabilities \mathbf{X}_{ij} will vanish, since it will be proportional to $e^{-6} \approx 2,48 \cdot 10^{-3}$, and the system of two states will adopt its equilibrium probability distribution, as described by the eigenvector corresponding to the zero eigenvalue. Based on this assumption about the pair connectivity of all states, one can calculate the necessary time t after which the two investigated states are in local equilibrium. Thus, in order to proceed with this algorithm, all states of the system have to be considered in pairs, so that the above described approach is valid. If two states i and j are found to be in equilibrium at time t , a cluster containing those two states is formed. If a third state m is then found to be in equilibrium with one of the previous states (say j), then it will also be in equilibrium with state i (according to the pair connectivity assumption), with which state j was found to be in local equilibrium in the first place. This means that now a new cluster of states has to be formed containing all three individual states i, j and m . If, at a later time $t_2 > t_1$, another state q is found to be in local equilibrium with state m , then state q will be assumed to be in local equilibrium with all states with which state m was in equilibrium by that time (in our example states i and j). Consequently, a new cluster will be build at time t_2 containing all four states (i, j, m and q) which are in local equilibrium with each other. The flow chart followed to create the temporal disconnectivity graph according to the above described assumption

is depicted in Figure 5.2(b). Note that the pair connectivity assumption used to create such temporal disconnectivity graphs is similar to the energy criteria in respect to the height of a barrier in the original disconnectivity graph applications^{105b} and to the construction of equilibration trees¹¹³ mapping out how the system moves towards equilibration. In contrast to this earlier work, both our approaches have no limitation concerning the connectivity of minima in terms of transition paths and the height of the barrier separating two minima or two sets of minima.

A comparison of the direct solution of the master equation and the pair connectivity approximation (cf. Fig. 5.2(a) and 5.2(b)) shows that, within the second approach (Fig. 5.2(b)) for the extraction of the system's connectivity as a function of time, two important and usually time-consuming steps are omitted. In particular, the diagonalization of the rate constant matrix, which for systems of large dimensionality can be slow, inaccurate and problematic, as well as the analytical solution of the master equation can be skipped. On the other hand, the pair connectivity approach is based on an assumption and not on an analytical solution of the master equation. This means that this approach (Fig. 2(b)) can be used as a “quick and dirty” alternative, whereas a more detailed and thorough representation is offered by the master-equation-based approach (Fig. 2(a)).

In the “Results and discussion” section of this chapter the temporal disconnectivity graphs are created based on the two methods described above (analytical solution of the master equation and clustering algorithm based on the pair connectivity assumption). The graphs obtained will be compared to each other and thus provide information on the validity of our assumptions. Additionally, as will be explained in Section 5.3, the results from the above approaches will be compared to a molecular dynamics (MD) method for the “on the fly” definition of metabasins, as well as to a lumping algorithm implemented on the initial system of states. The behavior of the lumped system will be depicted in a corresponding temporal disconnectivity graph, providing useful details about the dynamical characteristics of the lumped system and the efficiency of the implemented lumping algorithm.

5.3 Methodological and computational details

All results within this chapter have been obtained for a binary Lennard-Jones system, initially proposed by Kob and Andersen^{7, 84}. All details concerning this physical system have been sufficiently explained in Chapter 3.4 of this work. The data needed for the representation of the PEL by a temporal disconnectivity graph were provided with the help of a highly parallelizable sampling scheme designed for atomistic simulations of glassy materials⁵⁶. In order to ensure efficient dynamical sampling at temperatures about T_g , an “on the fly” definition of metabasins has been adopted. In order to calculate the necessary rate constant matrix for transitions between basins of the PEL, a swarm of microcanonical molecular dynamics trajectories has been initiated at phase-space points sampled with the help of a canonical molecular dynamics run that was artificially trapped within a metabasin, so as to make the sampling as extensive as possible.

Moreover, a lumping procedure has been implemented on the provided initial system, in a similar way as described in Chapter 4 of this work, in order to graphically represent, with the help of a temporal disconnectivity graph, the lumped system. The lumping methodology, as applied in this work, placed emphasis on the minimization of the lumping error E , as well as of the Frobenius norm W of the lumped rate constant matrix $\hat{\mathbf{K}}$, used as a measure of the efficiency of the applied lumping in describing accurately the dynamics of the system at long times. The dimensionality of the lumped system \hat{n} has been attributed a zero weight in comparison to the other two lumping criteria. More precisely, we keep \hat{n} fixed at a value of $\hat{n} = 43$ letting the algorithm find the optimal solution by minimizing an objective function only by varying the other two criteria (i.e., E and W). The adopted objective function for the optimization problem involved in lumping has form of equation (4.25).

$$z(E, W, \hat{n}) = z_1 \cdot E + z_2 \cdot W + z_3 \cdot \hat{n} \quad (5.8)$$

where the parameters z_1, z_2 and z_3 , specifying the importance of each one of the three corresponding lumping criteria (E, W, \hat{n}) in the final result, have the values listed in Table 5.1.

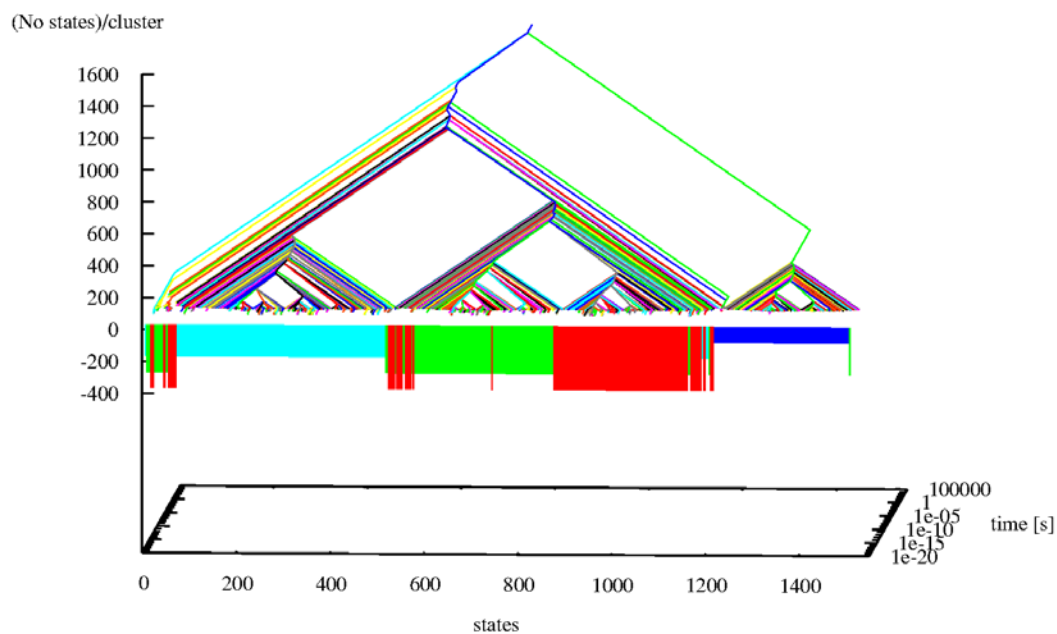
Table 5.1: Values of the parameters of the objective function $z(E, W, \hat{n})$ [Eq. (5.8)].

$z_1(\text{ps})$	$z_2(\text{ps})$	$z_3(-)$
0.5	0.5	0

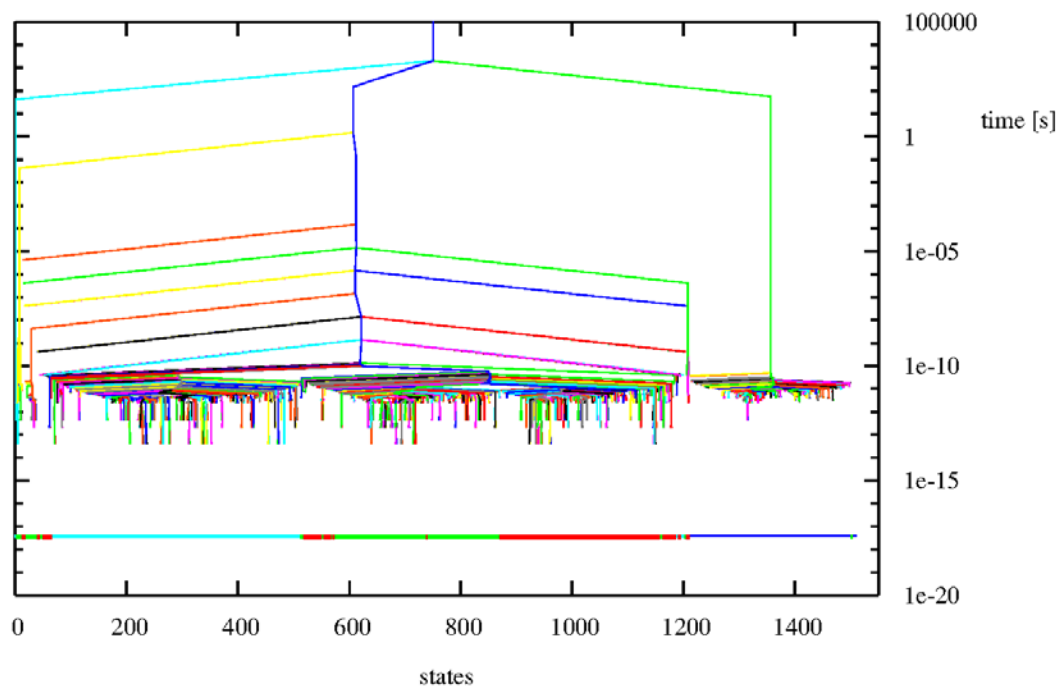
The search for the optimum lumping proceeded via Monte Carlo simulation based on the Wang-Landau scheme, which enables us to overcome entrapment in local minima in the space of the above mentioned lumping criteria E and W . The final outcome of the lumping algorithm is the $\hat{n} \times n$ transformation matrix \mathbf{M} , which in our case transforms the initial system of dimensionality $n = 1504$ states to a lumped system of reduced dimensionality $\hat{n} = 43$ lumped states. Matrix \mathbf{M} corresponds to the one yielding the smallest value for the defined objective function z [Eq. (5.8)].

5.4 Results and discussion

Based on the pair-connectivity of states and following the calculation steps described in Fig. 5.2(b), a typical temporal disconnectivity graph for the initial system consisting of $n = 1504$ minima of the PEL can be created (Fig. 5.3(a)):



(a)



(b)

Figure 5.3: Temporal disconnection graph for a system of 1504 minima (states) of the potential energy. The graph, shown in (a), is produced according to the assumption

of pair-connectivity. At small times ($t = 1 \times 10^{-18}$ s) the graph also provides color-coded information about the metabasin to which every single state belongs according to the "on the fly" definition of metabasins introduced by Tsalikis et al.⁵⁶. With blue color we represent metabasin 1, with cyan metabasin 2, with green metabasin 3 and with red we depict metabasin 4. In (b) one can see the floor plan of the temporal disconnectivity graph for a better understanding of the temporal evolution of states, basins and metabasins. Each colored line of the graph corresponds to a different state in all plots.

Figure 5.3(a) illustrates a typical temporal disconnectivity graph. The temporal disconnectivity graph is a 3D-plot with the following basic characteristics. The x -axis represents the number of states (basins, ISs, minima of the PEL) of the system. Each state is assigned a different number. The y -axis represents time in seconds, whereas the vertical axis shows the number of states included in each meta-state (metabasin) that is identified as time evolves. By observing this plot it can be concluded that at short times every state of the system has not been clustered with any other state. This means that for short times the system has not yet found time to establish internal equilibrium between individual states and so every state of the system finds itself on its own. This can be seen by observing the z -axis value for every state in Figure 5.3(a) at short times. This value is equal to one, since every state of the system is separate.

At short times, all branches of the inverted tree terminate at a local minimum of the energy (inherent structure). From Figure 5.3(b) it can be easily concluded that not all states start off at the same time. The reason for this is that the rate constant matrix, on which the generation of the temporal disconnectivity graph is based, has been created in the course of a dynamical trajectory sampled via a MD simulation. The start-off time for each state varies between $t = 1 \times 10^{-15}$ s and $t = 1 \times 10^{-10}$ s and corresponds to the longest time that a state has been observed alone, i.e. not as part of a "locally equilibrated" cluster. The longer the start-off time of the state, the longer it takes to achieve local equilibration. These time scales are characteristic of the common relaxation processes taking place in glassy materials.

As time grows, local equilibration is established between some states (according to the pair-connectivity assumption) and a cluster containing these states is formed. This is schematically depicted by the intersection of two neighboring branches and the formation of a node (branch point) in the inverted tree. The longer the time needed for the branches to collapse, the more it takes to reach “local equilibration”. In addition, the z -coordinate increases, showing the number of original states contained in the formed cluster. In this sense, as time evolves and longer and longer time scales are accessed, more and more states reach internal equilibration with each other and merge to new or to already existing meta-states (metabasins). The time at which two or more states unite to form a cluster of states corresponds to the time needed for these states to equilibrate mutually via transitions.

At long times Figure 5.3(a) shows that enough time has been given to the system to reach internal equilibration among all states accessed and thus one single branch (cluster) is observed, containing all 1504 states. Note that roughly 10^3 s are required for this. The physical meaning behind this observation is that, for those long time scales, all states of the system communicate with each other through transitions which are faster (shorter time) than the time required to escape from the formed cluster which contains all accessed states. In other words, at long time scales enough time has been given to the system for smaller basins to merge and form larger and wider metabasins, which, in turn, achieve internal equilibration with neighboring metabasins giving rise to even wider and bigger metabasins.

Moreover, Fig. 5.3(a) shows the connection between the temporal disconnectivity graph obtained via the pairwise connectivity assumption and a molecular dynamics-based method for an “on the fly” definition of metabasins⁵⁶. This extra information derived from the metabasin definition is drawn in front of the preexisting temporal disconnectivity graph. In particular, at an arbitrarily chosen short time (here $t = 1 \times 10^{-18}$ s), at which all branches of the disconnectivity graph have been terminated since they contain only one state (i.e. there are no clusters of states anymore), four different colored blocks have been drawn. These blocks have been created as sets of linear segments, where each linear segment corresponds to one of the $n = 1504$ states of the system and is colored according to the metabasin where it was found to belong based on the “on the fly” metabasin definition.

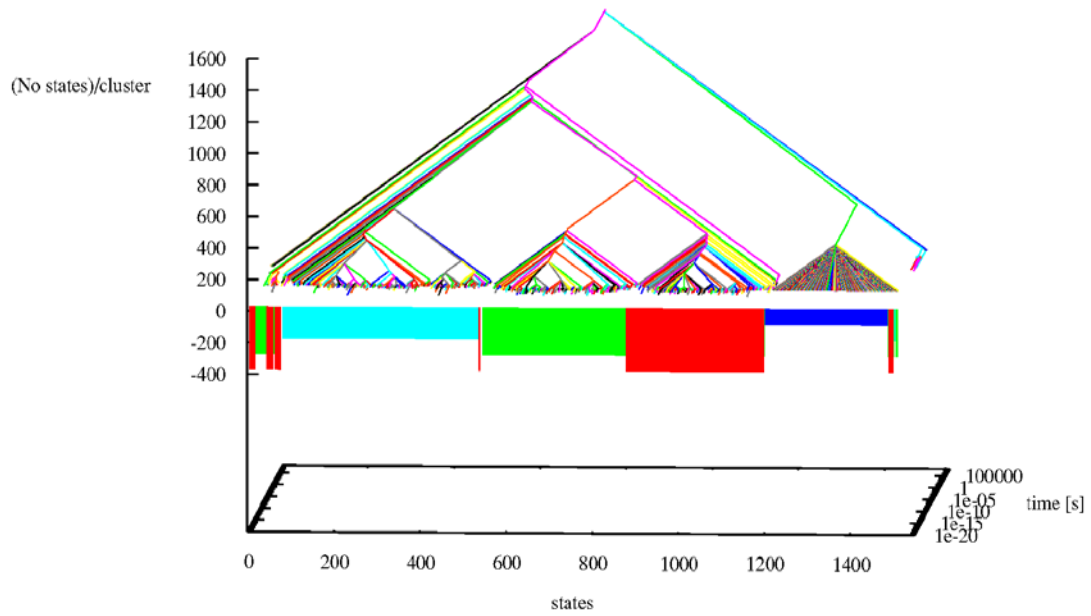
By observing the structure of the temporal disconnectivity graph, one can see that for short times ($t < 1 \times 10^{-10}$ s), where almost every branch corresponds to one single state, four different structures resembling small “rooftops” arise. These four structures correspond to four different metabasins in the considered system; clearly, they are strongly correlated to the metabasins identified “on the fly” via MD in the work of Tsalikis et al.⁵⁶, which are the four colored blocks. As time grows, the four different metabasins start to consolidate into bigger structures (meta-metabasins) until all four metabasins have been united into a single branch containing all 1504 states of the system. Hence, Figure 5.3(a) shows that the temporal disconnectivity graph describes well not only the existence and sampling of metabasins, but also the temporal evolution of these structures as they coalesce with time to form even larger meta-metabasins.

An additional advantage of this new representation approach is that from the temporal disconnectivity graph one can read off the times at which states merge to clusters and clusters into larger clusters, e.g., the time frames between which specific groupings into metabasins are useful. Furthermore, the graph also addresses the important question of which states merge with which states. Thus, the temporal disconnectivity graph reveals both the identity of the states to be merged and the time of the juncture. Furthermore, temporal disconnectivity graphs can provide a very good initial estimate of the lumping matrix \mathbf{M} , thus helping the lumping algorithm described in Chapter 4 to converge faster. This is relatively straightforward, since every line drawn on the xy -plane parallel to the x -axis, describing in the temporal disconnectivity graph the cluster connectivity at a certain time t , corresponds to a certain \mathbf{M} matrix. In particular, the number of clusters at time t defines the number of rows \hat{n} of matrix \mathbf{M} . Additionally, the identity of the states of the initial system, which are about to be lumped into one certain cluster, defines the position of the “1” in the row of \mathbf{M} corresponding to the formed cluster.

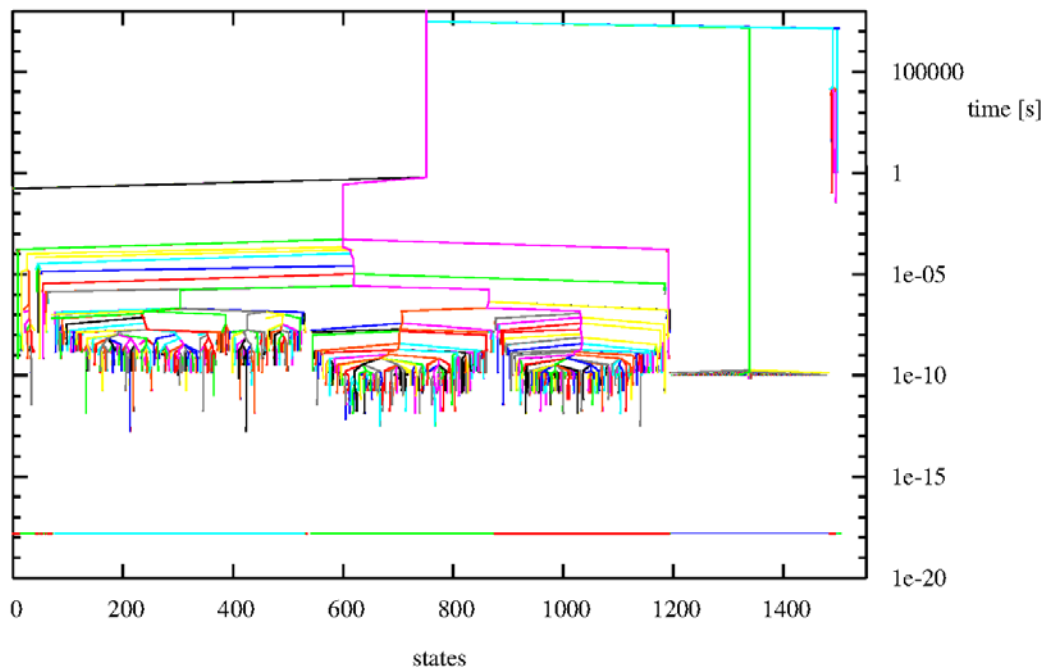
In Figure 5.3(b) one can see the floor plan (states versus time) of the disconnectivity graph, along with the four colored blocks at small times depicting the four verified metabasins.

We now turn to the master equation approach and construct the temporal disconnectivity graph according to the procedure outlined in Figure 5.2(a). Analytical

solution of the master equation under a given set of initial conditions leads to the temporal disconnectivity graph presented in Figure 5.4:



(a)

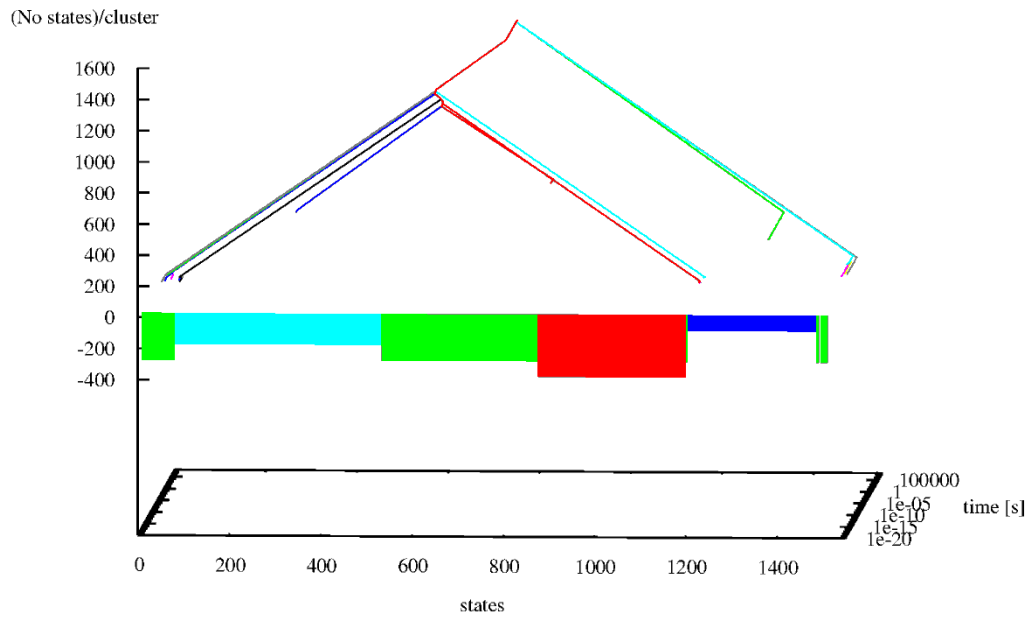


(b)

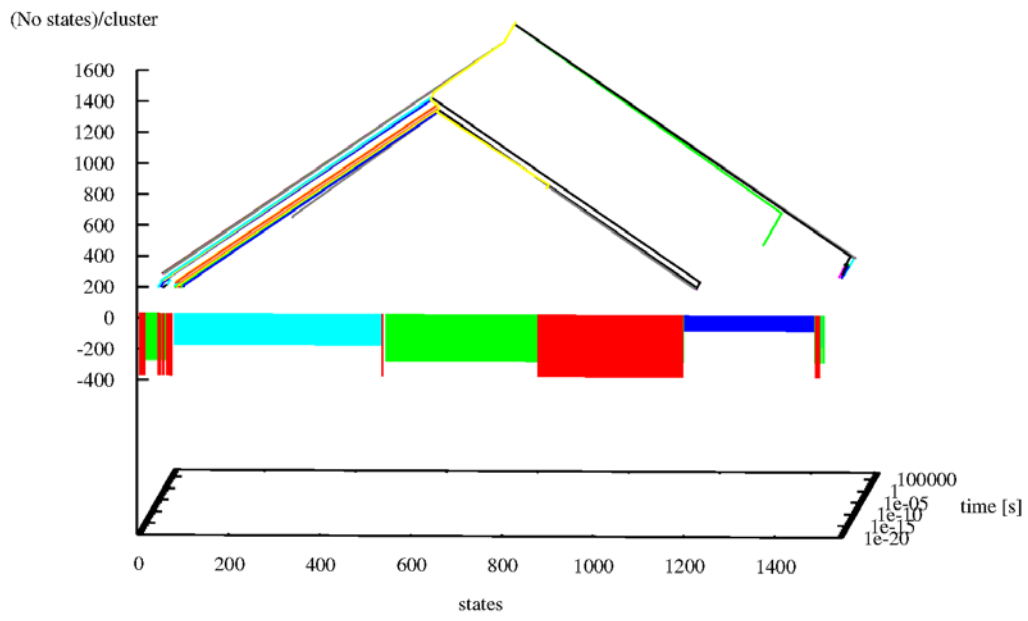
Figure 5.4: Temporal disconnectivity graph for a system of 1504 minima (states) of the potential energy. The graph, shown in (a), is derived from the analytical solution of the master equation [Eq. (5.3)] in the set of states considered. At small times ($t = 1 \times 10^{-18}$ s) the graph also provides information concerning the metabasin to which every single state belongs according to the "on the fly" definition of metabasins introduced by Tsalikis et al.⁵⁶. With blue, cyan, green, and red are represented states belonging to metabasins 1, 2, 3, 4, respectively. In (b) one can see the floor plan of the temporal disconnectivity graph, offering a clearer explanation of the temporal evolution of states, basins and metabasins. Each colored line of the graph corresponds to a different state in all plots.

Figure 5.4 represents, in an analogous way to Figure 5.3, the temporal disconnectivity graph for the considered system of $n = 1504$ states, created, however, based on the probability distribution among states as it results from the analytical solution of the master equation and on determining the times when the internal equilibration condition between states [Eq. (5.5)] is fulfilled. A direct comparison between Figures 5.3(a) and 5.4(a) shows very good agreement between the two plots. This agreement is seen not only in the general shape of the disconnectivity graphs, but also in the similarity of the time scales. Additionally, the correlation between the disconnectivity graph created via the master equation solution and the definition of metabasins "on the fly", in the course of a 3 ns-long MD simulation is excellent, better than in Figure 5.3. Clearly, there is good agreement between the "brute force" MD algorithm for defining metabasins in the studied system and the dynamical information contained in the master equation and visualized in the temporal disconnectivity graph of the PEL (Fig. 5.4(b)). By comparing Figures 5.3 and 5.4 we conclude that both approaches implemented in this work for constructing the temporal disconnectivity graph, as outlined in Figure 5.2, conserve the topology of connections between states and the corresponding rate information very well. Results from the master equation-based approach seem to be a bit more accurate (in better agreement with "brute force" MD), but are obtained at considerably higher (approximately by a factor of 3 in respect to CPU time) computational cost.

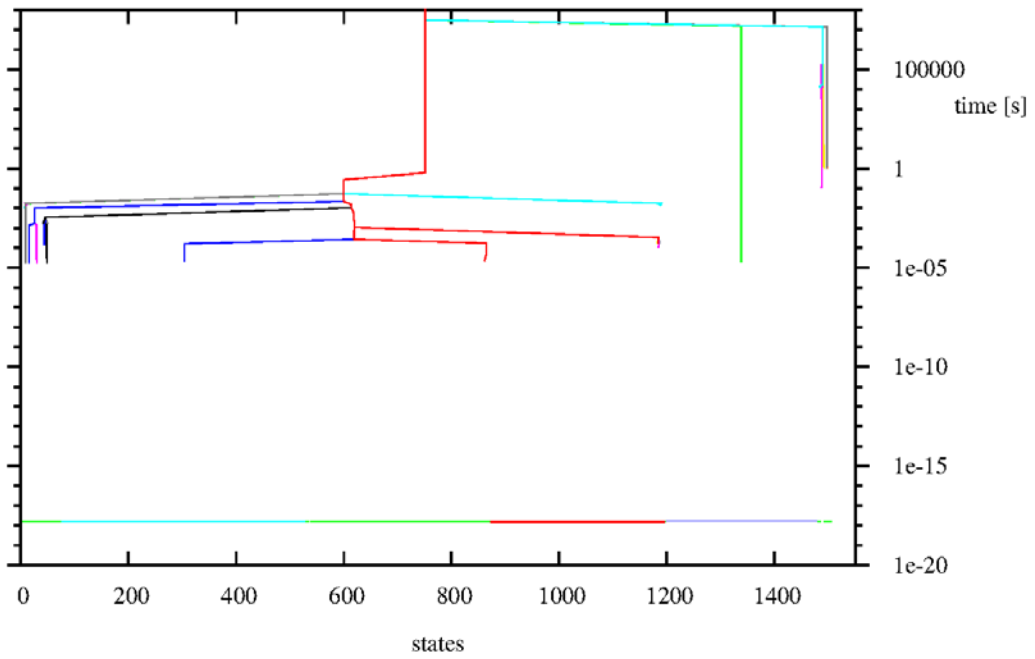
By lumping the initial system of $n = 1504$ states following the specifications described in paragraph 5.3, we obtain a system of smaller dimensionality $\hat{n} = 43$ capable of describing long-time dynamics of the initial system. The temporal disconnectivity graph of this lumped system, constructed on the basis of its master equation solved under a given set of initial conditions, can be seen in Figure 5.5(a) and 5.5(c):



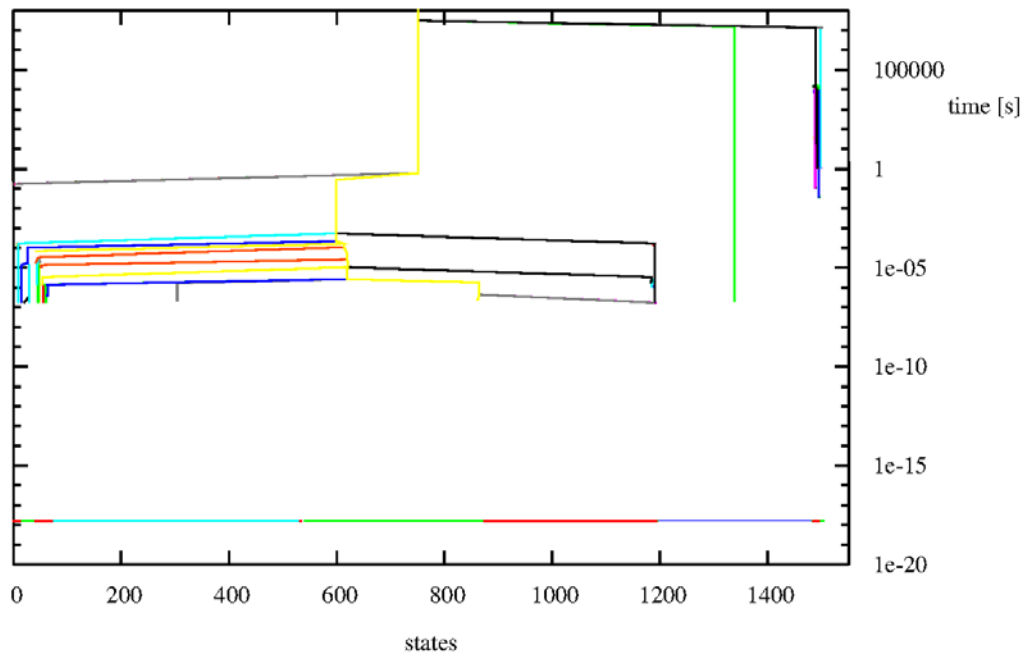
(a)



(b)



(c)



(d)

Figure 5.5: Temporal disconnectivity graph for the lumped system consisting of 43 metastates (lumped states). The lumped system is produced according to the lumping specifications described in paragraph 5.3, whereas the graph shown in (a) is created based on the analytical solution of its master equation under a given set of initial conditions [Eq. (5.3)]. For comparison, in (b) is shown the temporal disconnectivity graph of the initial system (presented in Figure 5.4(a)) for times greater than $t = 1 \times 10^{-7}$ s. The floor plan of (a) is shown in (c). In addition to (c), in (d) one can see the floor plan of the temporal disconnectivity graph of the initial system (as presented in Figure 5.4(b)) having omitted nonetheless times smaller than $t = 1 \times 10^{-7}$ s in order to facilitate direct comparison with (c). Each colored line of the graph corresponds to a different state in all plots. At small times ($t = 1 \times 10^{-18}$ s) (a) and (c) provide the information concerning the metabasin to which every single initial state (clustered in one of the 43 lumped clusters) belongs to, whereas (b) and (d) provide the same information according to the "on the fly" definition of metabasins introduced by Tsalikis et al.⁵⁶. With blue, cyan, green, and red we represent metabasins 1, 2, 3, and 4, respectively.

At this point a clarification is in order. The lumped system consists of $\hat{n} = 43$ lumped states. Every lumped state can consist of more than one states of the initial system. This means that every state out of the 1504 initial states belongs now to a lumped state. The way the initial states are being distributed among the new lumped states is defined by the outcome of the lumping algorithm, which is the lumping matrix \mathbf{M} . A lumped state may have resulted from combination of a green and a red initial state. The color attributed to the lumped state in the temporal disconnectivity graph of figure 5.5 is then the one that corresponds to the last overlapping initial state. Figures 5.5(a) and 5.5(c) show that lumped states, each containing more than one states of the initial system, merge with each other as time evolves to form metabasins. A direct comparison between Figure 5.5(a) and 5.5(b), as well as between Figure 5.5(c) and 5.5(d), shows a quite good resemblance between the temporal disconnectivity graphs of the lumped and the initial system. Figure 5.5(d), which is the floor plan of Figure 5.4(a) plotted only for times longer than $t = 1 \times 10^{-7}$ s, shows, in a clearer way, how well the lumped system can describe the long-time dynamics of the initial system. Moreover, Figure 5.5(c) offers a measure of how “pure” the formed 43 lumped states are in respect of the four metabasins defining the initial system (cf. Fig. 5.3(b) and Fig. 5.4(b)). In particular, Figure 5.5(c) at small times ($t = 1 \times 10^{-18}$ s) describes how the initial states of the four metabasins are distributed among the lumped states. We can see that every one of the 43 lumped states contains initial states originating from the same metabasin. This is depicted in the four colored blocks in front of the disconnectivity graph. As Figure 5.5(c) shows, every line segment of these four blocks has a unique color and is no mixture of colors, indicating that initial states of the same metabasin have been merged to one lumped state. Moreover, there is no overlap between blocks of different color. Hence, each lumped state contains initial states of the same metabasin of the initial system and thus no mixing of metabasins is observed during lumping. In this sense, lumped states can be characterized as “pure”.

If we try to compare the initial and lumped networks (cf. Figures 5.4 and 5.5) with respect to their time evolution, it is obvious that, for small times, where fast transitions take place, both networks seem to behave similarly. For both networks fast transitions take place for times 1×10^{-3} s $\geq t \geq 1 \times 10^{-12}$ s. Moreover, both networks gather all their states (states and lumped states) into one main branch at relatively long times $t > 1 \times 10^3$ s. The same piece of information is drawn with the help of the temporal

disconnectivity graph of the lumped system for relatively longer time scales $t > 1 \times 10^{-7}$ s (cf. Figures 5.5(c) and 5.5(d)), whereas the lumped system seems to accurately reproduce the basic connectivity and dynamics dictated by the PEL.

5.5 Conclusions

In this chapter a new, alternative representation of the potential energy landscape has been developed and presented for a binary Lennard-Jones glassy system. This representation is based on the disconnectivity graph theory already known from the literature. The innovative characteristics of the proposed graphical representation are firstly that, in contrast to the conventional disconnectivity graphs, the temporal disconnectivity graph replaces the energy (or temperature) axis with a time axis and secondly adds an extra dimension, making temporal disconnectivity graphs three-dimensional plots. These features allow monitoring all changes in the population of the PEL as time elapses and uncovering the underlying topology and communication rates between different parts of the landscape. Our temporal disconnectivity graphs, accumulated by processing the results of extensive temperature-accelerated MD simulations in two different ways, provide clear evidence that the PEL exhibits a hierarchical structure. Results from the pairwise-connectivity strategy for identifying local equilibration among states are in very good agreement with those from the more exact master equation solution strategy and thus provide a less computationally demanding alternative to the exact strategy. The identity of merging (locally equilibrating) states and the times where mergers take place can readily be extracted from temporal disconnectivity graphs.

The proposed graphical representation has also been applied to lumped systems, which provide a coarse-grained description of the dynamics in a landscape of greatly reduced dimensionality. In the context of this work it is schematically shown that lumped states contain states of the initial system belonging to the same metabasin, which are states communicating with each other through transitions that are faster than those required to access the rest of configuration space. Additionally, it is being schematically verified that the lumping algorithm predicts accurately the dynamic behavior of the initial system – in terms of connectivity between metabasins and resulting temporal

evolution – at long times. Beyond the visual advantages offered by temporal disconnectivity graphs, they can serve to provide a very good initial estimate of the lumping matrix \mathbf{M} , thus helping the lumping algorithm described in Chapter 4 to converge faster.

Our conclusions indicate that the proposed clustering based on pair local equilibration is an accurate approximation of the temporal evolution of the system. In case one is interested in achieving quantitative agreement with the temporal disconnectivity graph that results from the analytical solution of the master equation, it is proposed to re-evaluate the rate constants connecting clusters of states based on a local equilibration estimation of the conditional flux out of each cluster^{59d, 108a-d}. In other words, the effective rate constant out of each cluster is estimated as a product of the conditional probability of being in the state that leads out of the cluster (provided one is in the cluster) and the rate constant of the inter-cluster transition out of that state.

Chapter 6

Mechanical deformation computational experiments on glassy atactic polystyrene

The previous two chapters describe techniques (lumping and temporal disconnectivity graph, respectively) that are dedicated to better understanding the PEL, making use of its characteristics to extract useful information about properties and molecular mechanisms, and overcoming simulation-time related limitations appearing when one tries to track physical ageing in glassy materials. With the help of these specially designed, self-consistent methods combined with appropriately developed MD and MC techniques, a large variety of dynamical properties can be estimated even at time scales unreachable under use of conventional simulation techniques^{52, 102}. All this effort is related to the time evolution of the configuration of a glassy system and aims at explaining relaxation phenomena characterizing glassy materials. This chapter is, on the contrary, dedicated to revealing what happens to a glassy material, when an external perturbation is applied to it. More precisely, it is of great interest to investigate via computer simulation techniques the response of a glassy system during mechanical deformation.

In this chapter, the response to deformation of a detailed computer model of glassy atactic polystyrene, represented as a collection of basins on its potential energy landscape, is investigated. The volumetric behavior of the polymer is calculated via “brute force” molecular dynamics quenching simulations. Results are compared with corresponding estimates obtained by invoking the quasi-harmonic approximation (QHA) for a variety of temperatures below the glass temperature and with

experimental data. The stress-controlled uniaxial deformations fall in the linear elastic regime and the resulting strains are calculated as ensemble averages of QHA estimates over 200 uncorrelated inherent structures of the potential energy landscape. It will be demonstrated that the estimated elastic constants (Young's modulus and Poisson ratio) and their temperature dependence are found to be in very good agreement with experiments for glassy atactic polystyrene. Additionally, a classification of the deformed inherent structures in respect to the geometry and general shape of their energy minima is undertaken. A distortion of the potential energy basins upon mechanical deformation in the elastic regime is observed in all cases.

6.1 Introduction

Analyzing and predicting the mechanical response of a glassy polymer upon deformation is the primary goal of this chapter. This study builds upon early work on computing mechanical properties of glassy polymers¹¹⁴. In that work, quasi-static molecular mechanics simulations of deformation were used together with realistic atomistic models, in order to predict the experimentally measured response in the elastic regime followed by yielding, intrinsic strain softening and strain hardening¹¹⁵. Later modeling work focused on elucidating the complex and still partially explained phenomena of strain softening and strain hardening, as well as on investigating general yield and plastic deformation phenomena^{114d, 116}. From a macroscopic point of view, those phenomena have been captured quantitatively in finite element based methods by using suitable constitutive relations for the intrinsic material response¹¹⁷. Early molecular mechanics experiments did not incorporate time or temperature explicitly. They have been taken further in recent studies for the exploration of ageing and mechanical rejuvenation of simple model glasses¹¹⁸ and generic models of rugged landscapes¹¹⁹.

Parrinello and coworkers^{114e} showed that there is a direct correlation between the elastic strain fluctuations and the elastic constants for a general anisotropic material and proposed a fluctuation formula for calculating elastic constants from the thermal strain fluctuations. This equation has been further evolved and appropriately modified from Gusev et al.¹²⁰, providing an equation for the elastic constants of the classical first-nearest-neighbor Lennard-Jones fcc crystal, which, although having the same

validity as the Parrinello-Rahman fluctuation formula, has superior convergence properties as it takes into account the fact that in thermal fluctuations the instantaneous stresses and strains are correlated. The calculation of elastic constants can also proceed from corresponding fluctuation formulas based on simulations in the Thn and Ehn ensembles, where T is the temperature, E is the energy, n is the number of particles, and \mathbf{h} is a scaling matrix $\mathbf{h} = (\mathbf{a}, \mathbf{b}, \mathbf{c})$ made up of the vectors \mathbf{a}, \mathbf{b} and \mathbf{c} forming the simulation cell¹²¹. It is, of course, a significant question whether one can apply a fluctuation formula for a glass, which is an intrinsically non-equilibrium material exhibiting time-dependent mechanical properties. In practice, estimates of the elastic constants extracted from fluctuation formulae are in reasonable agreement with estimates based on external imposition of stress or strain, indicating that, for the time scales observed in the simulations, the model system achieves local equilibrium within a confined region of its configuration space.

In the case of polymeric nanocomposites, both molecular dynamics and Monte Carlo simulations have been conducted based on the Parrinello-Rahman approach for the calculation of corresponding stress-strain curves¹²². Furthermore, in the case of inhomogeneous systems, local elastic constants have been calculated based on a method of planes¹²³. In regard to copolymers with chemically connected glass and rubbery phases, a triblock copolymer has been studied using mixed finite element approaches to deliver elastic properties¹²⁴. Moreover, the temperature dependence of mechanical and structural properties of polymeric crystals has been simulated and thoroughly investigated by implementing a variety of techniques¹²⁵. Additionally, plastic deformation of glasses has been investigated by combining constant-stress MD simulations and fixed-cell energy minimizations showing that the plastic transition can be interpreted as a crossing between and a collapse onto each other of “ideal (thermodynamic) structures”¹²⁶.

Although considerable progress has been made in developing mathematical frameworks and models for both the small strain regime under a specific narrow spectrum of strain rates and temperatures¹²⁷, as well as for the regime of relatively larger deformations beyond the yield point¹²⁸, where strain hardening phenomena due to entanglements seem to play a dominant role, there are still unanswered questions regarding the structural mechanisms that govern the typical response of glassy polymers to deformation. This work is part of an effort to understand ageing and

deformation phenomena in polymer glasses based on the potential energy landscape picture. It is related to a simulation approach we have designed for tracking the temporal evolution of a glass as a succession of transitions between basins in its PEL⁵². At long times, when the number of explored basins (states) becomes prohibitively large, the lumping scheme described in Chapter 4 can be used to effectively reduce the dimensionality of the network of states without severe loss of information¹²⁹. A system's dynamical course on its PEL can be visualized with the help of temporal disconnectivity graphs¹³⁰ as shown in Chapter 5.

The purpose of this work is to investigate the mechanical response of a typical polymer glass (glassy atactic polystyrene) in the elastic regime, assuming that, upon imposition of stress, its configuration does not leave the basin within which it is confined. Similar to the tactic adopted in the previous chapters, we represent the polymer glass as a set of uncorrelated potential energy minima obtained via a combination of MD simulations and our technique for tracking the dynamical evolution on a network of discrete states⁵². We test how well a quasiharmonic approximation around the local energy minima (inherent structures) of the basins captures the volumetric and elastic response as a function of temperature. We also explore how the characteristics of the basins are modified upon imposition of mechanical deformation.

This chapter is organized as follows. In Section 6.2 we describe the model system, defining the basic theoretical framework on which our investigation was based, and present details of the procedure we have developed for generating configurations representative of the glassy state of atactic polystyrene. In Section 6.3 we provide computational details of our deformation experiments, whereas in section 6.4 we present and interpret the results obtained and finally in the last section 6.5 we summarize the conclusions and innovations of this work.

6.2 Model System and Methods

Atactic polystyrene was chosen as the model system, as it is one of the most widely used and most extensively studied polymer glasses^{41, 131}. The atactic form, typically obtained by free radical polymerization, has the additional advantage of not being able to exhibit large-scale crystallization upon cooling, which would complicate our

computational approach. The suppression of crystallization imparts the amorphous character to the investigated material. The simulated polymeric system is formed from a single chain of atactic polystyrene containing 80 monomer units, generated as a Bernoullian sequence of meso- and racemic dyads^{114a}. Each monomer unit consists of 8 united atoms, hydrogens being absorbed into the carbon atoms with which they are connected. Our polymeric chain, of chemical constitution $\text{CH}_3\text{-}[\text{CH}(\text{C}_6\text{H}_5)\text{-CH}_2]_{79}\text{-CH}(\text{C}_6\text{H}_5)\text{CH}_3$, thus consists of 641 united atoms.

The interaction potential used in all implemented simulations in this work is the one proposed by Lyulin et. al.⁴¹. It takes into account the following contributions to the system potential energy: (i) Lennard-Jones non-bonded interaction potential between all united atoms that are three or more bonds apart or belong to different images of the parent chain; (ii) bond stretching potential for every covalent bond; (iii) bending potential for all bond angles, including those in the phenyl rings; (iv) torsional potential for all rotatable backbone bonds; (v) torsional potential for the torsions of phenyl rings around their stems; (vi) out-of-plane bending potential to preserve the coplanarity of the phenyl and the phenyl stem; (vii) torsional potential about all bonds connecting aromatic carbons in the phenyl ring, to preserve the planarity of the ring; (viii) improper torsional potential to preserve the chirality of all carbons bearing a phenyl substituent. No tail corrections are used for the nonbonded interaction potential. This is because the original Lyulin et al. potential⁴¹, which was tailored to match volumetric properties in the melt state, does not incorporate tail corrections.

Although of relatively small size, it has been noted that the model system under investigation can be simulated best during the molecular dynamics quenching procedure (see below) when no long range corrections are taken into account. In particular, the system adopts density values close to those measured experimentally upon quenching into the glassy state; presumably, nonbonded interactions between united atoms at distances below the applied cut-off distance r_c are sufficient for capturing a reasonable volumetric response and system size effects are weak. The latter statement is supported by the fact that the system's radial distribution function $g(r)$ in the starting melt configurations and after quenching into the glassy state is found to be approximately 1 for $r > r_c$.

6.2.1 Generation of glassy configurations

Two hundred independent, completely uncorrelated initial configurations were generated by chain growth and subsequent energy minimization in a cubic box with periodic boundary conditions at a density of 0.97 g/cm^3 ^{114a}. The above procedure was realized by using MAPS (Materials Process and Simulations) simulation platform developed by Scienomics⁴². All these configurations were kept for use in the computational deformation experiments which will be described in detail in Section 6.3. For the purpose of studying the orthobaric volumetric behavior of the model as a function of temperature, however, only a subset of these configurations were employed, to keep the computing time reasonable. Five arbitrarily chosen configurations out of the 200 were subjected to isothermal-isobaric (NpT) molecular dynamics (MD) simulation under melt conditions $p=1 \text{ bar}$, $T = 460 \text{ K}$ for 40 ns. The velocity Verlet algorithm was used for all MD simulations, with a time step of 1 fs.

Glassy configurations were obtained from the melt by cooling down to a temperature far below the experimentally measured glass temperature of long-chain atactic polystyrene¹³² of $T_g \approx 373 \text{ K}$. To this end, the final configuration from each one of the melt NpT MD runs was subjected to further NpT simulation with the set temperature T lowered by 20 K every 40 ns (effective cooling rate 0.5 K/ns) down to a final temperature of 200 K. In this way, each one of the 5 initial liquid-state configurations provided a corresponding glassy configuration for our polymeric system.

6.2.2 Quasiharmonic approximation

From our cooling MD runs, we can track the average volume of our five polystyrene “specimens” as a function of temperature under $p = 1 \text{ bar}$. For temperatures in the vicinity of and far below the glass transition temperature T_g we have calculated the volumetric behavior as a function of temperature by following an alternative approach, based on the idea that the configuration of each specimen executes vibrations around the local energy minimum of the basin where it is trapped. In particular, we have adopted the quasi-harmonic approximation¹³³ (QHA) for the calculation of the system’s Gibbs energy.

According to the QHA, the Helmholtz energy A of a specimen of given spatial extent, defined by the edge vectors of our periodic simulation box, which fluctuates in the vicinity of a minimum energy configuration at temperature T , is composed of two contributions: a) the potential energy \mathcal{V}_{inh} of the minimum energy configuration (Stillinger and Weber's "inherent structure" ¹³⁴); and b) the contribution A_{vib} from vibrational motion about the inherent structure:

$$A = \mathcal{V}_{\text{inh}} + A_{\text{vib}} \quad (6.1)$$

At given spatial extent of the system, the inherent structure, hence \mathcal{V}_{inh} , can be computed by potential energy minimization with respect to the Cartesian coordinates of all atoms, starting from any configuration in the basin. A steepest descent algorithm should be used for this; conjugate-gradient minimization yields the same results for the systems of interest here.

Within the QHA the motion of the model system, comprised of N united atoms, can be described in terms of $3N - 3$ uncoupled, uncorrelated harmonic oscillators, whose frequencies are solutions to the following eigenvalue problem ¹³⁵:

$$\mathbf{H}' \cdot \mathbf{a} = \omega^2 \cdot \mathbf{a} \quad (6.2)$$

where \mathbf{H}' is the Hessian matrix of second derivatives of the potential energy with respect to the mass-weighted coordinates of the atoms ^{133b}. Three of the eigenvalues defined by Equation (6.2) are zero, as the system energy is invariant to translation along the edge vectors of the periodic simulation box. The remaining eigenvalues are the squared angular frequencies of the vibrational modes of the system residing in its basin. They are all positive (hence can be written as ω_i^2 for the i -th mode), as the diagonalization takes place at a minimum of the energy, where the Hessian with respect to the $3N - 3$ independent configurational degrees of freedom of the system is positive definite. Once these vibrational frequencies are known, the partition function for the vibrational motion of the system can be calculated (see below). Having calculated the partition function, the vibrational part of the Helmholtz energy, for the considered edge vectors of the simulation box, is obtained as:

$$A_{\text{vib}} = -k_{\text{B}} T \ln Q_{\text{vib}} \quad (6.3)$$

We make use of the QHA for the calculation of the vibrational part of the Helmholtz free energy. In the context of the QHA the system is envisioned as a set of $3N - 3$ uncorrelated harmonic oscillators around the energy minimum, vibrating with frequencies obtained by diagonalizing the Hessian matrix at fixed spatial extent of the simulation box (edge vectors). According to this approach the thermal motion is attributed only to harmonic motions, hence any anharmonicities are being neglected. For low temperatures ($T < T_g$) this seems to be reasonable. As temperature rises, anharmonic contributions to the thermal motion become more pronounced and the QHA would be expected to fail. The basic advantage of using QHA to describe thermal motion at low temperatures, instead of classical MD techniques, is that it couples very well to an approach we have designed for tracking the temporal evolution of the system as a succession of infrequent transitions between basins in configuration space.

“Dynamic Integration of a Markovian Web,” or DIMW, starts off from a highly localized initial distribution, and proceeds to create a network of basins based on stochastic dynamical importance sampling. Within this approach, one is not obliged to follow a single trajectory (as in the case of MD), but can rather use reaction path construction, transition state theory and kinetic Monte-Carlo techniques⁵² to simultaneously explore many directions in the $3N - 3$ dimensional configuration space. In that sense, a better sampling of configuration space is achieved in significantly reduced computational time. This can be a huge advantage in cases where kinetically trapped systems (such as glassy systems) are investigated and access to long time scales is problematic.

In this chapter we present a way to calculate the vibrational partition function Q_{vib} within the context of QHA through both a quantum mechanical and a classical formalism. According to the quantum mechanical formalism, Q_{vib} is equal to^{133b}:

$$Q_{\text{vib}}^{\text{qm}} = \prod_{i=1}^{3N-3} \frac{\exp\left(-\frac{\hbar\omega_i}{2k_{\text{B}}T}\right)}{1 - \exp\left(-\frac{\hbar\omega_i}{k_{\text{B}}T}\right)} \quad (6.4)$$

with k_{B} being the Boltzmann constant and $\hbar = h/(2\pi)$, h being Planck’s constant. If a classical formalism is adopted for the vibrational partition function, one obtains

$$Q_{\text{vib}}^{\text{cl}} = \prod_{i=1}^{3N-3} \left(\frac{k_{\text{B}}T}{\hbar\omega_i} \right) \quad (6.5)$$

Clearly, $Q_{\text{vib}}^{\text{cl}}$ is the limit of $Q_{\text{vib}}^{\text{qm}}$ when $\frac{\hbar\omega_i}{k_{\text{B}}T} \ll 1$ for all i .

For small deformations (changes in the edge vectors of the simulation box) around a reference state of volume V_0 , in the elastic regime, the elements of the stress tensor $\boldsymbol{\sigma}$ are related to the Helmholtz energy by ¹³⁶

$$\sigma_{ij} = \left. \frac{1}{V_0} \frac{\partial A}{\partial \varepsilon_{ij}} \right)_{T, \varepsilon_{[ij]}} = \left. \frac{1}{V_0} \frac{\partial \mathcal{V}_{\text{inh}}}{\partial \varepsilon_{ij}} \right)_{T, \varepsilon_{[ij]}} + \left. \frac{1}{V_0} \frac{\partial A_{\text{vib}}}{\partial \varepsilon_{ij}} \right)_{T, \varepsilon_{[ij]}} \quad (6.6)$$

where $\boldsymbol{\varepsilon}$, with elements ε_{ij} , is the strain tensor and the symbolism $\varepsilon_{[ij]}$ indicates that all elements of $\boldsymbol{\varepsilon}$ except ε_{ij} are held constant ¹³⁶.

Let us now consider our specimen confined in its basin under a given externally imposed stress tensor, $\boldsymbol{\sigma}$. In our calculations we use the Gibbs energy because we are considering stress-controlled experiments ⁶. We define a Gibbs energy for the specimen as the Legendre transform of A with respect to all elements of $\boldsymbol{\varepsilon}$, plus an isotropic pressure-volume term ¹³⁷:

$$G = A + p'V_0 - V_0 \sum_{ij} \sigma_{ij} \varepsilon_{ij} = \mathcal{V}_{\text{inh}} + A_{\text{vib}} + p'V_0 - V_0 \sum_{ij} \sigma_{ij} \varepsilon_{ij} \quad (6.7)$$

where $p' = -1/3\text{Tr}(\boldsymbol{\sigma})$. By substituting Equation (6.4) or (6.5) in Equation (6.3) and using the result in Equation (6.7) one can obtain the Gibbs energy of a glassy specimen according to a quantum mechanical or a classical formalism for the vibrations, for given edge vectors of a periodic simulation box. It is important to realize that \mathcal{V}_{inh} and A_{vib} in Eq. (6.7) are both functions of the spatial extent of the system. Under given externally imposed stress $\boldsymbol{\sigma}$, the system will adopt that spatial extent (edge vectors of the periodic simulation box) which minimizes G . We shall call G_{min} the value of G at that minimum. This is our estimate of the Gibbs energy of the specimen under stress $\boldsymbol{\sigma}$, confined to a given basin in configuration space. As $\boldsymbol{\sigma}$ changes, the spatial extent of the system changes. The potential energy hypersurface is distorted and the inherent structure configuration shifts. The system, however, remains in the same (deformed)

basin. This is the essence of the quasiharmonic approximation, which retains full anharmonicity in the dependence of $\mathcal{V}'_{\text{inh}}$ on the atomic coordinates, but assumes that thermal motion can be represented as a set of harmonic vibrations around the inherent structure.

The fundamental equation of thermodynamics for our specimen confined in its basin, in differential form, in the Gibbs energy representation, becomes

$$dG_{\text{min}} = -SdT + V_0 dp' - V_0 \sum_{ij} \varepsilon_{ij} d\sigma_{ij} \quad (6.8)$$

with S being the entropy.

In order to generate undeformed specimens of glassy atactic polystyrene according to the QHA at each temperature at pressure $p=1$ bar, we take the last configuration from our NpT MD run at that temperature and minimize its energy with respect to all atomic coordinates, under fixed spatial extent of the simulation box. Then we vary systematically the spatial extent (boundaries) of the simulation box, minimizing the potential energy of its contents and calculating the normal mode frequencies and vibrational free energy A_{vib} for each new set of boundaries, until we reach a minimum of $\mathcal{V}'_{\text{inh}} + A_{\text{vib}} + pV$ with respect to these boundaries. The minimum energy configuration and the vibrational frequencies at this minimum define our undeformed state, and its volume is taken as V_0 for that temperature. Clearly, this state point is a minimum of G defined by Eq. (6.7) with $\boldsymbol{\sigma}=\text{diag}(-p, -p, -p)$, $p'=p = 1$ bar and $\boldsymbol{\varepsilon}=\mathbf{0}$. In these calculations the simulation box shape is kept cubic at all times, so the spatial extent of the system is uniquely defined by the edge length of the periodic simulation box, l , the volume being given by $V=l^3$. The edge length is varied in steps of $\Delta l=0.001$ Å. The procedure is entirely analogous to that developed in Ref. ^{133b} for a Lennard-Jones glass.

Figure 6.1 depicts the comparison between the estimated volumetric behavior of the studied system obtained via our MD cooling runs in the NpT ensemble and corresponding results based on the QHA. Points correspond to averages over the 5 specimens generated. QHA results are shown based on both the quantum mechanical (Eq. (6.4)) and the classical (Eq. (6.5)) partition function. In addition, experimental volumetric data for long-chain atactic polystyrene are shown in the figure ¹³⁸.

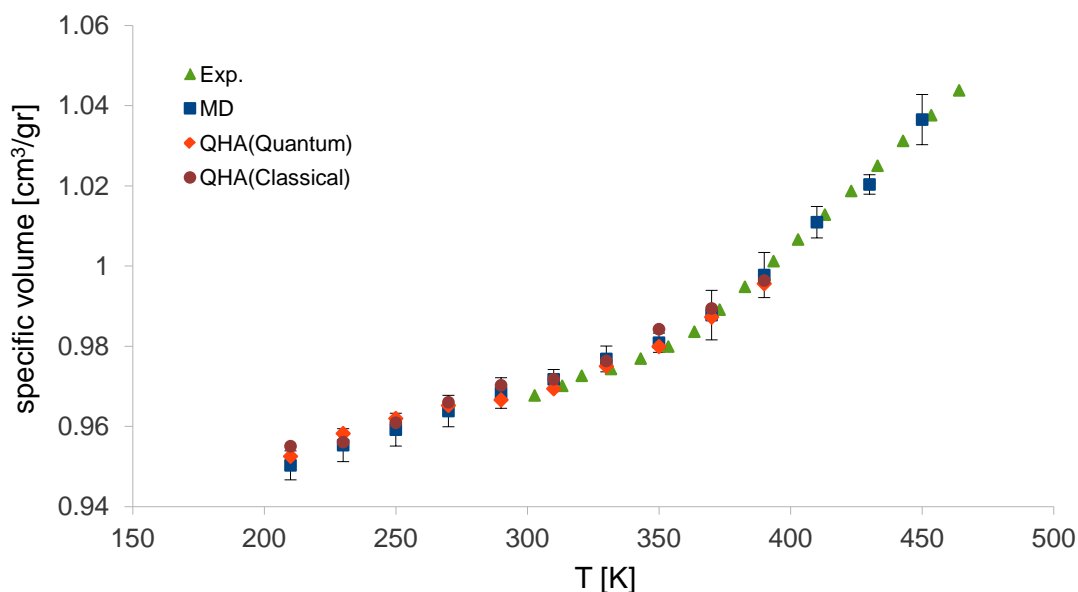


Figure 6.1: Schematic representation of the volumetric behavior of atactic polystyrene at 1 bar, as calculated via a) MD computational cooling experiments in the NpT statistical ensemble b) QHA with a quantum mechanical vibrational partition function, c) QHA with a classical partition function. Experimental volumetric data measured for high-molar mass atactic polystyrene from Ref. ¹³⁸ are also shown.

At this point the reader is reminded that all simulation results plotted in Figure 6.1 constitute ensemble average values over 5 different specimens, obtained from 5 completely uncorrelated initial configurations. Error bars in the figure represent standard deviations over these specimens. For the sake of clarity, only error bars corresponding to the MD cooling runs have been included in Figure 6.1. Use of all 200 configurations would certainly lead to lower statistical error, yet increase the computational load. Error bars from the QHA approaches are commensurate with those shown for MD.

Figure 6.1 can serve as a basis for a number of interesting observations. First of all, results from the quantum mechanical and from the classical QHA do not differ substantially. This is because temperatures in the considered range are high relative to the Debye temperature of glassy atactic polystyrene $\Theta_D \approx 100$ K ¹³⁹, so the classical

vibrational partition function constitutes a reasonable approximation for the quantum mechanical one. Secondly, volumes from QHA in the glassy region are in good agreement with corresponding MD volumes. This indicates that the effect of anharmonicities on the volumetric behavior is weak, making the quasiharmonic approximation a reasonable one over the considered temperature range. Thirdly, there is good agreement between simulation estimates and experimental specific volumes.

In the melt range this reflects that the force field⁴¹ has been developed so as to provide a reasonable representation of real atactic polystyrene. In the glassy range the agreement is partly fortuitous. The cooling rate employed in MD (0.5 K/ns) is many orders of magnitude higher than typical experimental cooling rates, and should cause T_g to appear higher in the simulated system than in experiment. In addition to that, it has been seen¹⁴⁰ that the diffusion of polymer chains in computer simulations of finite systems with periodic boundary conditions is slower (higher T_g) as the volume of the simulation box and the number of chains become smaller. On the other hand, the molar mass of the polystyrene simulated is small relative to that studied experimentally, causing a decrease in T_g compensating the above phenomena. As a consequence, the estimated glass temperature from simulation, $T_g \approx 380$ K, appears slightly higher than the experimental value $T_g \approx 373$ K^{132a, 141}. Note that the simulated glass transition is quite broad, as is typical of simulations¹⁴². The overall behavior of volumetric predictions in Figure 6.1 convinces us that the QHA yields reasonable results and that our model is satisfactory. Thus, we proceed to study its mechanical properties.

6.3 Computational deformation experiments

As described in Section 6.2.1, two hundred independent, completely uncorrelated initial configurations were generated by chain growth and subsequent energy minimization in a cubic box with periodic boundary conditions at a density of 0.97 g/cm³. Each one of those spatial configurations of the polymer chain was then made a starting point in the Dynamic Integration of a Markovian Web (DIMW) algorithm for tracking the dynamical evolution of a system evolving through infrequent transitions on a network of discrete states⁵², in order to monitor a single elementary transition from the starting potential energy minimum to an adjacent one at temperature T and

pressure $p = 1$ bar. To do this, we have invoked an appropriately modified version of the dimer method^{80c} for locating first order saddle points around a given minimum, and constructed transition paths to new minima according to Fukui's intrinsic reaction coordinate method⁸¹. In this way, the glassy system is envisioned as fluctuating in the vicinity of a local potential energy minimum, going over a first order saddle point and ending up in a neighboring minimum.

According to this, every minimum out of the 200 initial ones, led to a corresponding adjacent minimum via an elementary transition over a first order saddle point. Thus, 200 completely uncorrelated potential energy minima of glassy atactic polystyrene, close to the original ones, were obtained. The later 200 minima were used as initial configurations of our stress controlled deformation experiments. Unless stated otherwise, all results shown from this point on are ensemble averages over those 200 uncorrelated inherent structures. We note that the procedure of using structures obtained from the initial ones after an elementary transition over a saddle point is not essential to the calculations reported here; it was adopted as a test of our algorithm for effective elementary transitions in configuration space. Working with the initial 200 minima produces practically indistinguishable results.

The deformation experiments proceed in the following way: We start from a potential energy minimum, obtained as described in the previous paragraph. Each such minimum constitutes a specimen of minimal Gibbs energy with respect to the spatial extent of the system under temperature T and stress tensor $\boldsymbol{\sigma} = \text{diag}(-p, -p, -p)$ with $p = 1$ bar and defines the zero-strain state $\boldsymbol{\varepsilon} = 0$ for the deformations. We then perform uniaxial deformation experiments (both in tension and in compression) by imposing normal stresses acting on two opposing faces of our simulation box. All other faces of the simulation box are under atmospheric pressure. In other words, the stress tensor imposed is of the type $\boldsymbol{\sigma} = \text{diag}(\sigma_{xx}, -p, -p)$, $p = 1$ bar. Both $\sigma_{xx} > -p$ (tension) and $\sigma_{xx} < -p$ (compression) were used. All deformation simulations were realized at a temperature of $T = 200$ K and lateral pressure of $p = 1$ bar. The tensile stress σ_{xx} is varied in steps of $\Delta\sigma_{xx} = \pm 5$ MPa from 0 to ± 30 MPa. At each level of the imposed stress, using an affine transformation of the undeformed specimen configuration as an initial guess, we systematically vary the spatial extent of our system (edge vectors of the periodic simulation box). At each spatial extent we minimize the potential energy,

compute the vibrational free energy, and add a stress-strain contribution to obtain the Gibbs energy G of the system in its (deformed) basin via Eq. (6.7). Through these simulations we locate the spatial dimensions under which G attains a minimal value, G_{\min} . The minimum energy configuration and associated vibrational frequencies at G_{\min} define our model for the specimen under stress σ and the spatial dimensions of the system at G_{\min} define our strain tensor relative to the initial undeformed state. Having obtained the deformed state at the current level of stress, we increment the imposed stress by $\Delta\sigma_{xx}$ and repeat the whole procedure.

In the course of the variational computations in model system dimensions to determine G_{\min} , the geometry of the simulation box is kept orthogonal and the cross-section normal to the direction of deformation is kept square. The minimization of the Gibbs energy thus proceeds with respect to two box edge lengths, l_x and $l_y=l_z$. Edge lengths are varied in steps of $\Delta l=0.001 \text{ \AA}$. For every trial set of box edge lengths the elements of the strain tensor and the Poisson ratio are calculated according to the following equations:

$$\varepsilon_{xx} = \ln \frac{l_x}{l_{x,0}} \quad (6.9)$$

$$\varepsilon_{yy} = \ln \frac{l_y}{l_{y,0}} = \varepsilon_{zz} = \ln \frac{l_z}{l_{z,0}} \quad (6.10)$$

and

$$\nu = -\frac{\varepsilon_{yy}}{\varepsilon_{xx}} = -\frac{\varepsilon_{zz}}{\varepsilon_{xx}} \quad (6.11)$$

where $l_{\alpha,0}$ is the box edge length in the α -direction in the undeformed state and l_α is the corresponding box edge length after the imposed deformation step. Note that in Eqs. (6.10) and (6.11) the Hencky definition of strains is employed¹⁴³. For the small deformation regime examined here, this gives results that are practically indistinguishable from the conventional definition $\varepsilon_{xx} = \frac{l_x - l_{x,0}}{l_{x,0}}$ etc. Our stress-

controlled procedure for simulating deformation based on the QHA is outlined in Figure 6.2.

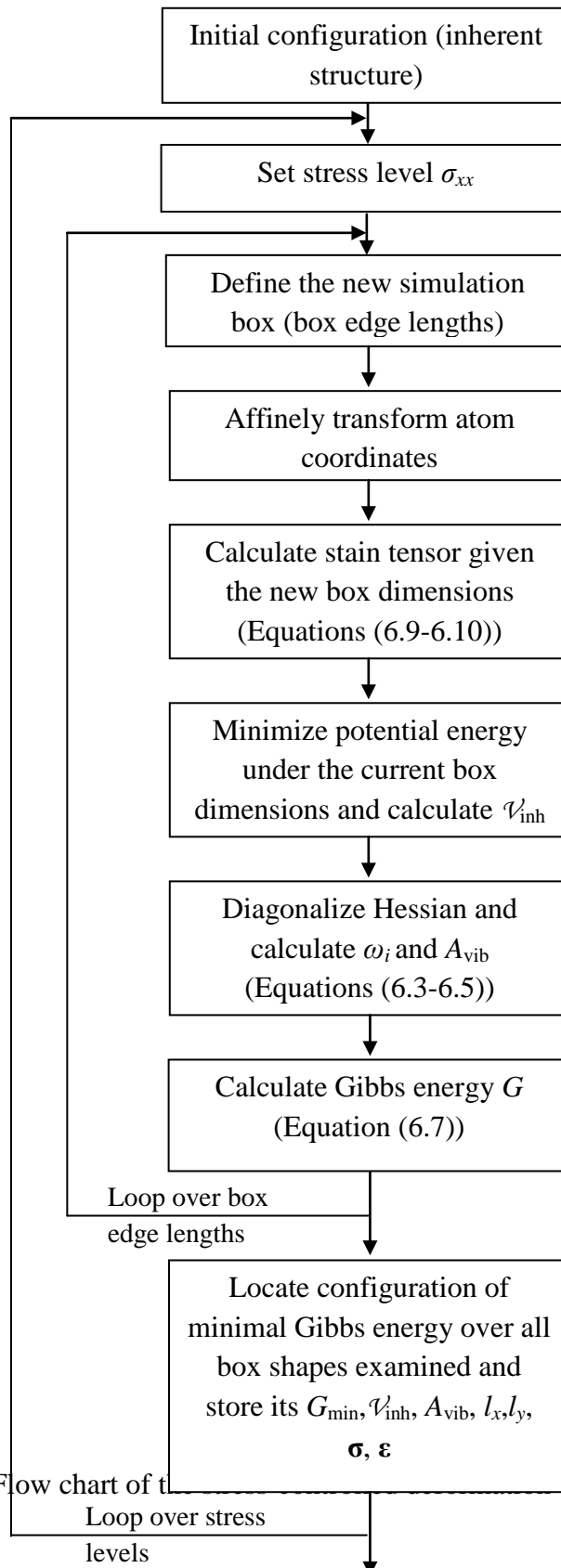


Figure 6.2: Flow chart of the computer experiments.

In the following section we will demonstrate and analyze the results obtained from the uniaxial tension and compression deformation experiments for the glassy atactic polystyrene system.

6.4 Results and discussion

We apply the deformation algorithm outlined in Figure 6.2 for all 200 initial, uncorrelated configurations, sampled in the way described in Section 6.2, for a series of imposed normal stresses in the x -direction shown in Table 6.1. We remind the reader that every deformation experiment is initialized from the undeformed state, where the simulation box is cubic and a normal stress of $-p = -1\text{atm}$ is acting upon each one of its lateral faces. Alternatively, we could initialize every deformation experiment from the previous immediately lower stress level and keep the stress steps constant and equal to $\Delta\sigma_{xx}=\pm 5$ MPa. The result of this alternative deformation procedure is expected and was confirmed to be the same to the adopted deformation course for the linear elastic regime investigated.

Table 6.1. Imposed normal stresses in the x -direction for a series of deformation experiments.

Experiment	1	2	3	4	5	6	7	8	9	10	11	12
σ_{xx} [MPa]	5	10	15	20	25	30	-5	-10	-15	-20	-25	-30

The above described deformation experiments were realized at four different temperatures, 200 K, 250 K, 300 K, and 350 K, all of which lie below the glass transition temperature of the model system and of real atactic polystyrene. The stress-strain curves obtained are shown in Figure 6.3.

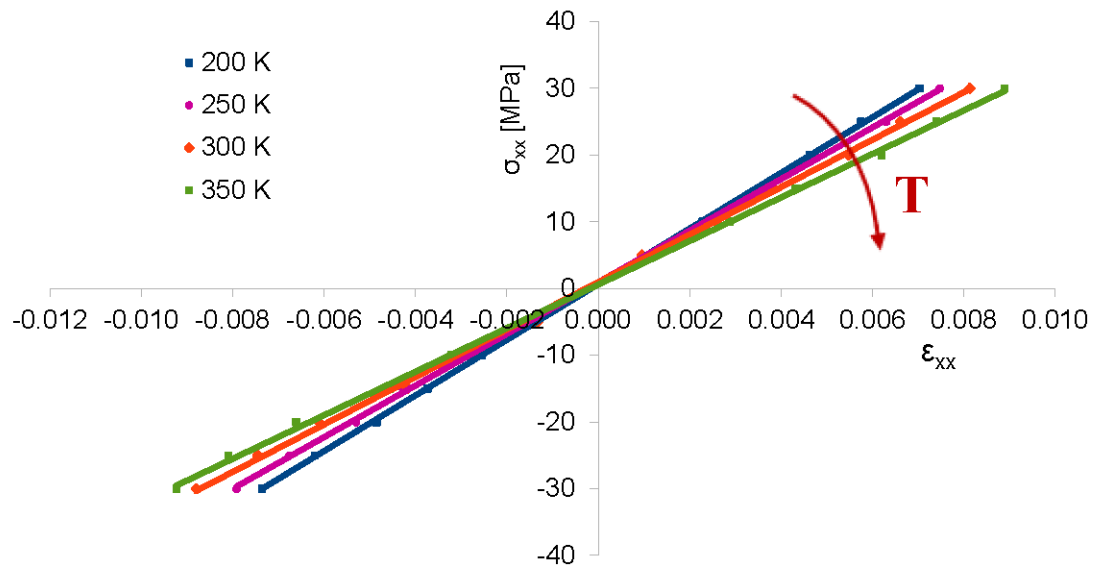


Figure 6.3: Stress-strain curves obtained via stress-controlled uniaxial deformation computer experiments in tension and compression under atmospheric pressure at four different temperatures below the glass temperature of atactic polystyrene. The points represent averages over 200 different “specimens” subjected to deformation. For each temperature, a linear fit through the simulation points is shown. The arrow indicates the direction of increasing temperature.

In Figure 6.3 we plot the ensemble average of the calculated strain for 200 inherent structures for every imposed stress listed in Table 6.1. Error bars have been omitted for clarity. They are on the order of $\pm 1 \times 10^{-4}$ in the strain. Over the explored regime of stresses (up to ± 30 MPa) and strains (up to $\pm 1\%$) the relationship between σ_{xx} and ϵ_{xx} is linear, to an excellent approximation. Deformation, as probed through our QHA computer experiments on the assumption that each specimen remains confined in its basin, is elastic. The slope of the fitted straight lines yields the Young’s modulus E . For the temperature of 300 K the slope equals $E = 3.55$ GPa, a value which is in very good agreement with experimental data reported in the literature^{132a} $E_{\text{exp}} = 3.2 - 3.4$ GPa. Other, more recent experimental sources report somewhat higher measured values of the Young’s modulus¹⁴⁴ for glassy atactic polystyrene at room temperature (~ 300 K): $E_{\text{exp}} = 3.5 - 3.7$ GPa. The calculated Young’s modulus $E = 3.55$ GPa is in good accordance with all these measurements.

The temperature dependence of the Young's modulus extracted from Figure 6.3 has also been tested and found to be in accordance with experimental measurements for polystyrene^{132a, 145}, as well as for other polymers, such as poly(butylene terephthalate), for temperatures below the glass temperature¹⁴⁶. The Young's modulus of glassy polymers is known to increase as temperature drops, i.e., with decreasing temperature the material becomes stiffer. Experimental measurements^{132a} have yielded a temperature dependence of the Young's modulus of glassy atactic polystyrene that is described by the following equation:

$$\frac{dE}{dT} = -4.48 \text{ MPa} \cdot \text{K}^{-1} \quad (6.12)$$

According to Equation (6.12), a temperature increase of $\Delta T=50$ K (equal to the temperature step used in Figure 6.3), should lead to a decrease of the Young's modulus by $\Delta E = -224 \text{ MPa} = -0.224 \text{ GPa}$. Table 6.2 shows the calculated Young's moduli, based on the slopes of the curves shown in Figure 6.3:

Table 6.2. Calculated Young's modulus of atactic polystyrene for the four investigated sub- T_g temperatures of Figure 6.3.

Temperature [K]	Young's modulus E [GPa]
200	4.17
250	3.87
300	3.55
350	3.26

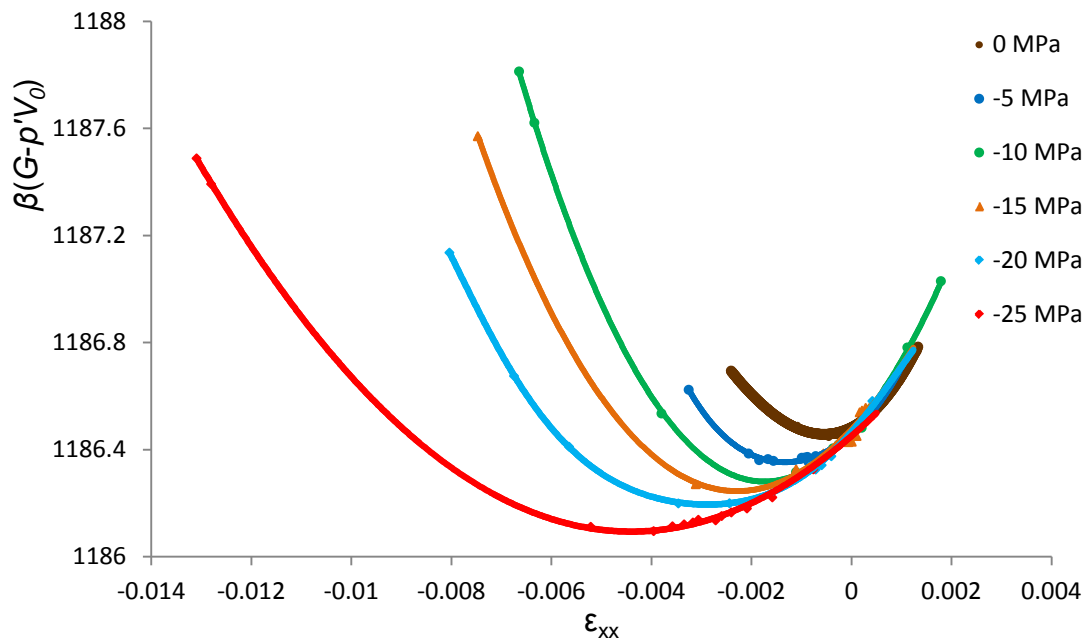
According to Table 6.2, the average Young's modulus change for a temperature increase of $\Delta T=50$ K ($\Delta T = 50$ K) is equal to $\langle \Delta E \rangle = -0.3 \text{ GPa}$. This result is in reasonable agreement with the experimental value of $\Delta E = -0.224 \text{ GPa}$ extracted with the help of Eq. (6.12), a fact indicating that the temperature dependence of the elastic response predicted by our QHA approach to small-strain deformation of the polymer glass is basically correct.

Another observable obtainable directly from our computer deformation experiments is the Poisson ratio (Eq. (6.11)). For the temperature of 300 K this was found to be $\nu = 0.35$, very close to the experimentally measured value^{132a, 145} of $\nu_{\text{exp}} = 0.33$. In addition to that, the temperature dependence of the Poisson ratio is found to be in qualitative agreement with the experimentally observed behavior¹⁴⁵⁻¹⁴⁷, i.e., the Poisson ratio increases slightly with increasing temperature. In particular, the change of Poisson ratio with temperature for temperatures close to or below the glass transition temperature is measured to be $\left(\frac{d\nu}{dT}\right)_{\text{exp}} \approx 0.00015 \text{ K}^{-1}$. Both the behavior of the Poisson ratio with increasing temperature is described qualitatively correctly based on our simulations, i.e., we predict a Poisson ratio increase with increasing temperature, and the corresponding value obtained from our simulation lies very close to the experimental one, $\left(\frac{d\nu}{dT}\right)_{\text{sim}} \approx 0.00022 \text{ K}^{-1}$. One possible explanation for this small deviation is that the QHA simulations presented here do not allow the glassy polymer configuration to depart from its original basin, while such departures do take place at high temperatures, close to T_g . Calculations are underway which relax this assumption. As temperature increases and goes above the transition temperature T_g , experimental measurements show that the Poisson ratio approaches the elastomeric value of $\nu \approx 0.5$ ¹⁴³.

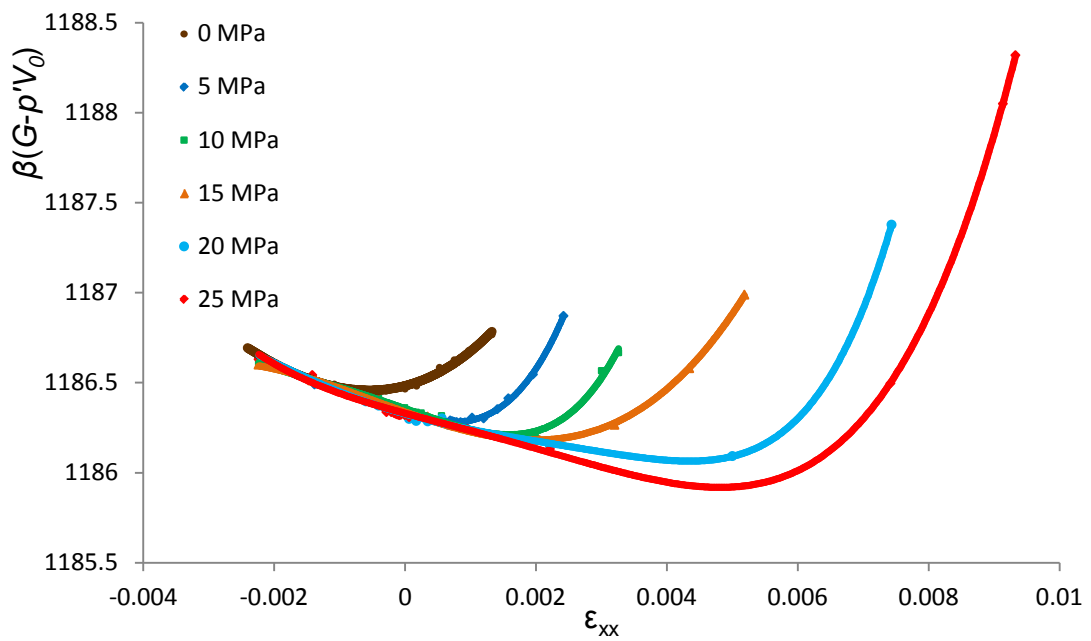
Another important matter which needs to be clarified within this work is the effect of the chain length on the simulated mechanical properties (i.e. Young modulus and Poisson ratio). Previous studies have shown that the molecular mass dependence of the Young modulus, although small, is of great importance from both a fundamental and practical perspective. It has been demonstrated¹⁴⁸ that low molecular mass polystyrene films exhibit a decreased Young modulus in comparison to systems of larger molecular weight. The dependence of the elastic constants on molar mass, or on nanoscopic confinement, has not been investigated in this work, although the methodology developed and adopted herein could be used for this purpose.

Examining the results obtained from the deformation of each one of our 200 glassy computer specimens allows some interesting observations to be made on how individual basins on the energy landscape respond to deformation in the elastic regime. We have found that the way in which the general shape and geometry of basins change

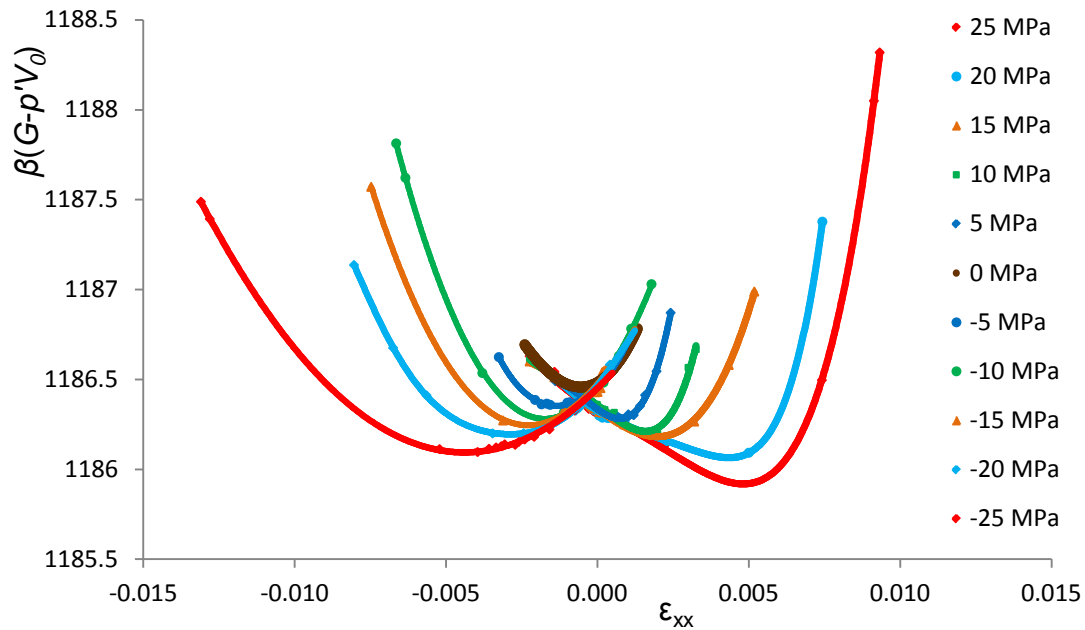
upon deformation can be categorized in three major types. Characteristic representatives of each one of these types are shown in Figures 6.4-6.6:



(a)

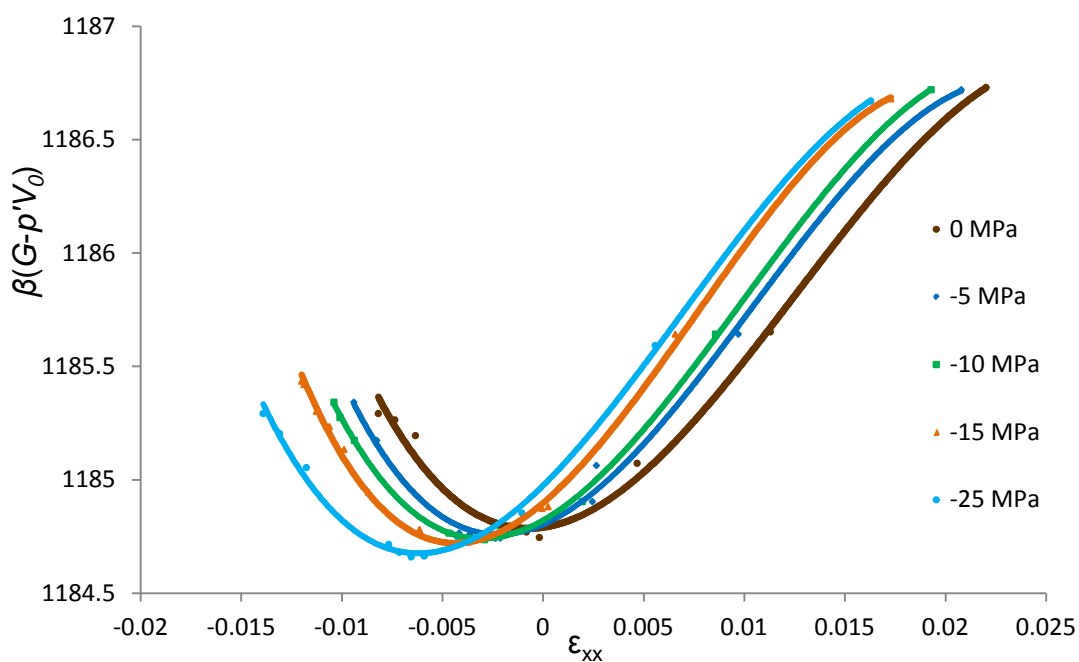


(b)



(c)

Figure 6.4: Graphical representation of the first type of an inherent structure's response to mechanical deformation for (a) compression, (b) tension and (c) both tension and compression. In all three diagrams data points for $G-p'V_0$ as a function of ϵ_{xx} are shown for every imposed stress level, along with polynomial fits (colored lines) through these data points. All deformation simulations were realized at a temperature of $T = 1/(k_B\beta) = 200$ K and external pressure of $p = 1$ bar.



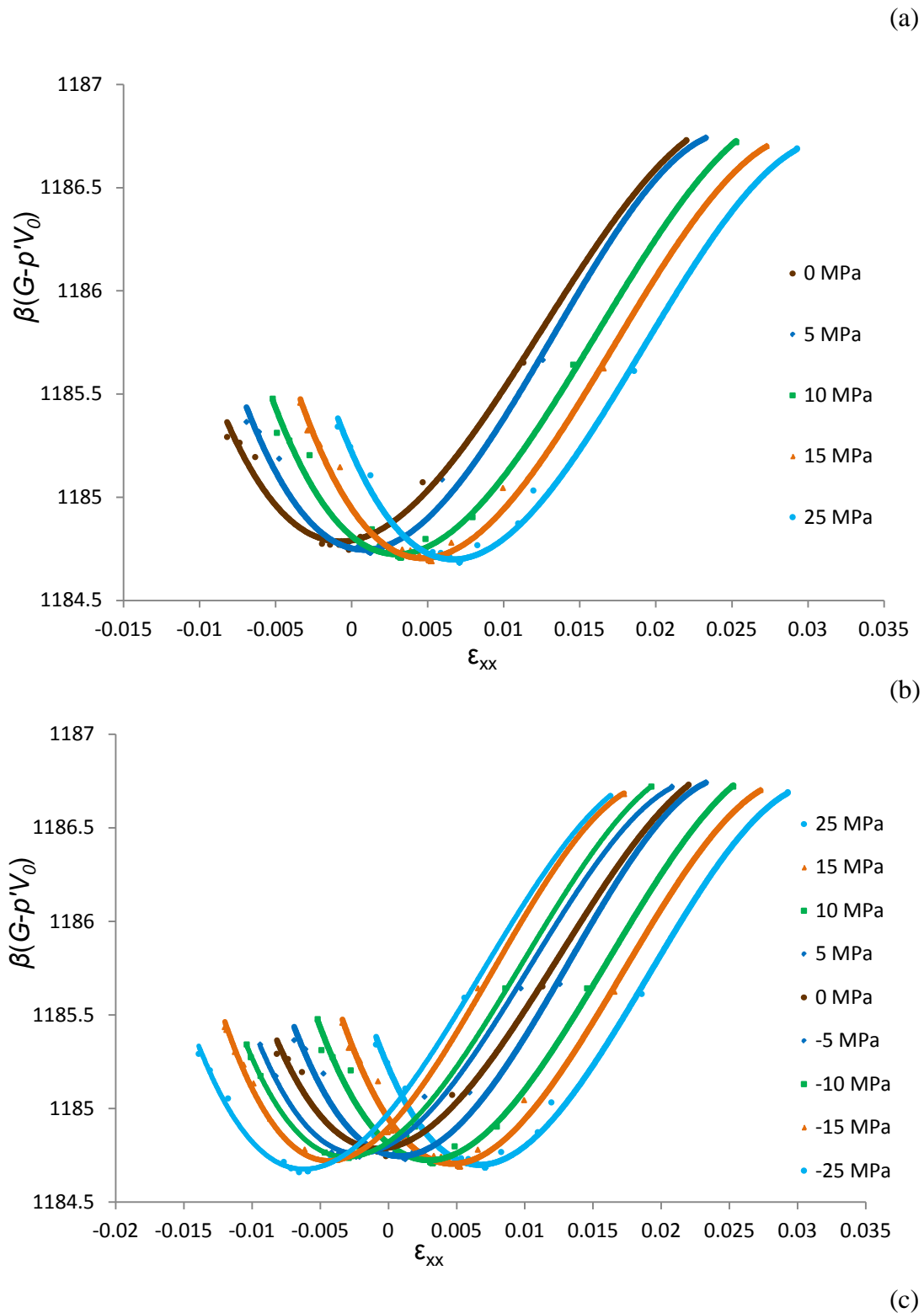
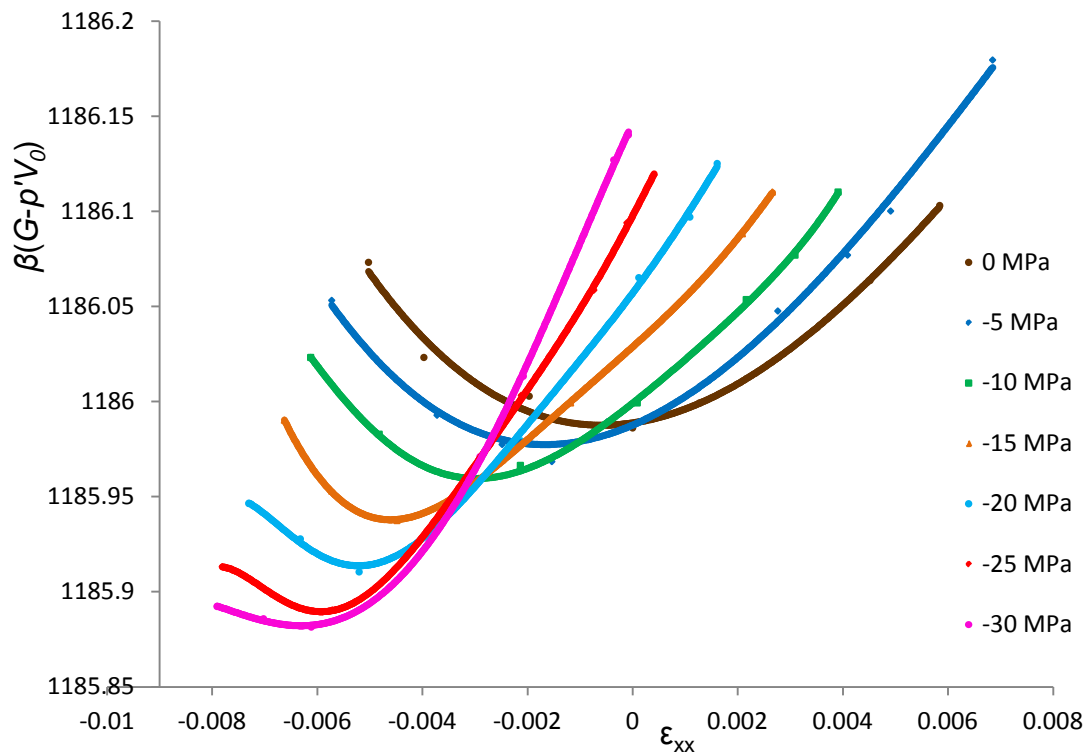


Figure 6.5: Graphical representation of the second type of an inherent structure's response upon mechanical deformation for (a) compression, (b) tension and (c) both tension and compression. In all three diagrams for $G-p'V_0$ as a function of ϵ_{xx} , data points for every imposed stress level are shown, along with polynomial fits (colored

lines) through these data points. All deformation simulations were realized at a temperature of $T = 200$ K and external pressure of $p = 1$ bar.



(a)

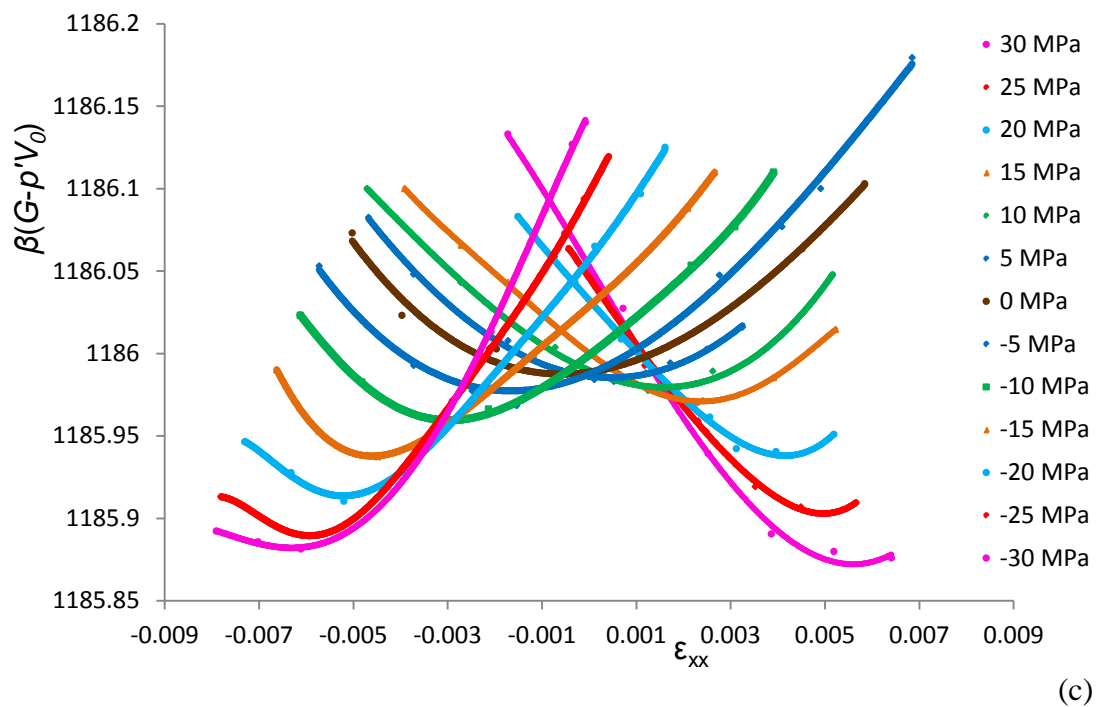
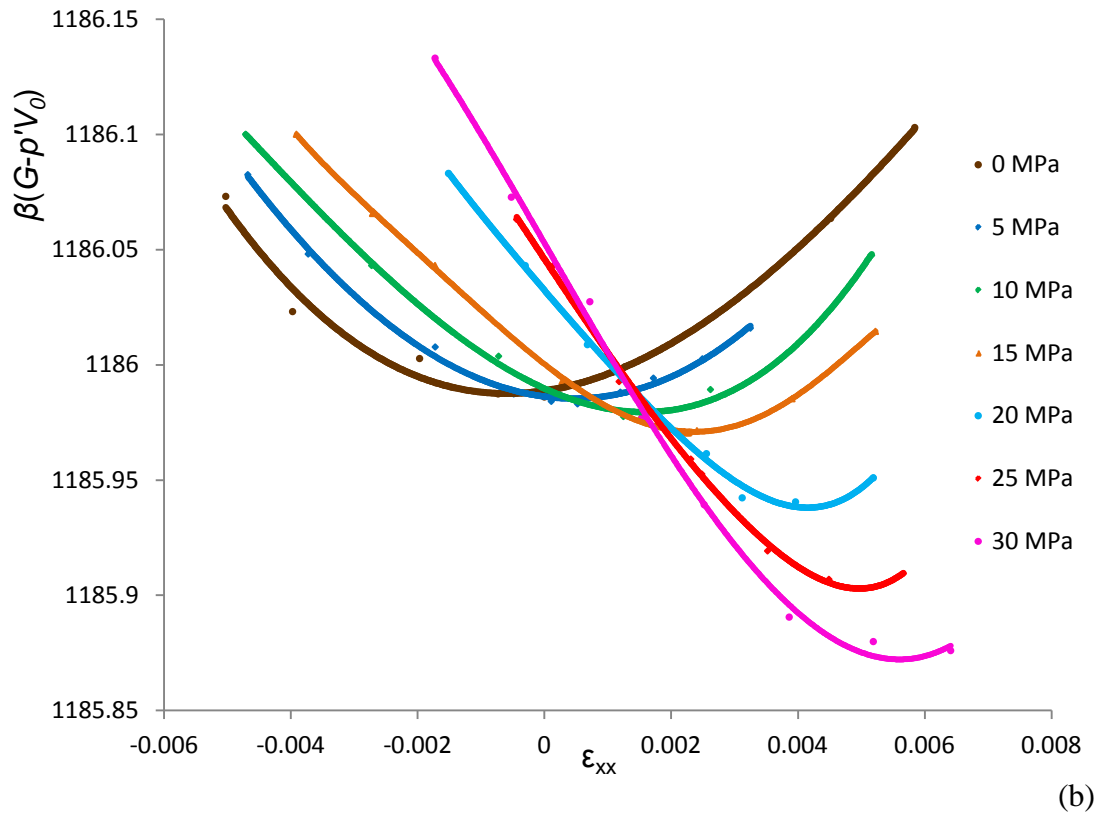


Figure 6.6: Graphical representation of the third type of an inherent structure's response upon mechanical deformation for (a) compression, (b) tension and (c) both tension and compression. In all three diagrams data points for $G-p'V_0$ as a function of ϵ_{xx} are shown for every imposed stress level, along with polynomial fits (colored lines)

through these data points. All deformation simulations were realized at a temperature of $T = 200$ K and hydrostatic pressure of $p = 1$ bar .

Each one of the figures 6.4-6.6 refers to a particular specimen (inherent structure) and shows the system's response to both compression and tension . The (a) part of each figure shows the response of the specimen to uniaxial compression, whereas the (b) part shows the response to uniaxial tension. Part (c) depicts the total behavior for both compression and tension. In part (c), it becomes clear that the response of the PEL's basin to imposed deformation is symmetric. This response is displayed as a set of curves for $G - p'V_0$ as a function of ε_{xx} , each curve corresponding to a different stress level (outer loop in the flow chart of Figure 6.2). Each curve is a set of points which resulted from a calculation of the Gibbs energy as a function of the spatial extent of the model system according to Equation (6.7) (inner loop in the flow chart of Figure 6.2). Each such point is a minimum of $G - p'V_0$ under the considered ε_{xx} with respect to $\varepsilon_{yy} = \varepsilon_{zz}$. The value of $\varepsilon_{yy} = \varepsilon_{zz}$ at that minimum is not shown. Each curve for $G - p'V_0$ as a function of ε_{xx} exhibits a well-defined minimum. The ordinate corresponding to this minimum is $G_{\min} - p'V_0$, while the abscissa marks the value of strain ε_{xx} with which the specimen responds to the stress level considered.

The strain values at which each curve for $G - p'V_0$ as a function of ε_{xx} attains its minimum can be seen to be in good agreement with the ensemble averaged strain values corresponding to the imposed stress, shown in Figure 6.3.

From Figure 6.4(c) it can be easily seen that upon deformation the initial, undeformed inherent structure (brown curve) changes its general shape and geometry in a symmetric way if compressed or extended.

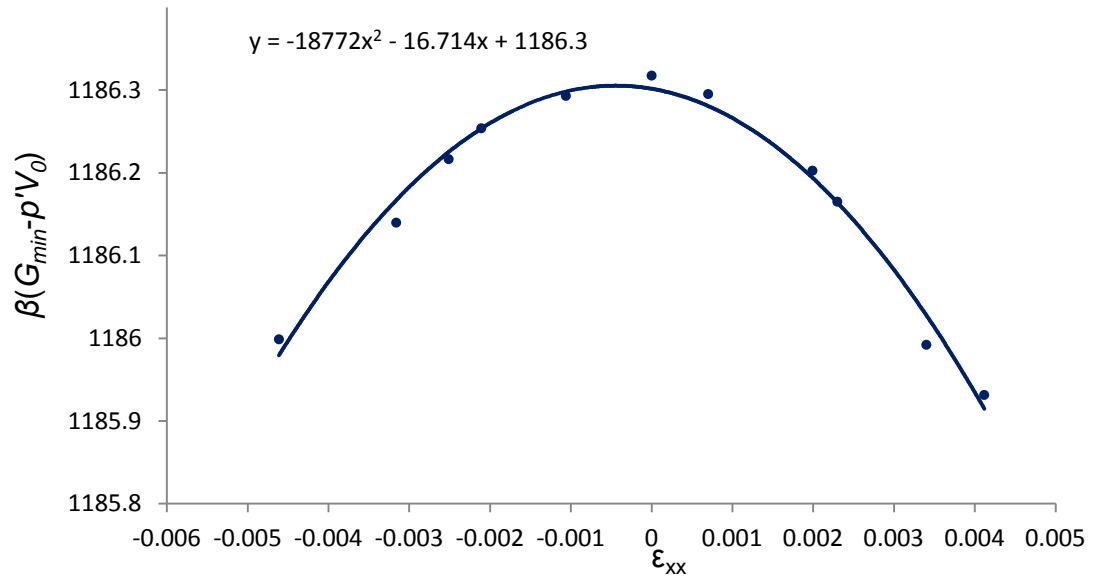
By observing figure 6.5(c) we can conclude that in this case the shape of the $G - p'V_0$ versus ε_{xx} curve changes only little with the imposed stress level. G_{\min} does become deeper upon both compression and tension relative to the undeformed state, but by less than in Figure 6.4(c). In this case the basin is broad and is not distorted significantly upon imposition of the deformation. The response is again symmetric around the undeformed state (brown curve in Figure 6.5(c)).

A third, and perhaps most interesting type of response is shown in Figure 6.6. Here the basin tilts upon imposition of deformation, either tensile or compressive changing as a result completely its shape. The minimum in $G - p'V_0$ as a function of ε_{xx} seems about to disappear at the highest stress levels considered.

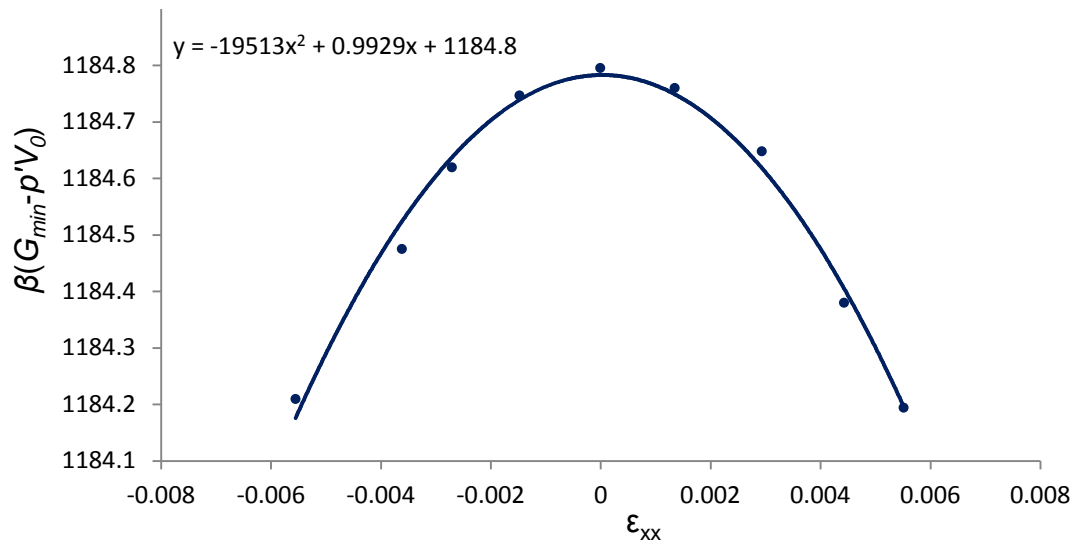
As in Figures 6.4(c) and 6.5(c), also in the case of Figure 6.6(c) the deformed basin seems to behave symmetrically around the initial, undeformed basin, depicted in the figure with a brown curve. In contrast to Figures 6.4(c) and 6.5(c), we now observe a significant change in the shape of the basin, which seems prone to merge with a neighboring basin. For this type of response we suspect that inherent structures existing in the undeformed state may be totally eliminated upon subjecting the system to sufficiently high deformation or, conversely, new basins may be generated upon imposition of deformation. Such events have been observed^{119, 125a} and mark the onset of plastic response.

Figures 6.4-6.6 provide clear evidence that the energy landscape of a glassy polymer changes its geometrical shape upon deformation. This conclusion has extremely important consequences. Changes in the geometry of the potential energy landscape imply that the dynamical behavior of a system evolving upon this landscape will also change⁵². This means that initially rare transitions between minima separated by high energy barriers could become more frequent, or adjacent minima of the potential energy landscape may merge with increasing deformation, forming a joint minimum and thus any former transitions between them will vanish.

The minimum values of $G - p'V_0$ for the curves depicted in the (c) part of Figures 6.4-6.6 have been isolated and plotted against ε_{xx} . The resulting plots derived from these figures are shown in Figure 6.7. All plots derived from Figures 6.4 to 6.6 exhibit similar behavior.



(a)



(b)

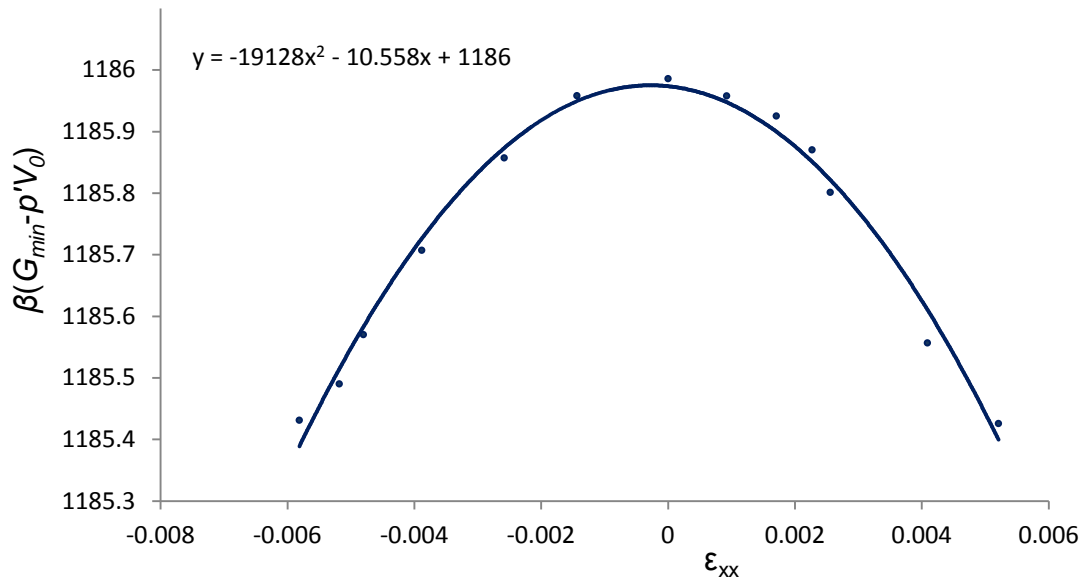


Figure 6.7: Graphical representation of $G_{\min} - p'V_0$ as a function of ϵ_{xx} for the basin response to mechanical deformation depicted in a) Figure 6.4(c), b) Figure 6.5(c) and c) Figure 6.6(c). A parabolic fit through the simulation points is also shown as a broken line. The curvature of the parabolae is directly related to the Young's moduli of the corresponding specimens as explained in main text. All results are for glassy atactic polystyrene at a temperature of $T = 200$ K and hydrostatic pressure of $p = 1$ bar.

As shown in all parts of Figure 6.7, the plot of $G_{\min} - p'V_0$ as a function of ϵ_{xx} has a parabolic shape, exhibiting a maximum at zero strain (or stress). In Table 6.3 we have collected the coefficients of the second order polynomial equations describing the response of the three specimens studied in figures 6.4(c), 6.5(c), and 6.6(c). As a measure of how well the simulation points can be described by the fitted parabolae, we use the coefficient of determination of the fit (R^2), which is also shown in Table 6.3 for all three specimens.

Table 6.3. Coefficient values of the second order polynomial equation $y = a \cdot x^2 + b \cdot x + c$ used to fit the simulation points obtained by plotting the minimum values of $(G - p'V_0)/(k_B T)$ against the strain ϵ_{xx} for each one of the curves depicted in

the (c) part of Figures 6.4-6.6. The coefficients of determination R^2 are also shown as measures of the agreement between simulation points and fitting equation. The standard deviation between simulated and fitted points is about 0.02. The simulation points derived from the (c) part of Figures 6.4 – 6.6, along with the fitted parabola, are shown in Figure 6.7.

Specimen	a	b	c	R^2
1	-18772	-16.714	1186.3	0.982
2	-19513	-0.9929	1184.8	0.987
3	-19128	-10.558	1186	0.984

What is the thermodynamic meaning of the slope and curvature of the $G_{\min} - p' V_0$ versus ε_{xx} curves? To answer this, we start from the definition of the Gibbs energy, Equation (6.7). At the point where G exhibits a minimum with respect to the spatial extent of a specimen, for the stress state $\boldsymbol{\sigma} = (\sigma_{xx}, -p, -p)$ applied in our simulations and under the shape constraints ($\varepsilon_{yy} = \varepsilon_{zz} = -\nu \varepsilon_{xx}$) imposed on our model system, this becomes:

$$G_{\min} = \mathcal{V}'_{\text{inh}} + A_{\text{vib}} + p'V_0 - V_0(\sigma_{xx} + 2\nu p)\varepsilon_{xx} \quad (6.13)$$

with $p' = (-\sigma_{xx} + 2p)/3$. On the other hand, from Eq. (6.7) and the condition that G at the considered point must be at a minimum with respect to the spatial extent of the system under the prevailing $\boldsymbol{\sigma}$ and T , assuming a deformation-independent ν , one obtains:

$$dG = d(\mathcal{V}'_{\text{inh}} + A_{\text{vib}} + p'V_0) - V_0(\sigma_{xx} + 2\nu p)d\varepsilon_{xx} = d(\mathcal{V}'_{\text{inh}} + A_{\text{vib}}) - V_0(\sigma_{xx} + 2\nu p)d\varepsilon_{xx} = 0$$

or

$$\left. \frac{\partial(\mathcal{V}'_{\text{inh}} + A_{\text{vib}})}{\partial\varepsilon_{xx}} \right|_{T,p} - V_0(\sigma_{xx} + 2\nu p) = 0 \quad (6.14)$$

Differentiating Equation (6.13) with respect to ε_{xx} under constant T and p , assuming a deformation-independent ν , yields

$$\left. \frac{\partial(G_{\min} - p'V_0)}{\partial \varepsilon_{xx}} \right|_{T,p} = \left. \frac{\partial(\mathcal{V}'_{\text{inh}} + A_{\text{vib}})}{\partial \varepsilon_{xx}} \right|_{T,p} - V_0(\sigma_{xx} + 2\nu p) - V_0 \varepsilon_{xx} \left. \frac{\partial \sigma_{xx}}{\partial \varepsilon_{xx}} \right|_{T,p} = 0 \quad (6.15)$$

Combining Equations (6.14) and (6.15) gives

$$\left. \frac{\partial(G_{\min} - p'V_0)}{\partial \varepsilon_{xx}} \right|_{T,p} = -V_0 \varepsilon_{xx} \left. \frac{\partial \sigma_{xx}}{\partial \varepsilon_{xx}} \right|_{T,p} \quad (6.16)$$

Equation (6.16) is actually a special form of the fundamental equation, (Eq. (6.8)), for the isothermal elastic uniaxial deformation considered here.

On the right hand side of Eq. (6.16) we recognize the derivative of stress with respect to strain as the Young's modulus E :

$$E = \left. \frac{\partial \sigma_{xx}}{\partial \varepsilon_{xx}} \right|_{T,p} \quad (6.17)$$

From Eqs. (6.16) and (6.17) one obtains:

$$\left. \frac{\partial(G_{\min} - p'V_0)}{\partial \varepsilon_{xx}} \right|_{T,p} = -V_0 \varepsilon_{xx} E \quad (6.18)$$

Differentiating Eq. (6.18) once more with respect to ε_{xx} and assuming a strain-independent E , we obtain

$$\left. \frac{\partial^2(G_{\min} - p'V_0)}{\partial \varepsilon_{xx}^2} \right|_{T,p} = -V_0 E \quad (6.19)$$

The physical meaning of the $G_{\min} - p'V_0$ versus ε_{xx} curve for a specific specimen becomes clear in the light of Eqs. (6.18) and (6.19). The slope of $G_{\min} - p'V_0$ with respect to ε_{xx} is the undeformed system's volume times the strain times the Young's modulus of the specimen. It is positive in the compressive, negative in the tensile part of the curve, and zero at $\varepsilon_{xx} = 0$. All these characteristics are confirmed by the three curves of Figure 6.7. The curvature of $G_{\min} - p'V_0$ with respect to ε_{xx} equals minus the undeformed system volume times the Young's modulus.

In Table 6.4, values of E for the three specimens considered in Figures 6.4-6.6 and Table 6.3 extracted from parabolic fits to the $G_{\min} - p' V_0$ versus ε_{xx} curve are compared to values of E extracted directly from the slopes of stress-strain curves of these specimens (cf. Figure 6.3 and Table 6.2) for the temperature of $T=200$ K. The agreement is excellent, confirming the thermodynamic consistency of our QHA approach to deformation.

Table 6.4. Calculated Young's moduli E of atactic polystyrene at $T=200$ K via Equation (6.19) using the curvature of $\beta(G_{\min} - p'V_0)$ versus ε_{xx} as shown in Figure 6.7 and through the corresponding slopes of the individual stress-strain curves (compare Figure 6.3) for the three specimens.

Specimen	$k_B T / V_0$ [MPa]	$ Curvature $ [-]	$E = k_B T / V_0 \cdot Curvature $ [GPa]	E calculated from $\sigma_{xx}(\varepsilon_{xx})$ slope [GPa]
1	0.21241	18772	3.99	4.15
2	0.21241	19513	4.14	4.19
3	0.21241	19128	4.06	4.14

6.5 Conclusions

In this chapter the mechanical properties of glassy atactic polystyrene have been studied in the elastic regime, using a thermodynamic formulation based on the quasiharmonic approximation (QHA). Model glassy polystyrene specimens characterized by periodic boundary conditions have been obtained via isobaric molecular dynamics quenching, at a very high cooling-rate, of 5 completely uncorrelated equilibrium liquid configurations. We have predicted the specific volume as a function of temperature at 1 bar based on the “brute force” MD trajectories.

Moreover, we have computed the same specific volume through the QHA at temperatures lying in the vicinity of and below the glass temperature of the model, using both a quantum mechanical and a classical expression for the vibrational partition function. Results from the QHA have been found to be in very good agreement with MD results and with available experimental measurements¹⁴⁹.

Additionally, a set of 200 uncorrelated specimens of glassy atactic polystyrene, each trapped in a basin of its potential energy landscape, have been generated using the QHA and subjected to uniaxial stress-controlled mechanical deformation computer experiments at four different sub-glass transition temperatures in isothermal uniaxial tension and compression under stresses up to 30 MPa. A formulation based on the QHA for extracting the Young's modulus E and Poisson ratio ν as averages over all specimens from these computer experiments has been developed and implemented. The deformation has been found to be elastic under the considered range of stresses, which brought about deformations less than 1%. Predicted values of E and ν and their temperature dependence are in good agreement with available experimental values, indicating that the QHA approach adopted here can successfully capture the elastic response of a polymer glass¹⁴⁹.

The Gibbs energy versus strain curves generated in the course of the QHA-based deformation simulations have been analyzed in detail to quantify how the geometric characteristics of basins and changes in these characteristics upon elastic deformation vary from specimen to specimen. Three general types of response to deformation have been identified, which differ in terms of changes in the value of Gibbs energy and in the shapes of the basins with strain. In the third type of response identified, strong tilting of the basins is observed, indicating that disappearance of the basins (emptying of the basins into nearby basins) may be imminent at strain levels higher than those considered here. Moreover, a method has been developed for extracting the Young's modulus from the curvature of the QHA Gibbs energy with respect to strain in the uniaxial deformations considered and used to show the thermodynamic consistency of our calculations¹⁴⁹.

Work reported in this chapter indicates that invoking the concept of basins in the energy landscape, along with the QHA, yields sound estimates for the volumetric properties and small-strain mechanical response of a polymer glass.

Chapter 7

Main conclusions and innovations

In this work, through the use of appropriately designed molecular simulation techniques, four main accomplishments have been brought to completion. First, by projecting the multidimensional configuration space onto a relatively simpler set, that of basins constructed around local minima of the potential energy function, and by analyzing transitions between adjacent basins as infrequent events, we were able to record structural rearrangements at an atomic level of the simulated system. In particular, in an atomic glass, cage-breaking events are observed to take place when relatively fast and frequent basin-to-basin transitions occur. On the other hand, a more complex structural rearrangement of atoms is observed to happen at larger time scales, when relatively infrequent and sparse metabasin-to-metabasin transitions are realized. The last kind of structural rearrangement demands a coordinated move of several atoms, moving in a more cooperative fashion, than in a cage-breaking event. Both kinds of movement are related to the particularly slow diffusive motion of atoms in the glassy state. The second kind of move is, however, more infrequent and influences a relatively larger area of the molecule since it prerequires the coordinated participation of a usually larger amount of structural units.

The second innovation developed in the context of this thesis constitutes the development, implementation and validation of the lumping algorithm, a mathematical tool constructed to deal with systems evolving through uncorrelated transitions in a network of discrete states according to a master equation. In our applications, the states are basins defined through the PEL of a glass. With the help of our lumping algorithm

one is able to selectively track the long-time dynamics of an arbitrarily large system of states, being described as a set of discrete basins of the PEL among which transitions take place, and completely ignoring the irrelevant short-time relaxation phenomena which can be monitored by almost any one of the known conventional simulation techniques. This is accomplished through the construction of an appropriate, equivalent in terms of long-time dynamics, consisting of substantially fewer lumped states. The number of states in the lumped system can be fixed *a priori*, in order to match the computational resources available for addressing the time scales of interest. The only prerequisite for this algorithm to work is that the initial system's dynamics should comply with a first order kinetic scheme.

Thirdly, a new graphical representation of the PEL has been proposed. This alternative methodology is based on graph theory and provides a rough but good first estimate for the lumping transformation matrix. Beyond this use, the temporal disconnectivity graph can be applied to visually verify and validate lumping results. Most importantly, it provides a visualization of the temporal evolution of a system on its PEL. In other words, it reveals how the connectivity of accessed states and the motion of the system among them change over time as the system evolves. This representation is unique, since all other pre-existing used visualization techniques are static, in the sense that they do not provide any kind of information related to how characteristics of the accessed part of the PEL, such as connectivity, diffusivity, rates of transition between basins etc. change with time.

All the above mentioned techniques aim at making the monitoring of long-time relaxation phenomena present in glassy materials feasible. In this sense, these techniques are focusing on time, since ageing is actually the phenomenon of gradual change in the properties of glassy materials as they slowly tend towards thermodynamic equilibrium. The characteristic times of the ageing phenomenon 20°C below T_g are at least 10 orders of magnitude longer than the longest times that can be simulated nowadays with "brute-force" molecular dynamics techniques with special-purpose hardware and software. Nevertheless, they can become accessible via the potential energy landscape-based approach in the context of which this thesis was carried out, thanks to its use of infrequent event techniques to compute rate constants for arbitrarily rate transitions from atomistic information.

A fourth new contribution of this thesis is mechanical deformation experiments have been successfully simulated and the response of a polymer glass to imposition of deformation in the elastic regime has been quantitatively estimated and validated by invoking a quasi-harmonic approximation for the thermal motion of the atomistic configurations within the energy basins where it is trapped. Moreover, uniaxial, stress-controlled deformation experiments showed that the PEL is distorted upon imposition of deformation and its geometry can significantly change, even for relatively small deformations in the elastic regime. This fact has as an undeniable consequence that the entire time-evolution of the system on its PEL, and thus ageing, is affected through deformation, since connectivity, transitions and rates between basins change with the imposed deformation.

Chapter 8

Research outlook

All of the methods developed and described within the context of this work make use of the features and special characteristics of the PEL to explain phenomena and estimate properties related either to the time evolution of the studied system or to its response to mechanical deformation. In other words, every result presented in this work is either time- or deformation-related. The ultimate goal of the research effort of which this thesis constitutes a part is to combine these two parameters and simulate the response of a glassy system evolving in time, while at certain times a given deformation is imposed to it. Towards this end, the QHA will be coupled with the DIMW method^{52, 150} for tracking temporal evolution as a succession of transitions between basins in a landscape that is progressively distorted by deformation, in order to compute temperature and deformation rate-dependent stress-strain curves for our glassy specimens over a larger range of strains, extending into the plastic deformation and yield regimes.

The DIMW method will be responsible for the time evolution and expansion of the network of states. Next to this method a deformation method should be developed and coupled to DIMW, which will be responsible for stepwise deforming the already explored via DIMW potential energy minima and relevant saddle points. The ultimate goal is to create a self-consistent mechanism which deforms the system with realistic deformation rates similar to the ones experimentally used ($\dot{\epsilon} \sim 10^{-3} - 10^{-1} \text{ [s}^{-1}\text{]}$). In addition, each time a deformation step is imposed, the rate constants for interbasin transitions in the network of basins accessed up to that point should be re-evaluated to

reflect the new system boundaries.

As we have seen mechanical deformation can change the form and shape of the PEL and thus the connectivity between states should be recalculated after every realized deformation step. After each deformation step $\Delta\varepsilon$, the distorted network of states will be left to evolve in time and relax its probability distribution among basins for a time interval dictated by the adopted constant deformation rate $\Delta t = \Delta\varepsilon / \dot{\varepsilon}$, whereas the re-scaled rate constant matrix for the new connectivity of the expanding network will be evaluated. Moreover, the system will be allowed to access additional basins according to the DIMW approach. After the time step Δt has expired, a new deformation step will be implemented and the process will repeat itself.

The big challenge with this procedure is to reach the yield point and enter the plastic regime at a reasonable $\dot{\varepsilon}$. At long times, the number of explored minima and saddle points can become enormous and lumping should be applied to reduce the dimension of the rate constant matrix without harming transitions between basins or metabasins that strongly affect long-time dynamics. The whole venture may be visualized with the help of a temporal disconnectivity graph. According to this procedure the evaluation of long-time relaxation processes (such as the β - and α -relaxation) can commence, whereas at the same time macroscopically observed phenomena beyond the yield point (such as strain-hardening and strain-softening) can be examined from a microscopic, atomistic perspective and potentially related to relaxation atomic mechanisms. The logical diagram presented in Figure 8.1 describes in bulk the step succession of the above described algorithm.

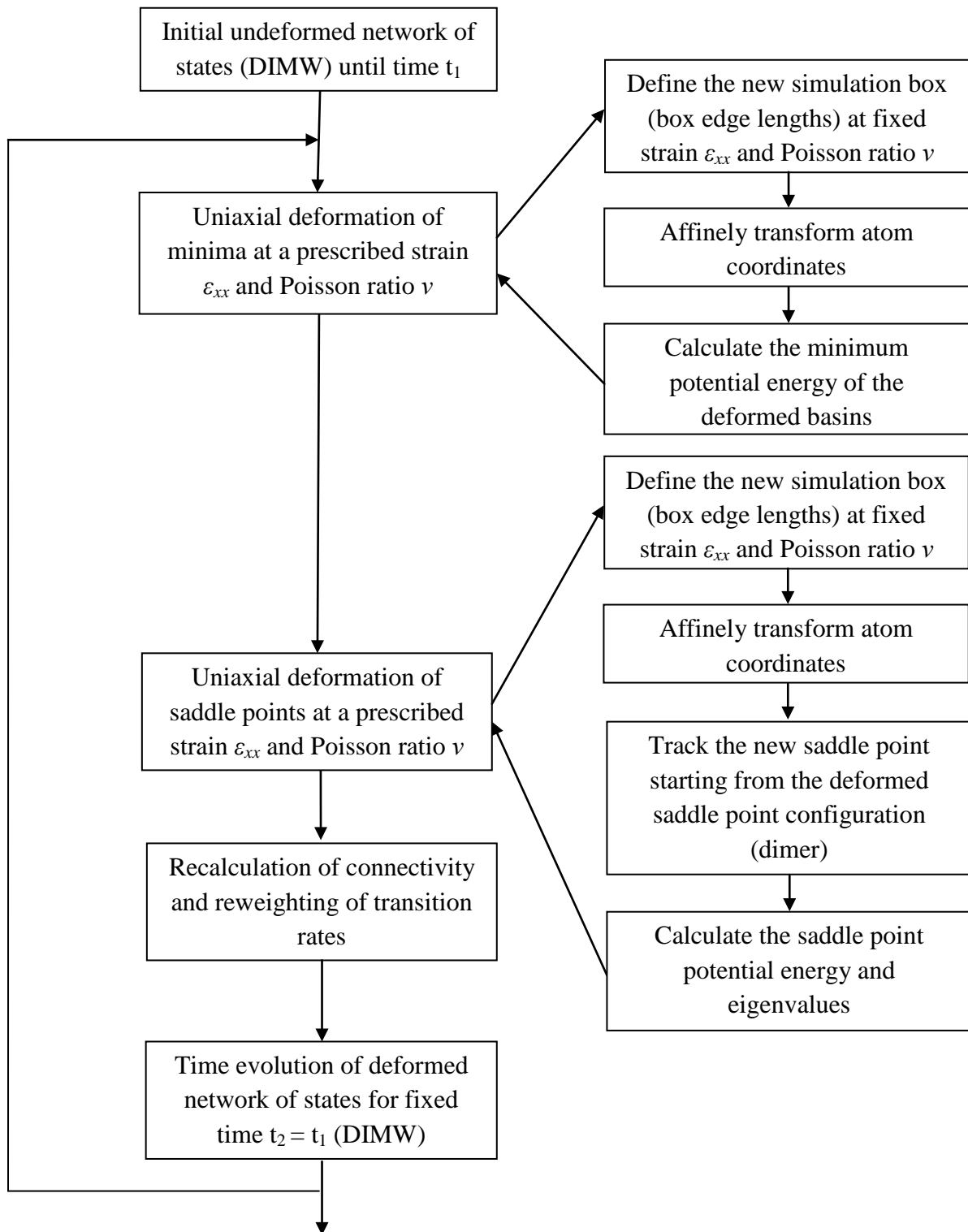


Figure 8.1: Logical diagram describing the time relaxation-deformation algorithm for simulationing mechanical deformation experiments under realistic deformation rates.

List of typical symbols

In the following list the most commonly used symbols of this work are explained. This list is not exhaustive and acts as a supplementary aid for a better understanding. The meaning of all symbols used in this work is explicitly stated in the main text.

Scalars and functions

a, b, c, d = constants of the weighting function h for tilting the flat probability distribution

$acc(o \rightarrow n)$ = probability of accepting the trial move

A = the system's Helmholtz energy

A = state space of the original (unlumped) system

B = constant in Vogel-Fulcher-Tammann equation

B' = constant

c = fraction of particles randomly chosen

C_p = heat capacity under constant pressure

D = activation energy in the Vogel-Fulcher-Tammann equation

D' = constant in Arrhenius-like equation

E = Frobenius norm of the error matrix or Young modulus

f	= modification factor of the Wang-Landau method
g	= density of states
$g(r)$	= radial distribution function
G	= the system's Gibbs energy
h	= weighting function
\mathcal{H}	= the system's Hamiltonian
H	= Histogram or system's enthalpy
\mathcal{K}	= the system's kinetic energy
$k_{i \rightarrow j}$	= rate constant for the transition $i \rightarrow j$
l	= the edge length of the periodic cubic simulation box
m_i	= mass of the i particle
m_q	= memory function
n	= dimension (number of states) of the considered system
N	= number of particles (atoms) in system
$N(o)$	= propability of being in the old configuration
$N(n)$	= propability of being in the new (trial) configuration
p	= pressure
p'	= fraction of sub-systems
P_i	= i th element of the probability column vector
Q	= the sum of the squares of the absolute values of the real parts of all eigenvalues of the rate matrix $\hat{\mathbf{K}}$ or partition function

R	= ratio
r_{ij}	= distance between atoms i and j
r_c	= cut-off distance
S	= the system's entropy
t	= time
T	= Temperature
T_b	= boiling temperature
T_c	= mode coupling critical temperature
T_f	= freezing temperature
T_g	= glass transition temperature
T_m	= melting temperature
T_0, T_K	= Kauzmann temperature
\dot{T}	= cooling rate
U	= the system's internal energy
\mathcal{V}	= the system's potential energy
V	= the system's volume
W	= Frobenius norm of the rate constant matrix of the lumped system $\hat{\mathbf{K}}$. Measure of the ability of the lumped system to reproduce long-time dynamics of the initial system or possibility of observing a structural rearrangement event
z	= objective function or number of atoms in a cooperatively rearranging sub-system
z_1, z_2, z_3	= parameters of the objective function z

Vectors and Matrices

- a** = the column vector of particle accelerations
- a, b, c** = the edge vectors forming the simulation box
- A** = a diagonal matrix of the equilibrium concentrations or a column composition vector
- B** = arbitrary non-square matrix
- D** = a diagonal matrix with diagonal elements the real parts of the eigenvalues of the symmetric rate constant matrix \mathbf{K}_s of the initial system
- E** = the non-square error matrix
- \mathbf{F}_i = force acting on particle i
- h** = scaling matrix
- K** = a square matrix containing the rate constant coefficients for transitions
- M** = the transformation matrix inducing lumping
- p** = generalized momenta
- $\mathbf{P}(t)$ = column vector of the occupancy probabilities at time t
- q** = generalized coordinates
- \mathbf{r}_i = position vector of atom i
- v** = the column vector of particle velocities
- X** = a point in the three dimensional space, defined by the values of E, W, \hat{n}
- V** = a square matrix containing as columns the eigenvectors of the symmetric rate constant matrix \mathbf{K}_s of the initial system
- $\boldsymbol{\varepsilon}$ = strain tensor

σ = stress tensor

Greek letters

α = thermal expansion

α_{forw} = attempt probability of a forward trial move

α_{back} = attempt probability of a reverse trial move

β = the thermodynamic beta, equal to $1/(k_B T)$ or isothermal compressibility

Δ, δ = change of any changeable quantity

ε_{ij} = the depth of the potential well of a binary Lennard-Jones system consisting of atoms of type i and j

ε_{ij} = the strain tensor element located at i -th row and j -th column

η = dynamic viscosity

θ = bond angle

λ = coupling parameter

λ_i = the i th eigenvalue of the rate constant matrix

μ_c = chemical potential of the crystalline state

μ_l = chemical potential of the liquid state

ν = molecular volume and Poisson ratio

ν^* = critical molecular volume value for molecular movement

ν_c = critical molecular volume value for distinction between atomic cells

ξ = typical length-scale

- $\pi(o \rightarrow n)$ = transition probability for going from the old to the new configuration
- ρ = density function
- σ_{ij} = the Van der Waals radius of a binary Lennard-Jones system consisting of atoms of type i and j
- σ_{ij} = the stress tensor element located at i -th row and j -th column
- σ_i = the i -th singular value of the rate constant matrix
- τ = relaxation time
- ϕ = torsional angle
- Φ_q = normalized form of the intermediate scattering function
- χ = torsional angle of phenyl-rings around their stems
- ψ = out-of-plane angle
- ω_i = angular frequency of the i -th vibrational mode

Symbols

- ∇ = nabla differential operator denoting standard derivation
- $\hat{}$ = any property related to the lumped system
- $*$ = conjugate transpose of a matrix
- \sim = any property characterizing the symmetrized rate constant matrix
- $\| \cdot \|_F$ = the Frobenius norm
- T = the transpose of a matrix
- s = a symmetric matrix

- ∞ = equilibrium values
- \cdot = first order derivative in respect to time
- $\ddot{}$ = second order derivative in respect to time
- \cdots = third order derivative in respect to time
- $\cdots\cdots$ = fourth order derivative in respect to time
- $\langle \rangle$ = mean value

References

1. Zallen, R., *The Physics of Amorphous Solids (Wiley Classics Library)*. Wiley-VCH: 1998.
2. Ediger, M. D.; Yu, L., Polymer glasses: From gas to nanoglobular glass. *Nature Materials* **2012**, *11* (4), 267-268.
3. Singh, S.; Ediger, M. D.; De Pablo, J. J., Ultrastable glasses from in silico vapour deposition. *Nature Materials* **2013**, *12* (2), 139-144.
4. Jaeger, G., The Ehrenfest Classification of Phase Transitions: Introduction and Evolution. *Arch Hist Exact Sc.* **1998**, *53* (1), 51-81.
5. Kopsias, N. P. Structural relaxation molecular simulations for inorganic and polymer glassy materials. Dissertation, N.C.S.R Demokritos, Athens, 2005.
6. Tsalikis, D. G.; Lempesis, N.; Boulougouris, G. C.; Theodorou, D. N., On the Role of Inherent Structures in Glass-Forming Materials: I. The Vitrification Process. *The Journal of Physical Chemistry B* **2008**, *112* (34), 10619-10627.
7. Kob, W.; Andersen, H. C., Scaling Behavior in the β -Relaxation Regime of a Supercooled Lennard-Jones Mixture. *Physical Review Letters* **1994**, *73* (10), 1376-1379.
8. Scott Shell, M.; Debenedetti, P. G.; Panagiotopoulos, A. Z., A conformal solution theory for the energy landscape and glass transition of mixtures. *Fluid Phase Equilibria* **2006**, *241* (1-2), 147-154.
9. Prigogine, I.; Defay, R., *Chemical Thermodynamics*. Longman: London, 1950; Vol. 1.
10. Angell, C. A., Structural instability and relaxation in liquid and glassy phases near the fragile liquid limit. *Journal of Non-Crystalline Solids* **1988**, *102* (1-3), 205-221.
11. Kauzmann, W., The Nature of the Glassy State and the Behavior of Liquids at Low Temperatures. *Chemical Reviews* **1948**, *43* (2), 219-256.
12. Dawson, K. A.; Foffi, G.; Sciortino, F.; Tartaglia, P.; Zaccarelli, E., Mode-coupling theory of colloids with short-range attractions. *Journal of Physics: Condensed Matter* **2001**, *13* (41), 9113.
13. Boulougouris, G. C.; Frenkel, D., Novel Monte Carlo scheme for systems with short-ranged interactions. *The Journal of Chemical Physics* **2005**, *122* (24), 244106-8.
14. (a) Fox, J. T. G.; Flory, P. J., Second-Order Transition Temperatures and Related Properties of Polystyrene. I. Influence of Molecular Weight. *Journal of Applied Physics* **1950**, *21* (6), 581-591; (b) Fox, T. G.; Flory, P. J., Further Studies on the Melt Viscosity of Polyisobutylene. *The Journal of Physical Chemistry* **1951**, *55* (2), 221-234.
15. Srivastava, Y.; Greenfield, M. L. In *Ultraviolet absorbers in polymer studied by molecular simulation*, 2004; p 975.

16. (a) Cohen, M. H.; Turnbull, D., Molecular Transport in Liquids and Glasses. *The Journal of Chemical Physics* **1959**, *31* (5), 1164-1169; (b) Turnbull, D.; Cohen, M. H., Free-Volume Model of the Amorphous Phase: Glass Transition. *The Journal of Chemical Physics* **1961**, *34* (1), 120-125; (c) Turnbull, D.; Cohen, M. H., On the Free-Volume Model of the Liquid-Glass Transition. *The Journal of Chemical Physics* **1970**, *52* (6), 3038-3041.
17. (a) Cohen, M. H.; Grest, G. S., A NEW FREE-VOLUME THEORY OF THE GLASS TRANSITION*. *Annals of the New York Academy of Sciences* **1981**, *371* (1), 199-209; (b) Grest, G. S.; Cohen, M. H., Liquids, Glasses, and the Glass Transition: A Free-Volume Approach. In *Advances in Chemical Physics*, John Wiley & Sons, Inc.: 2007; pp 455-525.
18. Doolittle, A. K., Studies in Newtonian Flow. II. The Dependence of the Viscosity of Liquids on Free-Space. *Journal of Applied Physics* **1951**, *22* (12), 1471-1475.
19. (a) Gibbs, J. H.; DiMarzio, E. A., Nature of the Glass Transition and the Glassy State. *The Journal of Chemical Physics* **1958**, *28* (3), 373-383; (b) DiMarzio, E. A.; Gibbs, J. H., Chain Stiffness and the Lattice Theory of Polymer Phases. *The Journal of Chemical Physics* **1958**, *28* (5), 807-813.
20. Adam, G.; Gibbs, J. H., On the Temperature Dependence of Cooperative Relaxation Properties in Glass-Forming Liquids. *The Journal of Chemical Physics* **1965**, *43* (1), 139-146.
21. Bestul, A. B.; Chang, S. S., Excess entropy at glass transformation [5]. *The Journal of Chemical Physics* **1964**, *40* (12), 3731-3733.
22. (a) Privalko, V. P., Excess entropies and related quantities in glass-forming liquids. *The Journal of Physical Chemistry* **1980**, *84* (24), 3307-3312; (b) Alba, C.; Busse, L. E.; List, D. J.; Angell, C. A., Thermodynamic aspects of the vitrification of toluene, and xylene isomers, and the fragility of liquid hydrocarbons. *The Journal of Chemical Physics* **1990**, *92* (1), 617-624.
23. Leutheusser, E., Dynamical model of the liquid-glass transition. *Physical Review A* **1984**, *29* (5), 2765-2773.
24. Bengtzelius, U.; Gotze, W.; Sjolander, A., Dynamics of supercooled liquids and the glass transition. *Journal of Physics C: Solid State Physics* **1984**, *17* (33), 5915.
25. Gotze, W.; Sjogren, L., Relaxation processes in supercooled liquids. *Reports on Progress in Physics* **1992**, *55* (3), 241.
26. Götze, W., *Aspects of structural glass transitions*. Elsevier Science Publishers: North-Holland, Amsterdam, 1991.
27. Elliott, S. R., *Physics of amorphous materials / S.R. Elliott*. Longman: London ; New York, 1984.
28. Biroli, G.; Garrahan, J. P., Perspective: The glass transition. *The Journal of Chemical Physics* **2013**, *138* (12), 12A301-13.
29. Chandler, D.; Garrahan, J. P., Dynamics on the Way to Forming Glass: Bubbles in Space-Time. *Annual Review of Physical Chemistry* **2010**, *61* (1), 191-217.
30. (a) Ediger, M. D., SPATIALLY HETEROGENEOUS DYNAMICS IN SUPERCOOLED LIQUIDS. *Annual Review of Physical Chemistry* **2000**, *51* (1), 99-128; (b) Glotzer, S. C., Spatially heterogeneous dynamics in liquids: insights from simulation. *Journal of Non-Crystalline Solids* **2000**, *274* (1-3), 342-355; (c) Andersen, H. C., Molecular dynamics studies of heterogeneous dynamics and dynamic crossover in supercooled atomic liquids. *Proceedings of the National Academy of Sciences of the United States of America* **2005**, *102* (19), 6686-6691.
31. (a) Dauchot, O.; Marty, G.; Biroli, G., Dynamical Heterogeneity Close to the Jamming Transition in a Sheared Granular Material. *Physical Review Letters* **2005**, *95* (26), 265701; (b) Keys, A. S.; Abate, A. R.; Glotzer, S. C.; Durian, D. J., Measurement of growing dynamical length scales and prediction of the jamming transition in a granular material. *Nature Physics* **2007**, *3* (4), 260-264; (c) Mayer, P.; Bissig, H.; Berthier, L.; Cipelletti, L.; Garrahan, J. P.; Sollich, P.; Trappe, V., Heterogeneous Dynamics of Coarsening Systems. *Physical Review Letters* **2004**, *93* (11), 115701.

32. Keys, A. S.; Hedges, L. O.; Garrahan, J. P.; Glotzer, S. C.; Chandler, D., Excitations Are Localized and Relaxation Is Hierarchical in Glass-Forming Liquids. *Physical Review X* **2011**, *1* (2), 021013.
33. (a) Candelier, R.; Dauchot, O.; Biroli, G., Building Blocks of Dynamical Heterogeneities in Dense Granular Media. *Physical Review Letters* **2009**, *102* (8), 088001; (b) Candelier, R.; Widmer-Cooper, A.; Kummerfeld, J. K.; Dauchot, O.; Biroli, G.; Harrowell, P.; Reichman, D. R., Spatiotemporal Hierarchy of Relaxation Events, Dynamical Heterogeneities, and Structural Reorganization in a Supercooled Liquid. *Physical Review Letters* **2010**, *105* (13), 135702.
34. Kirkpatrick, T. R.; Thirumalai, D.; Wolynes, P. G., Scaling concepts for the dynamics of viscous liquids near an ideal glassy state. *Physical Review A* **1989**, *40* (2), 1045-1054.
35. Wolynes, P.; Lubchenko, V., *Structural Glasses and Supercooled Liquids: Theory, Experiment, and Applications*. Wiley: 2012.
36. (a) Cammarota, C.; Biroli, G., Ideal glass transitions by random pinning. *Proceedings of the National Academy of Sciences* **2012**, *109* (23), 8850-8855; (b) Cammarota, C.; Biroli, G., Random pinning glass transition: Hallmarks, mean-field theory and renormalization group analysis. *The Journal of Chemical Physics* **2013**, *138* (12), 12A547-22.
37. Bhattacharyya, S. M.; Bagchi, B.; Wolynes, P. G., Facilitation, complexity growth, mode coupling, and activated dynamics in supercooled liquids. *Proceedings of the National Academy of Sciences* **2008**, *105* (42), 16077-16082.
38. Allen, M. P.; Tildesley, D. J., *Computer Simulation of Liquids*. Oxford University Press, USA: 1989.
39. Jones, J. E., On the Determination of Molecular Fields. II. From the Equation of State of a Gas. *Proceedings of the Royal Society of London. Series A* **1924**, *106* (738), 463-477.
40. Buckingham, R. A., The Classical Equation of State of Gaseous Helium, Neon and Argon. *Proceedings of the Royal Society of London. Series A, Mathematical and Physical Sciences* **1938**, *168* (933), 264-283.
41. Lyulin, A. V.; Michels, M. A. J., Molecular Dynamics Simulation of Bulk Atactic Polystyrene in the Vicinity of T_g. *Macromolecules* **2002**, *35* (4), 1463-1472.
42. Scienomics *Materials and Processes Simulations - MAPS Amorphous builder*, 3.2; 2009.
43. Maratos, N., *Optimization techniques, lecture notes*. Athens, 1990.
44. (a) TRACY, C. A., Introduction to Exactly Solvable Models in Statistical Mechanics. *Proceedings of Symposia in Pure Mathematics* **1989**, *49* (Part 1); (b) Deguchi, T., Introduction to solvable lattice models in statistical and mathematical physics. **2003**; (c) Wadati, M.; Akutsu, Y., Exactly Solvable Models in Statistical Mechanics. In *Solitons*, Lakshmanan, M., Ed. Springer Berlin Heidelberg: 1988; pp 282-306; (d) Baxter, R.; *Physics, Exactly Solved Models in Statistical Mechanics (Dover Books on Physics)*. Dover Publications: 2008; (e) Theodorou, D. N.; K., C. A., *Applied Molecular Theory for Chemical Engineers (lecture notes)*. U.C. Berkeley, 1993.
45. Frenkel, D.; Smit, B., *Understanding molecular simulation from algorithms to applications*. Academic Press: 2002.
46. (a) Gear, C. W., The automatic integration of ordinary differential equations. *Commun. ACM* **1971**, *14* (3), 176-179; (b) Gear, C. W., *Numerical Initial Value Problems in Ordinary Differential Equations*. Prentice Hall PTR: 1971; p 253; (c) van Gunsteren, W. F.; Berendsen, H. J. C., Algorithms for macromolecular dynamics and constraint dynamics. *Molecular Physics* **1977**, *34* (5), 1311-1327.
47. Verlet, L., Computer "Experiments" on Classical Fluids. I. Thermodynamical Properties of Lennard-Jones Molecules. *Physical Review* **1967**, *159* (1), 98-103.
48. Swope, W. C.; Andersen, H. C.; Berens, P. H.; Wilson, K. R., A computer simulation method for the calculation of equilibrium constants for the formation of physical clusters of

- molecules: Application to small water clusters. *The Journal of Chemical Physics* **1982**, *76* (1), 637-649.
49. (a) Streett W, B.; Tildesley D, J.; Saville, G., Multiple Time Step Methods and an Improved Potential Function for Molecular Dynamics Simulations of Molecular Liquids. In *Computer Modeling of Matter*, AMERICAN CHEMICAL SOCIETY: 1978; Vol. 86, pp 144-158; (b) Streett, W. B.; Tildesley, D. J.; Saville, G., Multiple time-step methods in molecular dynamics. *Molecular Physics* **1978**, *35* (3), 639-648.
50. (a) Kelvin, L., I. Nineteenth century clouds over the dynamical theory of heat and light. *Philosophical Magazine Series 6* **1901**, *2* (7), 1-40; (b) Student, PROBABLE ERROR OF A CORRELATION COEFFICIENT. *Biometrika* **1908**, *6* (2-3), 302-310.
51. Metropolis, N.; Ulam, S., The Monte Carlo Method. *Journal of the American Statistical Association* **1949**, *44* (247), 335-341.
52. Boulougouris, G. C.; Theodorou, D. N., Dynamical integration of a Markovian web: A first passage time approach. *The Journal of Chemical Physics* **2007**, *127* (8), 084903-7.
53. Uhlherr, A.; Theodorou, D. N., Hierarchical simulation approach to structure and dynamics of polymers. *Current Opinion in Solid State and Materials Science* **1998**, *3* (6), 544-551.
54. Matsuoka, S., Reflections on relaxation phenomena in polymers. *Journal of Polymer Science Part B: Polymer Physics* **1999**, *37* (7), 635-638.
55. Shaw, D. E., 166 Millisecond-long molecular dynamics simulations of proteins on a special-purpose machine. *Journal of Biomolecular Structure and Dynamics* **2013**, *31* (sup1), 108-108.
56. Tsalikis, D. G.; Lempesis, N.; Boulougouris, G. C.; Theodorou, D. N., Efficient Parallel Decomposition of Dynamical Sampling in Glass-Forming Materials Based on an "On the Fly" Definition of Metabasins. *Journal of Chemical Theory and Computation* **2010**, *6* (4), 1307-1322.
57. Sorensen, M. R.; Voter, A. F., Temperature-accelerated dynamics for simulation of infrequent events. *The Journal of Chemical Physics* **2000**, *112* (21), 9599-9606.
58. (a) Stillinger, F. H.; Weber, T. A., Hidden structure in liquids. *Physical Review A* **1982**, *25* (2), 978-989; (b) Stillinger, F. H.; Weber, T. A., Inherent structure in water. *The Journal of Physical Chemistry* **1983**, *87* (15), 2833-2840.
59. (a) Vineyard, G. H., Frequency factors and isotope effects in solid state rate processes. *Journal of Physics and Chemistry of Solids* **1957**, *3* (1-2), 121-127; (b) Gusev, A. A.; Müller-Plathe, F.; Gunsteren, W. F.; Suter, U. W., Dynamics of small molecules in bulk polymers. In *Atomistic Modeling of Physical Properties*, Monnerie, L.; Suter, U. W., Eds. Springer Berlin Heidelberg: 1994; Vol. 116, pp 207-247; (c) Stillinger, F. H., A Topographic View of Supercooled Liquids and Glass Formation. *Science* **1995**, *267* (5206), 1935-1939; (d) Wales, D. J.; Doye, J. P. K.; Miller, M. A.; Mortenson, P. N.; Walsh, T. R., Energy Landscapes: From Clusters to Biomolecules. In *Advances in Chemical Physics*, John Wiley & Sons, Inc.: 2007; pp 1-111; (e) Voter, A. F.; Doll, J. D., Dynamical corrections to transition state theory for multistate systems: Surface self-diffusion in the rare-event regime. *The Journal of Chemical Physics* **1985**, *82* (1), 80-92; (f) Wolynes, P. G., Energy landscapes and solved protein-folding problems. *Philosophical Transactions of the Royal Society A: Mathematical, Physical and Engineering Sciences* **2005**, *363* (1827), 453-467.
60. Chandler, D., Statistical mechanics of isomerization dynamics in liquids and the transition state approximation. *The Journal of Chemical Physics* **1978**, *68* (6), 2959-2970.
61. Bennett, C. H., *Diffusion in solids: recent developments*. Academic Press: New York, 1975.
62. Tsalikis, D. G.; Lempesis, N.; Boulougouris, G. C.; Theodorou, D. N., Temperature Accelerated Dynamics in Glass-Forming Materials. *The Journal of Physical Chemistry B* **2010**, *114* (23), 7844-7853.

63. Helfand, E., Brownian dynamics study of transitions in a polymer chain of bistable oscillators. *The Journal of Chemical Physics* **1978**, *69* (3), 1010-1018.
64. Feller, W., *An Introduction to Probability Theory and its Applications*. Wiley, New York: 1971; Vol. II.
65. Theodorou, D. N., Tracking the dynamics of systems evolving through infrequent transitions in a network of discrete states. In *Hierarchical Methods for Dynamics in Complex Molecular Systems*, Grotendorst, J.; Sutmann, G.; Gommper, G.; Marx, D., Eds. IAS series: Jülich, 2012; pp 347-389.
66. (a) Prater, C. D.; Silvestri, A. J.; Wei, J., On the structure and analysis of complex systems of first-order chemical reactions containing irreversible steps-I general properties. *Chemical Engineering Science* **1967**, *22* (12), 1587-1606; (b) Wei, J.; Kuo, J. C. W., Lumping Analysis in Monomolecular Reaction Systems. Analysis of the Exactly Lumpable System. *Industrial & Engineering Chemistry Fundamentals* **1969**, *8* (1), 114-123; (c) Kuo, J. C. W.; Wei, J., Lumping Analysis in Monomolecular Reaction Systems. Analysis of Approximately Lumpable System. *Industrial & Engineering Chemistry Fundamentals* **1969**, *8* (1), 124-133.
67. Jahnke, T.; Huisinga, W., Solving the chemical master equation for monomolecular reaction systems analytically. *J. Math. Biol.* **2007**, *54* (1), 1-26.
68. Tsalikis, D.; Lempeis, N.; Boulougouris, G. C.; Theodorou, D. N., On the Role of Inherent Structures in Glass-forming Materials: II. Reconstruction of the Mean Square Displacement by Rigorous Lifting of the Inherent Structure Dynamics. *The Journal of Physical Chemistry B* **2008**, *112* (34), 10628-10637.
69. (a) Middleton, T. F.; Wales, D. J., Energy landscapes of some model glass formers. *Physical Review B* **2001**, *64* (2), 024205; (b) Middleton, T. F.; Wales, D. J., Energy landscapes of model glasses. II. Results for constant pressure. *The Journal of Chemical Physics* **2003**, *118* (10), 4583-4593; (c) Middleton, T. F.; Wales, D. J., Comparison of kinetic Monte Carlo and molecular dynamics simulations of diffusion in a model glass former. *The Journal of Chemical Physics* **2004**, *120* (17), 8134-8143.
70. Kunz, R. E.; Berry, R. S., Statistical interpretation of topographies and dynamics of multidimensional potentials. *The Journal of Chemical Physics* **1995**, *103* (5), 1904-1912.
71. Elber, R.; Karplus, M., Multiple conformational states of proteins: a molecular dynamics analysis of myoglobin. *Science* **1987**, *235* (4786), 318-321.
72. La Nave, E.; Mossa, S.; Sciortino, F., Potential Energy Landscape Equation of State. *Physical Review Letters* **2002**, *88* (22), 225701.
73. Doliwa, B.; Heuer, A., Hopping in a supercooled Lennard-Jones liquid: Metabasins, waiting time distribution, and diffusion. *Physical Review E* **2003**, *67* (3), 030501.
74. Denny, R. A.; Reichman, D. R.; Bouchaud, J.-P., Trap Models and Slow Dynamics in Supercooled Liquids. *Physical Review Letters* **2003**, *90* (2), 025503.
75. Appignanesi, G. A.; Rodríguez Fris, J. A.; Montani, R. A.; Kob, W., Democratic Particle Motion for Metabasin Transitions in Simple Glass Formers. *Physical Review Letters* **2006**, *96* (5), 057801.
76. Büchner, S.; Heuer, A., Metastable States as a Key to the Dynamics of Supercooled Liquids. *Physical Review Letters* **2000**, *84* (10), 2168-2171.
77. (a) Mauro, J. C.; Loucks, R. J.; Gupta, P. K., Metabasin Approach for Computing the Master Equation Dynamics of Systems with Broken Ergodicity. *The Journal of Physical Chemistry A* **2007**, *111* (32), 7957-7965; (b) Mauro, J. C.; Loucks, R. J., Selenium glass transition: A model based on the enthalpy landscape approach and nonequilibrium statistical mechanics. *Physical Review B* **2007**, *76* (17), 174202.
78. Andreas, H., Exploring the potential energy landscape of glass-forming systems: from inherent structures via metabasins to macroscopic transport. *Journal of Physics: Condensed Matter* **2008**, *20* (37), 373101.

79. Makeev, A. G.; Maroudas, D.; Panagiotopoulos, A. Z.; Kevrekidis, I. G., Coarse bifurcation analysis of kinetic Monte Carlo simulations: A lattice-gas model with lateral interactions. *The Journal of Chemical Physics* **2002**, *117* (18), 8229-8240.
80. (a) Munro, L. J.; Wales, D. J., Defect migration in crystalline silicon. *Physical Review B* **1999**, *59* (6), 3969-3980; (b) J. Munro, L.; J. Wales, D., Rearrangements of bulk face-centred-cubic nickel modelled by a Sutton-Chen potential. *Faraday Discussions* **1997**, *106* (0), 409-423; (c) Henkelman, G.; Jonsson, H., A dimer method for finding saddle points on high dimensional potential surfaces using only first derivatives. *The Journal of Chemical Physics* **1999**, *111* (15), 7010-7022; (d) Barkema, G. T.; Mousseau, N., Event-Based Relaxation of Continuous Disordered Systems. *Physical Review Letters* **1996**, *77* (21), 4358-4361; (e) G. Bolhuis, P.; Dellago, C.; Chandler, D., Sampling ensembles of deterministic transition pathways. *Faraday Discussions* **1998**, *110* (0), 421-436; (f) Bolhuis, P. G.; Chandler, D.; Dellago, C.; Geissler, P. L., TRANSITION PATH SAMPLING: Throwing Ropes Over Rough Mountain Passes, in the Dark. *Annual Review of Physical Chemistry* **2002**, *53* (1), 291-318; (g) Voter, A. F., Parallel replica method for dynamics of infrequent events. *Physical Review B* **1998**, *57* (22), R13985-R13988; (h) Voter, A. F., Hyperdynamics: Accelerated Molecular Dynamics of Infrequent Events. *Physical Review Letters* **1997**, *78* (20), 3908-3911.
81. Fukui, K., The path of chemical reactions - the IRC approach. *Accounts of Chemical Research* **1981**, *14* (12), 363-368.
82. Helfand, E.; Wasserman, Z. R.; Weber, T. A., Brownian dynamics study of polymer conformational transitions. *The Journal of Chemical Physics* **1979**, *70* (4), 2016-2017.
83. de Souza, V. K.; Wales, D. J., Energy landscapes for diffusion: Analysis of cage-breaking processes. *The Journal of Chemical Physics* **2008**, *129* (16), 164507-13.
84. Kob, W.; Andersen, H. C., Testing mode-coupling theory for a supercooled binary Lennard-Jones mixture I: The van Hove correlation function. *Physical Review E* **1995**, *51* (5), 4626-4641.
85. de Souza, V. K.; Wales, D. J., Connectivity in the potential energy landscape for binary Lennard-Jones systems. *The Journal of Chemical Physics* **2009**, *130* (19), 194508-12.
86. Donati, C.; Douglas, J. F.; Kob, W.; Plimpton, S. J.; Poole, P. H.; Glotzer, S. C., Stringlike Cooperative Motion in a Supercooled Liquid. *Physical Review Letters* **1998**, *80* (11), 2338-2341.
87. (a) Wang, F.; Landau, D. P., Efficient, Multiple-Range Random Walk Algorithm to Calculate the Density of States. *Physical Review Letters* **2001**, *86* (10), 2050-2053; (b) Wang, F.; Landau, D. P., Determining the density of states for classical statistical models: A random walk algorithm to produce a flat histogram. *Physical Review E* **2001**, *64* (5), 056101.
88. Wei, J.; Prater, C. D., The Structure and Analysis of Complex Reaction Systems. 1962; Vol. 13, pp 203-392.
89. Liu, Y. A.; Lapidus, L., Observer theory for lumping analysis of monomolecular reaction systems. *AIChE Journal* **1973**, *19* (3), 467-473.
90. (a) Li, G.; Rabitz, H., A general analysis of exact lumping in chemical kinetics. *Chemical Engineering Science* **1989**, *44* (6), 1413-1430; (b) Li, G.; Rabitz, H., A general analysis of approximate lumping in chemical kinetics. *Chemical Engineering Science* **1990**, *45* (4), 977-1002.
91. (a) Xu, O.-g.; Su, H.-y.; Mu, S.-j.; Chu, J., 7-lump kinetic model for residual oil catalytic cracking. *Journal of Zhejiang University - Science A* **2006**, *7* (11), 1932-1941; (b) Ozawa, Y., The Structure of a Lumpable Monomolecular System for Reversible Chemical Reactions. *Industrial & Engineering Chemistry Fundamentals* **1973**, *12* (2), 191-196.
92. (a) Martinez, E. C., LUMPING OF COMPONENTS AND REACTIONS IN COMPLEX REACTION NETWORKS[†]. *Chemical Engineering Communications* **1990**, *93* (1), 1-24; (b) Chou, M. Y.; Ho, T. C., Continuum theory for lumping nonlinear reactions. *AIChE Journal* **1988**, *34*

- (9), 1519-1527; (c) Astarita, G.; Ocone, R., Lumping nonlinear kinetics. *AIChE Journal* **1988**, *34* (8), 1299-1309.
93. (a) Tomlin, A. S.; Li, G.; Rabitz, H.; Toth, J., A general analysis of approximate nonlinear lumping in chemical kinetics. II. Constrained lumping. *The Journal of Chemical Physics* **1994**, *101* (2), 1188-1201; (b) Li, G.; Tomlin, A. S.; Rabitz, H.; Toth, J., A general analysis of approximate nonlinear lumping in chemical kinetics. I. Unconstrained lumping. *The Journal of Chemical Physics* **1994**, *101* (2), 1172-1187.
94. (a) Carr, J. M.; Wales, D. J., Refined kinetic transition networks for the GB1 hairpin peptide. *Physical Chemistry Chemical Physics* **2009**, *11* (18), 3341-3354; (b) Carr, J. M.; Wales, D. J., Folding pathways and rates for the three-stranded β -sheet peptide Beta3s using discrete path sampling. *Journal of Physical Chemistry B* **2008**, *112* (29), 8760-8769; (c) Carr, J. M.; Wales, D. J., Global optimization and folding pathways of selected α -helical proteins. *Journal of Chemical Physics* **2005**, *123* (23); (d) Evans, D. A.; Wales, D. J., Free energy landscapes of model peptides and proteins. *Journal of Chemical Physics* **2003**, *118* (8), 3891-3897.
95. (a) Mortenson, P. N.; Evans, D. A.; Wales, D. J., Energy landscapes of model polyanilines. *Journal of Chemical Physics* **2002**, *117* (3), 1363-1376; (b) Mortenson, P. N.; Wales, D. J., Energy landscapes, global optimization and dynamics of the polyaniline Ac(ala)8NHMe. *Journal of Chemical Physics* **2001**, *114* (14), 6443-6454.
96. Middleton, T. F.; Hernández-Rojas, J.; Mortenson, P. N.; Wales, D. J., Crystals of binary Lennard-Jones solids. *Physical Review B - Condensed Matter and Materials Physics* **2001**, *64* (18), 1842011-1842017.
97. (a) Coxson, P. G.; Bischoff, K. B., Lumping strategy. 1. Introductory techniques and applications of cluster analysis. *Industrial & Engineering Chemistry Research* **1987**, *26* (6), 1239-1248; (b) Coxson, P. G.; Bischoff, K. B., Lumping strategy. 2. System theoretic approach. *Industrial & Engineering Chemistry Research* **1987**, *26* (10), 2151-2157.
98. Donath, W. E.; Hoffman, A. J., Lower bounds for the partitioning of graphs. *IBM J. Res. Dev.* **1973**, *17* (5), 420-425.
99. (a) Nadler, B.; Lafon, S.; Coifman, R. R.; Kevrekidis, I. G., Diffusion maps, spectral clustering and reaction coordinates of dynamical systems. *Applied and Computational Harmonic Analysis* **2006**, *21* (1), 113-127; (b) Nadler, B.; Lafon, S.; Coifman, R.; Kevrekidis, I. G., Diffusion maps - A probabilistic interpretation for spectral embedding and clustering algorithms. 2008; Vol. 58, pp 238-260.
100. Kampen, N. G. v., *Stochastic Processes in Physics and Chemistry*. North-Holland: Amsterdam, 1981.
101. Reichl, L. E., *A Modern Course in Statistical Physics*. 2nd ed.; Wiley: New York, 1998.
102. Boulougouris, G. C.; Theodorou, D. N., Probing subglass relaxation in polymers via a geometric representation of probabilities, observables, and relaxation modes for discrete stochastic systems. *The Journal of Chemical Physics* **2009**, *130* (4), 044905-7.
103. Metropolis, N.; Rosenbluth, A. W.; Rosenbluth, M. N.; Teller, A. H.; Teller, E., Equation of State Calculations by Fast Computing Machines. *The Journal of Chemical Physics* **1953**, *21* (6), 1087-1092.
104. (a) Cunha Netto, A. G.; Silva, C. J.; Caparica, A. A.; Dickman, R., Wang-Landau sampling in three-dimensional polymers. *Brazilian Journal of Physics* **2006**, *36* (3 A), 619-622; (b) Nguyen, P. H.; Mittag, E.; Torda, A. E.; Stock, G., Improved Wang-Landau sampling through the use of smoothed potential-energy surfaces. *The Journal of Chemical Physics* **2006**, *124* (15), 154107-6.
105. (a) Davidson, E. R., Molecular Mechanics and Modeling: Overview. *Chemical Reviews* **1993**, *93* (7), 2337-2337; (b) Becker, O. M.; Karplus, M., The topology of multidimensional potential energy surfaces: Theory and application to peptide structure and kinetics. *The Journal of Chemical Physics* **1997**, *106* (4), 1495-1517.

106. (a) Scala, A.; Starr, F. W.; La Nave, E.; Sciortino, F.; Stanley, H. E., Configurational entropy and diffusivity of supercooled water. *Nature* **2000**, *406* (6792), 166-169; (b) Sastry, S., The relationship between fragility, configurational entropy and the potential energy landscape of glass-forming liquids. *Nature* **2001**, *409* (6817), 164-167; (c) Saika-Voivod, I.; Poole, P. H.; Sciortino, F., Fragile-to-strong transition and polyamorphism in the energy landscape of liquid silica. *Nature* **2001**, *412* (6846), 514-517; (d) Mossa, S.; La Nave, E.; Stanley, H. E.; Donati, C.; Sciortino, F.; Tartaglia, P., Dynamics and configurational entropy in the Lewis-Wahnström model for supercooled orthoterphenyl. *Physical Review E* **2002**, *65* (4), 041205.
107. Goldstein, M., Viscous Liquids and the Glass Transition: A Potential Energy Barrier Picture. *The Journal of Chemical Physics* **1969**, *51* (9), 3728-3739.
108. (a) Wales, D. J.; Miller, M. A.; Walsh, T. R., Archetypal energy landscapes. *Nature* **1998**, *394* (6695), 758-760; (b) Wales, D. J., Discrete path sampling. *Molecular Physics* **2002**, *100* (20), 3285-3305; (c) Wales, D. J., Calculating rate constants and committor probabilities for transition networks by graph transformation. *The Journal of Chemical Physics* **2009**, *130* (20), 204111-7; (d) Berry, R. S.; Wales, D. J., Freezing, melting, spinodals, and clusters. *Physical Review Letters* **1989**, *63* (11), 1156-1159; (e) Wales, D., *Energy Landscapes*. University of Cambridge: Cambridge, 2004.
109. Frauenfelder, H.; Sligar, S.; Wolynes, P., The energy landscapes and motions of proteins. *Science* **1991**, *254* (5038), 1598-1603.
110. Debenedetti, P. G.; Stillinger, F. H., Supercooled liquids and the glass transition. *Nature* **2001**, *410* (6825), 259-267.
111. Kushima, A.; Lin, X.; Li, J.; Eapen, J.; Mauro, J. C.; Qian, X.; Diep, P.; Yip, S., Computing the viscosity of supercooled liquids. *The Journal of Chemical Physics* **2009**, *130* (22), 224504.
112. Trygubenko, S. A.; Wales, D. J., Graph transformation method for calculating waiting times in Markov chains. *The Journal of Chemical Physics* **2006**, *124* (23), 234110-16.
113. Doye, J. P. K.; Wales, D. J., On potential energy surfaces and relaxation to the global minimum. *The Journal of Chemical Physics* **1996**, *105* (18), 8428-8445.
114. (a) Theodorou, D. N.; Suter, U. W., Detailed molecular structure of a vinyl polymer glass. *Macromolecules* **1985**, *18* (7), 1467-1478; (b) Theodorou, D. N.; Suter, U. W., Atomistic modeling of mechanical properties of polymeric glasses. *Macromolecules* **1986**, *19* (1), 139-154; (c) Theodorou, D. N.; Suter, U. W., Local structure and the mechanism of response to elastic deformation in a glassy polymer. *Macromolecules* **1986**, *19* (2), 379-387; (d) Mott, P. H.; Argon, A. S.; Suter, U. W., Atomistic modelling of plastic deformation of glassy polymers. *Philosophical Magazine A* **1993**, *67* (4), 931-978; (e) Parrinello, M.; Rahman, A., Strain fluctuations and elastic constants. *The Journal of Chemical Physics* **1982**, *76* (5), 2662-2666.
115. (a) G'Sell, C.; Hiver, J. M.; Dahoun, A.; Souahi, A., Video-controlled tensile testing of polymers and metals beyond the necking point. *J Mater Sci* **1992**, *27* (18), 5031-5039; (b) Arruda, E. M.; Boyce, M. C., Evolution of plastic anisotropy in amorphous polymers during finite straining. *International Journal of Plasticity* **1993**, *9* (6), 697-720; (c) Boyce, M. C.; Arruda, E. M.; Jayachandran, R., The large strain compression, tension, and simple shear of polycarbonate. *Polymer Engineering & Science* **1994**, *34* (9), 716-725.
116. Argon, A. S.; Mott, P. H.; Suter, U. W., Simulation of Plastic Deformation in a Flexible Chain Glassy Polymer. *physica status solidi (b)* **1992**, *172* (1), 193-204.
117. (a) Meijer Han, E. H.; Govaert Leon, E.; Smit Robert, J. M., A Multi-Level Finite Element Method for Modeling Rubber-Toughened Amorphous Polymers. In *Toughening of Plastics*, American Chemical Society: 2000; Vol. 759, pp 50-70; (b) Aboulfaraj, M.; G'Sell, C.; Mangelinck, D.; McKenna, G. B., Physical aging of epoxy networks after quenching and/or plastic cycling. *Journal of Non-Crystalline Solids* **1994**, *172-174* (PART 1), 615-621; (c) Hasan, O. A.; Boyce, M. C., Energy storage during inelastic deformation of glassy polymers. *Polymer* **1993**, *34* (24), 5085-5092; (d) Van Melick, H. G. H.; Govaert, L. E.; Raas, B.; Nauta, W. J.;

- Meijer, H. E. H., Kinetics of ageing and re-embrittlement of mechanically rejuvenated polystyrene. *Polymer* **2003**, *44* (4), 1171-1179; (e) van Melick, H. G. H.; Govaert, L. E.; Meijer, H. E. H., On the origin of strain hardening in glassy polymers. *Polymer* **2003**, *44* (8), 2493-2502.
118. Utz, M.; Debenedetti, P. G.; Stillinger, F. H., Atomistic Simulation of Aging and Rejuvenation in Glasses. *Physical Review Letters* **2000**, *84* (7), 1471-1474.
119. Isner, B. A.; Lacks, D. J., Generic Rugged Landscapes under Strain and the Possibility of Rejuvenation in Glasses. *Physical Review Letters* **2006**, *96* (2), 025506.
120. (a) Gusev, A. A.; Zehnder, M. M.; Suter, U. W., Fluctuation formula for elastic constants. *Physical Review B* **1996**, *54* (1), 1-4; (b) Zehnder, M. M.; Gusev, A. A.; Suter, U. W., Predicting and understanding the elastic properties of polymers using atomistic simulation. *Revue de l'Institute Francais du Petrole* **1996**, *51* (1), 131-137.
121. (a) Ray, J. R.; Rahman, A., Statistical ensembles and molecular dynamics studies of anisotropic solids. *The Journal of Chemical Physics* **1984**, *80* (9), 4423-4428; (b) Squire, D. R.; Holt, A. C.; Hoover, W. G., Isothermal elastic constants for argon. theory and Monte Carlo calculations. *Physica* **1969**, *42* (3), 388-397; (c) Ray, J. R., Elastic constants and statistical ensembles in molecular dynamics. *Computer Physics Reports* **1988**, *8* (3), 109-151.
122. (a) Griebel, M.; Hamaekers, J., Molecular dynamics simulations of the elastic moduli of polymer-carbon nanotube composites. *Computer Methods in Applied Mechanics and Engineering* **2004**, *193* (17-20), 1773-1788; (b) Toepperwein, G. N.; Riggelman, R. A.; de Pablo, J. J., Dynamics and Deformation Response of Rod-Containing Nanocomposites. *Macromolecules* **2011**, *45* (1), 543-554; (c) Papakonstantopoulos, G. J.; Yoshimoto, K.; Doxastakis, M.; Nealey, P. F.; de Pablo, J. J., Local mechanical properties of polymeric nanocomposites. *Physical Review E* **2005**, *72* (3), 031801; (d) Van Workum, K.; de Pablo, J. J., Computer Simulation of the Mechanical Properties of Amorphous Polymer Nanostructures. *Nano Letters* **2003**, *3* (10), 1405-1410.
123. Van Workum, K.; de Pablo, J. J., Local elastic constants in thin films of an fcc crystal. *Physical Review E* **2003**, *67* (3), 031601.
124. Baeurle, S. A.; Fredrickson, G. H.; Gusev, A. A., Prediction of Elastic Properties of a Poly(styrene-butadiene-styrene) Copolymer Using a Mixed Finite Element Approach. *Macromolecules* **2004**, *37* (15), 5784-5791.
125. (a) Lacks, D. J.; Rutledge, G. C., Temperature Dependence of Structural and Mechanical Properties of Isotactic Polypropylene. *Macromolecules* **1995**, *28* (4), 1115-1120; (b) Rutledge, G. C.; Lacks, D. J.; Martonak, R.; Binder, K., A comparison of quasi-harmonic lattice dynamics and Monte Carlo simulation of polymeric crystals using orthorhombic polyethylene. *The Journal of Chemical Physics* **1998**, *108* (24), 10274-10280; (c) Lacks, D. J., Simple model for the temperature-dependent compressive strength of polymer fibers. *Materials Letters* **2000**, *44* (1), 12-13; (d) Lacks, D. J.; Rutledge, G. C., Simulation of the temperature dependence of mechanical properties of polyethylene. *The Journal of Physical Chemistry* **1994**, *98* (4), 1222-1231.
126. Fortunelli, A.; Geloni, C.; Lazzeri, A., Simulation of the plastic behavior of amorphous glassy bis-phenol-A-polycarbonate. *The Journal of Chemical Physics* **2004**, *121* (10), 4941-4950.
127. (a) Backhaus, G., F. J. Lockett, Nonlinear Viscoelastic Solids. XI + 195. S. m. Fig. London/New York 1972. Academic Press. Preis geb. £ 4.4. *ZAMM - Journal of Applied Mathematics and Mechanics / Zeitschrift für Angewandte Mathematik und Mechanik* **1974**, *54* (4), 288-288; (b) Markovitz, H., Theory of viscoelasticity. An introduction, R. M. Christensen, Academic Press, New York, 1971. 245 + xi pp. \$13.50. *Journal of Polymer Science Part B: Polymer Letters* **1971**, *9* (9), 704-705.
128. (a) Drabble, F.; Haward, R. N.; Johnson, W., Adiabatic models for deformation and cavitation in polystyrene. *British Journal of Applied Physics* **1966**, *17* (2), 241-252; (b) Boyce,

- M. C.; Parks, D. M.; Argon, A. S., Large inelastic deformation of glassy polymers. part I: rate dependent constitutive model. *Mechanics of Materials* **1988**, *7* (1), 15-33; (c) Boyce, M. C.; Arruda, E. M., An experimental and analytical investigation of the large strain compressive and tensile response of glassy polymers. *Polymer Engineering & Science* **1990**, *30* (20), 1288-1298; (d) James, H. M.; Guth, E., Theory of the Elastic Properties of Rubber. *The Journal of Chemical Physics* **1943**, *11* (10), 455-481; (e) Arruda, E. M.; Boyce, M. C., A three-dimensional constitutive model for the large stretch behavior of rubber elastic materials. *Journal of the Mechanics and Physics of Solids* **1993**, *41* (2), 389-412; (f) Wu, P. D.; Van Der Giessen, E., On improved network models for rubber elasticity and their applications to orientation hardening in glassy polymers. *Journal of the Mechanics and Physics of Solids* **1993**, *41* (3), 427-456; (g) Khan, A. S.; Lopez-Pamies, O.; Kazmi, R., Thermo-mechanical large deformation response and constitutive modeling of viscoelastic polymers over a wide range of strain rates and temperatures. *International Journal of Plasticity* **2006**, *22* (4), 581-601.
129. Lempeis, N.; Tsalikis, D. G.; Boulougouris, G. C.; Theodorou, D. N., Lumping analysis for the prediction of long-time dynamics: From monomolecular reaction systems to inherent structure dynamics of glassy materials. *The Journal of Chemical Physics* **2011**, *135* (20), 204507-17.
130. Lempeis, N.; Boulougouris, G. C.; Theodorou, D. N., Temporal disconnectivity of the energy landscape in glassy systems. *Journal of Chemical Physics* **2013**, *138* (12).
131. (a) Ayyagari, C.; Bedrov, D.; Smith, G. D., Structure of Atactic Polystyrene: A Molecular Dynamics Simulation Study. *Macromolecules* **2000**, *33* (16), 6194-6199; (b) Furuya, H.; Mondello, M.; Yang, H.-J.; Roe, R.-J.; Erwin, R. W.; Han, C. C.; Smith, S. D., Molecular dynamics simulation of atactic polystyrene. 2. Comparison with neutron scattering data. *Macromolecules* **1994**, *27* (20), 5674-5680; (c) Lyulin, A. V.; de Groot, J. J.; Michels, M. A. J., Computer simulation study of bulk atactic polystyrene in the vicinity of the glass transition. *Macromolecular Symposia* **2003**, *191* (1), 167-176; (d) Mondello, M.; Yang, H.-J.; Furuya, H.; Roe, R.-J., Molecular Dynamics Simulation of Atactic Polystyrene. 1. Comparison with X-ray Scattering Data. *Macromolecules* **1994**, *27* (13), 3566-3574; (e) Lyulin, A. V.; Balabaev, N. K.; Mazo, M. A.; Michels, M. A. J., Molecular Dynamics Simulation of Uniaxial Deformation of Glassy Amorphous Atactic Polystyrene. *Macromolecules* **2004**, *37* (23), 8785-8793; (f) Lyulin, A. V.; Balabaev, N. K.; Michels, M. A. J., Correlated Segmental Dynamics in Amorphous Atactic Polystyrene: A Molecular Dynamics Simulation Study. *Macromolecules* **2002**, *35* (25), 9595-9604; (g) Hudzinsky, D.; Lyulin, A. V., Confinement and shear effects for atactic polystyrene film structure and mechanics. *Modelling and Simulation in Materials Science and Engineering* **2011**, *19* (7), 074007; (h) Mulder, T.; Harmandaris, V. A.; Lyulin, A. V.; van der Vegt, N. F. A.; Kremer, K.; Michels, M. A. J., Structural Properties of Atactic Polystyrene of Different Thermal History Obtained from a Multiscale Simulation. *Macromolecules* **2008**, *42* (1), 384-391; (i) Chen, X.; Ye, Y.; Hao, L., Atomistic picture of isothermal volume relaxation behavior of atactic polystyrene glass provided by a molecular dynamics simulation. *The Journal of Chemical Physics* **2012**, *137* (4), 044907-7; (j) Lyulin, A. V.; Vorselaars, B.; Mazo, M. A.; Balabaev, N. K.; Michels, M. A. J., Strain softening and hardening of amorphous polymers: Atomistic simulation of bulk mechanics and local dynamics. *EPL (Europhysics Letters)* **2005**, *71* (4), 618.
132. (a) Mark, J. E., *Polymer Data Handbook*. Oxford University Press: New York, 1999; (b) Mark, J. E., *Physical Properties of Polymers Handbook*. AIP Press: Woodbury, New York, 1996; (c) Boyer, R. F., *Encyclopedia of Polymer Science and Technology*. John Wiley and Sons: New York, 1970; Vol. 13; (d) Krevelen, D. W. v.; Hoftyzer, P. J., *Properties of Polymers: Correlations with Chemical Structure*. Elsevier Publishing Company: Amsterdam, 1972.
133. (a) Born, M.; Huang, K., *Dynamical Theory of Crystal Lattices*. Clarendon Press, Oxford: 1996; (b) Kopsias, N. P.; Theodorou, D. N., Elementary structural transitions in the amorphous Lennard-Jones solid using multidimensional transition-state theory. *The Journal of Chemical Physics* **1998**, *109* (19), 8573-8582.

134. Stillinger, F. H.; Weber, T. A., Dynamics of structural transitions in liquids. *Physical Review A* **1983**, *28* (4), 2408-2416.
135. Goldstein, H., *Classical Mechanics*. Narosa: New Delhi, 1993.
136. Weiner, J. H., *Statistical Mechanics of Elasticity*. 1983.
137. Jr., J. W. M., Notes on the Thermodynamics of Solids. 2007; pp 366-411.
138. Zoller, P.; Walsh, D. J., *Standard Pressure-Volume-Temperature Data for Polymers*. Technomic: Lancaster, Pa, 1995.
139. Schäffer, E.; Steiner, U., Acoustic instabilities in thin polymer films. *The European Physical Journal E* **2002**, *8* (3), 347-351.
140. Dunweg, B.; Kremer, K., Molecular dynamics simulation of a polymer chain in solution. *The Journal of Chemical Physics* **1993**, *99* (9), 6983-6997.
141. Hintermeyer, J.; Herrmann, A.; Kahlau, R.; Goiceanu, C.; Rössler, E. A., Molecular Weight Dependence of Glassy Dynamics in Linear Polymers Revisited. *Macromolecules* **2008**, *41* (23), 9335-9344.
142. (a) Han, J.; Gee, R. H.; Boyd, R. H., Glass Transition Temperatures of Polymers from Molecular Dynamics Simulations. *Macromolecules* **1994**, *27* (26), 7781-7784; (b) McKechnie, J. I.; Brown, D.; Clarke, J. H. R., Methods of generating dense relaxed amorphous polymer samples for use in dynamic simulations. *Macromolecules* **1992**, *25* (5), 1562-1567.
143. Hencky, H., *Z. Techn. Phys.* **1928**, *9*, 214-223.
144. (a) Miyake, K.; Satomi, N.; Sasaki, S., Elastic modulus of polystyrene film from near surface to bulk measured by nanoindentation using atomic force microscopy. *Applied Physics Letters* **2006**, *89* (3), 031925-3; (b) Oral, I.; Guzel, H.; Ahmetli, G., Measuring the Young's modulus of polystyrene-based composites by tensile test and pulse-echo method. *Polym. Bull.* **2011**, *67* (9), 1893-1906.
145. Kono, R., The Dynamic Bulk Viscosity of Polystyrene and Polymethyl Methacrylate. *Journal of the Physical Society of Japan* *15* (Copyright (C) 1960 The Physical Society of Japan), 718.
146. Pandini, S.; Pegoretti, A., Time and temperature effects on Poisson's ratio of poly(butylene terephthalate). *eXPRESS Polymer Letters* **2011**, *5* (8), 685-697.
147. Mott, P. H.; Dorgan, J. R.; Roland, C. M., The bulk modulus and Poisson's ratio of "incompressible" materials. *Journal of Sound and Vibration* **2008**, *312* (4-5), 572-575.
148. Torres, J. M.; Stafford, C. M.; Vogt, B. D., Impact of molecular mass on the elastic modulus of thin polystyrene films. *Polymer* **2010**, *51* (18), 4211-4217.
149. Lempesis, N.; Vogiatzis, G. G.; Boulougouris, G. C.; van Breemen, L. C. A.; Hütter, M.; Theodorou, D. N., Tracking a glassy polymer on its energy landscape in the course of elastic deformation. *Molecular Physics* **2013**, 1-12.
150. Theodorou, D. N., Tracking the Dynamics of Systems Evolving through Infrequent Transitions in a Network of Discrete States. *Hierarchical Methods for Dynamics in Complex Molecular Systems* **2012**, *10*, 347.

Appendix A

Force field description and contributions to the total potential energy function for the united atom model of atactic polystyrene.

In this Appendix, a detailed schematic explanation is given of all bonded energy contributions [Eqs. (2.42)-(2.49)] to the total potential energy [Eq. (2.50)] introduced in Section 2.4.1, as well as a table containing all force field parameters. The basic parameters involved in every bonded energy contribution will be represented with the help of a small atactic polystyrene chain consisting of three monomers.

- Bond stretching potential for every covalent bond: $\mathcal{V}_{\text{BOND LENGTH}}^{\text{BOND}} = \sum_{\text{all bonds } i} \frac{1}{2} k_{\text{bond}} (l_i - l_{i,0})^2$

with l symbolizing the bond length:

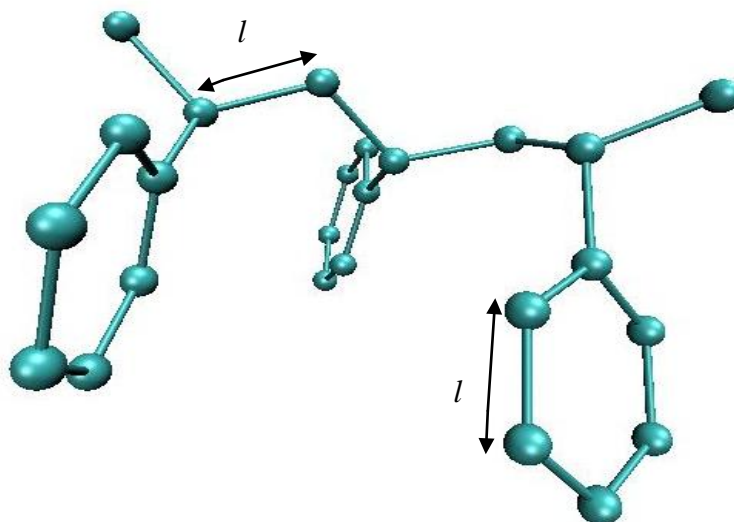


Figure A.1: Graphical depiction of the parameters of the harmonic bond stretching potential energy term.

- Bending potential for all bond angles, both in the backbone chain (θ) and in the

phenyl rings ($\hat{\theta}$): $\mathcal{V}_{\text{BOND ANGLE}}^{\text{BOND}} = \sum_{\text{all bond angles } i} k_{\theta} (\theta_i - \theta_{i,0})^2$, $\mathcal{V}_{\text{BOND ANGLE}}^{\text{PHENYL}} = \sum_{\text{all aromatic bond angles } i} \hat{k}_{\theta} (\hat{\theta}_i - \hat{\theta}_0)^2$

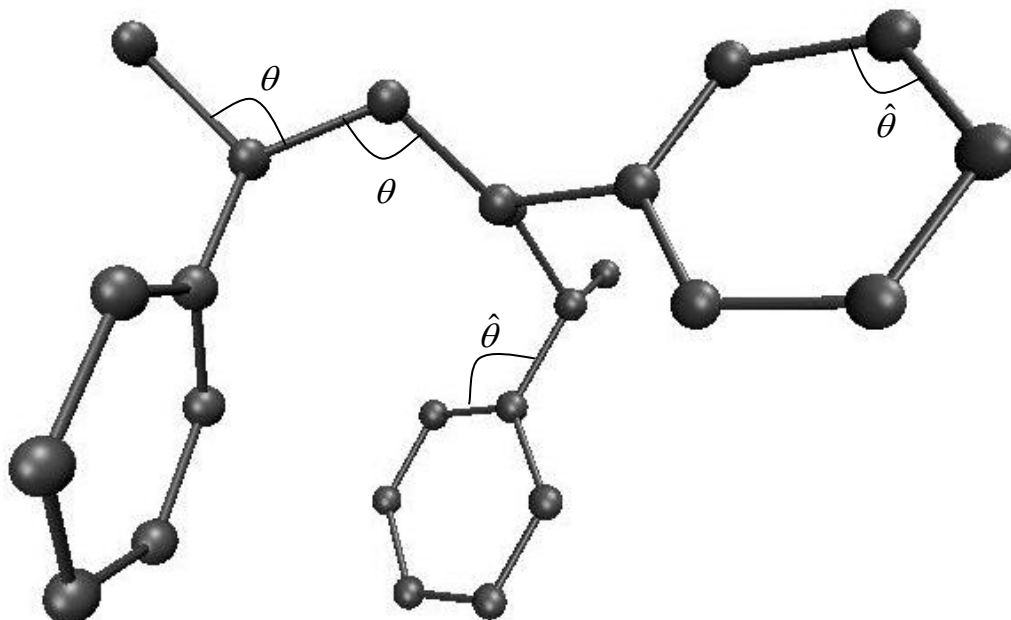


Figure A.2: Graphical representation of the parameters of the bending potential energy term for backbone and phenyl ring angles.

Concerning torsional angles an explanation is in order. In a chain of atoms A-B-C-D, the dihedral angle between the plane containing the atoms A,B,C and that containing B,C,D. In a Newman projection the torsion angle is the angle (having an absolute value between 0° and 180°) between bonds to two specified groups, one from the atom nearer (proximal) to the observer and the other from the further (distal) atom. The torsion angle between groups A and D is then considered to be positive if the bond A-B is rotated in a clockwise direction through less than 180° in order that it may eclipse the bond C-D: a negative torsion angle requires rotation in the opposite sense.

Stereochemical arrangements corresponding to torsion angles between 0° and $\pm 90^\circ$ are called syn (*s*), those corresponding to torsion angles between $\pm 90^\circ$ and 180° anti (*a*). Similarly, arrangements corresponding to torsion angles between 30° and 150° or between -30° and -150° are called clinal (*c*) and those between 0° and 30° or 150° and 180° are called periplanar (*p*). The two types of terms can be combined so as to define four ranges of torsion angle; 0° to 30° synperiplanar (*sp*); 30° to 90° and -30° to -90° synclinal (*sc*); 90° to 150° , and -90° to -150° anticlinal (*ac*); $\pm 150^\circ$ to 180° antiperiplanar (*ap*). The above definitions are depicted in the following figure:

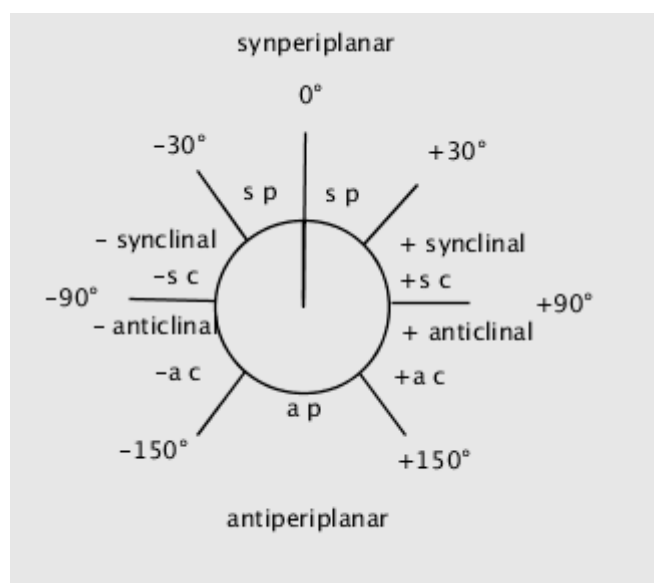


Figure A.3: Adopted convention for the definition of positive torsion angles

- Torsional potential for all rotatable backbone bonds:

$$\mathcal{V}_{\text{TORSIONAL BACKBONE}} = \sum_{\text{all torsion angles } i} k_{\phi} (1 - \cos 3\phi_i)$$

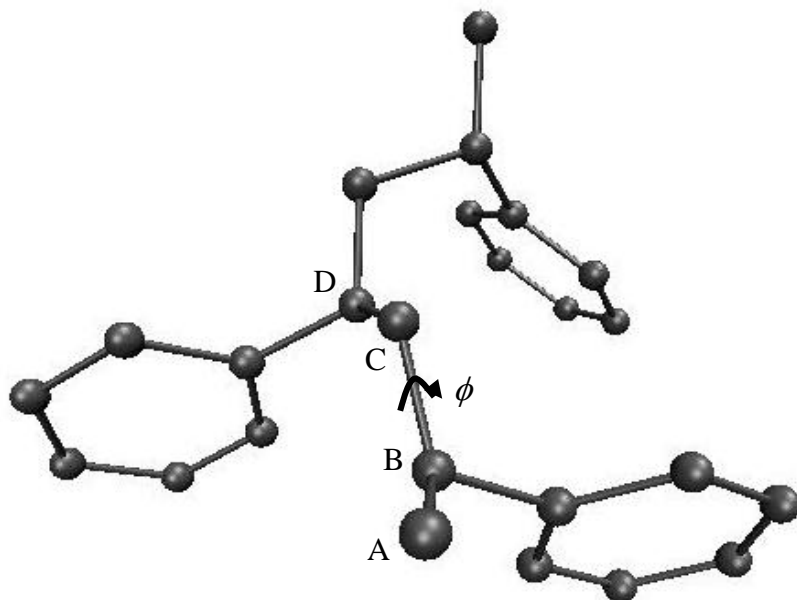


Figure A.4: Backbone torsional angle ϕ around bond B-C corresponding to the angle between the plane formed by the atoms A,B,C and the one formed by backbone atoms B,C,D

- Torsional potential for the torsions of phenyl rings around their stems:

$$\mathcal{V}_{\text{TORSIONAL PHENYL}} = \sum_{\text{all phenyl torsion angles } i} k_{\chi} \cos^2(\chi_i - \chi_0)$$

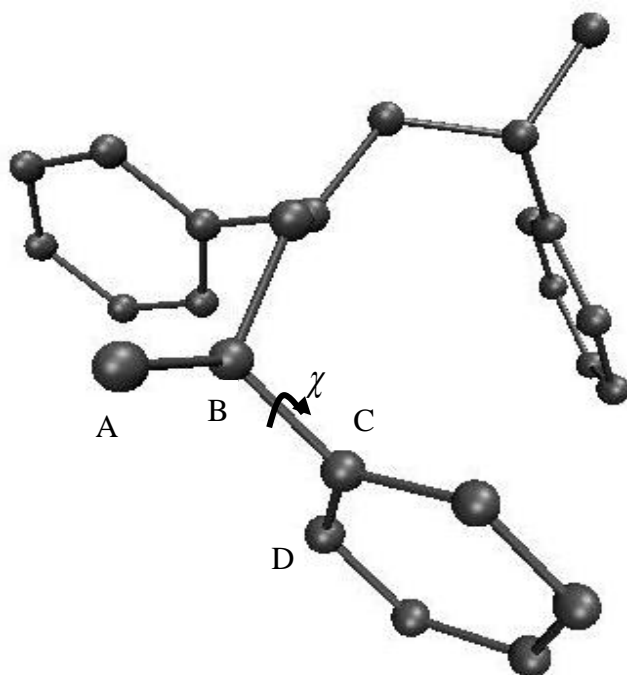


Figure A.5: Torsional angle χ around bond B-C corresponding to the angle between the plane formed by the atoms A,B,C and the one formed by atoms B,C,D

- Out-of-plane bending potential to preserve the coplanarity of the phenyl and the phenyl stem:

$$\mathcal{V}_{\text{COPLANARITY}}^{\text{PHENYL}} = \sum_{\text{all phenyls } i} k_{\psi} (\psi_i - \psi_0)^2$$

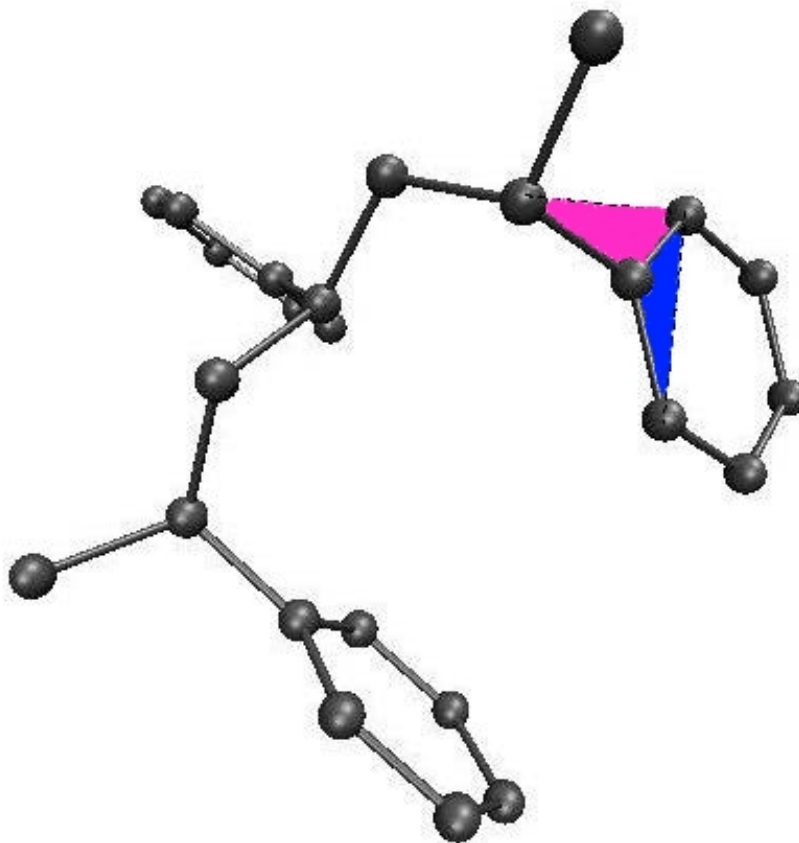


Figure A.6: Torsional angle ψ preserving coplanarity of the phenyl and the phenyl stem. The blue plane accounts for the planarity of the phenyl ring. Every atom of the phenyl ring is on that plane. The angle between the pink plane and the blue one is ψ . The equilibrium value for this angle, ψ_0 , is zero, since the phenyl stem and the phenyl ring should be on the same plane. Through the imposition of a large constant value k_ψ we make sure that the deviation from this equilibrium value is very small.

- Torsional angle $\hat{\phi}$ about all bonds connecting aromatic carbons in the phenyl ring,

to preserve the planarity of the ring:

$$V_{\text{RING PLANARITY}}^{\text{TORSIONAL}} = \sum_{\text{all phenyl torsion angles } i} \hat{k}_\phi (1 + \cos 2\hat{\phi}_i)$$

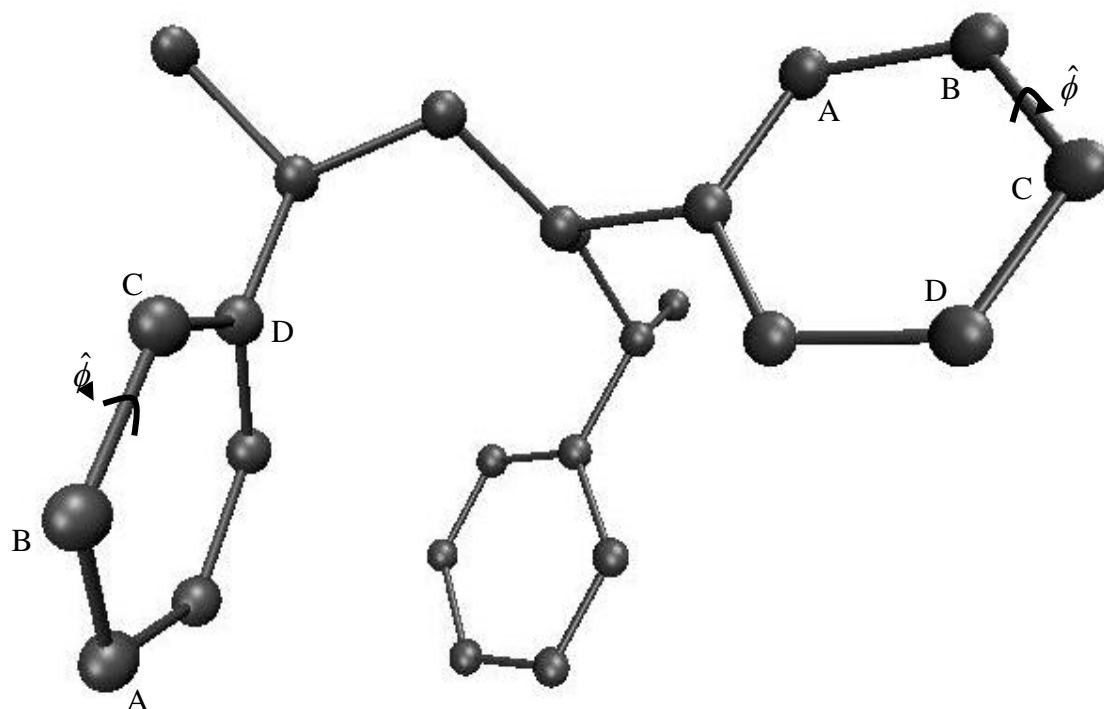


Figure A.7: Torsional angle $\hat{\phi}$ preserving planarity of the phenyl ring. Again in this case, as in the previous one, the equilibrium value for this angle, $\hat{\phi}_0$, is zero, since all aromatic atoms should be coplanar. Through the imposition of a large constant value \hat{k}_ϕ we make sure that the deviation from this equilibrium value is very small.

- Improper torsional potential to preserve the tacticity of every phenyl unit in respect

to the skeletal chain:
$$\mathcal{V}_{\text{IMPROPER}} = \sum_{\substack{\text{all chiral} \\ \text{carbons } m}} \frac{1}{6k'} (\Delta_{129,m} + \Delta_{123,m} + \Delta_{329,m})^6$$

For the definition of this kind of torsional angle, three different planes need to be defined for every monomer unit. The enumeration of the atoms is according to Figure 2.11:

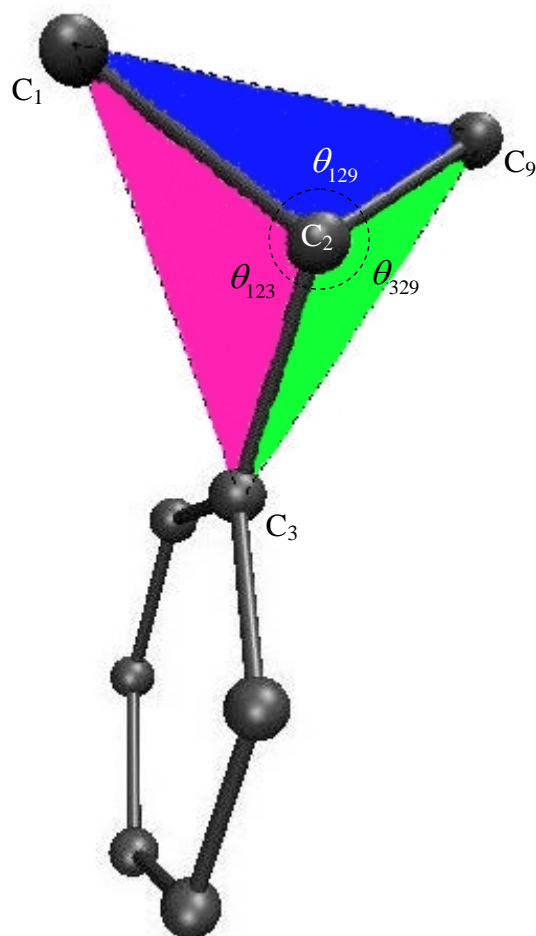


Figure A.8: Graphical representation of the improper torsional potential angles θ_{ijk} to preserve the chirality of all carbons bearing a phenyl substituent.

Followingly, Table A.1 gives the values for all parameters involved in every one of the above mentioned energy terms:

Table A.1: Parameter values for non-bonded and bonded potential energy contributions expressed through Eq. (2.50)

$V_{nb} = \epsilon[(r_0/r)^{12} - 2(r_0/r)^6]; \epsilon = (\epsilon_1\epsilon_2)^{0.5}$ $\epsilon = 0.12 \text{ kcal mol}^{-1}$ $\epsilon = 0.09 \text{ kcal mol}^{-1}$ $\epsilon = 0.12 \text{ kcal mol}^{-1}$ cutoff distance = 9 Å	1. Nonbonded Interactions $r_0 = (r_{0,1} + r_{0,2})/2$ $r_0 = 4.321 \text{ Å for CH}_2$ $r_0 = 4.153 \text{ Å for aliphatic CH}$ $r_0 = 4.153 \text{ Å for aromatic C and CH}$
$V_l = k_l(l - l_0)^2$ $k_l = 317 \text{ kcal mol}^{-1} \text{ Å}^{-2}$ $k_l = 317 \text{ kcal mol}^{-1} \text{ Å}^{-2}$ $k_l = 525 \text{ kcal mol}^{-1} \text{ Å}^{-2}$	2. Bond Lengths $l_0 = 1.53 \text{ Å for aliphatic CH}_2\text{-CH}$ $l_0 = 1.51 \text{ Å for CH(aliph)-C(arom)}$ $l_0 = 1.40 \text{ Å for CH(arom)-CH(arom)}$
$V_\theta = k_\theta(\theta - \theta_0)^2$ $k_\theta = 60 \text{ kcal mol}^{-1} \text{ rad}^{-2}$ $k_\theta = 63 \text{ kcal mol}^{-1} \text{ rad}^{-2}$ $k_\theta = 60 \text{ kcal mol}^{-1} \text{ rad}^{-2}$ $k_\theta = 70 \text{ kcal mol}^{-1} \text{ rad}^{-2}$ $k_\theta = 72 \text{ kcal mol}^{-1} \text{ rad}^{-2}$	3. Bond Angles $\theta_0 = 109.5^\circ \text{ for aliphatic CH}_2\text{-CH-CH}_2$ $\theta_0 = 109.5^\circ \text{ for aliphatic CH-CH}_2\text{-CH}$ $\theta_0 = 109.5^\circ \text{ for CH}_2(\text{aliph})\text{-CH(aliph)-C(arom)}$ $\theta_0 = 120^\circ \text{ for CH(aliph)-C(arom)-CH(arom)}$ $\theta_0 = 120^\circ \text{ for CH(arom)-CH(arom)-CH(arom)}$
4. Backbone Torsion (X-CH(aliph)-CH₂(aliph)-X)	
$V_\varphi = k_\varphi(1 - \cos 3\varphi)$ $k_\varphi = 1.4 \text{ kcal mol}^{-1}$ (trans taken as $\varphi = 0$)	
5. Torsion CH₂(aliph)-CH₂(aliph)-CH(arom)-CH(arom) (Phenyl Ring Torsion Around CH(aliph)-C(arom))	
$V_\varphi = k_\varphi(1 + \cos 2\varphi)$ $k_\varphi = 1 \text{ kcal mol}^{-1}$ (trans taken as $\varphi = 0$)	
6. Torsion CH(arom)-CH(arom)-CH(arom)-CH(arom)	
$V_\varphi = k_\varphi(1 + \cos 2\varphi)$ $k_\varphi = 12.9 \text{ kcal mol}^{-1}$ (trans taken as $\varphi = 0$)	
7. Improver torsion (To Maintain Chirality)	
$U_{imp} = (1/6K)(\Delta_{129} + \Delta_{123} + \Delta_{329})^6$ $\Delta_{ijk} = \cos \theta_{iik} - \cos \theta_0 \text{ with } \theta_0 = 109.5^\circ$ $K = 150k_\theta = 37\,355 \text{ kJ/mol}$	

Appendix B

Assessment of the efficiency of the Wang-Landau Algorithm in sampling the configuration space of the lumping problem

As explained in Section 4.3 of the main text, the lumping problem can be formulated as an equivalent minimization process:

$$\min_{\hat{n}, \mathbf{M}} z \quad (\text{B.1})$$

$$\text{with } z = z_1 W + z_2 E + z_3 \hat{n} \quad (\text{B.2})$$

where the objective function z is a linear combination of the long-time dynamics parameter W defined via Eq. (4.16), the lumping error E defined via Eqs. (4.9 - 4.12) and (4.14), and the size \hat{n} of the lumped system. In our calculations concerning the network of basins of a glassy Lennard-Jones mixture, the coefficients z_1 , z_2 , and z_3 are set to 0.5 ps, 0.3 ps, and 0.2, respectively. The minimization takes place with respect to the size \hat{n} of the lumped system and with respect to the structure (choice of “0” or “1” as elements) of the $\hat{n} \times n$ lumping matrix \mathbf{M} , subject to the constraint that every column of \mathbf{M} contains exactly one “1” and that every row contains at least one “1” (see also Section 4.2.1 of the main text).

In the main text we have described a Wang-Landau type algorithm for exploring the configuration space (\hat{n}, \mathbf{M}) , accumulating the density of states associated with various values of z , and identifying configurations of minimal z . In this Appendix we present

evidence that this algorithm is more efficient than alternative, more conventional, algorithms for exploring the same configuration space.

In particular, the assessment of the overall efficiency of the proposed Wang-Landau algorithm is sampling the configuration space of the lumping problem is implemented through a set of supplementary simulations. To address the efficiency of our algorithm, we have focused on a smaller network of basins than the one treated in Section 4.4 of this text. This smaller network encompasses 290 basins. We have employed our Wang-Landau scheme to explore the (\hat{n}, \mathbf{M}) space for lumping this network. In parallel, we have sampled the same space with Metropolis Monte Carlo simulations, using the objective function z (Eq. B.(2)) as the equivalent of an energy function and setting the “thermal energy” $k_B T$ equal to 1. Simulation results from both the Wang-Landau and Metropolis Monte Carlo runs are shown in Figures B.1 to B.4, where it becomes evident that the applied Wang-Landau MC scheme is indeed more efficient than alternative, more conventional algorithms for exploring the same configuration space.

In particular, in Figures B.1 to B.3 we plot the lumping error E , the long-time dynamics parameter W , and the lumped size \hat{n} for sampled (\hat{n}, \mathbf{M}) configurations of the 290-basin test system, as functions of the CPU time. These quantities are given for both Wang-Landau and for Metropolis sampling. The full objective function $z = z_1 W + z_2 E + z_3 \hat{n}$ as a function of CPU time is shown in Figure B.4 for both sampling schemes.

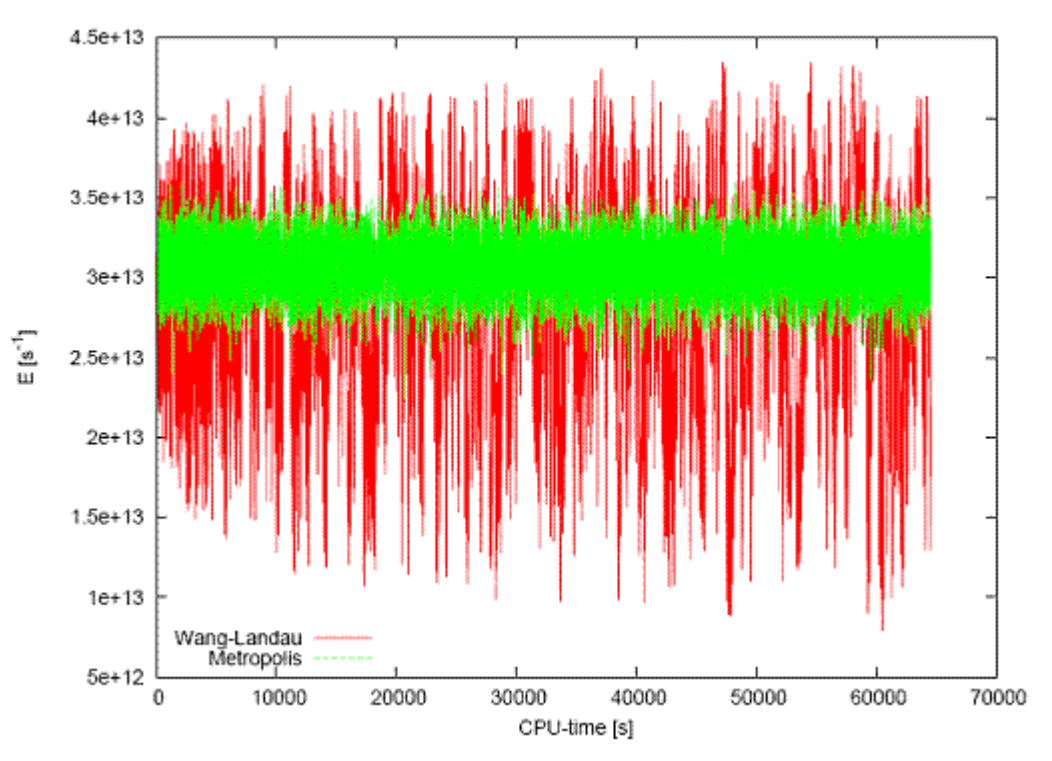


Figure B.1: Lumping error E as a function of CPU time for Wang-Landau sampling and for Metropolis sampling of the (\hat{n}, \mathbf{M}) configuration space considered for lumping a network of 290 basins of the glassy Lennard-Jones mixture described in the main text.

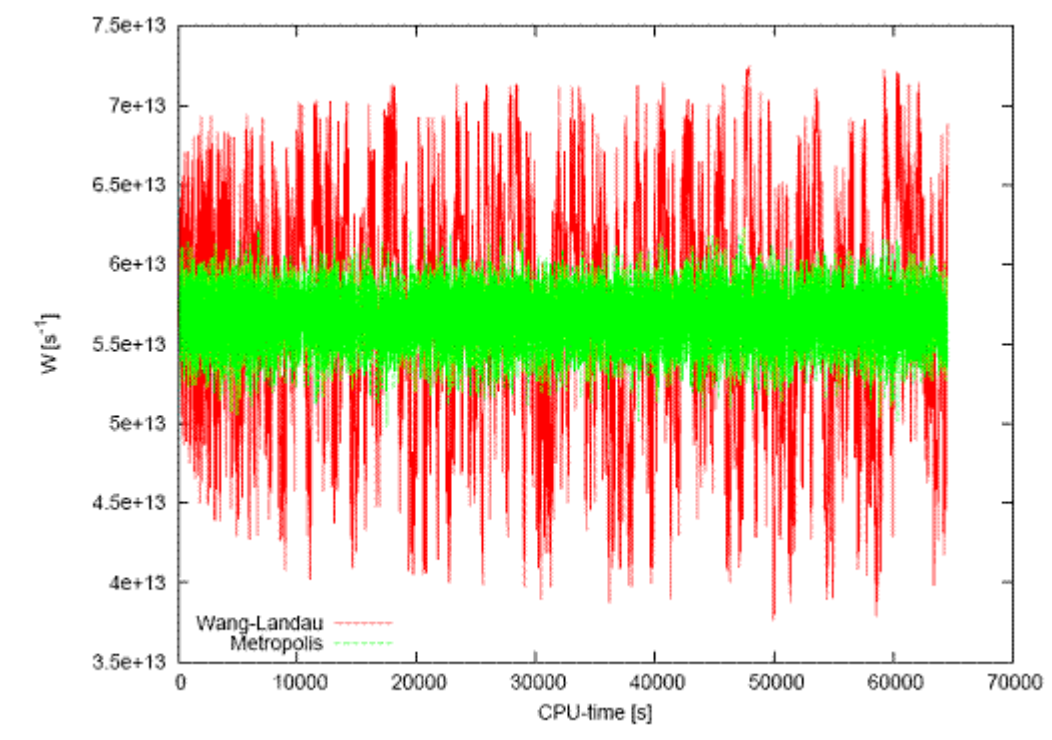


Figure B.2: Long-time dynamics parameter W as a function of CPU time for Wang-Landau sampling and for Metropolis sampling of the (\hat{n}, \mathbf{M}) configuration space considered for lumping a network of 290 basins of glassy Lennard-Jones mixture.

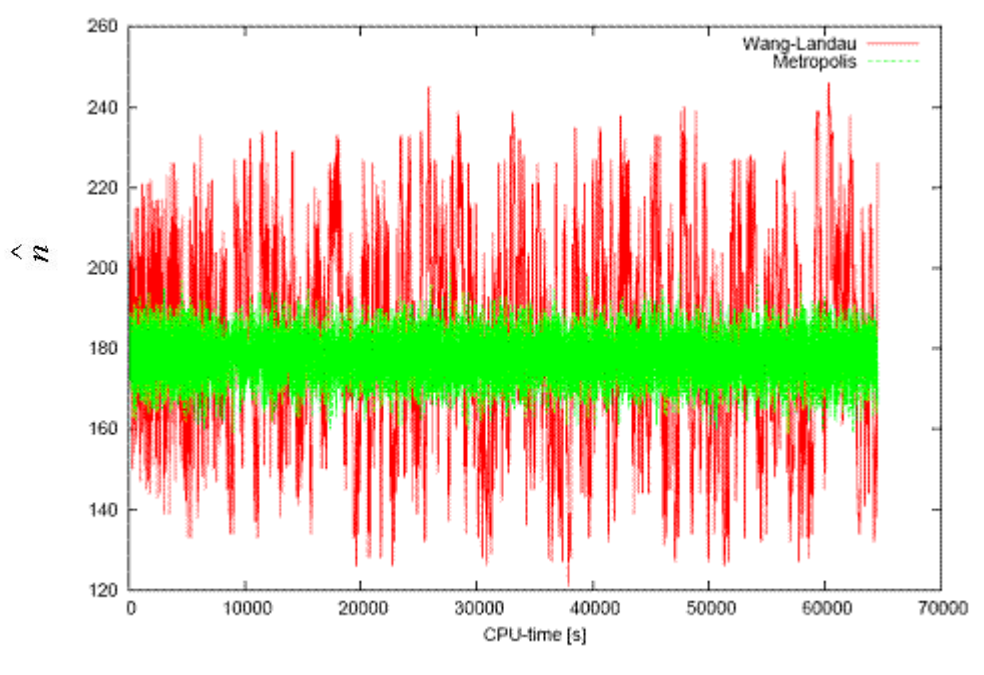


Figure B.3: Size \hat{n} of lumped system as a function of CPU time for Wang-Landau sampling and for Metropolis sampling of the (\hat{n}, \mathbf{M}) configuration space considered for lumping a network of 290 basins of the glassy Lennard-Jones mixture.

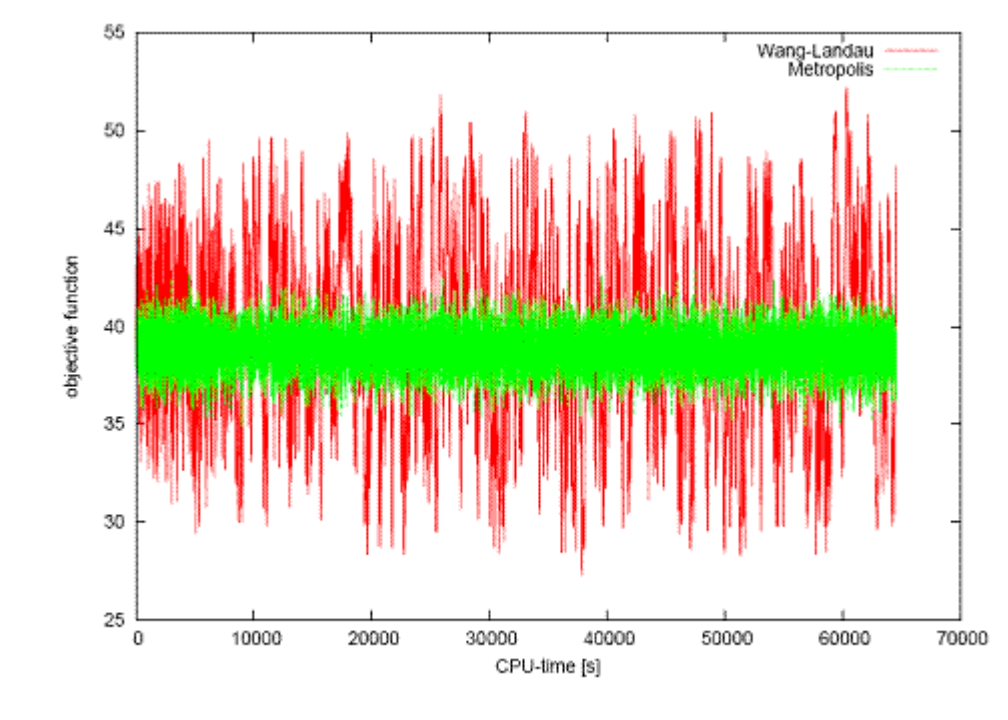


Figure B.4: Objective function $z = z_1 W + z_2 E + z_3 \hat{n}$ as a function of CPU time for Wang-Landau sampling and for Metropolis sampling of the (\hat{n}, \mathbf{M}) configuration space considered for lumping a network of 290 basins of glassy Lennard-Jones mixture.

Clearly, the Wang-Landau scheme visits a wide range of configurations characterized by a much broader range of E , W , \hat{n} , and z values than the Metropolis Monte Carlo scheme. In the latter, fluctuations are much smaller; for the whole duration of the simulation, the Metropolis Monte Carlo run appears trapped in the vicinity of a small set of local minima of z . In Figure B.5 is shown the minimum value of the objective function z sampled by either one of the two schemes as a function of CPU time.

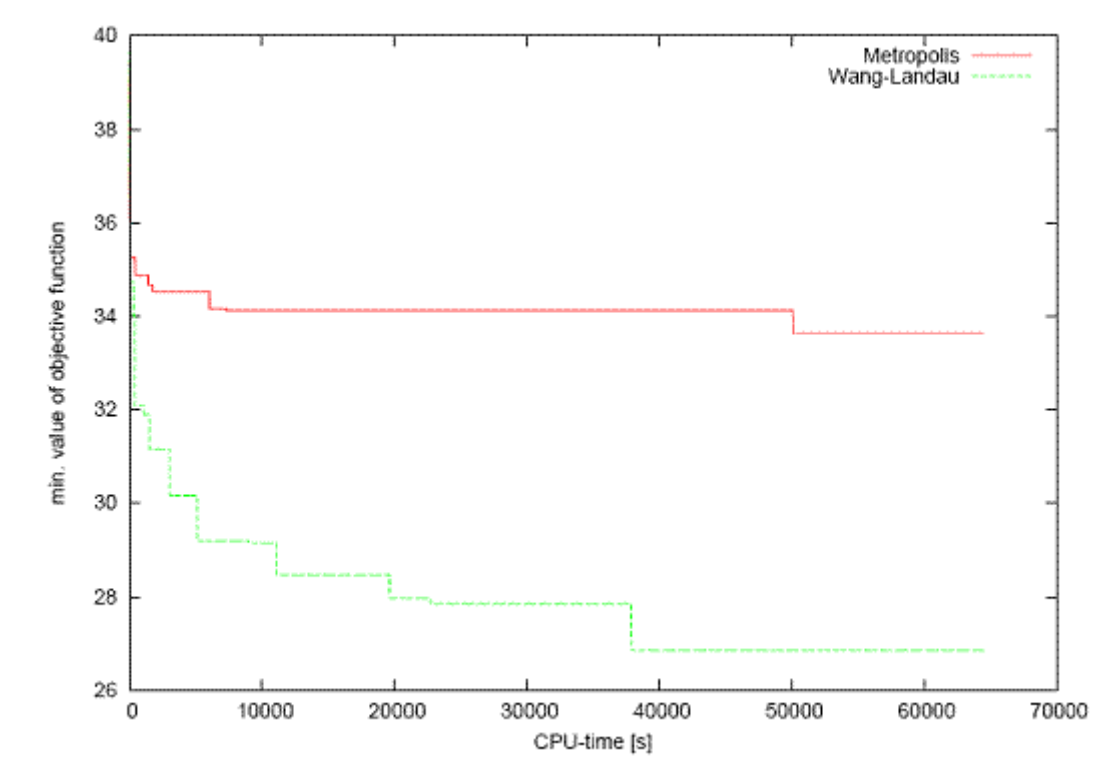


Figure B.5: Minimum value of the objective function among all visited configurations as a function of CPU time for Wang-Landau sampling and for Metropolis sampling of the (\hat{n}, \mathbf{M}) configuration space considered for lumping a network of 290 basins of the glassy Lennard-Jones mixture.

Clearly, the Wang-Landau scheme is much more effective in accessing configurations of low z . Therefore, it provides a much more satisfactory solution to problem of minimizing z than the Metropolis Monte Carlo scheme. The comparative advantage of the proposed Wang-Landau scheme in optimizing the lumping is evident from Figure B.5.

Curriculum Vitae

Nikolaos Lempesis

33 An. Manaki Str., Ilion Attikis, Athens, Greece, 131 22

Mobile: +30 694 2696621

Email: nic.0s@hotmail.com

RESEARCH INTERESTS

Mathematical, computational and simulation sciences that translate to the cutting edge of materials research. Developing and delivering theoretical frameworks that describe the underlying structure-property-function relationships to advance novel scientific endeavors. Facilitating the fusion of theory and experimentation by intelligent and intuitive software technologies.

POSITION

2008-now PhD student in COmputational Materials Science and Engineering group (CO.M.S.E),

Department of Materials Science and Engineering,

School of Chemical Engineering,

National Technical University of Athens (NTUA)

Project Title: "Molecular simulation of glass forming materials"

Role: to develop computational tools to aid material scientists in their research, discoveries and commercial activities.

BOARDS AND APPOINTMENTS

- 2008-now Member of the NTUA-council of PhD students
- 2003-now Member of the Top Industrial Managers of Europe (T.I.M.E.) association

EDUCATION

- 2008-now Doctor of Philosophy student in Chemical Engineering and Material Science, NTUA, Athens, Greece
- Title: "Molecular simulation of glass forming materials"
- 2007 Honors in graduation from NTUA, achieved 2nd rank with graduation grade 9.2/10, NTUA, Athens, Greece
- Diploma Thesis Title: "Computational study of the vitrification process by molecular simulation: the existence of inherent structures and their significance."
- 2006 Term paper in department of Fluid-process engineering, Technical University of Munich (TUM), Germany
- Project Title: "Multi-components diffusion in non-ideal liquid mixtures"
- 2005 Term paper in department of Biotechnology, TUM, Germany
- Project Title: "Redox enzymes in *Saccharomyces cerevisiae*"
- 2003-2007 Diploma in Chemical Engineering in direction Biotechnology in the context of the T.I.M.E. double-degree program, TUM, Munich, Germany (Graduation grade 1.9)
- 2000-2007 Diploma in Chemical Engineering in direction Material Science, NTUA, Athens, Greece
- 1995-2000 Higher School Certificate, 1st General Lyceum Ilion, Athens, Greece

INDUSTRIAL INTERNSHIP

- 2005-2006 Degussa AG: Computer Aided Process Engineering (CAPE) department. Project title: Dynamic simulation and optimization of a distillation column in the presence of a chemical reaction under use of the Aspen process simulation package. Rodenbacher Chaussee 4, D-63457 Hanau-Wolfgang, Germany

AWARDS, GRANTS, PROPOSALS AND SCHOLARSHIPS

- 2012 Award from the Technical Chamber of Greece (T.E.E.) for academic achievements at NTUA
- 2011 HPC-Europa2 Transnational Access program fellowship to visit GENCI-CINES (Oct 1, 2011 – Dec 31, 2011) in Paris-Montpellier/France
- 2010 “Thomaidion award” 2010 for scientific publication
- 2010 National Strategic Reference Framework (NSRF), Enhancement of research man power through the implementation of thesis – HERACLITUS II/ Hellenic Ministry of National Education and Religious Affairs: PhD scholarship (Sep 1, 2010 – Aug 31, 2013) for the project entitled “Molecular simulations of glass forming materials”
- 2008 Awarded with the silver medal “Prometheus Pyrforos”, emblem of NTUA, for graduating second in rank in the year 2007
- 2007-2009 Scholarship of the Department of Materials Science and Engineering of the NTUA
- 2007-2008 Scholarship of the Bodossakis Foundation
- 2007 Scholarship and award for the academic years 2000,2001 and 2003 offered by the National Scholarship Foundation of Greece (I.K.Y.) for the best effort during the first three academic years at NTUA.
- 2003 Scholarship from the European Union in support of the participation to the T.I.M.E. Double Degree Program
- 2000-2003 Kefalogianni award concerning the highest grades achieved for the period 2000-2003 at the NTUA.

COMMUNITY ENGAGEMENT

- Aug 2009 Member of the Organizing Committee, Diffusion Fundamentals III conference, Athens, Greece
- May 2007 Member of the International Organizing Committee, Conference on Properties and Phase Equilibria for Product and Process Design (PPEPPD 2007), Hersonissos, Crete, Greece

EMPLOYMENT

Jan 08- now Tutor and supervisor, Laboratory experiments of core undergraduate course Physical Chemistry II, NTUA

CO-SUPERVISION

2011-2012 Diploma Thesis student, Brotzakis Zacharias-Phaedon P., "Study of the dynamic behavior of atactic polystyrene", Computational Materials Science and Engineering Group, School of Chemical Engineering, NTUA

COURSES

Physical Chemistry II: States of matter – Phase Equilibria

SOFTWARE & CODING SKILLS

Mathematica, Matlab, Aspen, Microsoft (all), LINUX-UNIX,

Fortran 90 and Fortran 77, C, python, parallel programming in MPI

PUBLICATIONS

Researcher ID: <http://www.researcherid.com/rid/I-4765-2012>

H-index of 3, total citations of 25 and average impact factor of 3.52

1. N. Lempesis, G. G. Vogiatzis, G. C. Boulougouris, L. C. A. van Breemen, M. Hütter, and D. N. Theodorou, "Tracking a glassy polymer on its energy landscape in the course of elastic deformation", *Molecular Physics*, **2013**, 1
[Impact factor 1.670, Citations 0]
2. N. Lempesis, G. C. Boulougouris, D. N. Theodorou, "Temporal disconnectivity of the energy landscape in glassy systems", *J. Chem. Phys.*, **2013**, 138, 12A545
[Impact factor 3.333, Citations 0]
3. N. Lempesis, G. C. Boulougouris, D. N. Theodorou, "Lumping analysis for the prediction of long-time dynamics: from monomolecular reaction systems to inherent structure dynamics of glassy materials", *J. Chem. Phys.*, **2011**, 135, 204507
[Impact factor 3.333, Citations 2]

4. D. Tsalikis, N. Lempesis, G. C. Boulougouris, D. N. Theodorou, "Efficient parallel decomposition of dynamical sampling in glass forming materials based on an "on the fly" definition of metabasins.", *J. Chem. Theory Comput.*, **2010**, 6(4), 1307-1322
[Impact factor 5.215, Citations 4]
5. D. Tsalikis, N. Lempesis, G. C. Boulougouris, D. N. Theodorou, "Temperature accelerated dynamics in glass forming materials", *J. Phys. Chem. B*, **2010**, 114, 7844-53
[Impact factor 3.696, Citations 2]
6. D. Tsalikis; N. Lempesis; G. C. Boulougouris.; D.N. Theodorou.; "On the role of "inherent structures" in glass-forming materials: II. Reconstruction of the Mean Square Displacement by rigorous "lifting" of the inherent structure dynamics", *J. Phys. Chem. B*, **2008**, 112, 10628-10637
[Impact factor 3.696, Citations 7]
7. D. Tsalikis; N. Lempesis; G. C. Boulougouris.; D.N. Theodorou, "On the role of "inherent structures" in glass-forming materials: I. The vitrification process", *J. Phys. Chem. B.*, **2008**, 112, 10619-10627
[Impact factor 3.696, Citations 10]

CONFERENCE PAPERS AND POSTERS

1. N. Lempesis, G. C. Boulougouris, **D. N. Theodorou**, "Energy landscape analysis of atomic and polymer glasses", September 19th-21st 2012, Mainz Germany
2. N. Lempesis, G. C. Boulougouris, **D. N. Theodorou**, "Tracking the Dynamics of Systems Evolving through Infrequent Transitions in a Network of Discrete States", IAS Series 10 Hierarchical Methods for Dynamics in Complex Molecular Systems Lecture Notes, IAS Winter School, 5-9 March 2012, Jülich, Germany edited by J. Grotendorst, G. Sutmann, G. Gompper, D. Marx (2012)
3. D. Tsalikis, **N. Lempesis**, G. C. Boulougouris, D. N. Theodorou, "Energy Landscape-Based Study of Atomic Displacements in Glass Forming Materials", *Special Issue "Diffusion Fundamentals III"*, **11** (2009) 65, pp 1-2
4. D. Tsalikis, N. Lempesis, G. C. Boulougouris, **D. N. Theodorou**. "On the role of inherent structure dynamics in glass forming materials", AIChE Annual Meeting, Philadelphia, PA November 16-21, 2008

LANGUAGES

Greek, English, German

OTHER INTERESTS

Sports

Basketball, Trekking, Swimming, Spear fishing and Diving

Dancing

Music

Travel

England, France, Italy, the Netherlands, Cyprus, Germany and USA.

REFEREES

- Prof. Doros N. Theodorou Supervisor,
Department of Materials Science and Engineering,
School of Chemical Engineering,
National Technical University of Athens (NTUA)
9, Heroon Polytechniou Str., Zografou Campus, GR-157 80
Athens, Greece
Contact: phone +30 210-772-3157 | fax +30 210-772-3112 |
email doros@central.ntua.gr
- Dr. Georgios C. Boulougouris Adjunct Lecturer,
Department of Molecular Biology and Genetics
Democritus University of Thrace
GR-68100 Alexandroupolis
Contact: phone +30 210 6535098 | fax - | email
georgios.boul@gmail.com
- Dr. ir. Lambert C.A. van Breemen Assistant Professor,
Polymer Technology,
Department of Mechanical Engineering,
Technical University of Eindhoven (TUE)
Room: GEM-Z 4.136, P.O. Box 513, 5600 MB EINDHOVEN
Contact: phone +31 40-247 3092 | fax +31 40 244 7355 | email
l.c.a.v.breemen@tue.nl